UNIVERSITY OF CALIFORNIA
Los Angeles

Rediscovering the Crystal Chemistry of Superhard Dodecaborides and Other Higher Borides

A dissertation submitted in partial satisfaction of the
requirements for the degree Doctor of Philosophy
in Chemistry

by

Georgiy Akopov

2018

ABSTRACT OF THE DISSERTATION

Rediscovering the Crystal Chemistry of
Superhard Dodecaborides and
Other Higher Borides

by

Georgiy Akopov
Doctor of Philosophy in Chemistry
University of California, Los Angeles
Professor Richard B. Kaner, Chair

Almost all items used in everyday life are a result of the processing industry, as seen in the machining of modern metals to form appliances and car parts, precision machining parts for phones and computers, and drill tools for extracting oil to be used to power cars and provide reagents for plastics and chemical synthesis. Many tools used today are made using diamond. Diamond is the hardest mineral due to its structure, where the high density of carbon atoms and the large number of short covalent bonds produce both ultra-incompressibility and a large shear modulus. Due to both of these factors, diamond is superhard (Vickers hardness above 40 GPa), and is of utmost importance for such multi-billion dollar industrial processes as cutting (machining) and drilling (oil industry). However, diamond is expensive, both natural and man-made, due to supply limitations and synthetic costs of production from the high-pressure high-temperature conditions needed. Moreover, diamond readily forms carbides with iron and as such cannot be used to cut steel or other ferrous metals. As such, the majority of tools for cutting and machining are made

using less expensive tungsten carbide (WC). Unlike diamond, WC is a metal, therefore it can be processed (shaped and cut) using common electric discharge machining. Moreover, tungsten carbide is not superhard, having a hardness of only 25 GPa; therefore, the development of superhard substitutions is an important area of exploration.

The primary focus for the development of superhard metals to date has been on new compositions and crystal structures, as well as intrinsic and extrinsic hardening effects using solid-solution formation and morphological control of the surface and grain structure. The search for new superhard metals stands on the shoulders of boride crystallography. Metal borides come in a large variety of possible structures, primarily defined by the way the boron atoms are arranged: isolated boron atoms (e.g. Cr_4B), single and double chains (e.g. CrB and Ta_3B_4), networks of boron atoms (e.g. AlB_2, ReB_2, WB_4, ZrB_{12}), and structures based on boron icosahedra, B_{12} (e.g. ZrB_{50} and GdB_{66}). The first reported superhard metal boride was our work on rhenium diboride (ReB_2) however, due to the limited supply and cost of rhenium, there has been a great incentive to investigate the possibility of using less expensive metals. This resulted in the cheaper alternative superhard borides: tungsten tetraboride (WB_4) and dodecaborides (ZrB_{12} and YB_{12}). This in turn resulted in the metal boride field expanding to the use of alloys and solid-solutions via doping with metals analogous to tungsten (i.e. group 5, e.g. Ta and Nb), thus enhancing the bulk modulus and using structures with a 3D backbone of boron atoms ("cage"-structures) increasing the material's shear resistant due to it becoming more isotropic. However, metal borides also possess a large variety of ternary and higher order metal borides with unique structures and properties and this constitutes a significant part of the current work reported here. Such ternary metal borides have essentially been "forgotten" as apart from papers on the crystal structure of such phases, over the

past 50 years there have been only 2 papers on properties, both of which only reported electronic properties. Therefore, these phases represent a treasure trove of research opportunities.

The goal of this project has been to investigate higher borides (i.e. dodecaborides) for their properties. Furthermore, the project has attempted to expand the field of superhard material compositions by delving into the unstable/metastable phase space stabilizing high-pressure, high-temperature phases through solid solutions formation at ambient pressure.

The dissertation of Georgiy Akopov is approved.

William M. Gelbart

Hosea Martin Nelson

Stuart Brown

Richard B. Kaner, Committee Chair

University of California, Los Angeles

2018

Dedicated in loving memory of

my late mother, Nino Manelashvili

TABLE OF CONTENTS

LIST OF FIGURES

LIST OF TABLES

ACKNOWLEDGEMENT

The four years I have spent in the graduate school have been very interesting and somewhat strange. I have learned that research can be a very slow and painful process with many dead ends, however, I can also be very fulfilling and rewarding once you figure out the correct way of conducting a particular series of experiments or when an analysis proves one of your hypotheses.

I would like to express my gratitude to my advisor, Prof. Ric Kaner, for making graduate school a fun and rewarding experience and to my undergraduate advisor, Prof. Roger Lalancette, and Prof. Ivan Bernal for really falling in love with chemistry and crystallography. I would also like to thank my first undergraduate advisor, Prof. Jenny Lockard, for convincing me to try doing research.

A special thanks goes to my dissertation committee members Profs. Ric, Kaner, Hosea Nelson, William Gelbart and Stuart Brown.

Working on superhard materials involves making and analyzing an unholy amount of samples, and I would like to thank my undergraduates: Zach Sobell, Inwhan Roh and Hang Yin for weighing, arc-melting and polishing more than 1500 samples. I would like to thank Dr. Chris Turner for teaching me arc-melting. I would like to express my gratitude to Dr. Michael Yeung for spending the countless hours doing Vickers hardness in Dr. Ben Wu's lab and taking SEM images and performing EDS analysis on the fancy SEM instrument in the Engineering department.

I would also like to thank my labmates Cheng-Wei Lin and Wai Mak for the fun years in the lab and trips to Disneyland, Universal Studios as well as ACS research conferences in San Francisco and New Orleans.

I would also like to mention my other labmates Jialin Lei, Shanlin Hu, Matt Kowal, Lisa Pangilinan, Lindsay Chaney, Mit Muni and Stephanie Aguilar.

Finally I would like to thank my father and my late mother for shaping me into a person I am today.

Chapter 1 is reprinted (adapted) with permission from (Akopov, G.; Yeung, M.T.; Kaner, R.B. "Rediscovering the Crystal Chemistry of Borides" *Adv. Mater.* **2017**, 1604506 DOI: 10.1002/adma.201604506). Copyright (2017) John Wiley and Sons. Co-author contribution: Michael T. Yeung wrote sections on properties of the review paper, Richard B. Kaner was the P.I.

Chapter 2 is reprinted (adapted) with permission from (Akopov, G.; Yeung, M.T.; Sobell, Z.C.; Turner, C.L.; Kaner, R.B. "Superhard Mixed Transition Metal Dodecaborides" *Chem. Mater.* **2016**, *28*, 6605-6612 DOI: 10.1021/acs.chemmater.6b02632). Copyright (2016) American Chemical Society. Co-author contribution: Michael T. Yeung performed SEM/EDS analysis, Zachary C. Sobell and Christopher L. Turner prepared samples, Richard B. Kaner was the P.I.

Chapter 3 is reprinted (adapted) with permission from (Akopov, G.; Yeung, M. T.; Turner, C. L.; Li, R. L.; Kaner, R. B. "Stabilization of HfB_{12} in $Y_{1-x}Hf_xB_{12}$ under Ambient Pressure" *Inorg. Chem.* **2016**, 55, 5051−5055 DOI: 10.1021/acs.inorgchem.6b00627). Copyright (2016) American Chemical Society. Co-author contribution: Michael T. Yeung performed SEM/EDS analysis, Christopher L. Turner prepared samples, Rebecca L. Li performed Raman analysis Richard B. Kaner was the P.I.

Chapter 4 is reprinted (adapted) with permission from (Akopov, G.; Sobell, Z.C.; Yeung, M. T.; Kaner, R. B. "Stabilization of LnB_{12} (Ln = Gd, Sm, Nd, and Pr) in $Zr_{1-x}Ln_xB_{12}$ under Ambient Pressure" *Inorg. Chem.* **2016**, 55 (23), 12419-12426 DOI: 10.1021/acs.inorgchem.6b02311). Copyright (2016) American Chemical Society. Co-author contribution: Michael T. Yeung performed SEM/EDS analysis, Zachary C. Sobell prepared samples, Richard B. Kaner was the P.I.

Chapter 5 is a version of Akopov, G.; Roh, I.; Sobell, Z.C.; Yeung, M. T.; Kaner, R. B. "Investigation of Ternary Metal Dodecaborides ($M_1M_2M_3)B_{12}$ (M_1, M_2 and M_3 = Zr, Y, Hf and Gd)" *Dalton Trans.* **2018**, 47, 6683-6691. Co-author contribution: Michael T. Yeung performed SEM/EDS analysis, Inwhan Roh and Zachary C. Sobell prepared samples, Richard B. Kaner was the P.I.

Chapter 6 is reprinted (adapted) with permission from (Akopov, G.; Yeung, M. T.; Turner, C.L.; Mohammadi, R.; Kaner, R. B. "Extrinsic Hardening of Superhard Tungsten Tetraboride Alloys with Group 4 Transition Metals" *J. Am. Chem. Soc.* **2016**, 138 (17), 5714–5721 DOI: 10.1021/jacs.6b02676). Copyright (2016) American Chemical Society. Co-author contribution: Michael T. Yeung performed SEM/EDS analysis, Christopher L. Turner prepared samples, Reza Mohammadi was co-P.I., Richard B. Kaner was the P.I.

Chapter 7 is reprinted (adapted) with permission from (Akopov, G.; Roh, I.; Sobell, Z.C.; Yeung, M. T.; Pangilinan, L.; Turner, C.L.; Kaner, R. B. "Effects of Variable Boron Concentration on the Properties of Superhard Tungsten Tetraboride" *J. Am. Chem. Soc.* **2017**, 139, 17120–17127 DOI: 10.1021/jacs.7b08706). Copyright (2017) American Chemical Society. Co-author contribution: Michael T. Yeung performed SEM/EDS analysis, Inwhan Roh, Zachary C. Sobell, Lisa Pangilinan and Christopher L. Turner prepared samples, Richard B. Kaner was the P.I.

Chapter 8 is a version of Akopov, G.; Yeung, M. T.; Roh, I.; Sobell, Z.C.; Yin, H.; Mak, W.H.; Khan, S.I.; Kaner, R. B. "Effects of Dodecaboride Forming Metals on the Properties of Superhard Tungsten Tetraboride" *Chem. Mater.* **2018**, 30(10), 3559–3570. Co-author contribution: Michael T. Yeung performed SEM/EDS analysis, Inwhan Roh, Zachary C. Sobell and Hang Yin prepared

samples, Wai H. Mak performed XPS analysis, Saeed I. Khan performed single crystal XRD data collection and structure determination, Richard B. Kaner was the P.I.

Chapter 9 is a version of Akopov, G.; Pangilinan, L.; Mohammadi, R; Kaner, R.B. “Perspective: Superhard Metal Borides: A Look Forward” *APL Mater.* **2018**, *6*, 070901. All article content, except where otherwise noted, is licensed under a Creative Commons Attribution (CC BY) license (http://creativecommons.org/licenses/by/4.0/). All co-authors contributed equally to the writing of the perspective review.

I would like to express my gratitude to Professor Benjamin M. Wu of the UCLA Department of Bioengineering for the use of the micro-indentation system in his laboratory (chapters 2-4 and 6).

I would like to thank the National Science Foundation Division of Materials Research, Grant DMR-1506860 (R.B.K., chapters 1-9), Virginia Commonwealth University Startup Grant 137422 (R.M., chapter 6), and the National Science Foundation IGERT-MCTP Fellowship program (M.T.Y., chapters 1-4 and 6) for financial support.

VITA

2014 - 2018	Graduate Student Researcher with Prof. Richard Kaner University of California, Los Angeles Los Angeles, California
2014 - 2018	Teaching Assistant University of California, Los Angeles Los Angeles, California
2018	Inorganic Chemistry Dissertation Award University of California, Los Angeles Los Angeles, California
2018	Dissertation Year Fellowship University of California, Los Angeles Los Angeles, California
2018	Faculty Award for Innovation in Inorganic Chemistry University of California, Los Angeles Los Angeles, California
2014	Harold A. Fales Memorial Award Rutgers, The State University of New Jersey Newark, New Jersey
2012 - 2014	Bachelor of Arts in Chemistry (*Summa Cum Laude*) Rutgers, The State University of New Jersey Newark, New Jersey
2013	Summer Chemistry Research Fellowship Rutgers-Newark, The State University of New Jersey Newark, New Jersey
2013 - 2014	Undergraduate Researcher with Prof. Roger A. Lalancette Rutgers, The State University of New Jersey Newark, New Jersey
2012 - 2013	Undergraduate Researcher with Prof. Jenny Lockard Rutgers, The State University of New Jersey Newark, New Jersey
2012 - 2014	Phi Theta Kappa Honor Society Scholarship Rutgers, The State University of New Jersey Newark, New Jersey

LIST OF PUBLICATIONS

1. Akopov, G.; Yin, H.; Roh, I.; Pangilinan, L.E.; Yeung, M.T.; and Kaner, R.B. "Investigation of Hardness of Ternary Borides of the $YCrB_4$, Y_2ReB_6, Y_3ReB_7 and YMo_3B_7 Types" *Chem. Mater.* **2018**, 30 (18), 6494–6502.
2. Akopov, G.§; Pangilinan, L.E.**§**; Mohammadi, R.; and Kaner, R.B. *Invited Perspective:* "Superhard Metal Borides - A Look Forward" *APL Materials* **2018**, 6, 070901.
3. Akopov, G.; Roh, I.; Sobell, Z.C.; Yeung, M.T.; and Kaner, R.B. "Investigation of Ternary Metal Dodecaborides $(M_1M_2M_3)B_{12}$ (M_1, M_2 and M_3 = Zr, Y, Hf and Gd)" *Dalton Trans.* **2018**, 47, 6683-6691.
4. Akopov, G.; Yeung, M.T.; Roh, I.; Sobell, Z.C.; Khan, S.I.; and Kaner, R.B. "Effcts of Dodecaboride Forming Metals on the Properties of Superhard Tungsten Tetraboride" *Chem. Mater.* **2018**, 30(10), 3559–3570.
5. Akopov, G.; Yeung, M.T.; Roh, I.; Sobell, Z.C.; Pangilinan, L.E.; Turner, C.L.; and Kaner, R.B. "Effects of Variable Boron Concentration on the Properties of Superhard Tungsten Tetraboride" *J. Am. Chem. Soc.* **2017**, *139* (47), 17120–17127.
6. Akopov, G.§, Yeung, M.T.§, Kaner, R.B. *Review Article:* "Rediscovering the Crystal Chemistry of Borides" *Adv. Mater.* **2017**, 1604506.
7. Akopov, G.§; Sobell, Z.C.§; Yeung, M.T.; and Kaner, R.B. "Stabilization of LnB_{12} (Ln = Gd, Sm, Nd, and Pr) in $Zr_{1-x}Ln_xB_{12}$ under Ambient Pressure" *Inorg. Chem.* **2016**, *55* (23), 12419–12426.
8. Akopov, G.; Yeung, M.T.; Sobell, Z.C.; Turner, C.L.; Lin, C.-W.; and Kaner, R.B. "Superhard Mixed Metal Dodecaborides" *Chem. Mater.* **2016**, 28 (18), 6605-6612.
9. Akopov, G.; Yeung, M.T.; Turner, C.L.; Li, R.L.; and Kaner, R.B. "Stabilization of HfB_{12} in $Y_{1-x}Hf_xB_{12}$ Under Ambient Pressure" *Inorg. Chem.* **2016**, 55 (10), 5051-5055.
10. Akopov, G.; Yeung, M.T.; Turner, C.L.; Mohammadi, R.; and Kaner, R.B. "Extrinsic Hardening of Superhard Tungsten Tetraboride Alloys with Group 4 Transition Metals" *J. Am. Chem. Soc.*, **2016**, 138 (17), 5714–5721.

CHAPTER 1. REDISCOVERING THE CRYSTAL CHEMISTRY OF BORIDES

INTRODUCTION

There are very few compounds that can challenge the diversity of the crystal chemistry found in borides. Owing to boron's electron count, electronegativity, atomic size and ionization energy, boron compounds primarily exhibit bonding motifs possessing extended covalent networks. Borides can crystallize with complex polyhedra (due to multicenter bonding), notably octahedra, pentagonal bipyramids, trigonal dodecahedra, double-capped square antiprisms, cuboctahedra, and icosahedra.[1] These covalent networks encompass a plethora of structure forms ranging from 1-D chains to 2-D sheets to 3-D networks.

With such a wide variety of structures (a quick survey of the Inorganic Crystal Structure Database counts 1253 entries for binary boron compounds!), it is surprising that the applications of borides have been quite limited despite a great deal of fundamental research. If anything, the rich crystal chemistry found in borides could well provide the right tool for almost any application. The interplay between metals and boron results in even more varied material's properties, many of which can be tuned via chemistry. Thus, the aim of this review is to reintroduce to the scientific community the developments in boride crystal chemistry over the past 60 years. We tie structures to material properties, and furthermore, elaborate on convenient synthetic routes towards preparing borides. This review builds on several previous excellent works discussing crystal structure[1], mechanical properties[2], magnetic properties[3] and chemistry[4,5].

STRUCTURES OF METAL BORIDES

Metal borides form an interesting class of compounds with a wide range of possible applications, stemming from their mechanical, optical, electronic and refractory properties. The different physical properties can be explained by the crystal structure of each borides, which is determined by the arrangement of boron atoms. Metal borides can form with a metal to boron ratio generally ranging from 4 : 1 (Me_4B) to 1 : 12 (MB_{12}), with a few exceptions (e.g., MB_{50}, MB_{66}), for alkali (Li, Na, K), alkali-earth metals, group III - VIII transition metals, lanthanides and actinides (Th, U, Pu) (Tables 1-1 and 1-2). Kiessling suggested the following classification for the arrangements of boron atoms in borides: isolated boron atoms, pairs of boron atoms, chains of boron atoms, double chains of boron atoms, networks of boron atoms, and skeletons/backbones of boron atoms (Figure 1-1).[6] In some borides, having more than 50 at.% B, boron atoms form a backbone of corrugated nets (*CrB_4* and *MnB_4* structural types) or B_6 octahedra (*UB_4* and *CaB_6*). In metal borides possessing more than 85 at.% B, the backbone is represented by cuboctahedra (*UB_{12}* and *ScB_{12}*) or icosahedra (*AlB_{12}*, *MB_{50}* and *YB_{66}*).

1. BORIDES WITH ISOLATED BORON ATOMS

Several structural types of borides belong to this class: *$Fe_3C_{(ortho)}$*, *$CuAl_{2(tetr)}$*, *o-$Mn_2B_{(ortho)}$*, and the ternary τ-borides, *τ-$Cr_{23}C_{6(cub)}$* (Tables 1-1 and 1-2). *Cr_2B* possesses isolated boron atoms, which fill the parent metal structure voids, while the metal atoms are arranged in square antiprisms; this structure also possesses the longest B – B bonds related to other metal boride phases (Figure 1-2).[7] In *o-Mn_2B*, eight Mn atoms are arranged in an archimedean antiprism, which surrounds each boron atom.[8] For *F_3C* structure, the boron atoms are located in threefoldly capped trigonal prisms formed by the metal atoms, which are situated at the centers of 15- and 14-vertices polyhedra (Figure 1-

2).[9] τ-$Cr_{23}C_{6(cub)}$ borides have the general formula $M_{20}M'_3B_6$, where M = Ni, Co, Cr, Mn, Fe, Ru, Re, Ir and M' = Li, Mg, Al, Ga, In, Ge, Sm, Sb, Er, Lu, Tm or transition metals. The structure is characterized by M_{12} cuboctahedra, M_8 cubes, M' at the center of the cuboctahedra, isolated M' and boron atoms (Figure 1-2).[10–13]

2. BORIDES WITH PAIRED BORON ATOMS

One structural type belongs to this class: $U_3B_{2(tetr)}$ (Tables 1-1 and 1-2). In this structural type the boron atoms are isolated and the metal atoms form trigonal and square prisms. The trigonal prisms have boron atom pairs in their centers, while the square prisms have metal atoms in their centers (Figure 1-3).

3. BORIDES WITH ORDINARY CHAINS OF BORON ATOMS

Three structural types belong to this class: $CrB_{(ortho)}$, $FeB_{(ortho)}$ and α-$MoB_{(tetr)}$ (Tables 1-1 and 1-2). For these structural types the boron atoms form zig-zag chains and the three types of borides are distinguished by the relative position of trigonal prisms formed by the metal atoms (Figure 1-4). The W atoms in both $MoB_{(tet)}$ and $CrB_{(ortho)}$ form bilayers. The tetragonal *MoB* possesses boron chains which alternate orthogonally, whereas the orthorhombic *CrB* has all the boron chains aligned along the *a* axis (Figure 1-4).[14] In *FeB*, the boron atoms have 2 boron atom neighbors and a singly-capped trigonal prism of iron atoms, which is slightly distorted. The prisms containing a boron atom form an infinite column of prisms and share 2 faces (rectangular) with nearby prisms.[7] LiB_x is an interesting example of a boride with linear chains of boron (containing a borynide chain $[B^-]_n$), which is isoelectronic to carbyne (Table 1-2).[15]

4. BORIDES WITH DOUBLE CHAINS OF BORON ATOMS

Two structural types belong to this class: $Ta_3B_{4(rhomb)}$ and $V_5B_{6(rhomb)}$ (Tables 1-1 and 1-2). For the Ta_3B_4 structural type, boron atoms form double chains which penetrate metal atom prisms of two types. The prisms differ in size and the direction of their faces, with the smaller prisms being parallel to *a* direction and the larger parallel to the *b* direction (Figure 1-5). For the $V_5B_{6(ortho)}$ structural type, zig-zag boron chains exist parallel to the boron double chains.[16–18] In addition, these double chains can be considered as primitive elements of hexagonal unit cells, characteristic of $AlB_{2(hex)}$.

5. BORIDES WITH NETWORKS OF BORON ATOMS

This is the largest class of structural types as determined by the number of members: $AlB_{2(hex)}$, $RuB_{2(ortho)}$, $ReB_{2(hex)}$, $W_2B_{4(hex)}$ (previously *"*$W_2B_{5(hex)}$*"*), $Mo_2B_{4(rhomb)}$ (previously *"*$Mo_2B_{5(rhomb)}$*"*), $Mo_{0.8}B_{3(hex)}$ and $W_{1.9}B_{9(hex)}$ (Tables 1-1 and 1-2). The AlB_2 structural type consists of trigonal prisms with metal atoms in their vertices and boron atoms in the middle, forming graphite-like flat hexagonal boron nets. The boron and metal atom layers alternate, with each boron being surrounded by six metal and three boron atoms and each metal atom being surrounded by six metal and twelve boron atoms (Figure 1-6). Other structural types in this category can be considered as modifications of the AlB_2 structure with a different sequence of boron layers.[19] The metal layers can be close-packed, denoted as A, B and C, and additional modified boron layers are denoted as K, K', H and H'[19]; in addition, defect boron layers exist, as in the case of $Mo_{0.8}B_3$, denoted as A' and B'[20]. Using this classification system for the boron layers, the aforementioned structural types can be described in Table 1-3[19].

$RuB_{2(rhomb)}$ contains pseudo-hexagonal corrugated layers of boron atoms. The metal atoms have six nearest metal atom neighbors in each layer and eight boron atom neighbors, six of which are located in one boron layer and two in another. Each boron atom is surrounded by three boron atoms in a deformed boron layer and four metal atoms located in the vertices of a deformed tetrahedron, with one boron position being vacant (Figure 1-7).

$ReB_{2(hex)}$ (Figure 1-8), *$W_2B_{4(hex)}$* (*"$W_2B_{5(hex)}$"*; note that while the structure is referred to as having a "*$W_2B_{5(hex)}$"* structure, it has been shown recently that the stoicheometry is W_2B_4[21]; Figure 1-9), *$Mo_2B_{4(rhomb)}$* (previously *"$Mo_2B_{5(rhomb)}$"*, Figure 1-10) are similar to the *AlB_2* structure and have either regular or deformed two-dimensional boron layers. *$W_2B_{4(hex)}$* (previously *"$W_2B_{5(hex)}$"*) and *$Mo_2B_{4(rhomb)}$* (previously *"$Mo_2B_{5(rhomb)}$")* differ in the alternation order of metal layers.[22]

The *$Mo_{0.8}B_{3(hex)}$* structural type contains closed-packed layers of metal atoms, with one-third of the metal atoms absent and half of the remaining two-thirds being partially filled (Figure 1-11).[20,23] *$W_{1.9}B_{9(hex)}$* is similar to *$Mo_{0.8}B_{3(hex)}$* with one-third of the metal atoms absent, however, it also contains partially filled tungsten sites as well as boron atom trimers (Figure 1-12).[24–26]

6. BORIDES WITH A SKELETON/BACKBONE OF BORON ATOMS

Several structural types belong to this class: *$UB_{4(tetr)}$*, *$CrB_{4(ortho)}$*, *$MnB_{4(mono)}$*, *$CaB_{6(cub)}$*, *$ScB_{12(tetr)}$* and *$UB_{12(cub)}$* (Tables 1-1 and 1-2). The structure of *CaB_6* is cubic with the octahedra of boron atoms in each vertex of the cube. Boron atoms play a determining role in the structure and the size of the unit cell, with the metal atoms filling the voids that can accommodate the metal atoms without deforming the boron skeleton (Figure 1-13).[27] Metal atoms of groups II, except for Be and Mg, whose structures are different, group III transition metals (YB_6 and LaB_6), apart from Sc, and lanthanides can form borides of the *CaB_6* structural type.[27] Effective valence in *$CaB_{6(cub)}$* is very

close to the valence of the pure metals and changes in the lattice can be explained by the f electron count and lanthanide contraction.[27,28] Although alkaline-earth metals do not possess d-electrons, their hexaborides (SrB_6, BaB_6 and CaB_6) do exist.[29] It is believed that the metal-boron bonds in hexaborides come from the mixing of s- and d-orbitals of the metal with the 2s and 2p orbitals of boron.[30–32] This can be explained by their interaction with boron which allows the d-shell to get filled and their hexaborides to form, this in turn reduces the atomic size of Sr and Ba.[29]

Just like metal hexaborides, metal tetraborides possess three-dimensional boron atom backbones, which surround metal atoms located at the vertices of a tetragonal or cubic lattice. The structure of $UB_{4(tetr)}$ resembles a combination of AlB_2 and CaB_6 and is similar to V_3B_4, having two types of prisms for the boron arrangements: trigonal and square based (Figure 1-14). Tetragonal prisms have boron atoms in their centers, while the channels penetrating the square prisms contain octahedra of boron atoms.[33,34] The boron octahedra do not share vertices and are connected through pairs of boron atoms along the tetragonal axis, with the boron atoms forming four- and seven-membered rings. For this structural type the unit cell size decreases with the increase of the atomic number of the metal, except for cerium and ytterbium due to the change of valence.[35]

In $CrB_{4(ortho)}$ (Figure 1-15) structural type is similar to $UB_{4(tetr)}$ in the sense that the boron atoms form three dimensional nets, penetrated by channels of chromium atoms along the *c* direction.[36,37] The squares of boron atoms, parallel to the (001) plane along the *c* direction are connected into zig-zag layers by boron-boron bonds (1.91 Å).[38] By deforming the $CrB_{4(ortho)}$ unit cell in *c* axis direction, an $MnB_{4(mono)}$ cell can be created (Figure 1-15).[23,37,39,40]

Finally, metal dodecaborides encompass a large group which includes transition metal, lanthanide and actinide dodecaborides. Two structural types can be distinguished: $UB_{12(cub)}$, which

encompasses most of the dodecaborides, except for $ScB_{12(tet)}$. The tetragonal-ScB_{12} structure (Figure 1-16) consists of a body-centered tetragonal lattice of 24-atom boron cuboctahedra with the metal atoms being in the center of each boron cage.[41] ScB_{12} is the only member of the $ScB_{12(tet)}$ family, and moreover, it can be stabilized in the $UB_{12(cub)}$ structure with the addition of other transition metals (Zr, Y, Yb, etc.), forming a solid solution.[42,43] The cubic-UB_{12} (Figure 1-17) structure type consists of a face-centered cubic lattice of 24 boron atom cuboctahedra, with the metal atoms at the center of each of the boron cages.[44] In this arrangement, each boron atom is bonded to five other boron atoms and two metal atoms. The metal atoms inside of the boron cuboctahedron are equidistant from the centers of the twelve boron-boron bonds, therefore, they can be considered twelve coordinate. The primary requirement for the formation of the cubic-UB_{12} structure is the radius of the metal in a 12 coordinate environment, with yttrium and zirconium being the largest and smallest metals, respectively, capable of accommodating a boron cuboctahedron cage, with slight size deviation rendering the metal dodecaboride unstable under ambient pressure.[44–47] Notable exceptions are HfB_{12}, ThB_{12} and GdB_{12} all of which in pure form can only be synthesized under high pressure[46,48], or stabilized as a solid solution under ambient pressure: $Y_{1-x}Hf_xB_{12}$[49],$Th_{1-x}Zr_xB_{12}$[50] and $Zr_{1-x}Gd_xB_{12}$[51].

7. BORIDES WITH BORON ICOSAHEDRA (B_{12}) UNITS

This class contains the $YB_{66(cub)}$ as well as the $AlB_{12(tetr)}$ *and* $AlB_{12(ortho)}$ structural types (Tables 1-1 and 1-2). A boron-rich boride of sodium, $Na_2B_{29(mono)}$, also belongs to this class (Table 1-2).[52] For the $AlB_{12(tetr)}$ (Figure 1-18) the structure contains chains of B_{12} icosahedra arranged alternating along the *a* and *b* axes. This results in the formation of a three-dimensional icosahedral B_{12} framework with the B_{20} units occupying the voids between the B_{12} chains. In contrast, $AlB_{12(ortho)}$

(Figure 1-18) consists of tetrahedra of B_{12} icosahedral units at each vertex. The B_{20} units fill the voids created by the two layers of nets formed by the tetrahedral of B_{12} boron units.[53,54]

The unit cell of YB_{66} (Figure 1-19) contains 1584 boron atoms and 24 yttrium atoms. The boron atoms are arranged in two groups: one group (1248 boron atoms) consists of eight clusters of 156 boron atoms (which are composed of 13 B_{12} icosahedra), where each B_{12} unit is surrounded by 12 more B_{12} units forming a supericosahedra unit; the other 336 boron atoms form non-icosahedral cages and are located in the channels that result from the packing of the 13 B_{12} units.[55–57]

8. SOLID SOLUTIONS OF TRANSITION METALS IN β-RHOMBOHEDRAL BORON

This class contains the $MeB_{50\text{-}100(rhomb)}$ (Figure 1-20) structure type. Most transition metals are capable of forming this boride phase, which is essentially a solid solution of a transition metal in β-rhombohedral boron (Tables 1-1 and 1-2). The structure of this phase, similarly to pure β-rhombohedral boron, contains B_{12} boron icosahedral clusters, as well as single boron atoms. The main difference between this phase and pure β-rhombohedral boron is the substitution of some of the boron positions and interstitial vacancies by the transition-metal atoms.[41,58,59]

SELECT APPLICATIONS AND PROPERTIES OF METAL BORIDES

The variations in the structure and bonding of metal borides not surprisingly result in a diverse multitude of properties. What is surprising, though, is that the commercial applications of borides are limited. Here a short compilation of properties and potential applications is provided, which we hope will inspire further research into metal borides.

1. CATALYSIS

Since the 1960's, metal boride powders have been used as catalysts for a variety of organic reactions, most notably hydrogenations and reductions[60]. Because metal borides catalytically hydrolyze borohydride in water, they have also found uses in fuel cells as the hydrogen generator. Traditionally prepared by precipitation of metal salts with sodium borohydride[61], the nature of these catalytic borides were not fully understood until recently. As these borides are synthesized in solution at low temperatures, the resulting structure is amorphous. Annealing the precipitates of borides above 300 °C transforms the disordered structure into crystalline Ni_3B[62]. Unfortunately, the disorder obscures the role of boron toward catalytic activity; ostensibly, the high metal content is responsible for the catalytic activity. More recently, it has been hypothesized that boron may provide a stabilizing role against sintering. Computational studies have shown that the presence of strong boron-metal bonds lowers the chance of grain growth, thus preserving the surface area at high temperatures[63].

2. MAGNETIC PROPERTIES

While it is more interesting to discuss the role of extended boron networks (*i.e.* boron chains, sheets, etc.) on material properties, the role of boron in stabilizing the structures of functional structures must not be overlooked. These boron-stabilized structures usually contain isolated boron atoms due to low boron concentration, and thus lack an extended boron network. As there is no extended boron network, the bulk of material properties stem from the other elements that make up the majority of the stoichiometry. This is particularly relevant for magnetic materials as only in a compound do borides exhibit significant magnetism[64].

The strongest permanent magnets, known as neodymium magnets are of the composition $Nd_2Fe_{14}B$[65–67], and possess very high remnant magnetization. Thus, these rare earth magnets find uses in hard drives, speakers, electric motors, and any other applications that require a strong magnetic field. Ostensibly, the magnetism originates from the ferromagnetic elements iron and neodymium. The contribution of the boron towards the enhanced magnetism comes from the crystallographic arrangement. In $Nd_2Fe_{14}B$, boron coordinates to 6 iron atoms to form a trigonal prism, which is a common motif found in isolated boron metalloids[68]. This in turn aligns the magnetic moments of iron along the c-axis, resulting in strong magnetic anisotropy. Contrast this with another rare earth magnet, $SmCo_5$, which possesses a somewhat similar trigonal structure[66], but requires a higher rare earth to transition metal ratio. Perhaps not surprisingly, the contribution of magnetism from the alignment of iron around boron suggests that the rare earth element may not be required, and this is the rationale behind certain iron nitrides[69] ($Fe_{16}N_2$) Similar to $Nd_2Fe_{14}B$ where the boron coordinates to 6 iron atoms in a trigonal prism, for $Fe_{16}N_2$, the nitrogen coordinates to 6 iron atoms to form a distorted octahedron[70].

Aside from rare earth neodymium magnets, there are other magnetic borides. A more thorough review has been written by Bucher[3], so here only the magnetic properties will be listed briefly. It is noted that Co_2B (T_c = 429 K), Co_3B (T_c = 747 K), FeB (T_c = 598 K), Fe_2B (T_c = 1013 K), MnB (T_c = 573 K), MnB_2 (T_c = 157 K), and Mn_3B_4 (T_c = 392 K) all exhibit ferromagnetism. Beyond transition metals, many rare earth borides exhibit ferromagnetism; however, unlike the transition metals, the ferromagnetism is less robust and results in a lower T_c, as TbB_2 (T_c = 151 K), DyB_2 (T_c = 55 K), ErB_2 (T_c = 16 K), and HoB_2 (T_c = 15 K) each crystallize in an *AlB_2*-type structure, with all the rare earth metal spins aligned along the basal plane[71]. As one moves from 2-D boron sheets to 3-D boron networks of hexaborides and dodecaborides[64], one soon finds more

antiferromagnetic ordering with CeB_6 (T_N = 23 K), PrB_6 (T_N = 7 K), NdB_6 (T_N = 8.6 K), GdB_6 (T_N = 18 K), TbB_6 (T_N = 23 K), DyB_6 (T_N = 21.5 K), HoB_6 (T_N = 9 K), HoB_6 (T_N = 6.5 K), ErB_6 (T_N = 6.5 K), and TmB_6 (T_N = 4.2 K). For hexaborides, the antiferromagnetic ordering stems from the coupling between the conduction band and the 4f electrons[72]; there is one free electron per each trivalent metal.[73] Thus, divalent europium in ferromagnetic EuB_6 is the exception. Admittedly, the ordering in europium hexaboride is more complicated than a simple valence electron count, as it possesses two magnetic transitions[74]. Ferromagnetism has been induced in calcium doped lanthanum hexaboride[75]. As this compound does not possess unpaired d- or f-electrons, its ferromagnetism has been ascribed to electron-hole pairs.[76] However, this is subject to debate, as some have ascribed its ferromagnetism to parasitic iron impurities[77], although single crystals of CaB_6 have been shown to be magnetically independent of iron concentration[78].

3. HARD AND SUPERHARD MATERIALS

The propensity for boron to catenate usually results in extended 3-D networks of covalent bonds. This results in a high shear modulus as dislocations do not traverse across strong directional bonds. Preparing a boride with an ultraincompressible metal will result in a compound that approaches the incompressibility and hardness found in diamond. This has inspired the development of superhard metal borides, of which we have discovered several. As the focus of this review is towards the applications of boride materials, we direct the reader to more detailed reviews on the nature of superhard materials[2].

The current uses of hard borides have been largely limited to machining[79], but the high wear resistance afforded by borides may lead to other applications, such as prosthetics[80]. Applying a hard coating to mating surfaces will extend the lifetime of a prosthetic joint, reducing the need for

further surgery, thus avoiding additional complications. Fortunately, the majority of borides are known to be hard (Table 1-4) and protective films of borides can be prepared via straightforward methods. Borodizing is a process by which boron is diffused into the surface of metal workpiece. As this is a diffusion limited process, a metal rich boride is created on the surface of the metal, typically of composition M_2B. As these lower borides generally crystallize in the $CuAl_2$ structure, isolated borons sit in what can be considered as a true interstitial site. The strong metal-boron bond prevents the metal planes from sliding past each other, thus strengthening the surface with increased hardness which imparts increased wear resistance.

4. HIGH TEMPERATURE MATERIALS

As boron is the second highest melting main group element after carbon, it is not surprising that the majority of metal borides are refractory. Among the refractory borides is zirconium diboride (T_{mp} = 3230 ^{o}C)[81], which crystallizes in an *AlB_2*-type structure with 2-D honeycomb boron. Combining the high melting point with a high elastic modulus (from the pliable boron sheets) results in a robust structural material resistant to extreme thermal events. Zirconium diboride also exhibits excellent oxidation resistance, surviving thermal cycling up to 2700°C in air[82]. As the byproducts of oxidation are ZrO_2 and B_2O_3, significant oxidation only occurs above 1000°C resulting from the sublimation of B_2O_3, which exposes fresh surfaces for degradation[83]. The addition of silicon to form a composite results in a formation of a protective SiO_2 layer that prevents further oxidation up to the vaporization temperature of SiO_2 (T_{bp} = 2950 ^{o}C). Zirconium diboride has been investigated by the United States Air Force for use in rocket engines and United States Navy for hypersonic flight vehicles[84].

5. SUPERCONDUCTIVITY

The promise of high power transmission with limited resistance and levitated trains has spurred the development of superconductors. The ability to carry large currents without Ohmic heating enables the generation of strong magnetic fields[85], and as such, they are often used as the windings for NMR. Combining a superconductor with a topological insulator (see the section on topological insulators) results in what can be a crucial component for a solid state quantum computer. It is not surprising that with the plethora of bonding geometries found in borides, that there are several strong superconducting candidates.

Magnesium diboride has been used as an effective reagent to yield transition metal borides through solid state metathesis reactions[86], but perhaps its most interesting property is the loss of resistivity at 39 K.[87–89] This temperature exceeds all type-I superconductors, even exceeding $La_{2-x}Ba_xCuO_4$, the first type-II superconductor discovered[90]. Unlike traditional type-I superconductors, which rely on s-orbital overlap, MgB_2 also possesses significant p-orbital overlap, resulting in a higher heat capacity and higher T_c[91]. Noting that MgB_2 possesses one of the longest c-axis among the diborides (3.52 Å) and the deleterious role of pressure on T_c, Wan *et al.* theoretically modeled various MgB_2 lattice parameters and found that stretching the c-axis and compressing the a-axis should raise the T_c. Indeed, parallel experiments with NbB_{2+x} (T_c = 9.4 K)[92] and MoB_{2+x} (T_c = 7.5 K)[93] have shown that the addition of excess boron can help separate the boron layers and induce superconductivity in non-superconducting diborides. We envision further enhancements in the superconducting properties of borides through increased lattice expansion by doping or structural modifications.

Not surprisingly, there are many other borides[94] with superconducting properties, although none surpass the T_c of MgB_2. Metal-rich borides that possess isolated boron atoms, such as Mo_2B (T_c =

5.07 K) and W_2B (T_c = 3.22 K), superconduct because the valence electron count places the Fermi surface in contact with the reciprocal lattice[95]. Of the monoborides that crystallize with 1-D linear boron chains, TaB (T_c = 4 K) and NbB (T_c = 8.25 K), are known to superconduct. Virtually all higher borides[64] that do not possess antiferromagnetism superconduct, as can be seen with ScB_{12} (T_c = 0.39 K), YB_6 (T_c = 7.1 K), YB_{12} (T_c = 4.7 K), ZrB_{12} (T_c = 5.82 K), LaB_6 (T_c = 5.7 K), LuB_{12} (T_c = 0.48 K), and ThB_6 (T_c = 0.74 K).

6. KONDO INSULATORS

While many rare earth borides are known to superconduct at low temperatures, there are a select few that lose their conductivity, and they are known as Kondo insulators. This phenomenon occurs in rare earth borides where the rare earth elements possess mixed valency *i.e.* Yb can be Yb^{+2} or Yb^{+3}. This mixed valency results in the opening of a band gap at low temperatures. As seen in YbB_{12}, the valence band is comprised of 36 electrons from the boron cage and 2 electrons from the metal. The extra electron transferred from a trivalent rare earth solely occupies the conduction band. It is not too surprising then, that some borides were found to be ideal Kondo insulators as a result of the strong coupling[96] and the possession of mixed valency in the f-orbitals[97]. Samarium hexaboride became one of the first experimentally confirmed Kondo insulators, as indicated using resistivity and magnetic measurements[97].

7. TOPOLOGICAL INSULATORS

At first glance, topological insulators seem to be merely small band gap traditional insulators. However, due to intricacies in the spin-orbit coupling, topological insulators exhibit bulk insulating behavior like could traditional insulators, but also possess metallic conductivity on their surfaces. Thus, these materials could find applications where a topologically protected metallic

surface state is needed. It has been postulated that Majorana fermions can be found at the interface between a topological insulator and a superconductor, where the superconductor induces a superconducting surface state. As the vortex state is confined to the surface, this creates the aforementioned quasiparticle. These Majorana fermions can then be paired to form a quantum bit. Therefore, the search for new topological insulators has drawn considerable interest given the possibility of quantum computing.

Because topological insulators require strong spin-orbit coupling, the search for new ones has been largely restricted to the heavy elements of the p-block[98]. In 2010, Coleman *et al.*[99] noted that potential topological insulators can be found in cubic Kondo insulators. In addition to these materials becoming insulating at low temperatures due to a mixing of f-electrons and the conduction band, the cubic symmetry in hexaborides ensures that transport is limited to a few directions resulting in a strong topological insulator[100]. Shortly thereafter, the classical Kondo insulator SmB_6 confirmed theoretical predictions and demonstrated a topologically protected conductivity[101–103]. Angle resolved photoelectron spectroscopy[104] (ARPES) has shown that the topology of the Fermi surface is indeed topologically protected, and Fisk *et al.* has verifed that there is indeed a topologically protected state through torque magnetometry[105], tunneling spectroscopy[106–108] and Hall Effect[109] on single crystals. Beyond samarium, several ytterbium borides were hypothesized to be topological Kondo insulators[110].

8. OPTICAL PROPERTIES OF BORIDES

As most metal borides are metallic conductors, it may be somewhat surprising to see a section on optical properties. While borides generally do not possess any interesting optical properties in the visible spectrum (save for color), borides do interact with photons of other wavelengths[111], and

these properties have led to some niche applications of borides. For example, thin films of borides have been used as filters for ultraviolet light[112], which has potential applications for deep space telescopes.

For more terrestrial applications, lanthanum hexaboride is often used by crystallographers as an X-ray standard, SRM 660a. Isotopically enriching to yield $La^{11}B_6$ allows for the hexaboride to be used as a standard for neutron diffraction, SRM 660c. As lanthanum hexaboride possess a cubic structure, it exhibits a periodic arrangement of diffraction peaks, making it a reliable diffraction standard. Hexaborides also find uses as hot cathodes as low work function, refractory compounds. As such, a significant body of work has focused on the use of lanthanum hexaboride as cathodes for electron microscopes, where the improved oxidation resistance and enhanced electron emissivity has allowed it to supplant tungsten electrodes. Recently, lanthanum hexaboride nanoparticles have found uses as near infrared absorbers[113] for windows, selectively absorbing infrared light while transmitting visible photons due to free electron plasmon resonance[114].

Since YB_{66} possesses one of the largest unit cells known (a = 23.44 Å = 2.344 nm) from the presence of over 1600 atoms per unit cell, it can be used as an X-ray monochromator. More importantly, YB_{66} is comprised mainly of light boron atoms, allowing improved transmission of soft X-rays. YB_{66} is particularly useful for synchrotron radiation as it encompasses the entire 1-2 KeV range, replacing three crystals that had previously been needed[115]. Note that the high energy of the photons will heat the crystal upwards of 637 K, but fortunately, borides are refractory[116].

9. TWO DIMENSIONAL, LAYERED BORIDES

Historically, there are many borides that possess layered crystal structures (among them the type 1.5 superconductor MgB_2). However, recent trends have shifted towards 2-D covalent crystals held

together by Van der Waal forces. When properly exfoliated/grown, these materials afford single layers[117], and perhaps the progenitor of this class of materials is graphene[118]. These 2-D covalent crystals possess anisotropic electrical, thermal, and mechanical properties, and thus a great deal of effort has been spent towards finding new methods towards exfoliation, among them solvent exfoliation, chemical intercalation, and chemical vapor deposition. Indeed, as many of the borides are layered and possess planar honeycomb boron, there are several boride compounds that possess nearly the same propensity for exfoliation as graphene, and many of the techniques that have been used for graphene and other layered materials can be used for borides.

Magnesium diboride can be exfoliated via ultrasonication[119] in water via the formation of hydrophilic surface groups, similar to how graphene can be exfoliated through graphite oxide[120]. Titanium diboride has been exfoliated through the intercalation of alkali metals[121], much like what has been done with graphene[122] and MoS_2[123]. In another parallel with graphene, single layers of boron have been grown through vapor deposition. As boron tends to form compounds with many metals, borophene can only be grown on substrates that do not possess a boride, most notably silver[124,125]. From computation, borophene possess various potential applications, among them magnetism[126] and superconductivity[127]. However, note that borophene is not the only single layer allotrope of boron, as single layer γ-boron has also been grown on copper foils through chemical vapor deposition with oxygen[128]ta.

MAX phases (usually $M_{n+1}AlC_n$) have been exfoliated through the chemical etching of the aluminum layer, leaving behind a metal carbide layer more commonly known as MXene. These MXenes have been used in electrochemical devices owing to both their high surface area and their high electrical conductivities[129,130]. Recent explorations in ternaries have resulted in the MAX

phase MoAlB, which possesses the same layered structures found in MAX phases[131], and perhaps future work will result in a layered 2-D molybdenum boride. As interest in 2-D covalent crystals progress, the search for new materials should continue with borides that naturally crystallize into layered structures.

METHODS FOR SYNTHESIZING METAL BORIDES

Metal borides can be synthesized in a variety of different ways, which require different instrumentation, technological conditions, media in which the reactions proceed, purity and form of the produced boride (polycrystalline powder or single crystals) and their amount. Moreover most methods of boride synthesis require high temperatures. In addition, the methods differ in their scalability, with reduction methods of metal oxides with boron being the most cost effective and scalable. Synthesis methods from elemental boron and metals yield products with the highest purity. Boride synthesis from the elements, the electrolysis of molten mixtures, and chemical vapor deposition can be used to produce refractory and protective coatings on the surfaces of materials with different compositions and the production of tools with complex shapes possessing specific properties.[132] In this section, an overview of synthetic methods is provided. For specific synthetic conditions for a given boride phase, references are given in Table 1-2.

The most common techniques for synthesizing borides are:

1) *Synthesis from elemental metal and boron (through sintering or melting)*

   $xMe + yB \rightarrow Me_xB_y$;

2) *Carbothermal reduction (reduction of metal oxides and boron by carbon)*

   $MeO + B_2O_3 + C \rightarrow MeB + CO$;

3) *Borocarbothermal reduction (reduction of metal oxides by boron and carbon)*

$MeO + B + C \rightarrow MeB + B_xO_y + CO$;

4) *Boron carbide ("B_4C", $B_{13}C_2$) reduction of metal oxides*

$MeO + B_{13}C_2 \rightarrow MeB + CO$;

5) *Borothermal reduction of metal oxides*

$MeO + B \rightarrow MeB + B_xO_y$;

6) *Metallothermal reduction of mixtures of metal oxides and boron*

$MeO + B_2O_3 + Mg(Na, K) \rightarrow MeB + MgO\ (Na_2O, K_2O)$;

7) *Precipitation from the gaseous phase (chemical vapor deposition)*

$MeCl_4 + BCl_3 + H_2 \rightarrow MeB + HCl$;

8) *Electrolysis of molten mixtures of the following compositions*

$MeO + B_2O_3 + MeF_2$;

$MeO_2 + B_2O_3 + MgO\ (CaO) + MgF_2\ (CaF_2)$;

$\frac{1}{5}Me_2O_3 + 2B_2O_3 + Li_2O + LiF$;

$3B_2O_3{*}2CaO + CaF_2 + \frac{1}{10}(\frac{1}{5}; \frac{1}{4}; \frac{2}{3})\ Cr_2O_3$;

$\frac{1}{4}MeO_3 + 2B_2O_3 + NaF$;

$\frac{1}{9}WO_3 + 2B_2O_3{*}Na_2O + NaF$;

9) *Solid state metathesis of borides*

$MgB_2 + TM(Cl)_n \rightarrow MgCl_2 + TMB_n$ (TM = transition metal)

1) Synthesis of borides from elemental metal and boron involves the reaction $xMe + yB \rightarrow Me_xB_y$ carried out by melting the constituents in an arc-melter furnace, a high-frequency induction furnace or a high temperature furnace or through sintering of boron and metal powders under vacuum or in an inert atmosphere. For these methods the purity of the samples strongly depends on the purity

of the starting materials. This method also employs the synthesis of borides using stoichiometric amounts of the corresponding metal and boron. However, depending on the melting temperature of the metal in question relative to boron, a slight boron excess (~10 at%) might be required as some fraction of boron may sublime during the heating process and this might lead to the wrong stoichiometry of the prepared sample.[81,133,134] In addition, some boride phases require excess boron to be present in order to form. Most notably, WB_4 requires a tungsten to boron ratio of 1:12 in order to form, as only this ratio prevents the formation of the thermodynamically favorable WB_2 phase.[24,26,135–137]

For the synthesis of polycrystalline samples, the most common technique used is arc-melting of pressed metal and boron powders of appropriate stoichiometry on top of a copper water-cooled hearth in an inert atmosphere of argon or helium. The successful synthesis of metal borides using powders of pure metals and amorphous or crystalline boron via arc-melting includes such classes of borides as:

1) Lower metal borides and their alloys, e.g. TiB[138]; $W_{1-x}Ta_xB$[14]; ReB_2[139]; NbB_2 and TaB_2[140]; $Sc_{1-x}W_xB_2$ and $Sc_{1-x}Re_xB_2$[141]; Ru_2B_3 and WB_2[142];
2) Tungsten tetraboride (WB_4) and its alloys with transition metals (Ti, Zr, Hf, V, Nb, Ta, Cr, Mn, Re and Mo)[25,26,135,136,143,144];
3) Metal dodecaborides (MB_{12}) and their alloys: $Y_{1-x}Hf_xB_{12}$[49]; $Th_{1-x}Zr_xB_{12}$[50]; $Zr_{0.6}Y_{0.4}B_{12}$, ErB_{12} and UB_{12}[145]; $Zr_{1-x}Y_xB_{12}$, $Zr_{1-x}Sc_xB_{12}$, $Y_{1-x}Sc_xB_{12}$ and YB_{12}[43]; ScB_{12}[43,146] and ZrB_{12}[43,79];
4) β-rhombohedral boron[59] and its transition metal doping phases (HfB_{50}, ScB_{50})[41,58]; and
5) $YPtB_{50}$[147];

Another common boride synthesis technique is hot-pressing of mixtures of transition metal and boron powders; using this method boride tools can also be readily made. [148–150] In addition this technique can be used to make metal boride composites with other compounds, such as a TiB_2-B_4C composite.[151]

High-frequency induction furnace melting of sintered samples can be used to synthesize metal borides, especially in single crystal form. This technique was used to prepare all of the following boride samples for single crystal X-ray diffraction and Raman studies: YB_{66}[56], ZrB_{12}[152] and ScB_{12}[153] and REB_{12} (RE = U, Y, Dy, Ho, Er, Tm, Yb and Lu).[153] In addition single crystal of lower metal borides (diborides (MB_2) and monoborides (MB)) can be prepared using flux growth, with Al, Sn and Bi most commonly used as flux reagents with powders of pure metals and boron, as in the case of AlB_2[154] and ReB_2[155]; and through a mineralization reaction with iodine and pressed pellets of pure metals and boron in a sealed quartz tube at 1000 ^oC: CrB_4[38] and MnB_4[23].

Reactions carried in high temperature furnaces and spark plasma sintering (SPS) can also be used to form metal borides, as in the case of ReB_2[133,139,156,157], Y_2ReB_6[158], ZrB_2 and ZrB_{12}[81,159], and HfB_2[134].

Another variation of the elemental synthesis of borides is a reaction of boron with a metal hydride, nitride or sulfide.[160,161] The hydrogen gas evolved during the reaction of boron and a metal hydride protects the samples from oxidation and the reaction is accompanied by the formation of boron hydrides. TiB_2, VB_2 and CrB_2 were synthesized using a reaction of the sulfide of titanium, vanadium or chromium, respectively, and elemental boron at 700 - 1000 ^oC according to the following reaction: $Me_2S_3 + xB \rightarrow MeB_x + B_2S_3$.[161]

Self-propagating high temperature synthesis (SHS) is another interesting method. This method is based on using only the heat of the exothermic reaction of the reactants; the formation of the metal

boride is accompanied by a narrow, bright zone moving along the sample from the area of initiation from hotter layers to cooler ones. The samples are usually pressed into cylindrical pellets with the metal acting as the "fuel" and boron as the "oxidizer".[162] The composition of the product of the reaction is highly dependent on the initial stoichiometry as well as the density of the pellet. This method was used to synthesize monoborides of V, Nb, Ta, Cr and Mo, diborides of Ti, Zr, Hf, Nb, Ta, Cr, and dodecaborides of Zr and Ti.[162,163] SHS reactions have several advantages over previously mentioned reactions as they proceed extremely rapidly and do not require an external source of energy (apart from initiation).

Another technique for the synthesis of metal borides uses an induction coupled plasma torch. This method has several advantages including such as high temperature and energy density of the plasma and high speeds due to high thermal conductivity.[164,165]

2) Carbothermal reduction of metal oxides and boron by carbon is one of the oldest techniques, first reported in 1936, of forming metal borides and involves the following reaction: $MeO + B_2O_3 + C \rightarrow MeB + CO$.[166] In addition to the main reaction forming a metal boride a secondary reaction forming of metal and boron carbides and/or metal borocarbides takes place.[167,168] These secondary phases hinder the widespread use of this method, as purification steps or specific reaction conditions are needed, such as the use of excess B_2O_3 and high temperature (1900 ^oC) as in the case of formation of diborides of Ti, Zr, Hf, V, Nb and Cr.[169]

3) Borocarbothermal reduction of metal oxides by boron and carbon involves the following reaction: $MeO + B + C \rightarrow MeB + B_xO_y + CO$ at 1500 - 1800 ^oC in an atmosphere of hydrogen or vacuum.[28,170] This method has a significant disadvantage in that the synthesized metal borides

contain up to 6 wt% C, which can be explained by the fact that boron is a stronger reducing agent than carbon and plays a key role in the reduction reaction and formation of the metal boride.[171]

4) Boron carbide ("B_4C", $B_{13}C_2$) reduction of metal oxides is based on the reaction of metals, hydrides and carbides of transition metals with boron carbide plus the addition of boron anhydride, in an amount necessary to remove carbon from the reaction: MeO + $B_{13}C_2$ → MeB + CO. This method requires the use of a high temperature furnace as it requires 1750 - 2000 ^oC to proceed. Performing this reaction in vacuum ensures it goes completion and prevents oxidation of the reaction products.[172–174] Metal borides synthesized by this method are stoichiometric, containing negligible amounts of carbon, therefore are easy to carry out and scale up; as they do not require additional purification or specialized equipment.[175] ZrB_2 and ZrB_{12} have been successfully prepared using boron carbide reduction of ZrO_2.[176]

5) Borothermal reduction of metal oxides is based on the following reaction: MeO + B → MeB + B_xO_y and is the most common industrial method for the synthesis of alkali, rare-earth and refractory metal borides.[177–179] The method requires the presence of a slight excess of boron, as stoichiometric amount is insufficient for the complete reduction reaction.[170,171]

The most common oxide of boron formed during borothermal reduction is B_2O_2 and the reduction therefore proceeds via the following reaction MeO + $B_{(xs)}$ → MeB + B_2O_2. Here boron plays the role of not only a reducing agent, but also a source of boron. In order to remove the boron suboxide, the reaction can be carried out under vacuum, which additionally aids in the purification of the metal oxide and boron reactants. This allows considerable leeway in the quality of the starting materials used and enables the use of magnesiothermic boron (MgB_{12}), with a boron content of 90 - 92 at.%. At the reaction temperatures, magnesiothermic boron thermally decomposes into

elemental boron and magnesium, which almost completely gets removed during the reduction reaction (0.001 at.% residue).[180] For the borothermal method, the reaction speed and the degree with which the product metal boride is close to the stoichiometric boride is increased with increasing reaction temperature.[181] Borothermal synthesis under vacuum can be used to form borides of group IV - VI transition metals of the MeB_2 and MeB_6 structural type, however, it can also be used in the formation of lower (MB) and higher borides (MB_{12}).[181] Binary transition and lanthanide metal dodecaborides have been prepared using a borothermal reduction method with appropriate metal oxides (M_2O_3) and amorphous boron in an induction or high temperature furnace at 1400 - 1500 ^oC.[44,153,182–186] In addition, solid solutions of transition metal dodecaborides (UB_{12}, ScB_{12}, YB_{12}, DyB_{12}, HoB_{12}, ErB_{12}, TmB_{12}, YbB_{12} and LuB_{12}) covering a wide range of compositions can be prepared using this method.[42,153,187]

6) Metallothermal reduction of mixtures of metal oxides and boron is based on the reduction of the aforementioned reactants with aluminum, magnesium, calcium or silicon via the following reaction: $MeO + B_2O_3 + Al\ (Mg, Ca, Si, Na, K) \rightarrow MeB + Al\ (Mg, Ca, Si, Na, K)_xO_y$.[173]

The process of boride formation in this method proceeds via a series of oxidation and reduction reactions in which the reactants always remain in the solid state. The most common variation of metallothermal reduction method is the magnesiothermal technique.[174,188,189] This technique enables the synthesis of rare-earth and alkali metals hexaborides as well as diborides of titanium, vanadium, niobium, tantalum chromium, molybdenum and tungsten.[188] Metallothermal reduction of mixtures of metal oxides and boron is relatively straightforward from a scaling up stand point, and cost effective as it allows the use of boric acid (H_3BO_3) instead of boron trioxide (B_2O_3).[188]

7) Precipitation from the gaseous phase (chemical vapor deposition) method proceeds according to the following reaction: $MeCl_4 + BCl_3 + H_2 \rightarrow MeB_2 + nHCl$. Essentially this method involves decomposition of the reactants into their elements, their reaction in the gas phase and the formation of a boride product. This method encompasses a range of ionic and molecular reactions, proceeding in the gas phase under a reducing atmosphere, the presence of which is required to reduce the products of pyrolysis. This method can also be used to produce single crystals of metal borides, such as TiB_2.[190] In addition, this method allows the fabrication of tools of complex geometry[191], refractory metal boride films and coatings for rocket nozzles, combustion chambers, crucibles, turbine blades, chemical reactors and cutting tools.[192–194] The main challenges of this method is optimization of the reaction parameters to give the desired metal boride and materials with the desired properties, that are capable of performing in hazardous conditions at elevated temperatures and in an oxidative atmosphere.

8) Synthesis of borides through electrolysis involves passage of a current through molten mixtures of salts of strong electrolytes and the formation of borides via an electrochemical deposition reaction on either the cathode or the anode. The current densities, applied voltage and the temperature of the electrolysis bath can vary over a wide range. This method was used in the synthesis of several lower borides of chromium, which are deposited via reduction on the cathode and this method is most commonly used for surface coatings.[195]

9) *Solid state metathesis reactions of borides* proceed via the following reaction: $MgB_2 + TM(Cl)_n \rightarrow MgCl_2 + TMB_n$ (TM = transition metal). The refractory nature of most borides has usually been the rate-limiting step towards their mass production. As seen from the other aforementioned synthetic methods, boride preparation usually requires high temperature furnaces and other capital

expenses. This limitation has led to the development of other chemical routes towards borides as can be seen with solid state metathesis (SSM) reactions. These are double displacement reactions, where two precursors salt forming precursors are intimately mixed, then initiated. The resulting self-sustaining propagation generates high heat that facilitates the preparation of refractory borides, along with another thermodynamically favorable product (generally a salt) that can be removed with a solvent. This method has been successfully used to prepare a number of transition metal borides[86], among them ReB_2[139] and OsB_2[196]. Along with borides, SSM reactions have also been successfully utilized in the preparation of silicides, pnictides, and chalcogenides. For further details on the mechanism and kinetics behind metathesis reactions, an excellent review is provided by Parkin.[197]

CONCLUSIONS

For the past 60 years, the boride family has only been studied primarily for their rich crystal chemistry, which leads to a host of properties that provide many possibilities for applications. Here we present a non-exhaustive compilation of crystal structure data, materials properties, and synthetic routes towards metal borides. Given the chemical tunability of those properties, we encourage the materials community to revisit metal borides.

ACKNOWLEDGEMENTS

We thank the National Science Foundation Division of Materials Research, Grant DMR-1506860 (R.B.K.) and the National Science Foundation DGE-0654431 Fellowship program (M.T.Y.) for financial support.

Table 1-1. Arrangement of Boron Atoms in Metal Borides

Arrangement of boron atoms	Formula	Structure type	Lattice	Space group	Example
Isolated boron atoms	$M_{20}M'_3B_6$	*τ-$Cr_{23}C_6$*	Cubic	$Fm\bar{3}m$	$Fe_{23}B_6$, $Co_{23}B_6$
	Me_3B	*Fe_3C*	Orthorhombic	*Pnma*	Ni_3B, Pd_3B
	Me_2B	*o-Mn_2B*	Orthorhombic	*Fddd*	Mn_4B, Cr_4B
	Me_2B	*Al_2Cu*	Tetragonal	*I4/mcm*	Ti_2B, Ta_2B, Cr_2B
Paired boron atoms	Me_3B_2	*U_3Si_2*	Tetragonal	*P4/mbm*	V_3B_2, N_3B_2, Ta_3B_2
Single chains of boron atoms	MeB	*CrB*	Orthorhombic	*Cmcm*	VB, TaB, β-WB
		FeB	Orthorhombic	*Pnma*	MnB, FeB, CoB
		MoB	Tetragonal	*$I4_1/amd$*	MoB, α-WB
Double chains of boron atoms	Me_3B_4	*Ta_3B_4*	Orthorhombic	*Immm*	V_3B_4, Nb_3B_4, Ta_3B_4
	Me_5B_6	*V_5B_6*	Orthorhombic	*Cmcm*	V_5B_6, Nb_5B_6
Networks of boron atoms	MeB_2	*AlB_2*	Hexagonal	*P6/mmm*	TiB_2, ZrB_2, HfB_2
		ReB_2	Hexagonal	*$P6_3/mmc$*	ReB_2
		RuB_2	Orthorhombic	*Pmmn*	RuB_2, OsB_2
	MeB_2	*WB_2*	Hexagonal	*$P6_3/mmc$*	WB_2
		MoB_2	Rhombohedral	$R\bar{3}m$	MoB_2
	MeB_4	*$Mo_{0.8}B_3$*	Hexagonal	*$P6_3/mmc$*	MoB_4
		$W_{1.9}B_9$	Hexagonal	*$P6_3/mmc$*	WB_4
Skeletons/backbones of boron atoms	MeB_4	*UB_4*	Tetragonal	*P4/mbm*	UB_4, YB_4,ThB_4, LuB_4
		CrB_4	Orthorhombic	*Immm*	CrB_4
	MeB_6	*CaB_6*	Cubic	$Pm\bar{3}m$	CaB_6, YB_6, LuB_6
	MeB_{12}	*ScB_{12}*	Tetragonal	*I4/mmm*	ScB_{12}
		UB_{12}	Cubic	$Fm\bar{3}m$	ZrB_{12}, YB_{12}, HfB_{12}
Boron icosahedra (B_{12})	MeB_{12}	*AlB_{12}*	Tetragonal	*$P4_12_12$*	α-AlB_{12}
		AlB_{12}	Orthorhombic	*$P2_12_12$*	γ-AlB_{12}
	MeB_{66}	*$Y_{1.06}B_{66}$*	Cubic	$Fm\bar{3}c$	YB_{66}, ThB_{66}, NdB_{66}
Solid solution of transition metals in β-rhombohedral boron	$MeB_{50\text{-}100}$	*$MeB_{50\text{-}100}$*	Rhombohedral	$R\bar{3}m$	HfB_{50}, ScB_{50}, WB_{100}

Table 1-2. Metal Boride Crystal Structures and Densities

Metal	Boride	Lattice	Structure type	Space group	Unit cell (Å)			Density (g/cm^3)	Comments/ β-angle (°)	Reference
					a	b	c			
Li	$LiB_{0.8\text{-}1.0}$	Hexagonal	$LiB_{0.88}$	*$P6_3/mmc$*	4.020	-	2.794	1.51		15,198,199
	LiB_3	Tetragonal	LiB_3	*P4/mbm*	5.975	-	4.189	1.75		198,200
	Li_3B_{14}	Tetragonal	Li_3B_{14}	*I-42d*	10.764	-	8.947	2.2		198,201
	$Li_8B_{103.4}$	Rhombohedral	$Zr_2B_{102.1}$	*$R\bar{3}m$*	10.965	-	24.049	2.33		198,202
Na	Na_3B_{20}	Orthorhombic	Na_3B_{20}	*Cmmm*	18.695	5.701	4.151	-		203
	Na_2B_{29}	Monoclinic	Na_2B_{29}	*Im*	5.874	10.403	8.359	-		52
K	$K_{1\text{-}x}B_6$	Cubic	CaB_6	*$Pm\bar{3}m$*	4.222	-	-	-		204
Be	Be_4B	Tetragonal	Be_4B	*P4/nmm*	3.38	-	7.06	1.93		205,206
	Be_2B	Cubic	CaF_2	*$Fm\bar{3}m$*	4.663	-	-	1.89		206–208
	BeB_2	Hexagonal	AlB_2	*P6/mmm*	9.774	-	9.546	2.40		206,207,209
	BeB_6	Tetragonal	AlB_{12}	*$P4_1$*	10.16	-	14.28	2.64		206,207,210
	BeB_{12}	Tetragonal	$Be_{1.6}B_{25}$	*$P4_2/nnm$*	8.856	-	5.116	2.36		206,207,211
Mg	MgB_2	Hexagonal	AlB_2	*P6/mmm*	3.085	-	3.523	2.63		212–214
	MgB_4	Orthorhombic	MgB_4	*Pnma*	5.464	4.428	7.472	2.48		213–215
	MgB_7	Orthorhombic	MgB_7	*Imma*	5.970	10.480	8.125	2.61		213,216,217
	MgB_{20}	Rhombohedral	$Sc_{3.7}B_{101.8}$	*$R\bar{3}m$*	10.983	-	24.156	2.45		213,218
	$Mg_{\sim5}B_{44}$	Tetragonal	-	$P4_12_12$	10.380	-	14.391	2.56		217
Ca	CaB_6	Cubic	CaB_6	*$Pm\bar{3}m$*	4.145	-	-	2.45		27,29,219
Sr	SrB_6	Cubic	CaB_6	*$Pm\bar{3}m$*	4.198	-	-	3.42		27,220,221
Ba	BaB_6	Cubic	CaB_6	*$Pm\bar{3}m$*	4.268	-	-	4.32		27,220,222,223
Al	AlB_2	Hexagonal	AlB_2	*P6/mmm*	3.009	-	3.262	3.16		154,224–226
	AlB_{10}	Orthorhombic	$Al_{0.6}1B_{6.50}$	*Cmcm*	5.690	8.881	9.100	2.51		224,227
	α-AlB_{12}	Tetragonal	$Al_{1.67}B_{22}$	*$P4_12_12$*	10.161	-	14.283	2.55		54,224,228
	β-AlB_{12}	Orthorhombic	β-AlB_{12}	*$P2_12_12$*	12.34	12.631	10.161	2.6		54,224
	γ-AlB_{12}	Orthorhombic	$Al_{0.57}B_{8(ht)}$	*$P2_12_12$*	10.144	16.573	17.510	2.53		224,229

	AlB_{30}	Rhombohedral	$Al_{3.27}B_{103.1}$	$R\bar{3}m$	10.965	-	23.868	2.41		224,230
Sc	ScB_2	Hexagonal	AlB_2	*P6/mmm*	3.148	-	3.517	3.66		183,231–233
	ScB_{12}	Tetragonal	ScB_{12}	*I4/mmm*	5.22	-	7.35	2.88		41,146,153,159,232
	ScB_{19}	Tetragonal	ScB_{19}	$P4_12_12$	10.292	-	14.246	-		182
	ScB_{50}	Rhombohedral	$Sc_{1.06}B_{104}$	$R\bar{3}m$	10.953	-	-	2.37		41,58,148,232
Y	YB_2	Hexagonal	AlB_2	*P6/mmm*	3.304	-	3.846	5.05		231,234,235
	YB_4	Tetragonal	UB_4	*P4/mbm*	7.111	-	4.017	4.32		234,236
	YB_6	Cubic	CaB_6	$Pm\bar{3}m$	4.113	-	-	3.67		27,208,220,234
	YB_{12}	Cubic	UB_{12}	$Fm\bar{3}m$	7.500	-	-	3.44		27,49,153,159,208,234
	YB_{25}	Monoclinic	YB_{25}	*I2, Im, I2/m*	8.284	10.320	5.857	-	β=90.402°	185
	YB_{66}	Cubic	YB_{66}	$Fm\bar{3}c$	23.436	-	-	2.50		55–57,234,237,238
La	LaB_4	Tetragonal	UB_4	*P4/mbm*	7.324	-	4.181	5.39		27,239–241
	LaB_6	Cubic	CaB_6	$Pm\bar{3}m$	4.156	-	-	4.71		27,222,240,242,243
Ce	CeB_4	Tetragonal	UB_4	*P4/mbm*	7.205	-	4.090	5.74		34,241,244
	CeB_6	Cubic	CaB_6	$Pm\bar{3}m$	4.139	-	-	4.71		222,244,245
Pr	Pr_2B_5	Monoclinic	Pr_2B_5	*C2/c*	15.160	7.277	7.314	5.87	β=109.607°	246,247
	PrB_4	Tetragonal	UB_4	*P4/mbm*	7.235	-	4.116	5.68		241,247,248
	PrB_6	Cubic	CaB_6	$Pm\bar{3}m$	4.120	-	-	4.89		247,249
Nd	Nd_2B_5	Monoclinic	Nd_2B_5	*C2/c*	15.081	7.252	7.284	6.04	β=109.104°	250,251
	NdB_4	Tetragonal	UB_4	*P4/mbm*	7.219	-	4.102	5.82		241,250,251
	NdB_6	Cubic	CaB_6	$Pm\bar{3}m$	4.127	-	-	4.94		251,252
	NdB_{66}	Cubic	YB_{66}	$Fm\bar{3}c$	23.476	-	-	2.64		250,251
Pm	PmB_6	Cubic	CaB_6	*Pm3m*	4.126	-	-	-		253,254
Sm	Sm_2B_5	Monoclinic	Sm_2B_5	$P2_1/c$	7.179	7.18	7.205	6.49	β=102.02°	255
	SmB_4	Tetragonal	UB_4	*P4/mbm*	7.174	-	4.064	6.14		241,256
	SmB_6	Cubic	CaB_6	$Pm\bar{3}m$	4.134	-	-	5.00		228,257
	SmB_{66}	Cubic	YB_{66}	$Fm\bar{3}c$	23.468	-	-	2.66		237,258
Eu	EuB_6	Cubic	CaB_6	$Pm\bar{3}m$	4.185	-	-	4.91		222,228,252,259
Gd	Gd_2B_5	Monoclinic	Gd_2B_5	$P2_1/c$	7.179	7.136	7.183	6.84	β=102.68°	[97,98]
	GdB_4	Tetragonal	UB_4	*P4/mbm*	7.132	-	4.051	6.46		260,262–264
	GdB_6	Cubic	CaB_6	$Pm\bar{3}m$	4.112	-	-	5.3		220,241,260

	GdB_{12}	Cubic	UB_{12}	$Fm\bar{3}m$	7.524	-	-	4.48	high pressure phase	48
	GdB_{66}	Cubic	YB_{66}	$Fm\bar{3}c$	2.345	-	-	2.69		260,265
Tb	TbB_2	Hexagonal	AlB_2	*P6/mmm*	3.294	-	3.886	8.21		266,267
	TbB_4	Tetragonal	UB_4	*P4/mbm*	7.120	-	4.042	6.55		266,268
	TbB_6	Cubic	CaB_6	$Pm\bar{3}m$	4.11	-	-	5.35		266,269
	TbB_{12}	Cubic	UB_{12}	$Fm\bar{3}m$	7.504	-	-	4.54		45,266
	TbB_{66}	Cubic	YB_{66}	$Fm\bar{3}c$	2.346	-	-	2.69		237,266
Dy	DyB_2	Hexagonal	AlB_2	*P6/mmm*	3.287	-	3.834	8.51		231,270
	DyB_4	Tetragonal	UB_4	*P4/mbm*	7.021	-	3.972	6.98		270,271
	DyB_6	Cubic	CaB_6	$Pm\bar{3}m$	4.097	-	-	5.49		228,270,272
	DyB_{12}	Cubic	UB_{12}	$Fm\bar{3}m$	7.501	-	-	4.6		45,153,270
	DyB_{66}	Cubic	YB_{66}	$Fm\bar{3}c$	2.344	-	-	2.71		237,270
Ho	HoB_2	Hexagonal	AlB_2	*P6/mmm*	3.284	-	3.819	8.69		231,273
	HoB_4	Tetragonal	UB_4	*P4/mbm*	7.084	-	4.006	6.88		273,274
	HoB_6	Cubic	CaB_6	$Pm\bar{3}m$	4.091	-	-	5.57		273,275
	HoB_{12}	Cubic	UB_{12}	$Fm\bar{3}m$	7.491	-	-	4.66		45,153,273
	HoB_{66}	Cubic	YB_{66}	$Fm\bar{3}c$	2.344	-	-	2.72		237,273
Er	ErB_2	Hexagonal	AlB_2	*P6/mmm*	3.28	-	3.79	8.88		276,277
	ErB_4	Tetragonal	UB_4	*P4/mbm*	7.071	-	-	6.99		268,276
	ErB_6	Cubic	CaB_6	$Pm\bar{3}m$	4.11	-	-	5.58		45,276,278,279
	ErB_{12}	Cubic	UB_{12}	$Fm\bar{3}m$	7.482	-	-	4.71		45,153,276
	ErB_{66}	Cubic	YB_{66}	$Fm\bar{3}c$	2.334	-	-	2.73		276,280
Tm	TmB_2	Hexagonal	AlB_2	*P6/mmm*	3.261	-	3.755	9.15		277,281
	TmB_4	Tetragonal	UB_4	*P4/mbm*	7.050	-	3.985	7.11		231,241,281
	TmB_6	Cubic	CaB_6	$Pm\bar{3}m$	4.11	-	-	5.59		27,278,279
	TmB_{12}	Cubic	UB_{12}	$Fm\bar{3}m$	7.474	-	-	4.75		27,45,153,281
	TmB_{66}	Cubic	YB_{66}	$Fm\bar{3}c$	23.433	-	-	2.73		237,281
Yb	YbB_2	Hexagonal	AlB_2	*P6/mmm*	3.250	-	3.732	9.47		282,283
	YbB_4	Tetragonal	UB_4	*P4/mbm*	7.055	-	4.004	7.21		27,282,284
	YbB_6	Cubic	CaB_6	$Pm\bar{3}m$	4.148	-	-	5.54		243,252,282,285
	YbB_{12}	Cubic	UB_{12}	$Fm\bar{3}m$	7.468	-	-	4.83		45,153,282,286

	YbB_{66}	Cubic	YB_{66}	$Fm\bar{3}c$	23.422	-	-	2.75		237,282
Lu	LuB_2	Hexagonal	AlB_2	*P6/mmm*	3.244	-	3.706	9.66		27,231,287
	LuB_4	Tetragonal	UB_4	*P4/mbm*	7.038	-	-	7.37		231,287
	LuB_6	Cubic	CaB_6	$Pm\bar{3}m$	4.11	-	-	5.74		27,278,279
	LuB_{12}	Cubic	UB_{12}	$Fm\bar{3}m$	7.464	-	-	4.87		45,153,287
	LuB_{66}	Cubic	YB_{66}	$Fm\bar{3}c$	23.412	-	-	2.76		237,287
Ti	TiB	Orthorhombic	FeB	*Pnma*	6.12	3.06	4.56	4.57		19,138,288,289
	Ti_3B_4	Orthorhombic	Ta_3B_4	*Immm*	3.042	3.259	13.73	4.56		288,290,291
	TiB_2	Hexagonal	AlB_2	*P6/mmm*	3.038	-	3.239	4.46		19,151,225,288,291
	α-Ti_2B_5	Hexagonal	α-W_2B_5	-	2.98	-	20.48	-		162
	β-Ti_2B_5	Hexagonal	β-W_2B_5	$P6_3/mmc$	2.99	-	12.60	-		162
	ω-Ti_2B_5	Rhombohedral	-	-	3.64	-	27.51	-		162
	α-TiB_{12}	Tetragonal	α-AlB_{12}	$P4_12_12$	10.26	-	14.41	-		162
	β-TiB_{12}	Orthorhombic	β-AlB_{12}	-	12.43	12.79	10.16	-		162
	γ-TiB_{12}	Orthorhombic	γ-AlB_{12}	$P2_12_12$	16.62	17.94	10.16	-		162
	TiB_{25}	Orthorhombic	AlB_{10}	*Cmcm*	8.84	9.14	5.88	-		162
	TiB_{55}	Hexagonal	$Cr_{1.5}B_{104.9}$	$R\bar{3}m$	11.78	-	23.43	-		162
	TiB_{50}	Rhombohedral	$Ti_{2.0}B_{103.2}$	$R\bar{3}m$	10.925	-	23.913	2.44		58,148,288
	TiB_{66}	Cubic	SmB_{66}	$Fm\bar{3}c$	23.58	-	-	-		162
Zr	ZrB_2	Hexagonal	AlB_2	*P6/mmm*	3.169	-	3.531	6.1		81,149,176,292
	ZrB_{12}	Cubic	UB_{12}	$Fm\bar{3}m$	7.408	-	-	3.64		44,46,81,152,153,176, 293
	ZrB_{50}	Rhombohedral	$Sc_{1.6}B_{104.0}$	$R\bar{3}m$	10.932	-	23.849	2.42		81,148
Hf	HfB_2	Hexagonal	AlB_2	*P6/mmm*	3.144	-	3.479	11.16		19,134,149,292,294
	HfB_{12}	Cubic	UB_{12}	$Fm\bar{3}m$	7.377	-	-	5.09	high pressure phase	46,49
	HfB_{50}	Rhombohedral	$Sc_{1.6}B_{104.0}$	$R\bar{3}m$	10.975	-	24.034	2.96		134,148
V	V_3B_2	Tetragonal	U_3Si_2	*P4/mbm*	5,739	-	3.029	6.56		16,295–297
	VB	Orthorhombic	CrB	*Cmcm*	3.060	8.048	2.972	5.44		16,295,298,299
	V_5B_6	Orthorhombic	V_5B_6	*Cmmm*	2.977	21.12	3.061	5.48		16,17,295
	V_3B_4	Orthorhombic	Ta_3B_4	*Immm*	3.058	13.22	2.981	5.44		16,19,295,298
	V_2B_3	Orthorhombic	V_2B_3	*Cmcm*	3.061	18.40	2.984	5.3		16,17,19,295

	VB_2	Hexagonal	AlB_2	*P6/mmm*	2.998	-	3.055	5.07		295,299,300
	VB_{50}	Rhombohedral	$V_{1.7}B_{104.8}$	$R\bar{3}m$	10.972	-	23.908	2.43		58,148,295
Nb	Nb_3B_2	Tetragonal	U_3Si_2	*P4/mbm*	6.18	-	3.3	7.91		298,301–303
	NbB	Orthorhombic	CrB	*Cmcm*	3.296	8.722	3.165	7.57		301–304
	Nb_5B_6	Orthorhombic	V_5B_6	*Cmmm*	3.157	22.767	3.303	7.41		301,304
	Nb_3B_4	Orthorhombic	Ta_3B_4	*Immm*	3.143	33.033	14.076	7.32		301,302,304
	NbB_2	Hexagonal	AlB_2	*P6/mmm*	3.112	-	3.266	6.95		301,304
	NbB_{100}	Rhombohedral	$Fe_{1.2}B_{105.4}$	$R\bar{3}m$	10.938	-	23.858	2.4		148,301
Ta	Ta_2B	Tetragonal	$CuAl_2$	*I4/mcm*	5.783	-	4.866	15.21		305–309
	Ta_3B_2	Tetragonal	U_3Si_2	*P4/mbm*	6.184	-	3.284	14.93		303,305,309,310
	Ta_5B_6	Orthorhombic	V_5B_6	*Cmmm*	22.602	3.1385	3.289	-		17,18
	TaB	Orthorhombic	CrB	*Cmcm*	3.276	8.669	3.157	14.21		302,305,307,308
	Ta_3B_4	Orthorhombic	Ta_3B_4	*Immm*	3.13	14.0	3.29	13.5		302,305,307,308,311
	TaB_2	Hexagonal	AlB_2	*P6/mmm*	3.076	-	3.275	12.53		18,302,305,311
	TaB_{100}	Rhombohedral	$Ta_{1.1}B_{104.2}$	$R\bar{3}m$	10.942	-	23.898	2.66		148,305
Cr	Cr_2B	Orthorhombic	Mn_4B	*Fddd*	4.275	7.452	14.795	6.47		13,195,312
	Cr_5B_3	Tetragonal	Cr_5B_3	*I4/mcm*	5.46	-	10.64	6.12		19,195,312
	CrB	Orthorhombic	CrB	*Cmcm*	2.978	7.87	2.935	6.07		19,195,302,312,313
	Cr_3B_4	Orthorhombic	Ta_3B_4	*Immm*	2.952	3.000	13.018	5.74		312–316
	CrB_2	Hexagonal	AlB_2	*P6/mmm*	2.972	-	3.066	5.21		195,312,317,318
	CrB_4	Orthorhombic	CrB_4	*Immm*	2.866	4.744	5.477	4.25		36,38,312
				Pnnm	4.747	5.480	2.868	4.25		37,40
	CrB_{50}	Rhombohedral	$Cr_{1.5}B_{104.9}$	$R\bar{3}m$	10.983	-	23.908	2.42		58,148,312
Mo	Mo_2B	Tetragonal	$CuAl_2$	*I4/mcm*	5.547	-	4.739	9.23		6,19,306,319–321
	Mo_3B_2	Tetragonal	U_3Si_2	*P4/mbm*	6.00	-	3.15	9.06		319,322
	α-$MoB_{(rt)}$	Tetragonal	MoB	$I4_1/amd$	3.105	-	16.97	8.67		19,319,320
	β-$MoB_{(ht)}$	Orthorhombic	CrB	*Cmcm*	3.16	8.61	3.08	8.46		302,319,320,323
	α-$MoB_{2(rt)}$	Rhombohedral	Mo_2B_4 ($CaSi_2$(hR6))	$R\bar{3}m$	3.038	-	20.954	7.106		21
			Mo_2B_5	$R\bar{3}m$	3.015	-	20.971	7.09		19,319,320,324
	β-$MoB_{2(ht)}$	Hexagonal	AlB_2	*P6/mmm*	3.005	-	3.173	7.87		319,325
	MoB_4	Hexagonal	$Mo_{0.8}B_3$	$P6_3/mmc$	5.265	-	6.121	5.37		19,20,319,325

	MoB_{100}	Rhombohedral	MoB_{100}	$R\bar{3}m$	10.930	-	23.822	2.55		319,326
W	W_2B	Tetragonal	$CuAl_2$	*I4/mcm*	5.568	-	4.744	17.09		306,320,327,328
	β-$WB_{(ht)}$	Orthorhombic	CrB	*Cmcm*	3.2	8.41	3.1	15.5		320,327,329,330
	α-$WB_{(rt)}$	Tetragonal	MoB	$I4_1/amd$	3.097	-	16.957	15.9		142,320,327
	α-$WB_{2(ht)}$	Rhombohedral	Mo_2B_5	$R\bar{3}m$	3.01	-	20.93	12.79		22,142
	β-$WB_{2(rt)}$	Hexagonal	W_2B_4	$P6_3/mmc$	2.986	-	13.896	-		21
			W_2B_5	$P6_3/mmc$	2.983	-	13.879	12.76		19,22,142,320,327
	WB_4	Hexagonal	$W_{1.83}B_9$	$P6_3/mmc$	5.200	-	6.334	8.4		24,26,142,192,327
	WB_{100}	Rhombohedral	WB_{100}	$R\bar{3}m$	10.938	-	23.836	2.73		326,327
Mn	Mn_2B	Orthorhombic	o-Mn_2B	*Fddd*	14.540	7.291	4.208	7.19		8,316,331,332
	Mn_2B	Tetragonal	$CuAl_2$	*I4/mcm*	5.148	-	4.208	7.19		316,331–333
	MnB	Orthorhombic	FeB	*Pnma*	5.56	2.977	4.145	6.37		6,302,316,331,332
	Mn_3B_4	Orthorhombic	Ta_3B_4	*Immm*	2.96	3.032	12.86	5.99		6,302,316,331,334
	MnB_2	Hexagonal	AlB_2	*P6/mmm*	3.005	-	3.038	5.35		331,335,336
	MnB_4	Monoclinic	MnB_4	*C2/m*	5.503	5.367	2.949	4.45	β=122.71°	331,337
				$P2_1/c$	5.898	5.373	5.511	-	β=122.633°	23,39
	MnB_{100}	Rhombohedral	$Mn_{0.8}B_{105.9}$	$R\bar{3}m$	10.959	-	23.901	2.38		58,148,331
Tc	Tc_3B	Orthorhombic	Re_3B	*Cmcm*	2.891	9.161	7.246	10.55		302,338,339
	Tc_7B_3	Hexagonal	Th_7Fe_3	$P6_3mc$	7.417	-	4.777	10.48		302,338,339
	TcB_2	Hexagonal	ReB_2	$P6_3/mmc$	2.892	-	7.453	7.36		302,338,339
Re	Re_3B	Orthorhombic	Re_3B	*Cmcm*	2.89	9.313	7.258	19.36		157,302,340–342
	Re_7B_3	Hexagonal	Th_7Fe_3	$P6_3mc$	7.503	-	4.882	18.64		157,302,340,342,343
	ReB_2	Hexagonal	ReB_2	$P6_3/mmc$	2.9	-	7.478	12.67		139,157,302,340,344,345
	ReB_{100}	Rhombohedral	ReB_{100}	$R\bar{3}m$	10.928	-	23.828	2.74		326,340
Fe	$Fe_{23}B_6$	Cubic	τ-$Cr_{23}B_6$	$Fm\bar{3}m$	10.761	-	-	-		346
	Fe_2B	Tetragonal	$CuAl_2$	*I4/mcm*	5.109	-	4.249	7.34		302,347–349
	FeB	Orthorhombic	FeB	*Pnma*	5.495	2.946	4.053	6.75		302,347,349,350
	FeB_4	Orthorhombic	FeB_4	*Pnnm*	5.898	5.373	5.511	-		351–353
	FeB_{50}	Rhombohedral	$Cr_{2.5}B_{103.3}$	$R\bar{3}m$	10.96	-	23.887	2.49		58,347,354
Ru	Ru_7B_3	Hexagonal	Th_7Fe_3	$P6_3mc$	7.467	-	4.714	10.8		343,355,356
	$Ru_{11}B_8$	Orthorhombic	$Ru_{11}B_8$	*Pbam*	7.469	-	4.714	10.78		341

	$RuB_{1.1}$	Hexagonal	WC	$P\bar{6}m2$	11.609	11.342	2.836	-		142,302,357
	Ru_2B_3	Hexagonal	Ru_2B_3	$P6_3/mmc$	2.905	-	12.813	8.32		19,142,355
	RuB_2	Orthorhombic	RuB_2	$Pmmn$	2.867	4.644	4.045	7.57		314,355,356,358,359
	RuB_{100}	Rhombohedral	RuB_{100}	$R\bar{3}m$	10.928	-	23.624	2.58		326
Os	$OsB_{1.2}$	Hexagonal	WC	$P\bar{6}m2$	2.876	-	2.871	-		357
	Os_2B_3	Hexagonal	Ru_2B_3	$P6_3/mmc$	2.91	-	12.91	-		356,360,361
	OsB_2	Orthorhombic	RuB_2	$Pmmn$	2.872	4.684	4.076	12.83		358–360
	OsB_{100}	Rhombohedral	OsB_{100}	$R\bar{3}m$	10.932	-	23.826	2.75		326,360
Co	$Co_{23}B_6$	Cubic	τ-$Cr_{23}B_6$	$Fm\bar{3}m$	10.761	-	-	-		12
	Co_3B	Orthorhombic	Fe_3C	$Pnma$	5.229	6.631	4.432	8.11		362–365
	Co_2B	Tetragonal	$CuAl_2$	$I4/mcm$	5.016	-	4.22	8.05		302,348,362,364–366
	CoB	Orthorhombic	FeB	$Pnma$	5.243	3.037	3.948	7.37		302,350,362,365,366
	CoB_{50}	Rhombohedral	$Sc_{1.3}B_{105.2}$	$R\bar{3}m$	10.957	-	23.84	2.45		58,148,362
Rh	Rh_7B_3	Hexagonal	Th_7Fe_3	$P6_3mc$	7.469	-	4.777	10.83		302,367,368
	$RhB_{1.1}$	Hexagonal	NiAs	$P6_3/mmc$	3.309	-	4.224	9.43		341,367,369,370
	RhB_{100}	Rhombohedral	RhB_{100}	$R\bar{3}m$	10.929	-	23.816	2.56		326,367
Ir	$IrB_{1.15}$	Tetragonal	α-$ThSi_2$	$I4/amd$	2.810	-	10.26	16.73		369,371
	$IrB_{1.35}$	Monoclinic	$IrB_{1.35}$	$C2/m$	10.525	2.910	6.099	14.70	β=91.4°	19,302,359
Ni	Ni_3B	Orthorhombic	Fe_3C	$Pnma$	5.222	6.617	4.392	8.18		9,372–374
	Ni_2B	Tetragonal	$CuAl_2$	$I4/mcm$	4.989	-	4.246	8.06		6,302,314,348,372
	Ni_4B_3	Orthorhombic	$Ni_4B_{3(o)}$	$Pnma$	11.954	2.982	6.568	7.58		372,374,375
	Ni_4B_3	Monoclinic	$Ni_4B_{3(m)}$	$C2/c$	6.428	4.879	7.819	-	β=122.27°	372,374,375
	NiB	Orthorhombic	CrB	$Cmcm$	2.929	7.392	2.961	7.2		302,314,372,376
	Ni_7B_3	Hexagonal	$Th_7Fe_{3(disord)}$	$P6_3mc$	6.968	-	4.394	-		377
	NiB_{100}	Rhombohedral	$Ni_{0.95}B_{106.1}$	$R\bar{3}m$	10.955	-	23.865	2.42		148,372
Pd	$Pd_{16}B_3$	Monoclinic	Pd_6B	$C2/c$	4.890	8.467	9.364	11.29	β=100.03°	378,379
	Pd_3B	Orthorhombic	Fe_3C	$Pnma$	5.464	7.563	4.851	10.93		9,302,342,378
	Pd_5B_2	Monoclinic	Mn_5C_2	$C2/c$	12.786	4.955	5.472	10.69		302,342,378,380
	Pd_2B	Orthorhombic	$CaCl_2$	$Pnnm$	4.692	5.127	3.101	9.93		378,381
	PdB_{100}	Rhombohedral	PdB_{100}	$R\bar{3}m$	10.931	-	23.821	2.57		326,378
Pt	Pt_3B	Tetragonal	Pt_4B	-	2.63	-	3.83	-		369,382–384
	Pt_2B	Hexagonal	MoS_2	$P6_3/mmc$	2.794	-	10.486	18.79		382,383

	$PtB_{0.67}$	Orthorhombic	$PtB_{0.67}$	*Cmcm*	3.371	5.817	4.045	16.94		382,385
	PtB_{100}	Rhombohedral	PtB_{100}	$R\bar{3}m$	10.928	-	23.819	2.76		326,382
Th	ThB_4	Tetragonal	UB_4	*P4/mbm*	7.256	-	4.113	8.44		34,386
	ThB_6	Cubic	CaB_6	$Pm\bar{3}m$	4.113	-	-	7.08		220,386,387
	ThB_{12}	Cubic	UB_{12}	$Fm\bar{3}m$	7.612	-	-	5.45	high pressure phase	46,237
	ThB_{66}	Cubic	YB_{66}	$Fm\bar{3}c$	23.518	-	-	2.9		237,386
U	UB_2	Hexagonal	AlB_2	*P6/mmm*	3.130	-	3.988	12.74		388–390
	UB_4	Tetragonal	UB_4	*P4/mbm*	7.075	-	3.979	9.38		33,34,388
	UB_{12}	Cubic	UB_{12}	$Fm\bar{3}m$	7.473	-	-	5.85		153,159,388,391,392
Pu	PuB_2	Hexagonal	AlB_2	*P6/mmm*	3.186	-	3.949	12.7		390,393,394
	PuB_4	Tetragonal	UB_4	*P4/mbm*	7.1	-	4.014	9.43		390,393,394
	PuB_6	Cubic	CaB_6	$Pm\bar{3}m$	4.115	-	-	7.36		390,393,394
	PuB_{12}	Cubic	UB_{12}	$Fm\bar{3}m$	7.484	-	-	5.92		393,395
	$Pu_{0.66}B_{66}$	Cubic	YB_{66}	$Fm\bar{3}c$	23.43	-	-	2.71		393,395

Table 1-3. Stacking sequences in layered borides.

AlB_2	AHAHAH
"Mo_2B_5"	AHAKBHBKCHCK
$Mo_{0.8}B_3$	A'HB'H
"W_2B_5"	AHAK'BHBK'
ReB_2	AH'BK'AK'BK'

Table 1-4. Vickers Hardness for Select Metal Borides[a,b]

Boride	Vickers Hardness (H_v)		Applied Force Load		Reference
	(kg/mm^2)	(GPa)	(gram-force)	(N)	
Be_5B	623	6.11	-	-	[396]
Be_2B	890	8.73	-	-	[396]
BeB_2	3180	31.19	-	-	[396]
BeB_6	2577	25.27	-	-	[396]
CaB_6	2700 ± 220	26.48 ± 2.16	30	0.29	[397]
SrB_6	2920 ± 90	28.54 ± 088	30	0.29	[398]
BaB_6	3000 ± 290	29.42 ± 2.84	30	0.29	[397]
ScB_2	1780 ± 276	17.46 ± 2.71	200	1.96	[399]
ScB_{12}	-	41.7 ± 2.2	50	0.49	[43]
	4210	41.29	50	0.49	[58]
YB_4	2850 ± 150	27.94 ± 1.47	-	-	[264]
YB_6	2575 ± 100	25.25 ± 0.98	-	-	[264]
YB_{12}	4600	45.11	50	0.49	[400]
	-	40.9 ± 1.6	50	0.49	[43,49]
YB_{66}	-	38	50	0.49	[4]
	-	40.4 ± 1.8	50	0.49	[43,49]
LaB_6	2770 ± 60	27.16 ± 0.59	30	0.29	[397]
CeB_6	3140 ± 190	30.79 ± 1.86	30	0.29	[397]
PrB_6	2470	24.22	100	0.98	[401]
NdB_6	2540 ± 170	24.91 ± 1.68	70	0.69	[401]
SmB_6	2500 ± 300	24.52 ± 2.94	100	0.98	[402]
EuB_6	2660	26.09	100	0.98	[401]
GdB_4	1900 ± 50	18.63 ± 0.49	-	-	[264]
GdB_6	1850 ± 50	18.14 ± 0.49	-	-	[264]
TbB_6	2300	22.56	100	0.98	[401]
DyB_{12}	3100	30.40	50	0.49	[400]
HoB_{12}	2900	28.44	50	0.49	[400]
ErB_{12}	3500	34.32	50	0.49	[400]
TmB_{12}	3800	37.27	50	0.49	[400]
YbB_6	2660	26.09	100	0.98	[401]
	2200	21.57	50	0.49	[400]
LuB_{12}	3600	35.30	50	0.49	[400]
ThB_6	1740	17.06	20	0.19	[403]
ThB_{66}	2310	22.65	-	-	[237]
UB_2	1510	14.81	-	-	[404]
UB_4	2500	24.52	-	-	[404]
UB_{12}	2000	19.61	-	-	[404]
TiB	2800	27.46	30	0.29	[405]
TiB_2	3370 ± 60	33.05 ± 0.22	30	0.29	[406]

	3400	33.34	50	0.49	[151]
TiB_{50}	3640	35.70	50	0.49	[58]
ZrB	3600	35.30	30	0.29	[405]
ZrB_2	2252 ± 22	22.08 ± 0.22	30	0.29	[406]
	2200 - 2500	21.57 - 24.52	-	-	[176]
ZrB_{12}	2850	27.95	-	-	[81]
	4500 ± 150	44.13 ± 1.47	-	-	[176]
	-	40.4 ± 1.8	50	0.49	[43]
HfB_2	2900 ± 500	28.44 ± 4.90	30	0.29	[401]
	2900	28.44	-	-	[134]
HfB_{50}	4000	39.23	-	-	[134]
V_3B_2	2280	22.36	50	0.49	[401]
V_3B_4	2350	23.05	50	0.49	[401]
VB_2	2800 ± 13	27.46 ± 0.12	30	0.29	[406]
VB_{50}	3610	35.40	50	0.49	[58]
Nb_3B_2	2290	22.46	50	0.49	[401]
NbB	2195	21.53	50	0.49	[401]
Nb_3B_4	2290	22.46	30	0.29	[401]
NbB_2	2600	25.50	30	0.29	[401]
Ta_3B_2	2770	27.16	50	0.49	[401]
TaB	3130	30.69	50	0.49	[401]
Ta_3B_4	3350	32.85	50	0.49	[401]
TaB_2	2500 ± 42	24.52 ± 0.41	30	0.29	[401]
Cr_4B	1240 ± 60	12.16 ± 0.59	50	0.49	[401]
Cr_2B	1350 ± 100	13.24 ± 0.98	50	0.49	[401]
Cr_5B_3	1520	14.91	50	0.49	[132]
CrB	1300	12.75	100	0.98	[401]
Cr_3B_4	1500	14.71	100	0.98	[401]
CrB_2	2100 ± 80	20.59 ± 0.78	50	0.49	[401]
CrB_4	-	26.1 ± 1.0	100	0.98	[40]
CrB_{50}	4110	40.31	50	0.49	[58]
Mo_2B	2500	24.52	50	0.49	[401]
α-MoB	2350	23.04	50	0.49	[401]
β-MoB	2500	24.52	50	0.49	[401]
α-MoB_2	2350	23.04	50	0.49	[401]
β-MoB_2	1200	11.77	50	0.49	[401]
W_2B	2420 ± 20	23.73 ± 0.19	50	0.49	[406]
WB	3700	36.28	50	0.49	[406]
	2610 ± 100	25.60 ± 0.98	50	0.49	[407]
WB_2	2660 ± 12	26.09 ± 0.11	30	0.29	[406]
W_2B_5	2663	26.12	30	0.29	[408]
	2580 ± 100	25.30 ± 0.98	50	0.49	[407]
WB_4	4000 ± 200	39.23 ± 1.96	50	0.49	[26]
	3940 ± 200	38.64 ± 1.96	50	0.49	[142]

	-	43.3 ± 2.9	50	0.49	135,136,144
Mn_4B	1050 ± 50	10.30 ± 0.49	-	-	409
Mn_2B	1800 ± 50	17.65 ± 0.49	-	-	409
MnB	2050 ± 50	20.10 ± 0.49	-	-	409
Mn_3B_4	2000 ± 50	19.61 ± 0.49	-	-	409
MnB_2	1700 ± 50	16.67 ± 0.49	-	-	409
MnB_4	3600 ± 100	35.30 ± 0.49	-	-	409
MnB_{50}	4210	41.29	50	0.49	58
Re_3B	1690	16.57	-	-	157
Re_7B_3	1650	16.18	-	-	157
ReB_2	3100	30.40	-	-	157
	-	40.5 ± 2.4	50	0.49	155
	-	48.0 ± 5.6	50	0.49	139
	-	18.8 ± 2	300	2.94	156
Fe_2B	1340 ± 50	13.14 ± 0.49	-	-	132
FeB	1650	16.18	-	-	132
FeB_{50}	4010	39.32	50	0.49	58
Co_3B	1150	11.28	50	0.49	410
Co_2B	1150	11.28	50	0.49	410
CoB	1150	11.28	50	0.49	410
CoB_2	2575	25.25	50	0.49	410
CoB_{50}	3780	37.07	50	0.49	58
Ni_3B	1190	11.67	-	-	411
Ni_2B	1430	14.02	-	-	411
Ni_4B_3	1486	14.57	-	-	411
NiB	1546	15.16	-	-	411
NiB_{50}	3990	39.13	50	0.49	58
Rh_7B_3	777	7.62	50	0.49	412
$RhB_{1.1}$	1213	11.89	50	0.49	412
PdB_3	470	4.61	-	-	413
Pd_5B_3	595	5.83	-	-	412
$IrB_{1.15}$	1652	16.20	-	-	414

[a]hardness values given in kg/mm^2 were converted to GPa values;

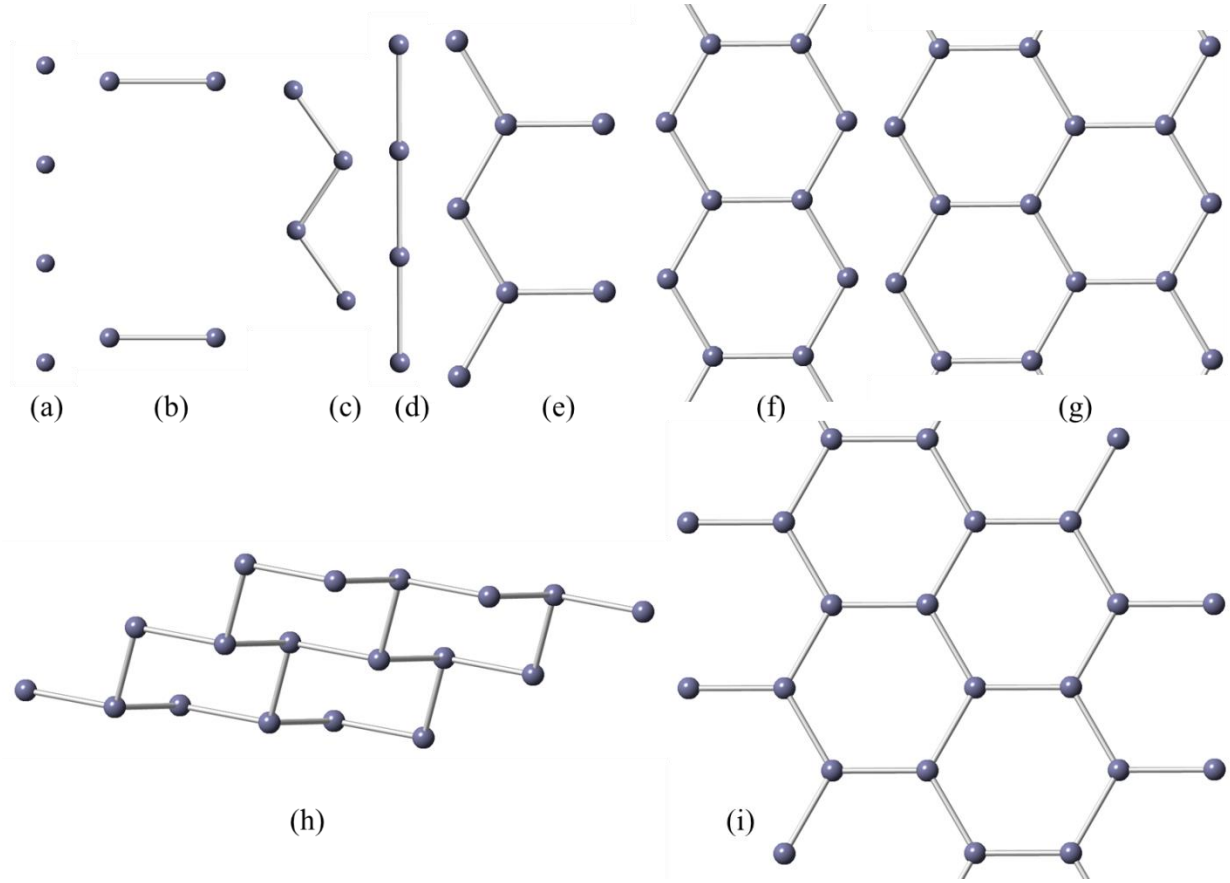

Figure 1-1. Different structural elements formed by boron atoms in metal borides: (a) isolated boron atoms; (b) pairs of boron atoms; (c) zig-zag chains of boron atoms; (d) straight (ordinary) chains of boron atoms; (e) extended chains of boron atoms; (f) double chains of boron atoms; (g) triple chains of boron atoms; (h) corrugated networks of boron atroms; (i) flat networks of boron atoms.

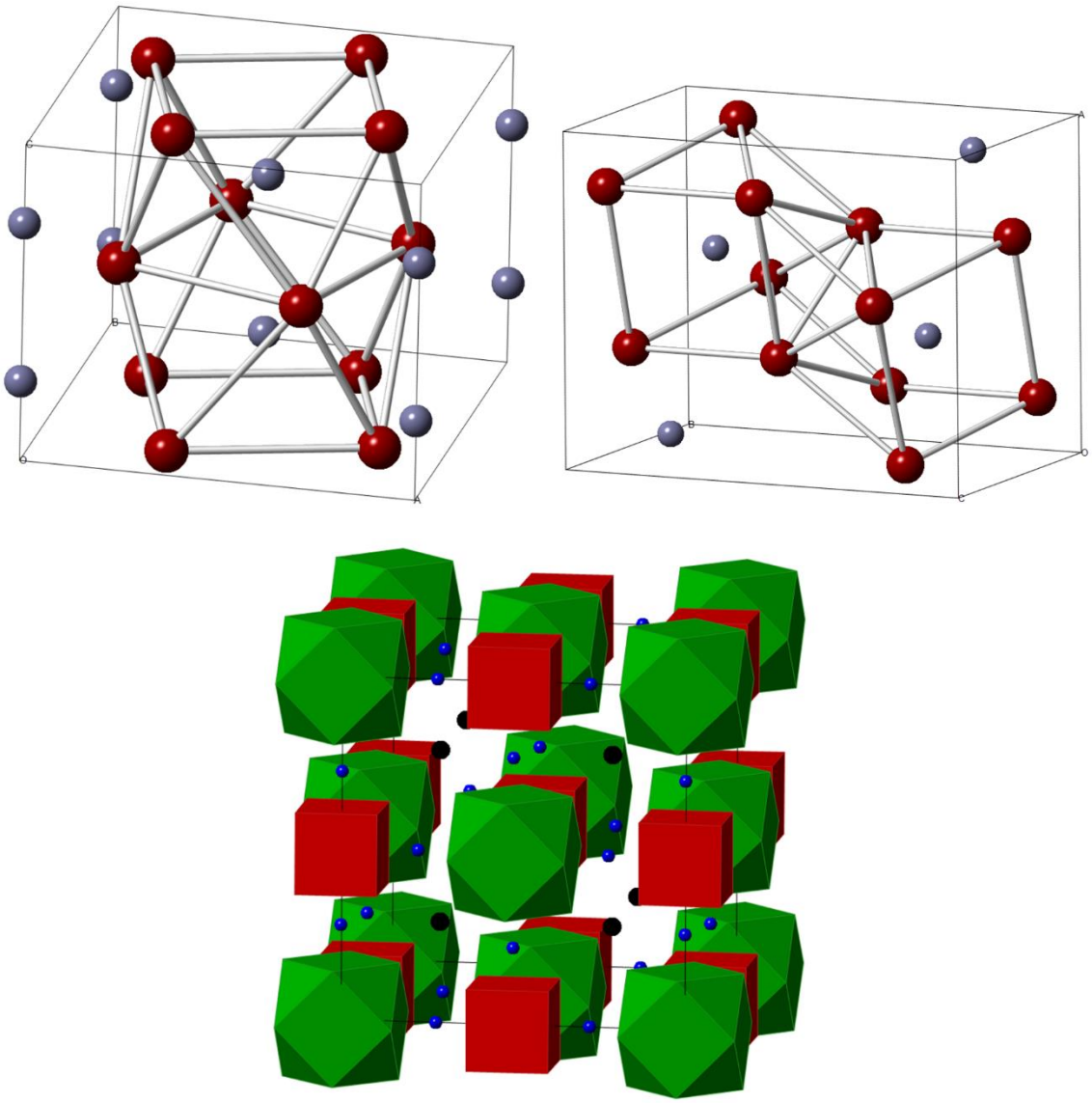

Figure 1-2. Borides with isolated boron atoms: (top) crystal structure of Fe_2B (ICSD 391328, *$CuAl_{2(tetr)}$* structure)[7] and (middle) Ni_3B (ICSD 409893, *$Fe_3C_{(ortho)}$* structure)[9]. ICSD – Inorganic Crystal Structure Database. Boron atoms are in gray, metal atoms are in magenta. (bottom) polyhedra model of the crystal structure of $Co_{23}B_6$ (ICSD 419735, *τ-$Cr_{23}B_{6(cub)}$* structure)[12]. Ni_{12} cuboctahedra are shown in green (each cuboctahedron also contains a Ni atom in its center), Ni_8 cubes are in red, isolated Ni atoms are in black and isolated boron atoms are in blue.

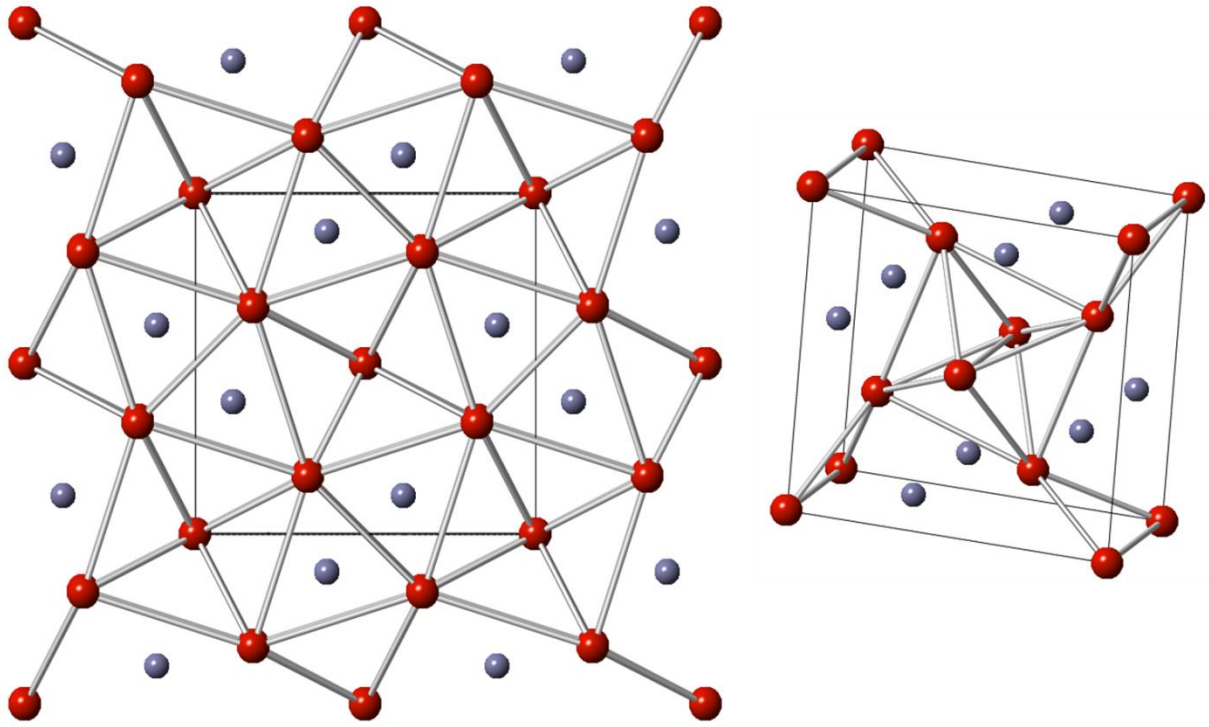

Figure 1-3. Borides with paired boron atoms: crystal structure of V_3B_2 (ICSD 88317, $U_3Si_{2(tetr)}$ structure)[296]. Boron atoms are in gray, metal atoms are in red.

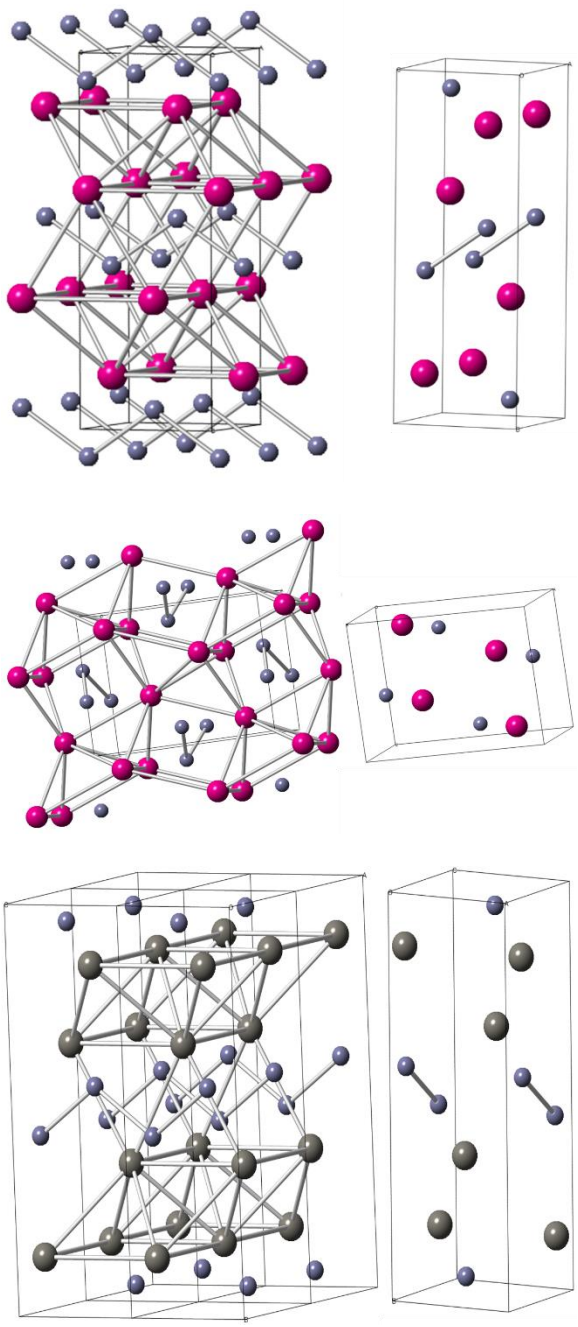

Figure 1-4. Borides with ordinary chains of boron atoms: (top) crystal structure of CrB (ICSD 44249, *TaB*$_{(ortho)}$ structure)[313], (middle) crystal structure of MnB (ICSD 76630, *FeB*$_{(ortho)}$ structure)[6], and (bottom) crystal structure of α-WB (ICSD 424240, *MoB*$_{(tet)}$ structure)[415]. Boron atoms are in gray, metal atoms are in magenta.

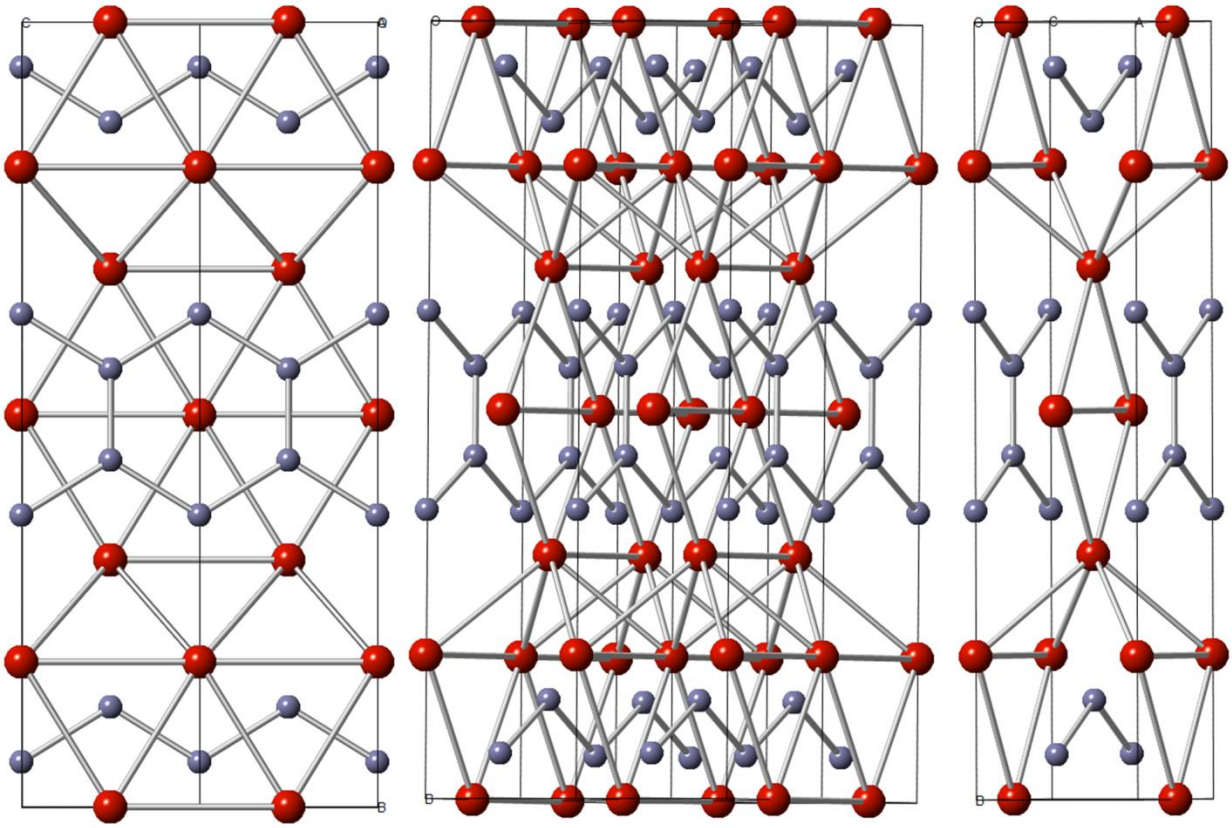

Figure 1-5. Borides with double chains of boron atoms: crystal structure of V_3B_4 (ICSD 615671, *Ta_3B_4 (rhomb)* structure)[298]. Boron atoms are in gray, metal atoms are in red.

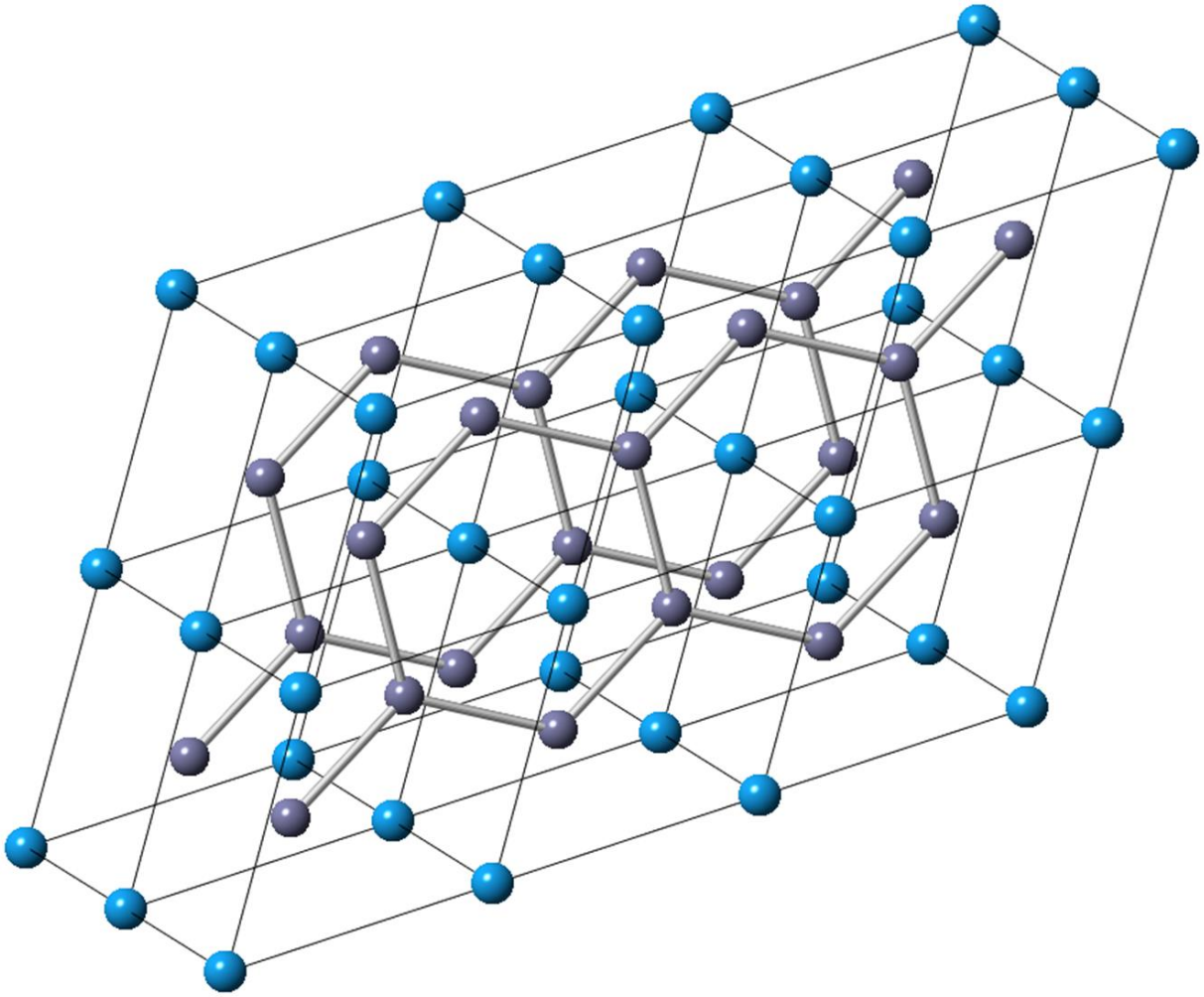

Figure 1-6. Borides with networks of boron atoms: crystal structure of AlB_2 (ICSD 193381, $AlB_{2\,(hex)}$ structure)[416]. Boron atoms are in gray, metal atoms are in blue.

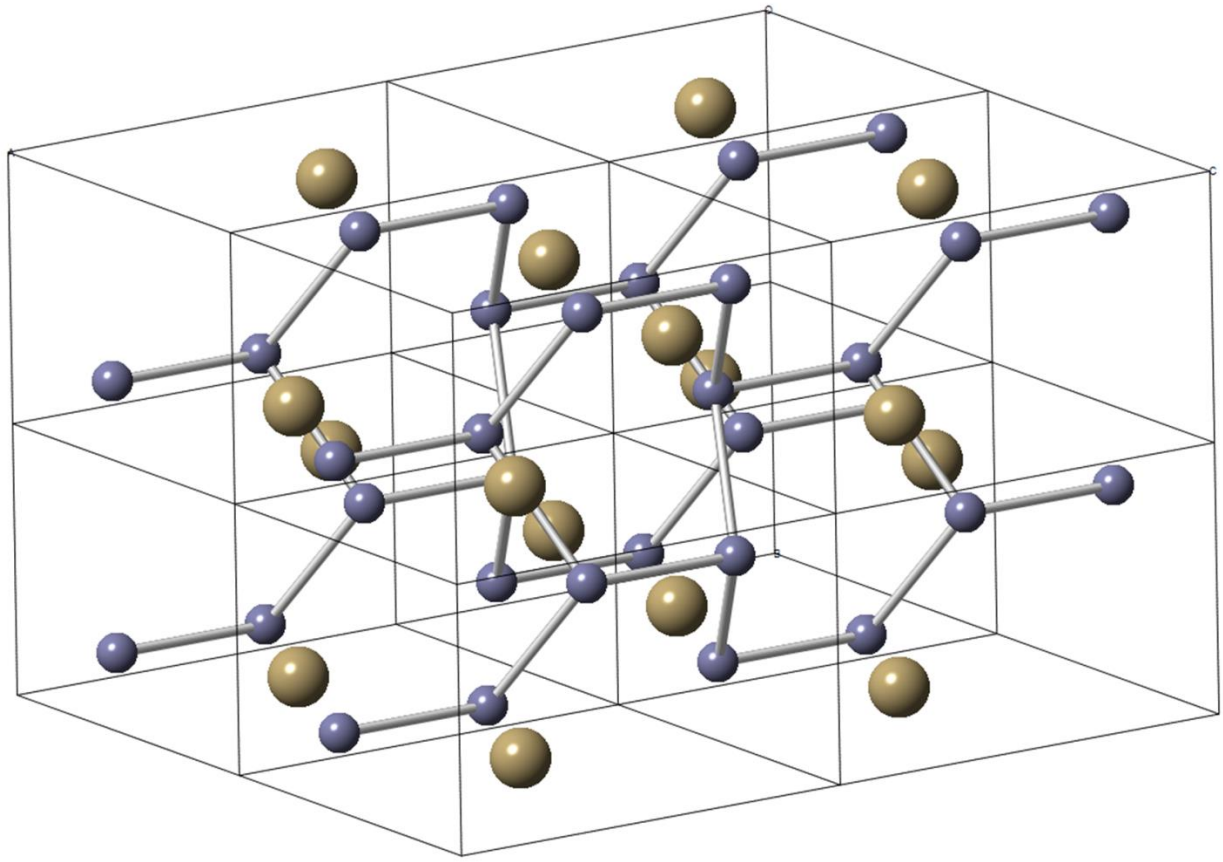

Figure 1-7. Borides with networks of boron atoms: crystal structure of OsB_2 (ICSD 421523, $RuB_{2\,(rhomb)}$ structure)[417]. Boron atoms are in gray, metal atoms are in gold.

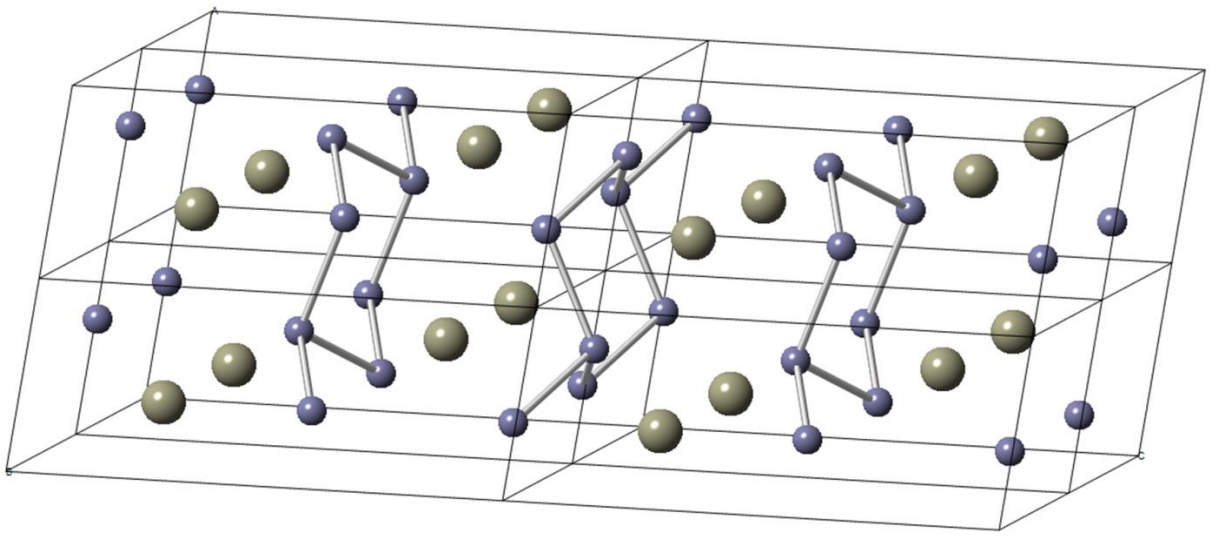

Figure 1-8. Borides with networks of boron atoms: crystal structure of ReB_2 (ICSD 165834, $ReB_{2\,(hex)}$ structure)[418]. Boron atoms are in gray, metal atoms are in gold.

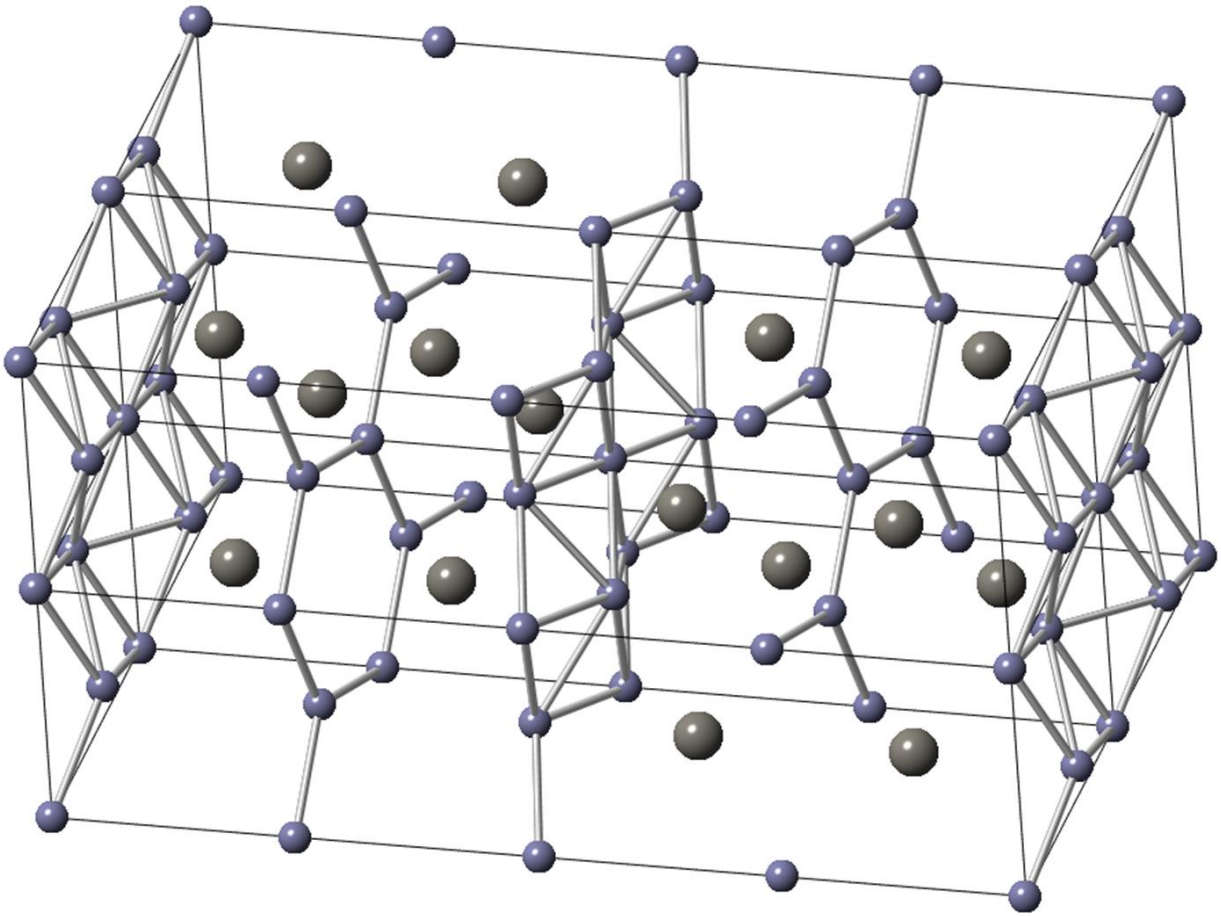

Figure 1-9. Borides with networks of boron atoms: crystal structure of β-WB_2 (ICSD 24283, "*$W_2B_{5(hex)}$*" structure)[320]. Note that while the structure is referred to as having a "*$W_2B_{5(hex)}$*" structure, it has been shown recently that the stoicheometry is W_2B_4.[21] Boron atoms are in gray, metal atoms are in dark gray.

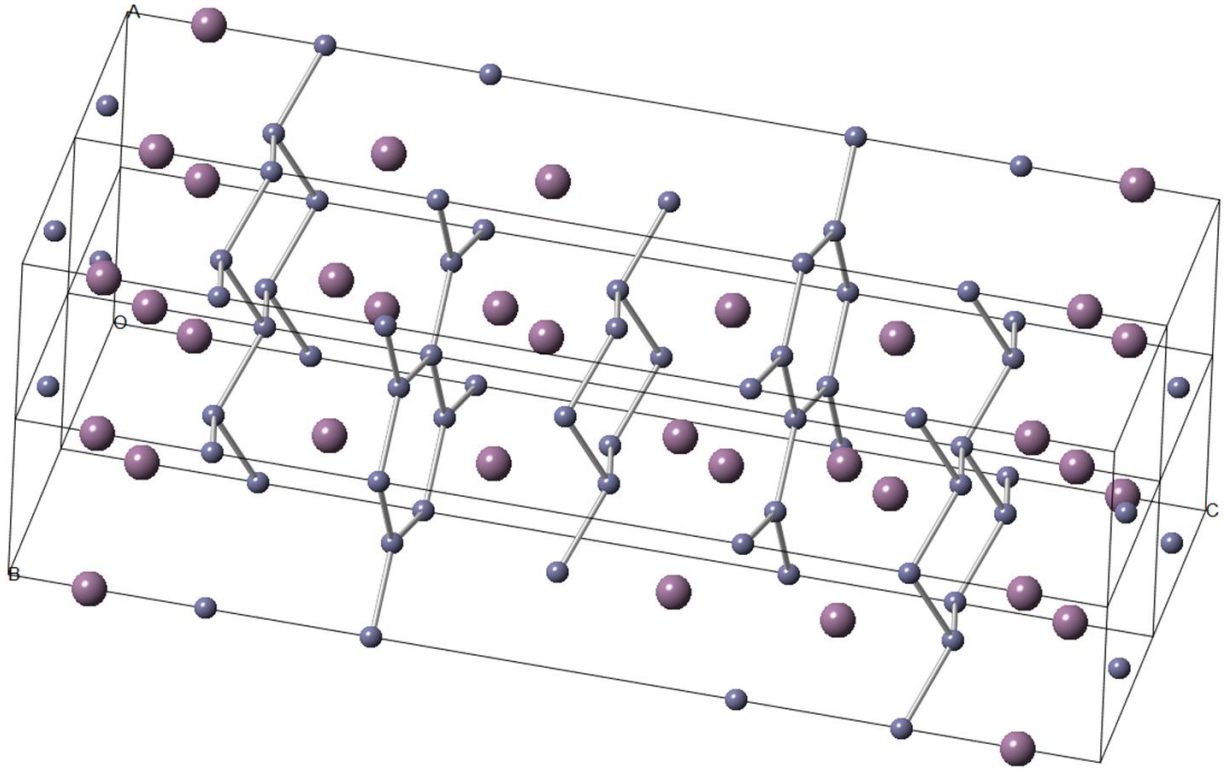

Figure 1-10. Borides with networks of boron atoms: crystal structure of α-$MoB_{2(rt)}$ (ICSD 418397, $Mo_2B_{4(rhomb)}$ structure)[21]. The structure in older literature is referred to as "Mo_2B_5".[19,319,320,324] Boron atoms are in gray, metal atoms are in violet.

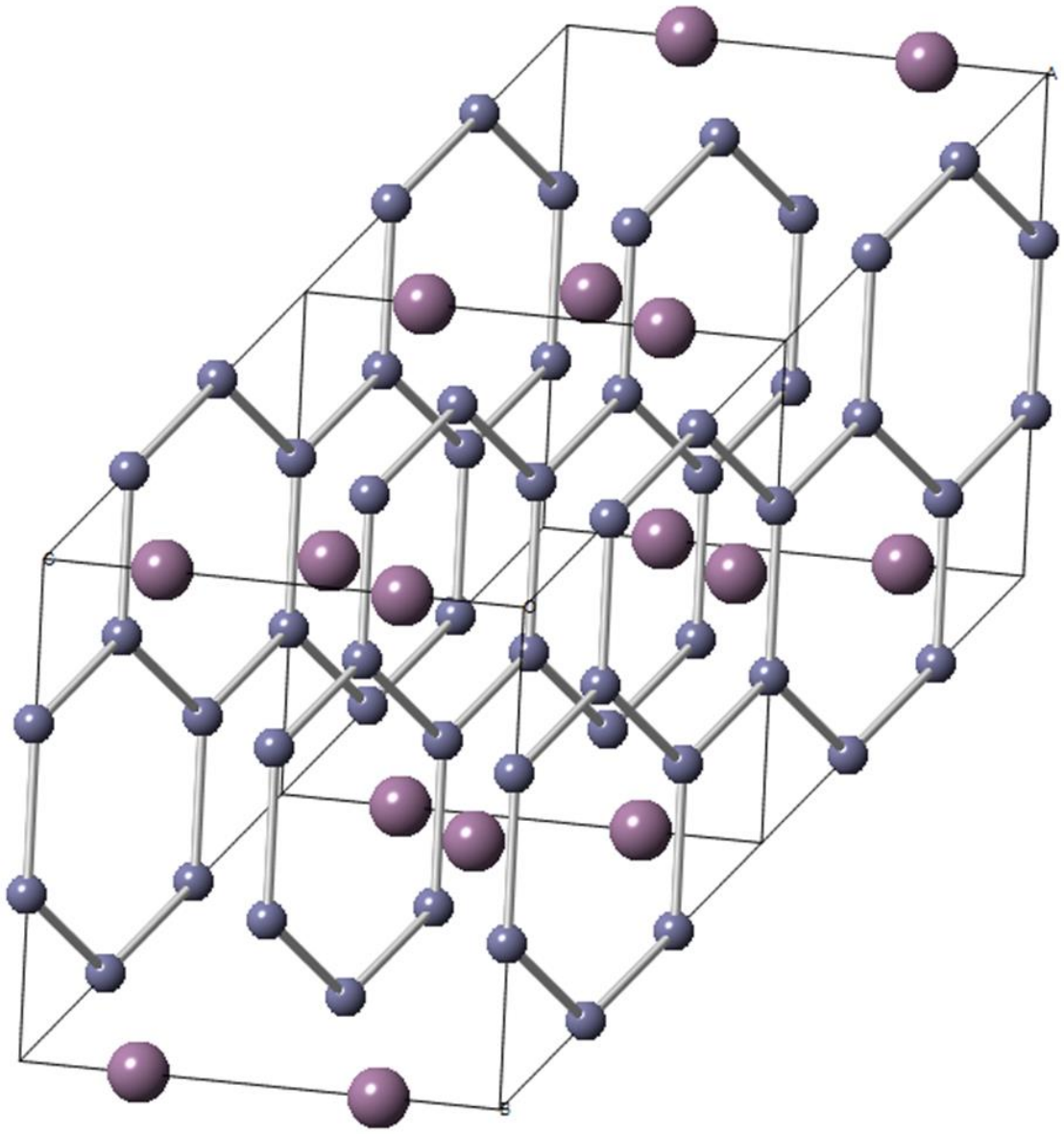

Figure 1-11. Borides with networks of boron atoms: crystal structure of MoB_4 (ICSD 81807, $Mo_{0.8}B_{3\ (hex)}$ structure)[325]. Boron atoms are in gray, metal atoms are in violet.

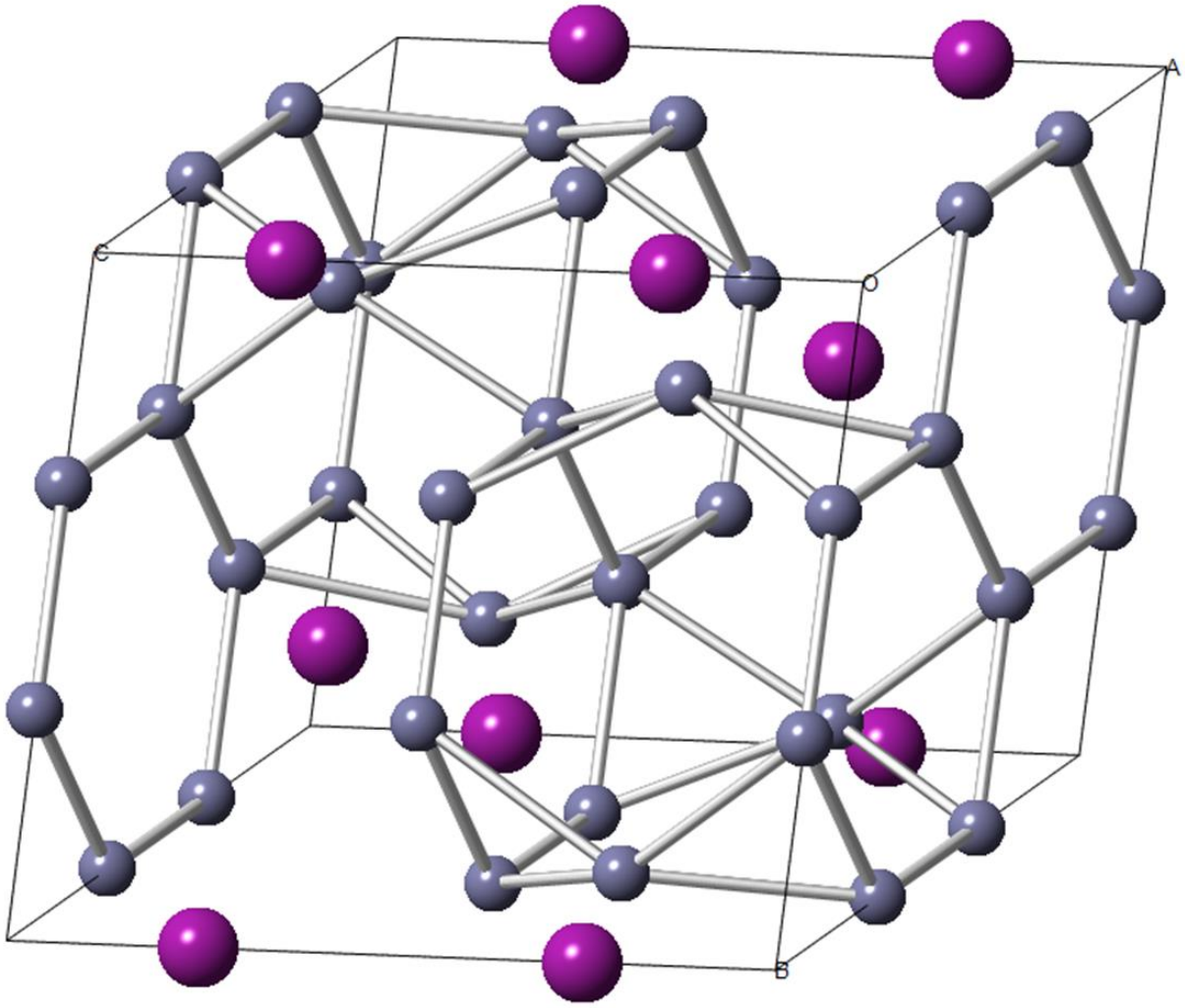

Figure 1-12. Borides with networks of boron atoms: crystal structure of WB_4 (ICSD 291124, $W_{1.6}B_{9\ (hex)}$ structure)[24]. Boron atoms are in gray, metal atoms are in violet.

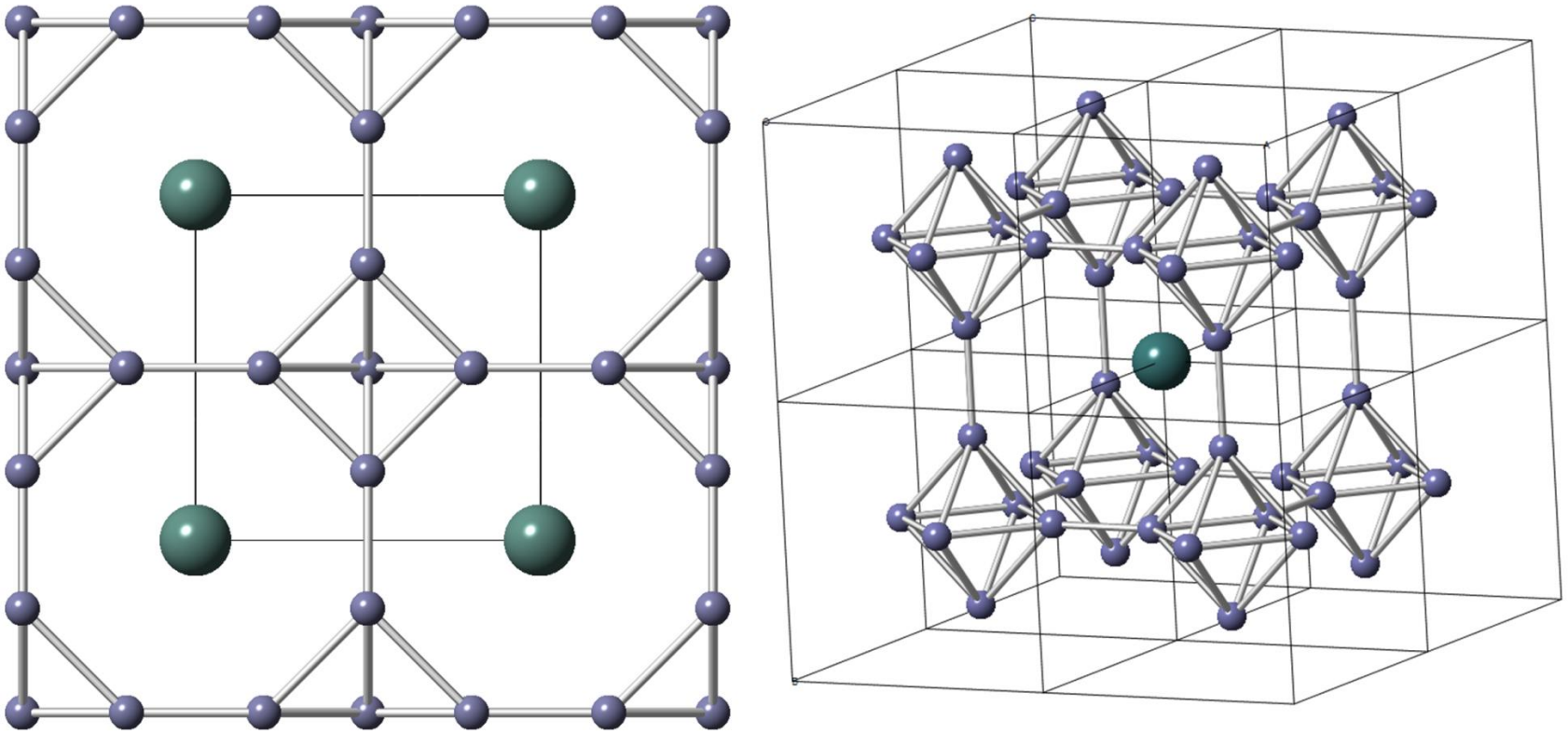

Figure 1-13. Borides with skeletons/backbones of boron atoms: crystal structure of YB_6 (ICSD 54730, *$CaB_{6\ (cub)}$* structure)[419]. Boron atoms are in gray, metal atoms are in teal.

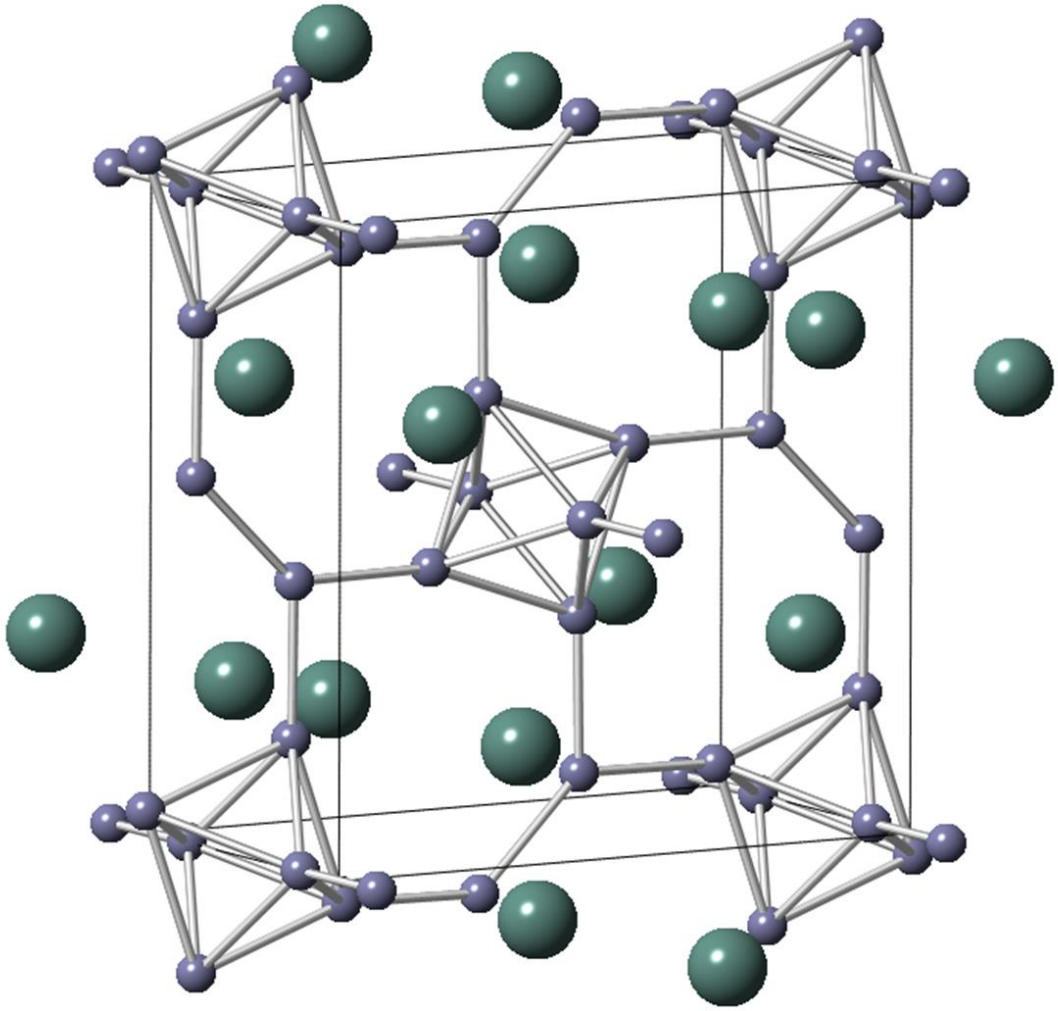

Figure 1-14. Borides with skeletons/backbones of boron atoms: crystal structure of YB_4 (ICSD 26777, $YB_{4\ (cub)}$ structure)[35]. Boron atoms are in gray, metal atoms are in violet.

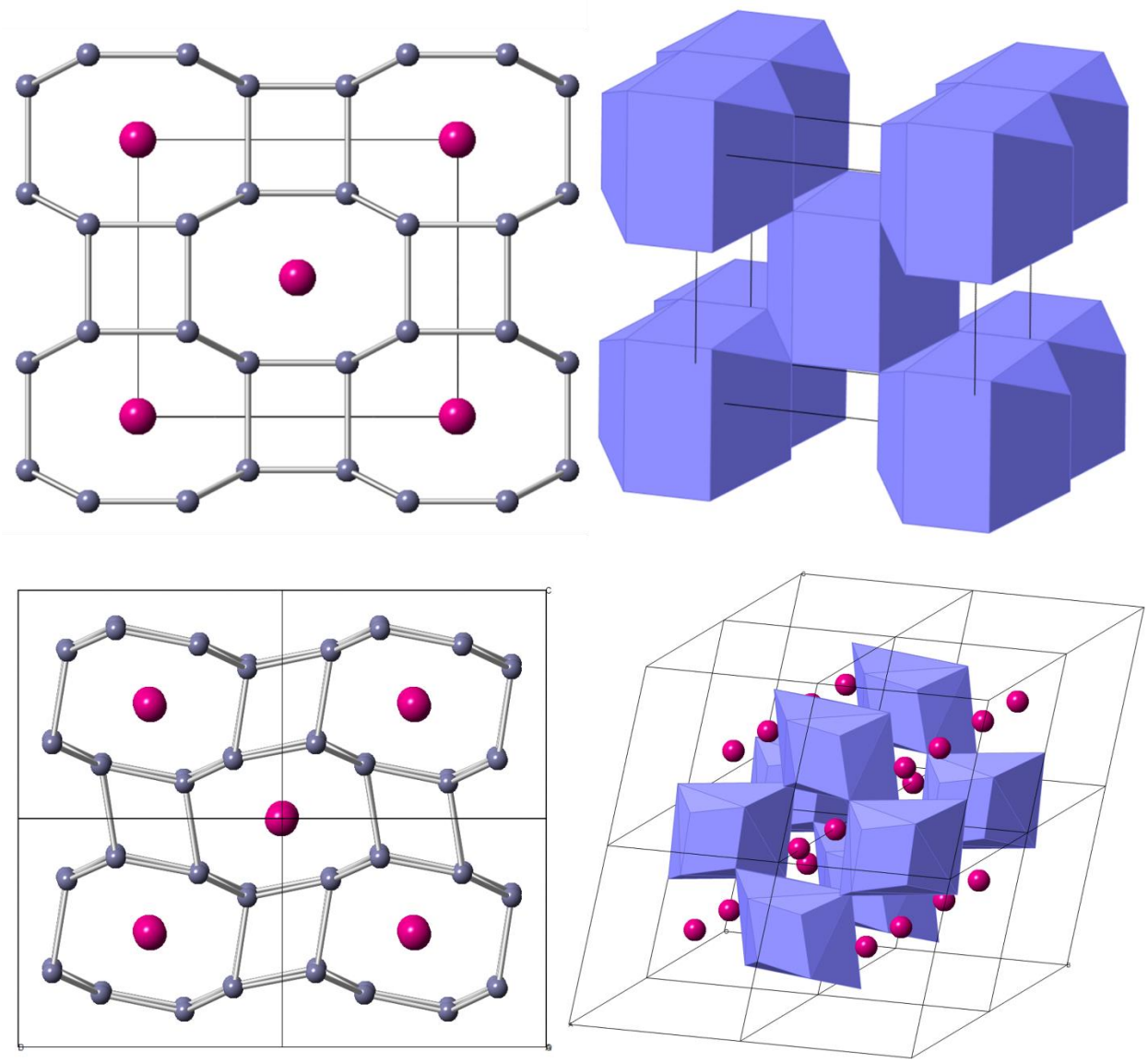

Figure 1-15. Borides with skeletons/backbones of boron atoms: (top) crystal structure of CrB_4 (ICSD 423380, *$CrB_{4\ (ortho)}$* structure)[40]; (bottom) crystal structure of MnB_4 (ICSD 425100, *$MnB_{4(mono)}$* structure[39]. Boron atoms are in gray, metal atoms are in magenta. Cages formed by boron atoms are in slate blue; for CrB_4 each cage contains a metal atom in its center.

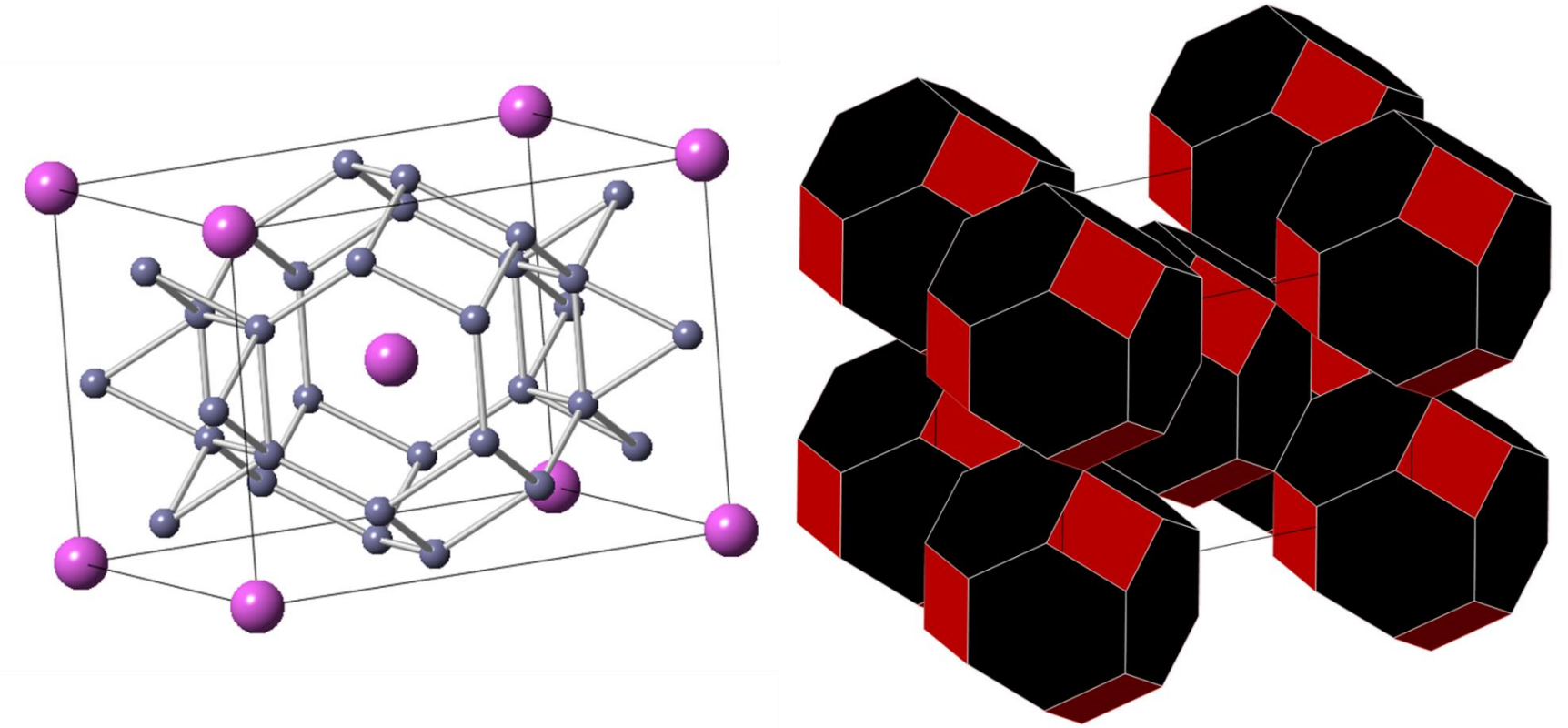

Figure 1-16. Borides with skeletons/backbones of boron atoms: crystal structure of ScB_{12} (ICSD 68028, *$ScB_{12\ (tetr)}$* structure)[146]. Boron atoms are in gray, metal atoms are in magenta. 24 boron atom cuboctahedra, shown in maroon (square faces) and black (hexagonal faces), are arranged in a body-centered tetragonal (BCT) lattice arrangement; each cuboctahedron has a metal atom in its center.

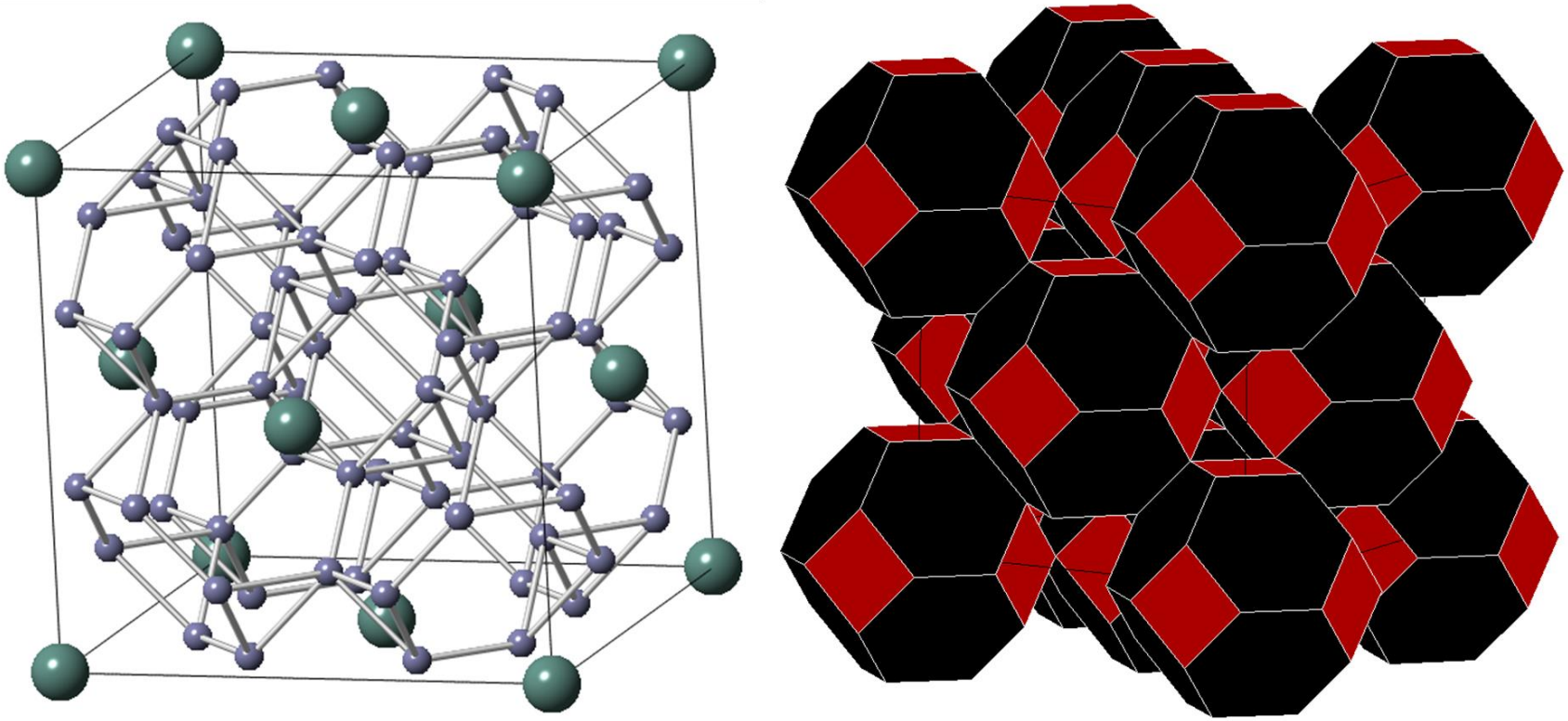

Figure 1-17. Borides with skeletons/backbones of boron atoms: crystal structure of ZrB_{12} (ICSD 409635, $UB_{12\ (cub)}$ structure)[152]. Boron atoms are in gray, metal atoms are in teal. 24 boron atom cuboctahedra, shown in maroon (square faces) and black (hexagonal faces), are arranged in a face-centered cubic (FCC) lattice arrangement; each cuboctahedron has a metal atom in its center.

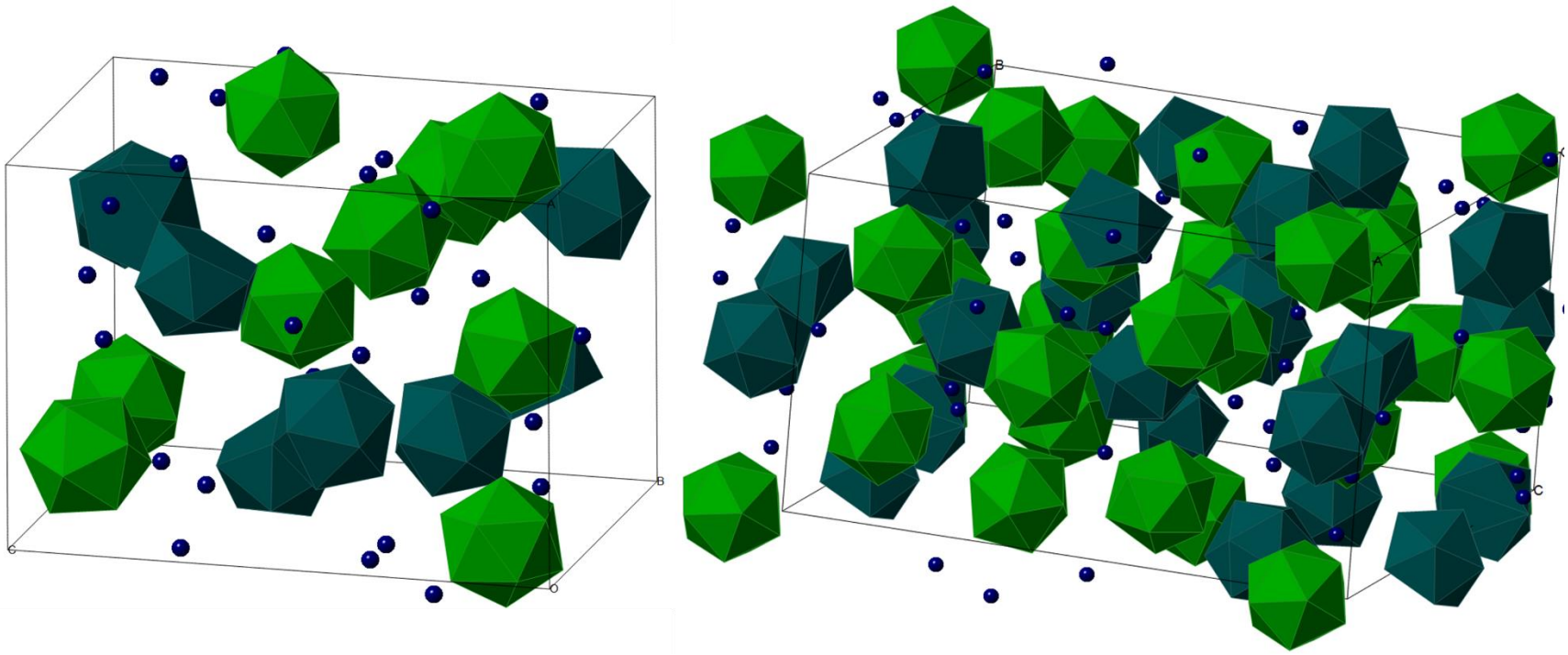

Figure 1-18. Borides with boron icosahedra (B_{12}): (left) crystal structure of α-AlB_{12} (ICSD 1459, *$AlB_{12\ (tetr)}$* structure)[420], (right) crystal structure of γ-AlB_{12} (ICSD 38057, *$AlB_{12\ (rhomb)}$* structure)[53]. Metal atoms are in blue, full B_{12} boron icosahedra are in green, partial boron icosahedra are in teal.

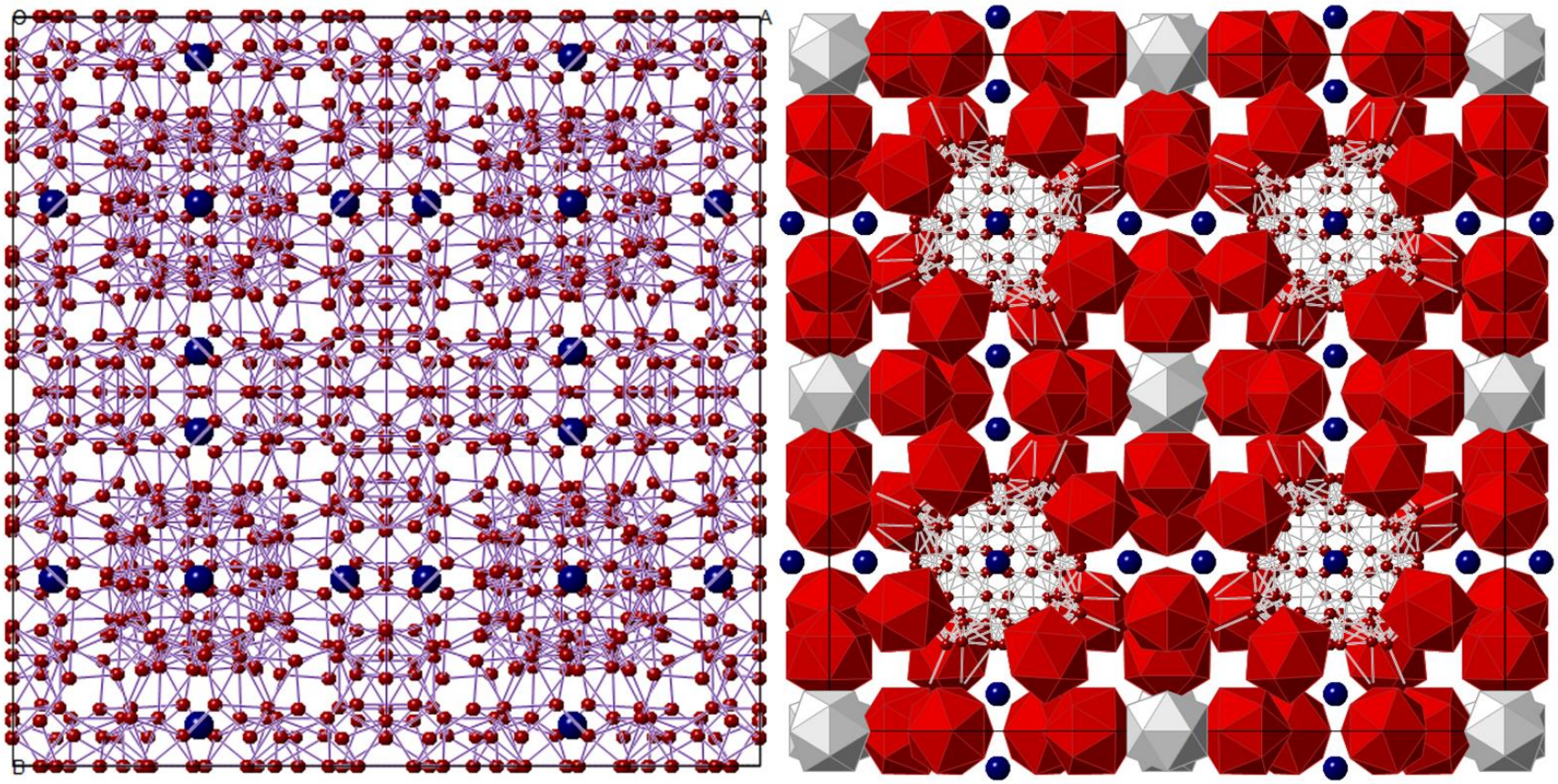

Figure 1-19. Borides with boron icosahedra (B_{12}): crystal structure of YB_{66} (ICSD 23186, $Y_{1.06}B_{66\ (cub)}$ structure)[56]. B_{12} boron icosahedra are in maroon and grey (indicating two different icoahedra symmetry positions), non-icosahedra boron atoms are in maroon, metal atoms are in dark blue.

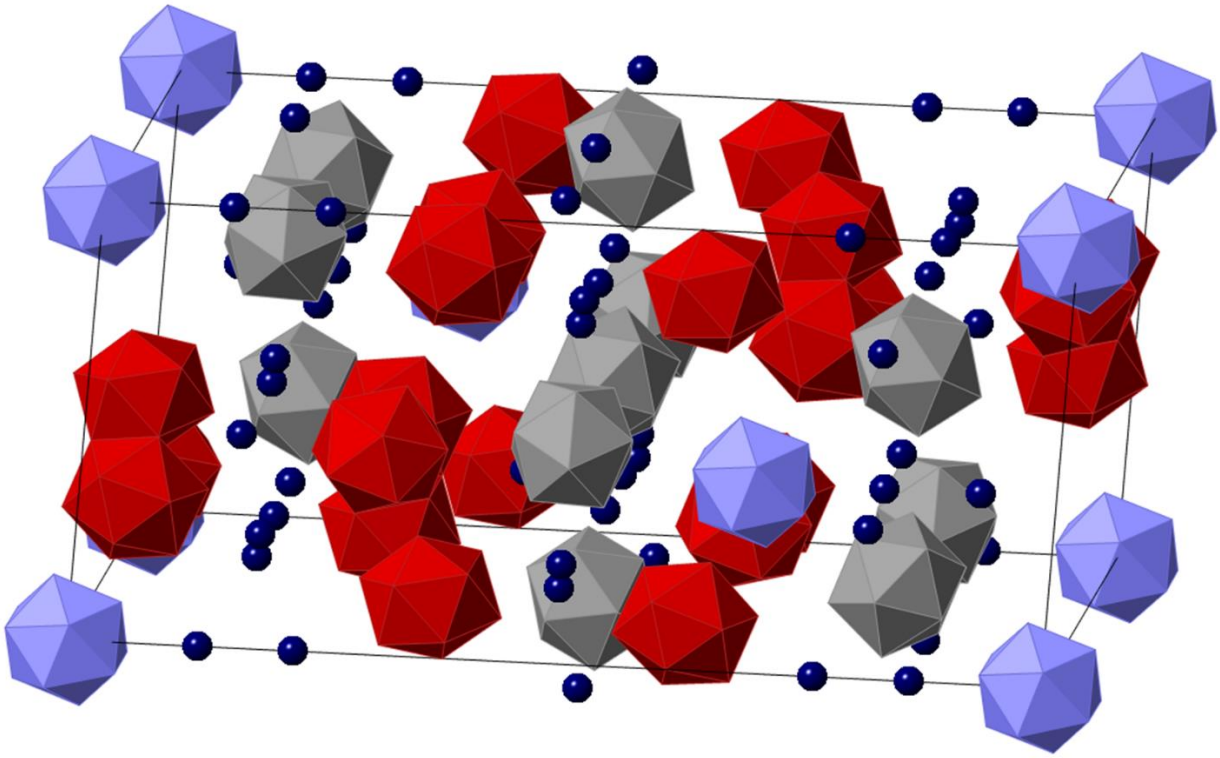

Figure 1-20. Solid solution of transition metals in β-rhombohedral boron: crystal structure of HfB_{50} (ICSD 40396, *$MeB_{50\ (rhomb)}$* structure)[421]. B_{12} boron icosahedra are in maroon, grey and slate blue (indicating three different symmetry positions), metal atoms are in dark blue.

REFERENCES

1. Albert, B. & Hillebrecht, H. Boron: Elementary challenge for experimenters and theoreticians. *Angew. Chemie - Int. Ed.* **48,** 8640–8668 (2009).

2. Yeung, M. T., Mohammadi, R. & Kaner, R. B. Ultraincompressible, Superhard Materials. *Annu. Rev. Mater. Res.* **46,** 465–485 (2016).

3. Buschow, K. H. J. Magnetic Properties of Borides. in *Boron and Refractory Borides* (ed. Matkovich, V. I.) 494–515 (Springer Berlin Heidelberg, 1977). doi:10.1007/978-3-642-66620-9_26

4. Lundström, T. Borides: Solid-state Chemistry. in *Encyclopedia of Inorganic Chemistry* 481–494 (2006).

5. Fokwa, B. P. T. Borides: Solid-State Chemistry. *Encycl. Inorg. Bioinorg. Chem.* 1–14 (2014). doi:10.1002/9781119951438.eibc0022.pub2

6. Kiessling, R., Samuelson, O., Lindstedt, G. & Kinell, P.-O. The Borides of Manganese. *Acta Chemica Scandinavica* **4,** 146–159 (1950).

7. Kapfenberger, C., Albert, B., Pottgen, R. & Huppertz, H. Structure refinements of iron borides Fe2B and FeB. *Zeitschrift für Krist.* **221,** 477–481 (2006).

8. Tergenius, L. E. Refinement of the crystal structure of orthorhombic Mn2B (formerly denoted Mn4B). *J. Less-Common Met.* **82,** 335–340 (1981).

9. Gumeniuk, R., Borrmann, H. & Leithe-Jasper, A. Refinement of the crystal structures of trinickel boron, Ni3B, and tripalladium boron, Pd3B. *Zeitschrift fur Krist. - New Cryst.*

Struct. **221,** 425–426 (2006).

10. Sologub, O., Rogl, P. & Giester, G. The tau-borides tau-(Fe0.54Ir0.46)20Fe3B6 and tau-(Co0.64Ir0.36)21Co0.16B4B6. *Intermetallics* **18,** 694–701 (2010).

11. Steurer, W., Rogl, P. & Nowotny, H. Die tau-Boride in den SystemenTa-Co-B und (Nb,Ta)-Ru-B. *Monatshefte für Chemie* **110,** 791–798 (1979).

12. Kotzott, D., Ade, M. & Hillebrecht, H. Single crystal studies on Co-containing tau-borides Co23-xMxB6 (M=Al, Ga, Sn, Ti, V, Ir) and the boron-rich tau-boride Co12.3Ir8.9B10.5. *J. Solid State Chem.* **182,** 538–546 (2009).

13. Kotzott, D., Ade, M. & Hillebrecht, H. Synthesis and crystal structures of alpha- and beta-modifications of Cr2IrB2 containing 4-membered B4 chain fragments, the tau-boride Cr7.9Ir14.1B6 and orthorhombic Cr2B. *Solid State Sci.* **10,** 291–302 (2008).

14. Yeung, M. T. *et al.* Superhard Monoborides: Hardness Enhancement through Alloying in W1−xTaxB. *Adv. Mater.* 6993–6998 (2016). doi:10.1002/adma.201601187

15. Wörle, M. & Nesper, R. Infinite, linear, unbranched borynide chains in LiB(x) - Isoelectronic to polyyne and polycumulene. *Angew. Chemie - Int. Ed.* **39,** 2349–2353 (2000).

16. Spear, K. E. & Gilles, P. W. Phase and structure relationships in the vanadium boron system. *High Temp. Sci.* **1,** 86 (1969).

17. Bolmgren, H., Lundström, T., Tergenius, L. E., Okada, S. & Higashi, I. The crystal structure of Ta5B6. *J. Less-Common Met.* **161,** 341–345 (1990).

18. Okada, S., Kudou, K., Higashi, I. & Lundström, T. Single crystals of TaB, Ta5B6, Ta3B4 and TaB2, as obtained from high-temperature metal solutions, and their properties. *J. Cryst. Growth* **128,** 1120–1124 (1993).

19. Lundström, T. Preparation and Crystal Chemistry of some refractory Borides and Phosphides. *Ark. Kemi* **31,** 227–266 (1969).

20. Lundström, T. & Rosenberg, I. The crystal structure of the molybdenum boride Mo1-xB3. *J. Solid State Chem.* **6,** 299–305 (1973).

21. Frotscher, M. *et al.* M2B5 or M2B4? A Reinvestigation of the Mo/B and W/B System. *Zeitschrift für Anorg. und Allg. Chemie* **633,** 2626–2630 (2007).

22. Kuz'ma, Y. B., Serebryakova, T. I. & Plakhina, A. M. The polymorphic transformation of W2B5. *Russ. J. Inorg. Chem.* **12,** 288–289 (1967).

23. Knappschneider, A. *et al.* Manganese Tetraboride, MnB4: High-Temperature Crystal Structure, p–n Transition, 55Mn NMR Spectroscopy, Solid Solutions, and Mechanical Properties. *Chem. – A Eur. J.* **21,** 8177–8181 (2015).

24. Lech, A. T., Turner, C. L., Mohammadi, R., Tolbert, S. H. & Kaner, R. B. Structure of superhard tungsten tetraboride: A missing link between MB 2 and MB 12 higher borides. *Proc. Natl. Acad. Sci.* **112,** 3223–3228 (2015).

25. Romans, P. A. & Krug, M. P. Composition and crystallographic data for the highest boride of tungsten. *Acta Crystallogr.* **20,** 313–315 (1966).

26. Bodrova, L. G., Koval'chenko, M. S. & Serebryakova, T. I. Preparation of tungsten

tetraboride. *Sov. Powder Metall. Met. Ceram.* **13,** 1–3 (1974).

27. Samsonov, G. V. *Refractory compounds of metals with nonmetals [in Russian]*. (Metallurgiya, 1964).

28. Post, B., Moskowitz, D. & Glaser, F. W. Borides of Rare Earth Metals. *J. Am. Chem. Soc.* **78,** 1800–1802 (1956).

29. Pauling, L. & Weinbaum, S. Kürzere Originalmitteilungen und Notizen. The Structure of Calcium Boride, CaB6. *Z. Krist.* **87,** 181–182 (1934).

30. Hossain, F. M., Riley, D. P. & Murch, G. E. *Ab initio* calculations of the electronic structure and bonding characteristics of <math display='inline'> <mrow> <msub> <mi>LaB</mi> <mn>6</mn> </msub> </mrow> </math>. *Phys. Rev. B* **72,** 235101 (2005).

31. Massidda, S., Continenza, A., de Pascale, T. M. & Monnier, R. Electronic structure of divalent hexaborides. *Zeitschrift für Phys. B Condens. Matter* **102,** 83–89 (1996).

32. Etourneau, J. & Hagenmuller, P. Structure and physical features of the rare-earth borides. *Philos. Mag. B Phys. Condens. Matter; Stat. Mech. Electron. Opt. Magn. Prop.* **52,** 589–610 (1985).

33. Zalkin, A. & Templeton, D. H. The crystal structures of CeB4, ThB4 and UB4. *J. Chem. Phys.* **18,** 391 (1950).

34. Zalkin, A. & Templeton, D. H. The crystal structures of CeB 4 ThB 4 and UB 4. *Acta Crystallogr.* **6,** 269–272 (1953).

35. Giese, R. F. jr., Matkovic, V. I. & Economy, J. The crystal structure of YB4. *Zeitschrift fuer Krist. Krist. Krist. Krist.* **122,** 423–432 (1965).

36. Andersson, S., Lundström, T., Andresen, A. F. & Pearson, W. B. The crystal structure of CrB_4. *Acta Chemica Scandinavica* **22,** 3103–3110 (1968).

37. Niu, H. *et al.* Structure, bonding, and possible superhardness of CrB4. *Phys. Rev. B* **85,** 144116 (2012).

38. Knappschneider, A., Litterscheid, C., Kurzman, J., Seshadri, R. & Albert, B. Crystal structure refinement and bonding patterns of CrB4: A boron-rich boride with a framework of tetrahedrally coordinated B atoms. *Inorg. Chem.* **50,** 10540–10542 (2011).

39. Knappschneider, A. *et al.* Peierls-distorted monoclinic MnB4 with a mn-Mn bond. *Angew. Chemie - Int. Ed.* **53,** 1684–1688 (2014).

40. Knappschneider, A. *et al.* Possible superhardness of CrB4. *Inorg. Chem.* **52,** 540–542 (2013).

41. Callmer, B. A Single-Crystal Diffractometry Boron Investigation of Scandium in beta-rhombohedral boron. *J. Solid State Chem.* **23,** 391–398 (1978).

42. Paderno, Y. & Shitsevalova, N. Stabilization of cubic scandium dodecaboride. *J. Alloys Compd.* **219,** 119–123 (1995).

43. Akopov, G., Yeung, M. T., Sobell, Z. C., Turner, C. L. & Kaner, R. B. Superhard Mixed Metal Dodecaborides. *Chem. Mater.* **28,** 6605–6612 (2016).

44. La Placa, S., Binder, I. & Post, B. Binary dodecaborides. *J. Inorg. Nucl. Chem.* **18,** 113–

117 (1961).

45. Paderno, Y. B., Odintsov, V. V., Timofeeva, I. I. & Klochkov, L. A. Thermal expansion of metal dodecaborides. *High Temp.* **9,** 175–177 (1971).

46. Cannon, J. F. & Farnsworth, P. B. High pressure syntheses of ThB12 and HfB12. *J. Less-Common Met.* **92,** 359–368 (1983).

47. Hägg, G. Ubergangselementen in' binaren Sistem mit Bor, Kohlenstoff und Stickstoff. *Z. Phys. Chem.* **B12,** 33 (1931).

48. Cannon, J. F., Cannon, D. M. & Tracy Hall, H. High pressure syntheses of SmB2 and GdB12. *J. Less-Common Met.* **56,** 83–90 (1977).

49. Akopov, G., Yeung, M. T., Turner, C. L., Li, R. L. & Kaner, R. B. Stabilization of HfB12 in Y1-xHfxB12 under Ambient Pressure. *Inorg. Chem.* **55,** 5051–5055 (2016).

50. Renosto, S. T. *et al.* Superconductivity in the Th0.93Zr0.07B12 compound with UB12 prototype structure. *Phys. Lett. A* **379,** 2498–2501 (2015).

51. Akopov, G., Sobell, Z. C. C., Yeung, M. T. T. & Kaner, R. B. B. Stabilization of LnB12 (Ln = Gd, Sm, Nd, and Pr) in Zr1−xLnxB12 under Ambient Pressure. *Inorg. Chem.* **55,** 12419–12426 (2016).

52. Albert, B. *et al.* 'NaB15': A New Structural Description Based on X-ray and Neutron Diffraction, Electron Microscopy, Solid-state NMR Spectroscopy. *Chem. Eur. J.* **6,** 2531–2536 (2000).

53. Higashi, I. Aluminum distribution in the boron framework of ??-AlB12. *J. Solid State*

Chem. **47,** 333–349 (1983).

54. Kohn, J. A. & Eckart, D. W. Aluminum Boride, AlB12. *Anal. Chem.* **32,** 296–298 (1960).

55. Tanaka, T., Otani, S. & Ishizawa, Y. PREPARATION OF SINGLE CRYSTALS OF YB66. *J. Cryst. Growth* **73,** 31–36 (1985).

56. Richards, S. M. & Kaspar, J. S. The crystal structure of YB66. *Acta Crystallogr. Sect. B Struct. Crystallogr. Cryst. Chem.* **25,** 237–251 (1969).

57. Higashi, I. & Kobayashi, K. Structure Refinement of YB 62 and YB 56 of the YB 66 - Type Structure. *J. Solid State Chem.* **20,** 16–20 (1997).

58. Carlsson, J. O. & Lundström, T. The solution hardening of β-rhombohedral boron. *J. Less-Common Met.* **22,** 317–320 (1970).

59. Hoard, J. L., Sullenger, D. B., Kennard, C. H. L. & Hughes, R. E. The structure analysis of beta-rhombohedral boron. *J. Solid State Chem.* **1,** 268–277 (1970).

60. Ganem, B. & Osby, J. O. Synthetically useful reactions with metal boride and aluminide catalysts. *Chem. Rev.* **86,** 763–780 (1986).

61. Schlesinger, H. I. *et al.* Sodium Borohydride, Its Hydrolysis and its Use as a Reducing Agent and in the Generation of Hydrogen1. *J. Am. Chem. Soc.* **75,** 215–219 (1953).

62. Kapfenberger, C., Hofmann, K. & Albert, B. Room-temperature synthesis of metal borides. *Solid State Sci.* **5,** 925–930 (2003).

63. Dadras, J., Jimenez-Izal, E. & Alexandrova, A. N. Alloying Pt Sub-nano-clusters with Boron: Sintering Preventative and Coke Antagonist? *ACS Catal.* **5,** 5719–5727 (2015).

64. Matthias, A. B. T. *et al.* Superconductivity and Antiferromagnetism in Boron-Rich Lattices. *Science (80-.).* **159,** 530 (1968).

65. Croat, J. J., Herbst, J. F., Lee, R. W. & Pinkerton, F. E. High-energy product Nd-Fe-B permanent magnets. *Appl. Phys. Lett.* **44,** 148 (1984).

66. Shoemaker, C. B., Shoemaker, D. P. & Fruchart, R. The structure of a new magnetic phase related to the sigma phase: iron neodymium boride Nd2Fe14B. *Acta Crystallogr. Sect. C Cryst. Struct. Commun.* **40,** 1665–1668 (1984).

67. Herbst, J. F., Croat, J. J., Pinkerton, F. E. & Yelon, W. B. Relationships between crystal structure and magnetic properties in Nd 2 Fe 14 B. *Phys. Rev. B* **29,** 4176–4178 (1984).

68. Gaskell, P. H. Similarities in amorphous and crystalline transition metal-metalloid alloy structures. *Nature* **289,** 474–476 (1981).

69. McCallum, R. W., Lewis, L., Skomski, R., Kramer, M. J. & Anderson, I. E. Practical Aspects of Modern and Future Permanent Magnets. *Annu. Rev. Mater. Res.* **44,** 451–477 (2014).

70. Matar, S. The magnetic properties of iron nitride: Fe8N. *Z. Phys. B. - Condens. Matter* **87,** 91–96 (1992).

71. Mori, T. *et al.* Ferromagnetism and electronic structure of TmB 2. *Phys. Rev. B* **79,** 104418 (2009).

72. Coles, B. R., Cole, T., Lambe, J. & Laurance, N. Electrical Resistivity and Paramagnetic Resonance in Gadolinium Hexaboride. *Proc. Phys. Soc.* **79,** 84–86 (1962).

73. Hacker, H., Shimada, Y. & Chung, K. S. Magnetic properties of CeB6, PrB6, EuB6, and GdB6. *Phys. Status Solidi* **4,** 459–465 (1971).

74. Degiorgi, L., Felder, E., Ott, H. R., Sarrao, J. L. & Fisk, Z. Low-Temperature Anomalies and Ferromagnetism of EuB 6. *Phys. Rev. Lett.* **79,** 5134–5137 (1997).

75. Young, D. P. *et al.* High-temperature weak ferromagnetism in a low-density free-electron gas. *Nature* **397,** 412–414 (1999).

76. Zhitomirsky, M. E., Rice, T. M. & Anisimov, V. I. Magnetic properties: Ferromagnetism in the hexaborides. *Nature* **402,** 251–253 (1999).

77. Matsubayashi, K., Maki, M., Tsuzuki, T., Nishioka, T. & Sato, N. K. Parasitic ferromagnetism in a hexaboride? *Nature* **420,** 143–144 (2002).

78. Young, D. P. *et al.* Response to: Parasitic ferromagnetism in a hexaboride? *Nature* **420,** 144 (2002).

79. Paderno, Y. B. *et al.* Zirconium dodecaboride-based cutting material. *Powder Metall. Met. Ceram.* **43,** 546–548 (2004).

80. Svanidze, E. *et al.* High hardness in the biocompatible intermetallic compound β-Ti3Au. *Sci. Adv.* **2,** (2016).

81. Portnoi, K. I., Romashov, V. M. & Burobina, L. N. Constitution diagram of the system Zirconium-Boron. *Sov. Powder Met. Met. Ceram.* **7,** 68–71 (1970).

82. Kaufman, L. Boride composites - A new generation of nose cap and leading edge materials for reusable lifting reentry systems. in *Advanced Space Transportation Meeting*

(American Institute of Aeronautics and Astronautics, 1970). doi:doi:10.2514/6.1970-278

83. Upadhya, K., Yang, J. M. & Hoffman, W. *Advanced Materials for Ultrahigh Temperature Structural Applications Above 2000 deg C*. (1997).

84. Opeka, M. M., Talmy, I. G. & Zaykoski, J. A. Oxidation-based materials selection for 2000{\textdegree}C + hypersonic aerosurfaces: Theoretical considerations and historical experience. *J. Mater. Sci.* **39,** 5887–5904 (2004).

85. Kunzler, J. E., Buehler, E., Hsu, F. S. L. & Wernick, J. H. Superconductivity in ${\mathrm{Nb}}_{3}$Sn at High Current Density in a Magnetic Field of 88 kgauss. *Phys. Rev. Lett.* **6,** 89–91 (1961).

86. Gillan, E. G. & Kaner, R. B. Synthesis of Refractory Ceramics via Rapid Metathesis Reactions between Solid-State Precursors. *Chem. Mater.* **8,** 333–343 (1996).

87. Bud'ko, S. L. *et al.* Boron isotope effect in superconducting MgB2. *Phys. Rev. Lett.* **86,** 1877–80 (2001).

88. Nagamatsu, J., Nakagawa, N., Muranaka, T., Zenitani, Y. & Akimitsu, J. Superconductivity at 39[thinsp]K in magnesium diboride. *Nature* **410,** 63–64 (2001).

89. Slusky, J. S. *et al.* Loss of superconductivity with the addition of Al to MgB2 and a structural transition in Mg1-x[thinsp]AlxB2. *Nature* **410,** 343–345 (2001).

90. Bednorz, J. G. & Müller, K. A. Possible highTc superconductivity in the Ba−La−Cu−O system. *Zeitschrift f{ü}r Phys. B Condens. Matter* **64,** 189–193 (1986).

91. Choi, H. J., Roundy, D., Sun, H., Cohen, M. L. & Louie, S. G. The origin of the

anomalous superconducting properties of MgB2. *Nature* **418,** 758–760 (2002).

92. Mudgel, M. *et al.* Superconductivity of various borides: The role of stretched c-parameter. *J. Appl. Phys.* **105,** 07E313 (2009).

93. Cooper, A. S., Corenzwit, E., Longinotti, L. D., Matthias, B. T. & Zachariasen, W. H. Superconductivity: The Transition Temperature Peak Below Four Electrons per Atom. *Proc. Natl. Acad. Sci.* **67,** 313–319 (1970).

94. Buzea, C. & Yamashita, T. Review of the superconducting properties of MgB 2. *Supercond. Sci. Technol.* **14,** R115 (2001).

95. Havinga, E. E., Damsma, H. & Kanis, J. M. Compounds and pseudo-binary alloys with the CuAl2 (C16)-type structure IV. Superconductivity. *J. Less Common Met.* **27,** 281–291 (1972).

96. Kasuya, T. Gap State in YbB 12 and SmB 6 : Real Kondo Insulators. *Europhys. Lett.* **26,** 277–281 (1994).

97. Nickerson, J. C. *et al.* Physical Properties of Sm B 6. *Phys. Rev. B* **3,** 2030–2042 (1971).

98. Fu, L. & Kane, C. Topological insulators with inversion symmetry. *Phys. Rev. B* **76,** 45302 (2007).

99. Dzero, M., Sun, K., Galitski, V. & Coleman, P. Topological Kondo insulators. *Phys. Rev. Lett.* **104,** 106408 (2010).

100. Alexandrov, V., Dzero, M. & Coleman, P. Cubic topological Kondo insulators. *Phys. Rev. Lett.* **111,** 226403 (2013).

101. Kim, D. J., Xia, J. & Fisk, Z. Topological surface state in the Kondo insulator samarium hexaboride. *Nat Mater* **13,** 466–470 (2014).

102. Wolgast, S. *et al.* Low-temperature surface conduction in the Kondo insulator SmB 6. *Phys. Rev. B* **88,** 180405 (2013).

103. Kim, D. J., Grant, T. & Fisk, Z. Limit cycle and anomalous capacitance in the Kondo insulator SmB6. *Phys. Rev. Lett.* **109,** 96601 (2012).

104. Neupane, M. *et al.* Surface electronic structure of the topological Kondo-insulator candidate correlated electron system SmB6. *Nat. Commun.* **4,** 1–7 (2013).

105. Li, G. *et al.* Two-dimensional Fermi surfaces in Kondo Insulator SmB 6. *Science (80-.).* **346,** 1208–1212 (2014).

106. Rößler, S. *et al.* Hybridization gap and Fano resonance in SmB 6. *Proc. Natl. Acad. Sci.* **111,** 4798–4802 (2014).

107. Park, W. K. *et al.* Topological surface states interacting with bulk excitations in the Kondo insulator SmB $_6$ revealed via planar tunneling spectroscopy. *Proc. Natl. Acad. Sci.* **113,** 201606042 (2016).

108. Roessler, S. *et al.* Surface and electronic structure of SmB6 through Scanning Tunneling Microscopy. *Philos. Mag.* **0,** 1–12 (2016).

109. Kim, D. J. *et al.* Surface Hall Effect and Nonlocal Transport in SmB 6: Evidence for Surface Conduction. *Sci. Rep.* **3,** 1–4 (2013).

110. Weng, H., Zhao, J., Wang, Z., Fang, Z. & Dai, X. Topological crystalline Kondo insulator

in mixed valence ytterbium borides. *Phys. Rev. Lett.* **112,** 16403 (2014).

111. Werheit, H. Optical properties of the crystalline modifications of boron and boron-rich borides. *Prog. Cryst. Growth Charact.* **16,** 179–223 (1988).

112. Labov, S., Bowyer, S. & Steele, G. Boron and silicon: filters for the extreme ultraviolet. *Appl. Opt.* **24,** 576–578 (1985).

113. Schelm, S., Smith, G. B., Garrett, P. D. & Fisher, W. K. Tuning the surface-plasmon resonance in nanoparticles for glazing applications. *J. Appl. Phys.* **97,** (2005).

114. Takeda, H., Kuno, H. & Adachi, K. Solar Control Dispersions and Coatings With Rare-Earth Hexaboride Nanoparticles. *J. Am. Ceram. Soc.* **91,** 2897–2902 (2008).

115. Rek, Z. U. *et al.* Characterization of YB66 for use as a soft x-ray monochromator crystal. *Proc. SPIE* **1740,** 173–180 (1993).

116. Smith, A. D., Cowie, B. C., Sankar, G. & Thomas, J. M. Use of YB(66) as monochromator crystals for soft-energy EXAFS. *J. Synchrotron Radiat.* **5,** 716–8 (1998).

117. Nicolosi, V., Chhowalla, M., Kanatzidis, M. G., Strano, M. S. & Coleman, J. N. Liquid Exfoliation of Layered Materials. *Science (80-.).* **340,** 1226419 (2013).

118. Geim, A. K. & Novoselov, K. S. The rise of graphene. *Nat. Mater.* **6,** 183–91 (2007).

119. Das, S. K., Bedar, A., Kannan, A. & Jasuja, K. Aqueous dispersions of few-layer-thick chemically modified magnesium diboride nanosheets by ultrasonication assisted exfoliation. *Sci. Rep.* **5,** 1–11 (2015).

120. Li, D., Müller, M. B., Gilje, S., Kaner, R. B. & Wallace, G. G. Processable aqueous

dispersions of graphene nanosheets. *Nat. Nanotechnol.* **3,** 101–105 (2008).

121. Lim, C. S., Sofer, Z., Mazánek, V. & Pumera, M. Layered titanium diboride: towards exfoliation and electrochemical applications. *Nanoscale* **7,** 12527–12534 (2015).

122. Viculis, L. M., Mack, J. J. & Kaner, R. B. Chemical Route to Carbon. *Science (80-.).* **299,** 1361 (2003).

123. Chou, S. S. *et al.* Ligand conjugation of chemically exfoliated MoS2. *J. Am. Chem. Soc.* **135,** 4584–4587 (2013).

124. Alducin, D. *et al.* Synthesis of borophenes: Anisotropic, two-dimensional boron polymorphs. *Science (80-.).* **350,** 1513–1516 (2015).

125. Feng, B. *et al.* Experimental realization of two-dimensional boron sheets. *Nat. Chem.* **8,** 563–568 (2016).

126. Zhou, X. F. *et al.* Two-dimensional magnetic boron. *Phys. Rev. B* **93,** 1–6 (2016).

127. Penev, E. S., Kutana, A. & Yakobson, B. I. Can Two-Dimensional Boron Superconduct? *Nano Lett.* **16,** 2522–2526 (2016).

128. Tai, G. *et al.* Synthesis of Atomically Thin Boron Films on Copper Foils. *Angew. Chemie - Int. Ed.* **54,** 15473–15477 (2015).

129. Lukatskaya, M. R. *et al.* Cation Intercalation and High Volumetric Capacitance of Two-Dimensional Titanium Carbide. *Science (80-.).* **341,** 1502–1505 (2013).

130. Ghidiu, M., Lukatskaya, M. R., Zhao, M. Q., Gogotsi, Y. & Barsoum, M. W. Conductive two-dimensional titanium carbide ‘clay’ with high volumetric capacitance. *Nature* **516,**

78–81 (2015).

131. Kota, S. *et al.* Synthesis and characterization of an alumina forming nanolaminated boride: MoalB. *Sci. Rep.* **6,** 1–11 (2016).

132. Samsonov, G. V., Serebriakova, T. I. & Neronov, V. A. *Borides [in Russian]*. (Atomizdat, 1975).

133. Xie, M. *et al.* Raman scattering from superhard rhenium diboride under high pressure. *Appl. Phys. Lett.* **104,** 11904 (2014).

134. Portnoi, K. I., Romashov, V. M., Romanovich, I. V., Levinskii, Y. V. & Prokof'ev, S. A. Phase diagram of the system Hf-B. *Inorg. Mater.* **7,** 1769–1772 (1971).

135. Mohammadi, R. *et al.* Toward inexpensive superhard materials: Tungsten tetraboride-based solid solutions. *J. Am. Chem. Soc.* **134,** 20660–20668 (2012).

136. Akopov, G., Yeung, M. T., Turner, C. L., Mohammadi, R. & Kaner, R. B. Extrinsic hardening of superhard tungsten tetraboride alloys with group 4 transition metals. *J. Am. Chem. Soc.* **138,** 5714–5721 (2016).

137. Mackie, W. & Hinrichs, C. H. Preparation of ZrCx single crystals by an arc melting floating zone technique. *J. Cryst. Growth* **87,** 101–106 (1988).

138. Decker, B. F. & Kasper, J. S. The crystal structure of TiB. *Acta Crystallogr.* **7,** 77–80 (1954).

139. Chung, H.-Y. *et al.* Synthesis of Ultra-Incompressible Superhard Rhenium Diboride at Ambient Pressure. *Science (80-.).* **316,** 436–439 (2007).

140. Lundström, T., Lönnberg, B. & Westman, I. A study of the microhardness in the homogeneity ranges of NbB2 and TaB2. *J. Less Common Met.* **96,** 229–235 (1984).

141. Mikhalenko, S. I., Zavalii, L. V., Kuz'ma, Y. B. & Boiko, L. I. Isothermal sintering of the Sc-W-B and Sc-Re-B. *Powder Metall.* **8,** 681–683 (1992).

142. Lundström, T. The structure of Ru2B3 and WB2.0 as etermined by single-crystal diffractometry, and some notes on the W-B system. *Ark. Kemi* **30,** 115–127 (1968).

143. Mohammadi, R. *et al.* Enhancing the Hardness of Superhard Transition-Metal Borides: Molybdenum-Doped Tungsten Tetraboride. *Chem. Mater.* **28,** 632–637 (2016).

144. Mohammadi, R. *et al.* Tungsten tetraboride, an inexpensive superhard material. *Proc. Natl. Acad. Sci. U. S. A.* **108,** 10958–10962 (2011).

145. Mar, R. W. & Stout, N. D. High Temperature Enthalpies of Binary Dodecaborides. *J. Chem. Phys.* **57,** 5342–5349 (1972).

146. Bruskov, V. A. & Zavalii, L. V. Crystal Structure of ScB12. *Izv. Akad. Nauk SSSR, Neorg. Mater.* **24,** 506–507 (1988).

147. Sologub, O. *et al.* Incorporation of platinum atoms in a silicon-free boride of the YB50-type structure. *J. Alloys Compd.* **675,** 99–103 (2016).

148. Slack, G. A., Hejna, C. I., Garbauskas, M. & Kasper, J. S. X-ray study of transition-metal dopants in beta-boron. *J. Solid State Chem.* **76,** 64–86 (1988).

149. Glaser, F. W., Moskowitz, D. & Post, B. A study of some binary hafnium compounds. *J. Met.* **5,** 1119–1120 (1953).

150. Glaser, F. W. Contribution to the Metal-Carbon-Boron Systems. *J. Met.* **4,** 391–632 (1952).

151. Portnoi, K. I., Samsonov, G. V. & Frolova, K. I. Some properties of alloys of titanium boride and double titanium-chromium boride wuth boron carbide. *Zhurnal Prikl. Khimii* **33,** 577–582 (1958).

152. Leithe-Jasper, A., Sato, A. & Tanaka, T. Refinement of the crystal structure of zirconium dodecaboride, ZrB 12, at 140 K and 293 K. *Zeitschrift fur Krist. - New Cryst. Struct.* **217,** 319–320 (2002).

153. Werheit, H. *et al.* Raman scattering and isotopic phonon effects in dodecaborides. *J. Phys. Condens. Matter* **23,** (2011).

154. Whittaker, M. L. & Cutler, R. A. Effect of synthesis atmosphere, wetting, and compaction on the purity of AlB2. *J. Solid State Chem.* **201,** 93–100 (2013).

155. Levine, J. B. *et al.* Preparation and properties of metallic, superhard rhenium diboride crystals. *J. Am. Chem. Soc.* **130,** 16953–8 (2008).

156. Qin, J. *et al.* Is rhenium diboride a superhard material? *Adv. Mater.* **20,** 4780–4783 (2008).

157. Portnoi, K. I. & Romashov, V. M. Phase diagram of the system rhenium-boron. *Sov. Powder Metall. Met. Ceram.* **7,** 112–114 (1968).

158. Kuz'ma, Y. B. & Svarichevskaya, S. I. Crystal structure of Y2ReB6 and its analogues. *Sov. Phys. - Crystallogr.* **17,** 569–571 (1972).

159. Matkovich, V. I., Economy, J., Giese, R. F. & Barrett, R. The structure of metallic

dodecarborides. *Acta Crystallogr.* **19,** 1056–1058 (1965).

160. Baehren, F. D., Thümmler, F. & Vollath, D. Die Kinetik der Bildung von Boriden des Molybdän, wolfram und rhenium aus Bornitrid-Metallpulvergemischen. *J. Less Common Met.* **18,** 295–303 (1969).

161. Cueilleron, J., Lahet, G., Thevenot, F. & Paris, R. A. Nouvelle Methode D'Obtention de Borures Metalliques. *J. Less-Common Met.* **24,** 317–322 (1971).

162. Lepakova, O. K., Raskolenko, L. G. & Maksimov, Y. M. Titanium borides prepared by self-propagating high-temperature synthesis. *Inorg. Mater.* **36,** 568–575 (2000).

163. Borovinskaya, I. P. & Merzhanov, A. G. Self-propagating high temperature synthesis of refractory inorganic compounds [in Russian]. in *Metallothermic processes in chemistry and metallurgy* 58 (Nauka, 1971).

164. Bentz, G., Provost, G. & Urban, C. Etude de la projection, des borures et des nitrures au chalumean a plasma. *Bull. Soc. Fr. Ceram.* **78,** 5–17 (1968).

165. Tridre, H., Talayrach, B. & Besomber-Vaiehe, Z. No Title. *Methodeu Phys. D'Analyse* **5,** 343 (1969).

166. Mc Kenna, P. M. No Title. *Ind. Engng Chem.* **28,** 767 (1936).

167. Vekshina, N. V. & Markovskii, L. Y. Research of reactions accompanying the synthesis of hexaborides of alkali-earth metals via reduction with carbon [in Russian]. *J. Appl. Chem. USSR* **2,** 30–37 (1962).

168. Markovskii, L. Y. & Vekshina, N. V. Synthesis of borides of alkali-earth metals via

reduction of carbon metal oxides by carbon [in Russian]. *J. Appl. Chem. USSR* **31,** 1293–1299 (1958).

169. Karasev, A. I. Preparation of technical zirconium diboride by the carbothermic reduction of mixtures of zirconium and boron oxides. *Sov. Powder Metall. Met. Ceram.* **12,** 926–929 (1973).

170. Post, B., Moskovitz, D. & Glaser, F. *Refractory and oxidation resistant metalloceramic materials [in Russian]*. (Oborongiz., 1959).

171. Post, B., Moskovitz, D. & Glaser, F. *Borides of Rare Earth and Related Metals. Warmfeste und Korrosionstandige. Z. Plansee Siminar 'de re metallica'* (Springer-Verlag, 1956).

172. Samsonov, G. V. & Meerson, G. A. Vacuum-thermal synthesis of borides of refractory metals [in Russian]. *J. Appl. Chem. USSR* **27,** 1115–1120 (954).

173. Samsonov, G. V. & Markovskii, L. Y. Chemistry of Borides [in Russian]. *Russ. Chem. Rev.* **25,** 190–241 (1956).

174. Samsonov, G. V., Markovskii, L. Y., Zhigach, A. F. & Valyashko, M. G. *Boron, Its Compounds and Alloys [in Russian]*. (House of the Academy of the Sciences Ukrainian SSR, 1960).

175. Samsonov, G. V. & Vinitskii, I. M. *Refractory compounds [in Russian]*. (Atomizdat, 1975).

176. Kuzenkova, M.A., Kislyi, P. S. preparation of Zircoium diboride. *Powder Metall.* **12,**

966–969 (1965).

177. Serebryakova, T. I. & Samsonov, G. V. Borothermal method of synthesis of borides [in Russian]. *J. Chem. Ukr. SSR* **29,** 876–887 (1963).

178. Serebryakova, T. I. & Marek, E. V. Conditions of preparation of calcium and barium hexaboride powders. *Sov. Powder Metall. Met. Ceram.* **8,** 608–612 (1969).

179. Serebryakova, T. I. & Marek, E. V. Synthesis of borides via borothermal reduction of oxides of metals in vacuum. in *Metallothermal processes in chemistry and metallurgy [in Russian]* 78 (Nauka, 1971).

180. Perminov, V. P. & Neronov, V. A. Magnesium-Thermal Non-furnace Production of Boron from Boron Anhydride. *Powder Metall.* **1,** 1–4 (1969).

181. Serebryakova, T. I. & Samsonov, G. V. Research of conditions of synthesis of chromium borides [in Russian]. *J. Appl. Chem. USSR* **60,** 3 (1967).

182. Tanaka, T., Okada, S. & Gurin, V. A new scandium boride: ScB19. *J. Alloys Compd.* **267,** 211–214 (1998).

183. Lyutaya, M. D. & Akinina, Z. S. Chemical and Thermal Stability of Scandium Borides. *Inorg. Mater.* **1,** 1039–1043 (1965).

184. Meerson, G. A. On some properties of yttrium borides [in Russian]. *Inorg. Mater.* **2,** 608–616 (1966).

185. Tanaka, T., Okada, S., Yu, Y. & Ishizawa, Y. A New Yttrium Boride: YB25. *J. Solid State Chem.* **133,** 122–124 (1997).

186. Przybylska, M., Reddoch, A. H. & Ritter, G. J. The Preparation and Structure of Lutetium Diboride, Scandium Dodecaboride and Lutetium Antimonide. *J. Am. Chem. Soc.* **85,** 407–411 (1963).

187. Hamada, K. *et al.* Phase transition in the Zr1-xScxB12 system. *Phys. Rev. B* **48,** 6892–6898 (1993).

188. Markovskii, L. Y., Vekshina, N. V., Bezruk, E. T., Sukhareva, G. E. & Voevodskaya, T. K. A Magnesium-thermic method for the preparations of etal borides. *Powder Metall. Met. Ceram.* **5,** 350–354 (1969).

189. Sindeband, S. & Schwarzkopf, P. The Metallic Nature of Metal Borides. *Powder Metall. Bull.* **5,** 42 (1950).

190. Peshev, P. Synthesis of crystal of titanium diboride by chemical vapor deposition [in Bulgarian]. *Proc. Bulg. Acad. Sci.* **4,** 53 (1966).

191. Huggins, R. A. Thermodynamic considerations relating to the use of electrochemical techniques for the growth of single crystals of borides BORIDES. *Mat. Res. Bull.* **5,** 391–402 (1970).

192. Galasso, F. & Paton, A. The tungsten borides in boron fible cores. *Trans. Met. Soc. AIME* **236,** 1750 (966).

193. Galasso, F., Pinto, J. & Paton, A. The metal borides in boron fible cores; Identification of MoB4. *Trans. Met. Soc. AIME* **242,** 754 (1968).

194. Bakish, R. & Gellas, C. A. Vapor phase metallurgy and ceramics. *Metals (Basel).* **14,** 770

(1962).

195. Bertaut, F. & Blum, P. Etude des borures de chrome. *C. R. Hebd. Seances Acad. Sci.* **5,** 1055–1056 (1953).

196. Cumberland, R. W. *et al.* Osmium diboride, an ultra-incompressible, hard material. *J. Am. Chem. Soc.* **127,** 7264–7265 (2005).

197. Parkin, I. P. Solid state metathesis reaction for metal borides, silicides, pnictides and chalcogenides: ionic or elemental pathways. *Chem. Soc. Rev.* **25,** 199 (1996).

198. Borgstedt, H. B. & Guminski, C. The B-Li (Boron-Lithium) system. *J. Phase Equilib.* **24,** 572–574 (2003).

199. Liu, Z., Qu, X., Huang, B. & Li, Z. Crystal structure and morphology of a new compound, LiB. *J. Alloy. Compd.* **311,** 256–264 (2000).

200. Mair, G., von Schnering, H. G., Worle, M. & Nesper, R. Dilithium Hexaboride, Li2B6. *Z. Anorg. Allg. Chem.* **625,** 1207–1211 (1999).

201. Mair, G., Nesper, R. & von Schnering, H. G. Trilithium tetradecaboride Li3B14: Synthesis, structure, and properties. *J. Solid State Chem.* **75,** 30–40 (1988).

202. Kobayashi, M., Higashi, I., Matsuda, H. & Kimura, K. Rietveld analysis of LiB13 with beta-rhombohedral boron structure. *J. Alloys Compd.* **221,** 120–124 (1995).

203. Albert, B. & Hofmann, K. Synthesis , Characterization , and Crystal Structure of Na 3 B 20 , determined and refined from X-ray and Neutron Powder Data. *Z. Anorg. Allg. Chem.* **625,** 709–713 (1999).

204. Ammar, A. *et al.* Investigation of the electronic and structural properties of potassium hexaboride, KB6, by transport, magnetic susceptibility, EPR, and NMR measurements, temperature-dependent crystal structure determination, and electronic band structure calculations. *Inorg. Chem.* **43,** 4974–4987 (2004).

205. Becher, H. J. & Schäfer, A. Darstellung und Struktur des Berylliumborids Be4B. *Z. Anorg. Allg. Chem.* **318,** 304–312 (1962).

206. Okamoto, H. & Tanner, L. E. B-Be (Boron-Beryllium). in *Binary Alloy Phase Diagrams, Vol 1* (ed. Massalski, T. B.) 460–463 (ASM International, 1990).

207. Sands, D. E., Cline, C. F., Zalkin, A. & Hoenig, C. L. The beryllium–boron system. *Acta Crystallogr.* **14,** 309–310 (1961).

208. Meerson, G.A., Zhuravlev, N.N., Manelis, R.M., Runov, A.D., Stepanov, A.A., Grishina, L. I. Some Properties of Yttrium Boride [in Russian]. *Inorg. Mater.* **2,** 608–616 (1966).

209. Chan, J. Y., Fronczek, F. R., Young, D. P., DiTusa, J. . & Adams, P. . Synthesis, Structure, and Superconductivity in Be1.09B3. *J. Solid State Chem.* **163,** 385–389 (2002).

210. Hoenig, C. L., Cline, C. F. & Sands, D. E. Investigation of the System Beryllium-Boron. *J. Amer. Ceram. Soc.* **44,** 385–390 (1961).

211. Zhang, F. X., Xu, F. F. & Tanaka, T. A new ‘old’ boron-rich compound: Be8(1−x)(B48)B2—single crystal growth and structure analysis. *J. Solid State Chem.* **177,** 3070–3074 (2004).

212. Vekshina, N. V., Markovskii, L. Y., Kondrashev, Y. D. & Voevodskaya, T. K. Double

borides of aluminum and magnesium. *J. Appl. Chem. USSR* **44,** 970–974 (1971).

213. Okamoto, H. B-Mg (Boron-Magnesium). *J. Phase Equilibria Diffus.* **27,** 428–428 (2006).

214. Markovskii, L. Y., Kondrashev, Y. D. & Kaputovskaya, G. V. Composition and chemical properties of borides of magnesium. *J. Org. Chem. USSR* **25,** 433 (1955).

215. Guette, A., Naslain, R. & Galy, J. Structure cristalline du tetraborure de magnesium. *C. R. Seances Acad. Sci., Ser. C* **275,** 41–44 (1972).

216. Guette, A. *et al.* Crystal structure of magnesium heptaboride Mg2B14. *J. Less-Common Met.* **82,** 325–334 (1981).

217. Pediaditakis, A., Schroeder, M., Sagawe, V., Ludwig, T. & Hillebrecht, H. Binary boron-rich borides of magnesium: Single-crystal investigations and properties of MgB7 and the new boride Mg∼5B 44. *Inorg. Chem.* **49,** 10882–10893 (2010).

218. Brutti, S. *et al.* Synchrotron powder diffraction Rietveld refinement of MgB20 crystal structure. *Intermetallics* **10,** 811–817 (2002).

219. Okamoto, H. B-Ca (Boron-Calcium). in *Binary Alloy Phase Diagrams, Vol 1* (ed. Massalski, T. B.) 466–467 (ASM International, 1990).

220. Blum, P. & Bertaut, F. Contribution à l'étude des borures à teneur élevée en bore. *Acta Crystallogr.* **7,** 81–86 (1954).

221. Okamoto, H. B-Sr (Boron-Strontium). in *Binary Alloy Phase Diagrams, Vol. 1* (ed. Massalski, T. B.) 539–540 (ASM International, 1990).

222. Olsen, G. H. & Cafiero, A. V. Single-crystal growth of mixed (La, Eu, Y, Ce, Ba, Cs)

hexaborides for thermionic emission. *J. Cryst. Growth* **44,** 287–290 (1978).

223. Okamoto, H. B-Ba (Boron-Barium). in *Binary Alloy Phase Diagrams, Vol. 1* (ed. Massalski, T. B.) 460–461 (ASM International, 1990).

224. Carlson, O. N. Al-B (Aluminum-Boron). in *Binary Alloy Phase Diagrams, Vol. 1* (ed. Massalski, T. B.) 123–125 (ASM International, 1990).

225. Aivazov, M. I. & Domashnev, I. A. Electrophysical properties of titanium diboride and alloys in the system Ti-B-N. *Inorg. Mater.* **7,** 1551–1553 (1977).

226. Felten, J. The Preparation of Aluminum Diboride , AlB2. *J. Am. Chem Soc.* **78,** 5977–5978 (1956).

227. Kohn, I. A., Katz, G. & Giardini, A. A. AlB10, a new phase and a critique on the aluminum borides. *Z. Krist.* **3,** 53–62 (1958).

228. Arabei, B. G., Shtrom, E. N. & Lapitskii, Y. A. Characteristics of the manufacturing technology of dense parts from, and the mechanical properties of, some hexaborides of the rare-earth metals. *Powder Metall. Met. Ceram.* **5,** 406–409 (1964).

229. Kohn, I. A. & Eckart, D. W. Gamma-AlB12. A new structure and its relation to alpha-AlB12 as shown by twinned space groups. *Z. Krist.* **116,** 134–142 (1961).

230. Higashi, I. *et al.* Single-crystal X-ray diffraction study of AlB31 of the beta-rhombohedral boron structure. *J. Solid State Chem.* **82,** 230–238 (1989).

231. Klesnar, H. P. & Rogl, P. Phase relations in the ternary systems rare-earth metal (RE)-boron-nitrogen, where RE= Tb, Dy, Ho, Er, Tm, Lu, Sc, and Y. *High Temp. - High Press.*

22, 453–457 (1990).

232. Spear, K. E. & Liao, P. K. B-Sc (Boron-Scandium). in *Binary Alloy Phase Diagrams, Vol. 1* (ed. Massalski, T. B.) 531–533 (ASM International, 1990).

233. Peshev, P., Etourneau, J. & Naslain, R. Boron-Scandium System. *Mat. Res. Bull.* **5,** 319–328 (1970).

234. Liao, P. K. & Spear, K. E. The B-Y (boron-yttrium) system. *J. Phase Equilibria* **16,** 521–524 (1995).

235. Markovskii, L. Y. Conditions of formation of yttrium diboride, its structure and some properties [in Russian]. *J. Appl. Chem. USSR1* **42,** 2690 (969).

236. Guette, M., Vlasse, J. E. & Naslain, R. Structure cristalline du tetraborure d'yttrium. *C. R. Seances Acad. Sci., Ser. C* **291,** 145–148 (1980).

237. Schwetz, K., Ettmayer, R., Kieffer, R. & Lipp, A. Uber die Hektoboridphasen der Lanthaniden und Aktiniden. *J. Less-Common Met.* **26,** 99–104 (1972).

238. Smith, P. K. & Gilles, P. W. Rare earth hectoborides. *J. Inorg. Nucl. Chem.* **26,** 1465–1467 (1964).

239. Kato, K., Kawada, I., Oshima, C. & Kawai, S. Lanthanum tetraboride. *Acta Crystallogr. Sect. B* **30,** 2933–2934 (1974).

240. Okamoto, H. B-La (Boron-Lanthanum). in *Binary Alloy Phase Diagrams, Vol. 1* (ed. Massalski, T. B.) 494–495 (ASM International, 1990).

241. Fisk, Z. Preparation and Lattice Parameters of the Rare Earth Tetraborides. *Mat. Res. Bull.*

7, 285–291 (1972).

242. Korsukova, M. M., Lundström, T., Gurin, V. N. & Tergenius, L.-E. An X-ray diffractometry study of LaB6 single crystals, prepared by high-temperature solution growth. *Z. Krist.* **168,** 299–306 (1984).

243. Mercurio, J. P. Specific Heats of some Hexaborides of type CaB6. *Compt. Rend. Acad. Sci. Colon.* **268,** 1766 (1969).

244. Liao, P. K., Spear, K. E. & Schlesinger, M. E. The B-Ce (Boron-Cerium) system. *J. Phase Equilibria* **18,** 280–283 (1997).

245. Blomberg, M. K., Merisalo, M. J., Korsukova, M. M. & Gurin, V. N. SINGLE-CRYSTAL X-RAY DIFFRACTION STUDY ON Cel1-xLaxBa6 SOLUTIONS. *Sci. York* **168,** 313–319 (1991).

246. Kuz'ma, Y. B., Babizhetskii, V. S., Guérin, R. & Mikhalenko, S. I. Crystal Structure of Pr2B5 Boride. *Kristallografiya* **48,** 619–623 (2003).

247. Liao, P. K. & Spear, K. E. B-Pr (Boron-Praseodymium). in *Binary Alloy Phase Diagrams, Vol 1* (ed. Massalski, T. B.) 519–522 (ASM International, 1990).

248. Berrada, A., Mercurio, J. ., Chevalier, B., Etourneau, J. & Hagenmuller, P. Synthese, cristallogenese, proprietes magnetiques et effets magnetostrictifs spontanes de quelques tetraborures de terres rares. *Mat. Res. Bull.* **11,** 1519–1526 (1976).

249. McCarthy, C. M. *et al.* Low temperature phase transitions and magnetic structure of PrB6. *Solid State Commun.* **36,** 861–868 (1980).

250. Roger, J., Babizhetskyy, V., Jardin, R., Halet, J.-F. & Guerin, R. Solid state phase equilibria in the ternary Nd-Si-B system at 1270 K. *J. Alloy. Compd.* **415,** 73–84 (2006).

251. Liao, P. K. & Spear, K. E. The B-Nd (Boron-Neodymium) System. *J. Phase Equilib.* **17,** 335–339 (1996).

252. Blomberg, M. K., Merisalo, M. J., Korsukova, M. M. & Gurin, V. N. Single-crystal X-ray diffraction study of NdB6, EuB6 and YbB6. *J. Alloys Compd.* **217,** 123–127 (1995).

253. Liao, P. K. & Spear, K. E. B-Pm (Boron-Promethium). in *Binary Alloy Phase Diagrams, Vol 1* (ed. Massalski, T. B.) 517–520 (ASM International, 1990).

254. Eick, H. A. & Gilles, P. W. Precise Lattice Parameters of Selected Rare Earth Tetra- and Hexa-borides. *J. Am. Chem. Soc.* **81,** 5030–5032 (1959).

255. Zavalii, L. V. & Kuz'ma, Y. B. Sm2B5 boride and its structure. *Powder Metall.* **29,** 471–473 (1990).

256. Zavalii, L. V., Bruskov, V. A. & Kuz'ma, Y. B. Determination of the structure of SmB4. *Inorg. Mater.* **24,** 1350–1351 (1988).

257. Malyshev, A. L. *et al.* Neutron powder diffraction studies of mixed Ce1-xLax11B6 and isotope substituted 152.76SmB6. *Mater. Sci. Forum* **62–64,** 69–70 (1990).

258. Paderno, Y. B. & Lundström, T. On the Homogeneity Ranges of LaB6, EuB6 and SmB6. *Acta Chem. Scand. A* **37,** 609–612 (1983).

259. Liao, P. K. & Schlesinger, M. E. The B-Eu (Boron-Europium) System. *J. Phase Equilib.* **18,** 379–381 (1997).

260. Liao, P. K., Spear, K. E. & Schlesinger, M. E. The B-Gd (Boron-Gadolinium) System. **17,** 330–334 (1996).

261. Schwarz, C. & Simon, A. Die Kristallstruktur von Gd2B5. *Z. Naturforsch. B* **42b,** 935–939 (1982).

262. Garland, M. T., Wiff, J. P., Bauer, J., Guérin, R. & Saillard, J.-Y. The X-ray and electronic structures of GdB4. *Solid State Sci.* **5,** 705–710 (2003).

263. Artamonov, A. Y., Bezykornov, A. I. & Ivanov, A. N. Abrasive Power of Refractory Compounds. *Powder Metall. Met. Ceram.* **9,** 722–725 (1966).

264. Manelis, R. M. *et al.* Vacuum-thermal preparation of yttrium and gadolinium borides, and some of their properties. *Sov. Powder Metall. Met. Ceram.* **5,** 904–909 (1966).

265. Blanks, J. H. Phase behavior in the gadolinium-boron system and calculation of metal boride equilibria. *Diss. Abstr. Int. B* **40,** 402 (1980).

266. Liao, P. K. & Spear, K. E. B-Tb (Boron-Terbium). in *Binary Alloy Phase Diagrams, Vol .1* (ed. Massalski, T. B.) 542–544 (ASM International, 1990).

267. Will, G., Buschow, K. H. J. & Lehmann, V. Magnetic properties and neutron diffraction of TbB2. *Conf. Ser. - Inst. Phys.* **37,** 255–260 (1978).

268. Will, G., Schäfer, W., Pfeiffer, F., Elf, F. & Etourneau, J. Neutron diffraction studies of TbB4 and ErB4. *J. Less Common Met.* **82,** 349–355 (1981).

269. Samsonov, G. V., Paderno, Y. B. & Serebryakova, T. I. The borides of praesodymium, erbium and terbium. *Sov. Phys. Crystallogr.* **4,** 510–512 (1960).

270. Liao, P. K. & Spear, K. E. B-Dy (Boron-Dysprosium). in *Binary Alloy Phase Diagrams, Vol. 1* (ed. Massalski, T. B.) 476–478 (ASM International, 1990).

271. Schäfer, W. & Will, G. The crystal structures of ErB4 and DyB4 studied by neutron diffraction. *Z. Krist.* **144,** 217–225 (1976).

272. Timofeeva, I. I. & Timofeeva, E. N. Physicochemical properties of lanthanide hexaborides. *Inorg. Mater.* **4,** 1559–1561 (1968).

273. Liao, P. K. & Spear, K. E. B-Ho (Boron-Holmium). in *Binary Alloy Phase Diagrams, Vol. 1* (ed. Massalski, T. B.) 491–493 (ASM International, 1990).

274. Waśkowska, A. *et al.* Thermoelastic properties of ScB2, TiB2, YB4 and HoB4: Experimental and theoretical studies. *Acta Mater.* **59,** 4886–4894 (2011).

275. Mordovin, O. A. & Timofeeva, E. N. Rare-earth Element Hexaborides. *Russ. J. Inorg. Chem.* **13,** 1627–1629 (1968).

276. Liao, P. K., Spear, K. E. & Schlesinger, M. E. The B-Er (Boron-Erbium) System. *J. Phase Equilib.* **17,** 326–329 (1996).

277. Castellano, R. N. Crystal growth of TmB2 and ErB2. *Mater. Res. Bull.* **7,** 261–265 (1972).

278. Portnoi, K. I., Timofeev, V. A. & Timofeeva, V. N. Thermodynamics of reactions of synthesis of rare-earth hexaborides [in Russian]. *Inorg. Mater.1* **9,** 1513–1520 (1965).

279. Timofeev, V. A. & Timofeeva, E. N. Standard heats of formation of oxides and hexaborides of rare-earth metals [in Russian]. *J. Inorg. Chem. USSR* **11,** 1233–1235 (1966).

280. Nichols, M. C. & Mar, R. W. Erbium Hektoboride. *inorg. Chem.* **12,** 1710–1711 (1973).

281. Liao, P. K. & Spear, K. E. B-Tm (Boron-Thulium). in *Binary Alloy Phase Diagrams, Vol. 1* (ed. Massalski, T. B.) 549–551 (ASM International, 1990).

282. Liao, P. K. & Spear, K. E. B-Yb (Boron-Ytterbium). in *Binary Alloy Phase Diagrams, Vol. 1* (ed. Massalski, T. B.) 557–559 (ASM International, 1990).

283. Bauer, J. Sur le diborure d'ytterbium. *C. R. Seances Acad. Sci., Ser. C* **279,** 501–504 (1974).

284. Etourneau, J. *et al.* The magnetic and electrical properties of some rare earth tetraborides. *Boron* **67,** 531–539 (1979).

285. Dytchak, Y. I. Thermal oscillation of atoms of some metal hexaborides [in Russian]. *Izv. Vyzov. Fiz.* **1,** 154–156 (1973).

286. Iga, F. *et al.* Transport properties under high pressure of the dense Kondo compounds CePdSn and YbB12. *Phys. B Phys. Condens. Matter* **186–188,** 419–421 (1993).

287. Liao, P. K. & Spear, K. E. B-Lu (Boron-Lutetium). in *Binary Alloy Phase Diagrams, Vol. 1* (ed. Massalski, T. B.) 496–498 (ASM International, 1990).

288. Murray, J. L., Liao, P. K., Spear, K. E. & Murray J.L., Liao P.K., and S. K. E. B-Ti (Boron-Titanium). in *Binary Alloy Phase Diagrams, Vol. 1* (ed. Massalski, T. B.) 544–548 (ASM International, 1990).

289. Polty, A. E., Margolin, R. & Nilsen, T. No Title. *Trans. Amer. Soc. Met.* **46,** 312 (1954).

290. Adsit, N. R. Kinetics of the Formation of NiB. *Trans. Met. Soc. AIME* **236,** 804 (1966).

291. Fenish, R. G. A new intermediate compound in the Titanium-Boron System, Ti3B4. *Trans. Met. Soc. AIME* **236,** 804 (1966).

292. Bsenko, L. & Lundstrom, T. The high-temperature hardness of ZrB2 and HfB2. *J. Less-Common Met.* **34,** 273–278 (1974).

293. Kennard, C. H. L. & Davis, L. Zirconium dodecarborides ZrB12. Confirmation of the B12 cubooctahedral unit. *J. Solid State Chem.* **47,** 103–106 (1983).

294. Rudy, E. & Benesovsky, F. Untersuchungen in den Systemen: Hafnium - Bor - Stickstoff. *Monatsh. Chem.* **92,** 415–441 (1961).

295. Spear, K. E., Liao, P. K. & Smith, J. F. B-V (Boron-Vanadium). in *Binary Alloy Phase Diagrams, Vol. 1* 551–554 (1990).

296. Riabov, A. B. *et al.* Hydrogenation behaviour, neutron diffraction studies and microstructural characterization of boron oxide-doped Zr-V alloys. *J. Alloys Compd.* **293,** 93–100 (1999).

297. Giese, R. F., Economy, J. & Matkovish, V. I. Interstitial Derivatives of beta-Boron. *Z. Krist.* **122,** 144–147 (1965).

298. Kuz'ma, Y. B., Telegus, V. S. & Kovalyk, D. A. X-ray diffraction investigation of the ternary systems V - Cr - B, Nb - Cr - B, and Mo - Cr - B. *Sov. Powder Metall. Met. Ceram.* **8,** 403–410 (1969).

299. Norton, J., Blumenthal, H. & Sindeband, J. Structure of Diborides of Titanium, Zirconium, Columbium, Tantalum and Vanadium. *Met. Trans.* **1,** 19, 749–751 (1949).

300. Lonnberg, B. Thermal expansion studies on the group IV-VII transition metal diborides. *J. Less-Common Met.* **141,** 145–156 (1988).

301. Peçanha, R. M., Ferreira, F., Coelho, G. C., Nunes, C. A. & Sundman, B. Thermodynamic modeling of the Nb-B system. *Intermetallics* **15,** 999–1005 (2007).

302. Aronsson, B., Lundström, T. & Rundqvist, S. *Borides, Silicides and Phosphides.* (Methuen, 1965).

303. Nowotny, H. & Wittmann, A. Zur Struktur der metallreichen Borid-Phase bei V, Nb und Ta. *Monatsh. Chem.* **89,** 220–224 (1958).

304. Okada, S., Hamano, K., Lundström, T. & Higashi, I. Crystal growth of the new compound Nb2B3, and the borides NbB, Nb5B6, Nb3B4, and NbB2. *AIP Conf. Proc.* **231,** 456–459 (1991).

305. Okamoto, H. Comment on B-Ta (boron-tantalum). *J. Phase Equilibria* **14,** 393–394 (1993).

306. Havinga, E. E., Damsma, H. & Hokkeling, P. Compounds and pseudo-binary alloys with the CuAl2(C16)-type structure I. Preparation and X-ray results. *J. Less-Common Met.* **27,** 169–186 (1972).

307. Kiessling, R., Norman, N. & Sillén, L. G. A Method for Preparing Boron of High Purity. *Acta Chemica Scandinavica* **2,** 707–712 (1948).

308. Kiessling, R. The Borides of Tantalum. *Acta Chem. Scand* **3,** 603–615 (1949).

309. Leitnaker, J. M., Bowman, M. G. & Gilles, P. W. High-Temperature Phase Studies in the

Tantalum-Boron System between Ta and TaB. *J. Electrochem. Soc* **108,** 568–572 (1951).

310. Portnoi, K. I., Romashev, V. M. & Salibekov, S. E. Constitution Diagram of The System Tantalum-Boron. *Sov. Powder Met. Met. Ceram.* **10,** 925–927 (1971).

311. Rudy, E., Benesovsky, F. & Toth, L. Dreistoff Systeme der ’Va und VIa-Metalle mit Bund C. *Z. Met.* **54,** 345–353 (1963).

312. Liao, P. K. & Spear, K. E. B-Cr (Boron-Chromium). in *Binary Alloy Phase Diagrams, Vol. 1* (ed. Massalski, T. B.) 471–474 (ASM International, 1990).

313. Okada, S., Atoda, T. & Higashi, I. Structural investigation of Cr2B3, Cr3B4, and CrB by single-crystal diffractometry. *J. Solid State Chem.* **68,** 61–67 (1987).

314. Andersson, L.-H., Kiessling, R., Lindstedt, G. & Kinell, P.-O. Investigations on the Binary Systems of Boron with Chromium, Columbium, Nickel, and Thorium, Including a Discussion of the Phase ‘TiB’ in the Titanium-Boron System. *Acta Chemica Scandinavica* **4,** 160–164 (1950).

315. Elfstrom, M. The Crystal Structure of Cr3B4. *Acta Chem. Scand.* **15,** 1178 (1961).

316. Kiessling, R. The Borides of Some Transition Elements. *J. Electrochem. Soc.* **98,** 166–170 (1951).

317. Portnoi, K. I., Romashov, V. M. & Romanovich, I. V. Diagram of state of the chromium-boron system. *Sov. Powder Metall. Met. Ceram.* **8,** 298–302 (1969).

318. Epelbaum, V. A. On phases in Cr-B system [in Russian]. *J. Inorg. Chem. USSR* **3,** 2545–2552 (1958).

319. Spear, K. E. & Liao, P. K. B-Mo (Boron-Molybdenum). in *Binary Alloy Phase Diagrams, Vol. 1* (ed. Massalski, T. B.) 502–503 (ASM International, 1990).

320. Kiessling, R. The crystal structures of Molybdenium and Tungsten Borides. *Acta Chem. Scand.* **1,** 893–916 (1947).

321. Steinitz, R., Binder, I. & Moskovitz, D. System Molybdenum-Boron and Some Properties of the Molybdenum-Borides; The System Mo-B. *J. Met.* **4,** 983–987 (1952).

322. Wittmann, A., Nowotny, H. & Boller, H. Ein Beitrag zum Dreistoff Titan-Molybdaen-Bor. *Monatshefte fur Chemie* **91,** 608–615 (1960).

323. Haschke, H., Benesovsky, H. & Nowotny, F. Untersuehungen in den Dreistoffen : {Mo, W}-{Fe, Co, Ni}-B. *Mh. Chem.* **844,** (1966).

324. Higashi, I., Takahashi, Y. & Okada, S. Crystal structure of MoB2. *J. Less-Common Met.* **123,** 277–283 (1986).

325. Klesnar, H., Aselage, T. L., Morosin, B. & Kwei, G. H. The diboride compounds of molybdenum: MoB2−x and Mo2B5−y. *J. Alloys Compd.* **241,** 180–186 (1996).

326. Crespo, A. J., Tergenius, L. E. & Lundstrom, T. The solid solution of 4d, 5d and some p elements in beta-rhombohedral boron. *J. Less-Common Met.* **77,** 147–150 (1981).

327. Duschanek, H., Rogl, P. *et al.* Critical assessment and thermodynamic calculation of the binary system boron-tungsten (B-W). *J. Phase Equilibria* **16,** 150–161 (1995).

328. Nowotny, H., Haschke, H. & Benesovsky, F. Bor-reiche Wolframboride. *Monatshefte f??r Chemie* **98,** 547–554 (1967).

329. Kuz'ma, Y. B., Lakh, V. I., Stadnyk, B. I. & Voroshikov, Y. V. X-ray Diffraction Study of the System Niobium-Tungsten-Boron. *J. Chem. Inf. Model.* **5,** 491–493 (1966).

330. Post, B. & Glaser, F. Borides of Some Transition Metals. *J. Chem. Phys.* **20,** 1050–1051 (1952).

331. Okamoto, H. B-Mn (boron-manganese). *J. Phase Equilibria* **14,** 121–122 (1993).

332. Bezruk, E. G. & Markovskii, L. Y. Some physical properties of borides [in Russian]. *Inorg. Mater.* **4,** 447 (1968).

333. Cely, A., Tergenius, L. E. & Lundstrom, T. Microhardness measurements and phase analytical studies in the MnB system. *J. Less-Common Met.* **61,** 193–198 (1978).

334. Kasaya, M., Hihara, T. & Koi, J. Magnetic Susceptibility of Single Crystal Mn3B4. *J. Phys. Soc. Japan* **30,** 296 (1971).

335. Bowman, A. L. & Nereson, N. G. Low-temperature thermal expansion of MnB2. *AIP Conf. Proc.* **17,** 34–36 (1974).

336. Binder, I. & Post, B. Manganese diboride. *Acta Crystallogr.* **13,** 356–356 (1960).

337. Andersson, S. *et al.* The Crystal Structure of MnB4. *Acta Chemica Scandinavica* **24,** 1791–1799 (1970).

338. Okamoto, H. B-Tc (Boron-Technetium). in *Binary Alloy Phase Diagrams, Vol. 1* (ed. Massalski, T. B.) 544–545 (ASM International, 1990).

339. Trzebiatowski, W. & Rudzinski, J. The composition and structure of technetium nitride and technetium borides. *J. Less Common Met.* **6,** 244–245 (1964).

340. Portnoi, K. I. & Romashev, V. M. B-Re (Boron-Rhenium). in *Binary Alloy Phase Diagrams, Vol. 1* (ed. Massalski, T. B.) 525–526 (ASM International, 1990).

341. Aselius, J., Aronsson, B., Baeckman, M., R. S. & Aselius, J. The crystal structure of Ru11B8. *Acta Chemica Scandinavica* **14,** 1001–1005 (1960).

342. Portnoi, K. I. & Romashov, V. M. Binary constitution diagrams of systems composed of various elements and boron - A review. *Sov. Powder Metall. Met. Ceram.* **11,** 378–384 (1972).

343. Khachfi, M., Bauer Grosse, E., Morniroli, J. P., Lundström, T. & Gantois, M. Microstructural study of borides of the type M7B3. Relationships with M7C3 carbides. in *Wegliki, Azotki, Borki, Miedzynar. Konf.* 40–44 (1984).

344. Chung, H.-Y. *et al.* Response to Comment on 'Synthesis of Ultra-Incompressible Superhard Rhenium Diboride at Ambient Pressure'. *Science (80-.).* **318,** 1550 (2007).

345. La Placa, S. J. & Post, B. The crystal structure of rhenium diboride. *Acta Crystallogr.* **15,** 97–99 (1962).

346. Idzikowski, B., Szajek, A., Greneche, J.-M. & Kovač, J. Nanogranular FexNi23−xB6 phase formation during devitrification of nickel-rich Ni64Fe16Zr7B12Au1 amorphous alloy. *Appl. Phys. Lett.* **85,** 1392 (2004).

347. Liao, P. K. & Spear, K. E. B-Fe (Boron-Iron). in *Binary Alloy Phase Diagrams, Vol. 1* (ed. Massalski, T. B.) 480–483 (ASM International, 1990).

348. Aronsson, B., Lundström, T. & Engström, I. Some Aspects of the Crystal Chemistry of

Borides, Boro-Carbides and Silicides of the Transition Metals. in *Anisotropy in Single-Crystal Refractory Compounds: Proceedings of an International Symposium on Anisotropy in Single-Crystal Refractory Compounds, held on June 13--15, 1967, in Dayton Ohio. Sponsored by the Ceramics and Branch of the air Force Materials L* (eds. Vahldiek, F. W. & Mersol, S. A.) 3–22 (Springer US, 1968). doi:10.1007/978-1-4899-5307-0_1

349. Portnoi, K. I., Levinskaya, M. K. & Romashov, V. M. Constitution diagram of the system iron-boron. *Powder Metall. Met. Ceram.* **8,** 657–659 (1969).

350. Bjurström, T. Röntgenanalyse der Systeme Eisen-Bor, Kobalt-Bor und Nickel-Bor. *Ark. Kemi Miner. Geol.* **11A,** 1–12 (1933).

351. Yang, M. *et al.* Structural distortion and band gap opening of hard MnB4 in comparison with CrB4 and FeB4. *J. Solid State Chem.* **213,** 52–56 (2014).

352. Wang, Q. *et al.* Is orthorhombic iron tetraboride superhard? *J. Mater.* **1,** 45–51 (2015).

353. Gou, H. *et al.* Discovery of a superhard iron tetraboride superconductor. *Phys. Rev. Lett.* **111,** 1–5 (2013).

354. Takizawa, H., Haze, N., Okamoto, K., Uheda, K. & Endo, T. Microwave synthesis of Fe-doped β-rhombohedral boron. *Mater. Res. Bull.* **37,** 113–121 (2002).

355. Obrowski, W. B-Ru (Boron-Ruthenium). in *Binary Alloy Phase Diagrams, Vol. 1* (ed. Massalski, T. B.) 527–529 (ASM International, 1990).

356. Kemper, C. P. & Fries, R. J. Crystallography of the Ru-B and Os-B Systems. *J. Chem.*

Phys. **34,** 1994–1995 (1961).

357. Buddery, J. H. & Welch, A. J. E. Borides and silicides of the platinum metals. *Nature* **167,** 362 (1951).

358. Roof, R. B. & Kempter, C. P. New Orthorhombic Phase in the Ru-B and Os-B Systems. *J. Chem. Phys.* **37,** 1473–1476 (1962).

359. Aronsson, B., Leden, I., Sunner, S., Hatanaka, A. & Munch-Petersen, J. The Crystal Structure of RuB2, OsB2, and IrB1.35 and Some General Comments on the Crystal Chemistry of Borides in the Composition Range MeB - MeB3. *Acta Chemica Scandinavica* **17,** 2036–2050 (1963).

360. Okamoto, H. B-Os (Boron-Osmium). in *Binary Alloy Phase Diagrams, Vol. 1* (ed. Massalski, T. B.) 513–514 (ASM International, 1990).

361. Frotscher, M., Senyshyn, A. & Albert, B. Neutron diffraction at metal borides, Ru2B3 and OS2B3. *Zeitschrift fur Anorg. und Allg. Chemie* **638,** 2078–2080 (2012).

362. Liao, P. & Spear, K. The B− Co (Boron-Cobalt) system. *J. Phase Equilibria* **9,** 452–457 (1988).

363. Buschow, K. H. J., van Engen, P. G. & Jongebreur, R. Magneto-optical properties of metallic ferromagnetic materials. *J. Magn. Magn. Mater.* **38,** 1–22 (1983).

364. Rundqvist, S. Two borides with the cementite structure. *Nature* **181,** 259–260 (1958).

365. Rundqvist, S. Crystal Structure of Ni3B and Co3B. *Acta Chem. Scand* **12,** (1958).

366. Shinohara, T. & Watanabe, N. Nuclear Magnetic Resonance of Co{59} in Ferromagnetic

Cobalt Compounds Co3B and Co2B. *J. Phys. Soc. Japan* **20,** 2020–2027 (1965).

367. Okamoto, H. B-Rh (Boron-Rhodium). in *Binary Alloy Phase Diagrams, Vol. 1* (ed. Massalski, T. B.) 527–528 (ASM International, 1990).

368. Beck, M., Ellner, M. & Mittemeijer, E. J. The formation of interstitial solid solutions based on solvents showing the fcc structure: Elastic versus chemical interaction. *Acta Mater.* **49,** 985–993 (2001).

369. Aronsson, B., Stenberg, E. & Åselius, J. Borides of Rhenium and the Platinum Metals. The Crystal Structure of Re7B3, ReB3, Rh7B3, RhB~1.1, IrB~1.1 and PtB. *Acta Chem. Scand.* **14,** 733–741 (1960).

370. Aronsson, B. The Crystal Structure of Ru7B3. *Acta Chemica Scandinavica* **13,** 109–114 (1959).

371. Aronsson, B., Stenberg, E. & Åselius, J. Borides of ruthenium, osmium and iridium. *Nature* **195,** 377–378 (1962).

372. Liao, P. K. & Spear, K. E. B-Ni (Boron-Nickel). in *Binary Alloy Phase Diagrams, Vol. 1* (ed. Massalski, T. B.) 508–510 (ASM International, 1990).

373. Rundqvist, S. *et al.* An X-Ray Investigation of the Nickel-Boron System. The Crystal Structures of Orthorhombic and Monoclinic Ni4B3. *Acta Chemica Scandinavica* **13,** 1193–1208 (1959).

374. Rundqvist, S. *et al.* Crystal Structure Refinements of Ni3B, o-Ni4B3, and m-Ni4B3. *Acta Chemica Scandinavica* **21,** 191–194 (1967).

375. Marion, S. M. Preparation des Borures de Nickel par Electrolyse Ignee. *Bull. Soc. Chim. Fr.* **23,** 522–525 (1957).

376. Lugscheider, E., Knotek, O. & Reimann, H. Das Dreistoffsystem Nickel - Chrom - Bor. *Monatshefte für Chemie* **105,** 80–90 (1974).

377. Hofmann, K. *et al.* Metastable Ni7B3: A New Paramagnetic Boride from Solution Chemistry, Its Crystal Structure and Magnetic Properties. *Inorg. Chem.* **54,** 10873–10877 (2015).

378. Liao, P. K., Spear, K. E. & Schlesinger, M. E. The B-Pd (Boron-Palladium) System. *J. Phase Equilib.* **17,** 340–346 (1996).

379. Berger, T. G. *et al.* On the formation and crystal structure of the Pd6B phase. *Zeitschrift für Krist.* **221,** 450–463 (2006).

380. Stenberg, E. The Crystal Structures of Pd5B2, (Mn5C2) and Pd3B. *Acta Chem. Scand.* **15,** 861–870 (1961).

381. Tergenius, L. E. & Lundström, T. The Crystal Structure of Pd2B. *J. Solid State Chem.* **31,** 361–367 (1980).

382. Okamoto, H. B-Pt (Boron-Platinum). in *Binary Alloy Phase Diagrams, Vol. 1* (ed. Massalski, T. .) 522–523 (ASM International, 1990).

383. Hassler, E., Lundstrom, T. & Tergenius, L. E. The crystal chemistry of platinum metal borides. *J. Less-Common Met.* **67,** 567–572 (1979).

384. Wald, F. & Rosenberg, A. J. Constitutional Investigations in the Boron-Platinum System.

Trans. Met. Soc. AIME **233,** 796–799 (1965).

385. Ellner, M., Grin, Y., Fischer, P. & Rogl, P. Röntgen- und Neutronenbeugungsuntersuchungen der Struktur von Pt3B2. *Z. Met.* **84,** 788–791 (1993).

386. Okamoto, H. B-Th (Boron-Thorium). in *Binary Alloy Phase Diagrams, Vol. 1* (ed. Massalski, T. B.) 544–546 (ASM International, 1990).

387. Brewer, L., Sawyer, D. & Templeton, D. A study of the refractory borides. *J. Amer. Ceram. Soc.* **34,** 173 (1951).

388. Okamoto, H. B-U (Boron-Uranium). in *Binary Alloy Phase Diagrams, Vol. 1* (ed. Massalski, T. B.) 551–552 (ASM International, 1990).

389. Dancausse, J. P. *et al.* Compression study of uranium borides UB2, UB4 and UB12 by synchrotron X-ray diffraction. *J. Alloys Compd.* **189,** 205–208 (1992).

390. McDonald, B. J. & Stuart, W. I. The crystal structure of some plutonium borides. *Acta Crystallogr.* **13,** 447–448 (1960).

391. Bertaut, F. & Blum, P. La structure des borures d'uranium. *Compt. Rend. Acad. Sci. Colon.* **229,** 666–667 (1949).

392. Howlett, B. W. A Note on the Uranium-Boron Alloy System. *J. Inst. Met.* **88,** 91–92 (1959).

393. Rogl, P. & Potter, P. E. The B-Pu (Boron-Plutonium) System. *J. Phase Equilib.* **18,** 467–473 (1997).

394. Chipaux, R., Bonnisseau, D., Boge, M. & Jarroque, J. Crystallographic and Mossbauer

Investigation on Np1-xPuxB2. *J. Magn. Magn. Mater.* **74,** 67–73 (1988).

395. Eick, H. A. Plutonium Borides. *Inorg. Chem.* **4,** 1237–1239 (1965).

396. Stecher, J. & Aldinger, A. A. No Title. *Z. Met.* **64,** 684–689 (973).

397. Samsonov, G. V. & Grodshtein, A. E. No Title. *J. Appl. Chem. USSR* **30,** 379–382 (1956).

398. Samsonov, G. V., Serebryakova, T. I. & Bolgar, A. S. No Title. *J. Inorg. Chem. USSR* **6,** 2243–2248 (1961).

399. Samsonov, G. V. No Title. *Proc. Acad. Sci. USSR* **133,** 1344–1346 (1960).

400. Odintsov, V. V. Hardness of metal dodecaborides of UB12 structure type [in Russian]. *Inorg. Chem. USSR* **10,** 366–367 (1974).

401. Ivankov, A. A. *Handbook of Hardness Data*. (Naukova Dumka, 1968).

402. Samsonov, G. V. & Zhuravlev, N. N. No Title. *Kristallografiya* **4,** 538–542 (1959).

403. Samsonov, G. V. & Zorina, O. N. No Title. *J. Inorg. Chem. USSR* **1,** 2260–2263 (1956).

404. Kieffer, R. & Benesovskii, F. *Hard Materials [Russian translation]*. (Metallurgiya, 1968).

405. Samsonov, G. V. No Title. *Vopr. Porosh. Met. Prochn. Mater.*. **7,** 72–98 (1959).

406. Samsonov, G. V. No Title. *Proc. Acad. Sci. USSR* **113,** 1299–1302 (1957).

407. Portnoi, K. I., Romashev, V. M., Levinskii, Y. V. & Romanovich, I. V. Phase diagram of the system tungsten-boron. *Powder Metall.* **5,** 398–402 (1967).

408. Samsonov, G. V. & Neshpor, V. S. No Title. *Vopr. Porosh. Met. Prochn. Mater.* **5,** 3–8

(1958).

409. Markovskii, L. Y. & Bezruk, E. T. No Title. *Inorg. Mater.* **3,** 2165–2169 (1967).

410. Kolomyitsev, P. T. No Title. *Proc. Acad. Sci. USSR* **124,** 1247–1250 (1959).

411. Sobolev, A. S. & Fedorov, A. . No Title. *Inorg. Mater.* **3,** 723–727 (1967).

412. Kosenko, V. A. & Rud', B. M. No Title. *Proc. Acad. Sci. USSR* **7,** 1455–1456 (1971).

413. Samsonov, G. V. & Kosenko, V. A. No Title. *Izv. Vyss. Uchebn. Zaved. Fiz.* **6,** 146–148 (1972).

414. Samsonov, G. V. & Kosenko, V. A. No Title. *Inorg. Mater.* **8,** 771–772 (1972).

415. Kayhan, M. *et al.* Neutron diffraction and observation of superconductivity for tungsten borides, WB and W2B4. *Solid State Sci.* **14,** 1656–1659 (2012).

416. Merz, M., Schweiss, P., Wolf, T., Löhneysen, H. Von & Schuppler, S. Electronic structure of single-crystalline MgxAl 1-xB2 probed by X-ray diffraction multipole refinements and polarization-dependent X-ray absorption spectroscopy. *J. Phys. Soc. Japan* **83,** 1–8 (2014).

417. Frotscher, M., Hölzel, M. & Albert, B. Crystal structures of the metal diborides ReB2, RuB2, and OsB2 from neutron powder diffraction. *Zeitschrift fur Anorg. und Allg. Chemie* **636,** 1783–1786 (2010).

418. Zogał, O. J. *et al.* Crystal structure, electric field gradient, and electronic charge densities in ReB2: A single crystal x-ray, B11 nuclear magnetic resonance, and first-principles study. *J. Appl. Phys.* **106,** (2009).

419. Jäger, B. *et al.* Characterization of the electronic properties of YB4 and YB 6 using 11B NMR and first-principles calculations. *J. Alloys Compd.* **383,** 232–238 (2004).

420. Kasper, J. S., Vlasse, M. & Naslain, R. The alpha-AlB12 structure. *J. Solid State Chem.* **20,** 281–285 (1977).

421. Slack, G. A., Hejna, C. I., Garbauskas, M. F. & Kasper, J. S. The crystal structure and density of β-rhombohedral boron. *J. Solid State Chem.* **76,** 52–63 (1988).

CHAPTER 2. SUPERHARD MIXED TRANSITION METAL DODECABORIDES

"Reprinted (adapted) with permission from (Akopov, G.; Yeung, M.T.; Sobell, Z.C.; Turner, C.L.; Kaner, R.B. "Superhard Mixed Transition Metal Dodecaborides" *Chem. Mater.* 2016, *28*, 6605 DOI: 10.1021/acs.chemmater.6b02632). Copyright (2016) American Chemical Society."

ABSTRACT

Solid solutions of mixed metal dodecaborides of ZrB_{12}, YB_{12} and ScB_{12} were prepared by arc-melting and studied for their mechanical properties. $Zr_{1-x}Y_xB_{12}$ formed an essentially perfect solid solution, closely following Vegard's law. $Zr_{1-x}Sc_xB_{12}$ and $Y_{1-x}Sc_xB_{12}$ undergo a face centered-cubic (FCC) to body-centered tetragonal (BCT) transition at 90-95 at. % Sc as determined by powder X-ray diffraction and transmission electron microscopy. The compounds $Zr_{0.5}Y_{0.5}B_{12}$, $Zr_{0.5}Sc_{0.5}B_{12}$ and $Y_{0.5}Sc_{0.5}B_{12}$ are superhard (Vickers hardness ≥ 40 GPa) and demonstrate an increase in hardness to 45.8 ± 1.3, 48.0 ± 2.1 and 45.2 ± 2.1 GPa under a load of 0.49 N, respectively, compared to 40.4 ± 1.8, 40.9 ± 1.6 and 41.7 ± 2.2 GPa for pure ZrB_{12}, YB_{12} and ScB_{12}. In addition, $Zr_{0.5}Y_{0.5}B_{12}$, $Zr_{0.5}Sc_{0.5}B_{12}$ and $Y_{0.5}Sc_{0.5}B_{12}$ solid solutions show a substantial increase in oxidation resistance to ~630 ^oC, ~685 ^oC and ~695 ^oC, respectively, when compared to other superhard metal borides (e.g. ~400 ^oC for WB_4) and their alloys and the traditional cutting tools material tungsten carbide (~400 ^oC). Moreover, $Zr_{0.5}Y_{0.5}B_{12}$, $Zr_{0.5}Sc_{0.5}B_{12}$ and $Y_{0.5}Sc_{0.5}B_{12}$ have relatively low densities: 3.52, 3.32 and 3.18 g/cm^3, respectively, comparable to or even lower than that of diamond (3.52 g/cm^3), and significantly lower than other superhard borides such as ReB_2 (12.67 g/cm^3) and WB_4 (8.40 g/cm^3) and traditional cutting tools materials, e.g. WC (15.77

g/cm^3), making them of potential interest for lightweight protective coatings and/or as materials for cutting and machining.

INTRODUCTION

The development of new materials with superior mechanical properties is challenging because of the many attributes that need to be controlled, ranging from hardness to oxidation resistance. Of the many requisite physical attributes, first and foremost these new material formulations need to be superhard (defined as having Vickers hardness (H_v) greater than 40 GPa at a given force of applied load), so that they may be able to supplant tungsten carbide (H_v = 13 - 25 GPa at 0.5 N of applied loading, force comparable to that experienced by materials during cutting and machining)[1], the current industrial standard for drilling and machining, as well as having similar or superior oxidation resistance. This has inspired the superhard metal boride field, with compounds such as ReB_2 capable of scratching diamond, yet not requiring high pressure and temperature for their synthesis.[2] Virtually every superhard metal boride to date has been the highest boride of the respective metal, including rhenium diboride (ReB_2)[3], chromium tetraboride (CrB_4)[4] and tungsten tetraboride (WB_4)[5], with only a few exceptions (e.g. $W_{0.5}Ta_{0.5}B$)[6].

Indeed, the discovery of new superhard materials in higher borides comes from attempts to simulate diamond, the hardest material known thus far[7]. Diamond is both highly incompressible and resistant to shear; together, this accounts for diamond's superior resistance to surface deformation and thus, high hardness. Not surprisingly, there are few compounds that possess the requisite attributes for superhardness, and among them are the higher metal borides. For ReB_2, CrB_4 and WB_4, the high electron density of the transition metal provides the ultra-incompressibility, while the high density of covalent bonds prevents the propagation of slip. Not

surprisingly, there have been several excellent theoretical exploration of superhard higher borides, most notably in the metal tetraborides[8], explaining the structural peculiarities (boron dimers and honeycomb boron lattice), which give rise to the high hardness; and the metal triborides[9–11], again giving insight into the origin of high hardness, due to the covalent framework of boron atoms and zig-zag tungsten-boron bonds.

Metal dodecaborides (MB_{12}) constitute a class of boron rich compounds previously studied for their magnetic, optical and electronic properties.[12–19] The structure of all dodecaborides contains boron cuboctahedron cages composed of 24 atoms, each containing a 12-coordinate metal in its center. The cages are usually arranged in a face-centered cubic close packed arrangement, forming the cubic-UB_{12} ($Fm\bar{3}m$) structure; however, ScB_{12} forms its own structural type - tetragonal-ScB_{12} (*I4/mmm*), where the cuboctahedra are arranged in a body-centered tetragonal close-packed structure (Figure 2-1).[20] Dodecaborides are known to exist for a number of metals: transition metals (Zr, Hf, Y and Sc), lanthanides (Tb, Dy, Ho, Er, Tm, Yb and Lu) and actinides (U and Th).[20,21] For the most part, the aforementioned dodecaborides have been prepared via arc melting from the elements, or by borothermal reduction of the metal oxide under vacuum, to yield fully dense ingots or compacts, respectively.[17,22–28] HfB_{12} and ThB_{12} are especially interesting, since in pure form they can only be formed under high pressure (6.5 GPa) and high temperature (1660 ^{o}C)[29]; however, they can be stabilized under ambient pressure in the matrices of ZrB_{12} ($Zr_{1-x}Th_xB_{12}$)[24] and YB_{12} ($Y_{1-x}Hf_xB_{12}$).[28]

Pure dodecaborides are superhard, which can be attributed to their high isotropy and stiff metal-boron bonds as well as boron-boron bonds forming the cuboctahedra.[28,30,31] MB_{12}, as secondary phases, are also known to increase the hardness of other borides, such as WB_4, through extrinsic hardening mechanisms.[32] Atomic radii may play a determining role in the different structural types

of tetragonal-ScB_{12} and cubic-$MB_{12,}$[25] but electronic structure of the atoms also plays an important role. Scandium, although being a transition metal, behaves more like an alkaline-earth metal.[13] Unfortunately, it is still not completely understood why some MB_{12} prefer a body-centered tetragonal unit cell over a cubic cell.

Apart from the fundamental interest of metal MB_{12} due to their unique structure, their properties are also of interest in industrial applications, such as Zr-based cutting tools and abrasives (with abrasive qualities comparable to that of diamond, but producing less roughening of surfaces).[33] Therefore, the mechanical properties (superhardness), lightweight (due to density comparable or lower than that of diamond (3.52 g/cm^3)) and enhanced oxidation resistance properties are of interest for potential applications in machining industries and as lightweight protective coatings. Here, we examine the parent structure of the most common metal dodecaborides by creating solid solutions and speculate on the mechanism behind a cubic to body-centered tetragonal phase transformation. We hope that the outstanding mechanical and oxidation resistance properties of these dodecaborides will lend themselves to multiple materials applications.

EXPERIMENTAL PROCEDURE

Mixed dodecaboride solid solutions, $Zr_{1-x}Y_xB_{12}$, (x = 0.00, 0.05, 0.25, 0.50, 0.75, 0.95 and 1.00), $Zr_{1-y}Sc_yB_{12}$, $Y_{1-y}Sc_yB_{12}$ (y = 0.00, 0.05, 0.25, 0.50, 0.75, 0.80, 0.85, 0.90, 0.95 and 1.00), ScB_{50} and YB_{66} were synthesized using metal and boron powders of high-purity: amorphous boron (99+%, Strem Chemicals, U.S.A.), zirconium (99.5%, Strem Chemicals, U.S.A.), yttrium (99.9%, Strem Chemicals, U.S.A.) and scandium (99.9%, Sigma-Aldrich, U.S.A.). In order to prevent the formation of the lower boride phases, a metals to boron ratio of 1:20 was used for the dodecaborides, 1:65 for ScB_{50} and 1:70 for YB_{66}. The powders of boron and transition metals were

weighed, homogenized in an agate mortar and pestle and pressed into pellets using a hydraulic press (Carver) under a 10 ton load. The samples were then arc-melted ($I \geq 70$ amps, $t = 1\text{-}2$ mins) in an ultra-high purity argon atmosphere.

Prepared ingots were bisected using a diamond saw (Ameritool Inc., U.S.A.). One half was crushed into a sub 325 (45 μm) mesh powder and used for powder X-ray diffraction (PXRD) analysis; the other half was used for energy-dispersive X-ray spectroscopy (EDS) analysis and Vicker's hardness measurements. For the latter two, the samples were encapsulated in epoxy using an epoxy/hardener set (Allied High Tech Products Inc., U.S.A.). In order to achieve an optically flat surface, the samples were polished on a semi-automated polisher (South Bay Technology Inc., U.S.A.), using the following abrasives: SiC discs of 120 - 1200 grit sizes (Allied High Tech Products Inc., U.S.A.) and 30 - 1 micron particle diamond films (South Bay Technology Inc., U.S.A.).

Powder XRD was carried out on a Bruker D8 Discover Powder X-ray Diffractometer (Bruker Corporation, Germany) utilizing $Cu_{K\alpha}$ X-ray radiation ($\lambda = 1.5418$ Å). The following scan parameters were used: $5\text{-}100^{o}$ 2θ range, time per step of 0.3 sec, step size of 0.0353^{o} with a scan speed of 0.1055^{o}/sec. In order to determine the phases present in the powder X-ray diffraction data, the Joint Committee on Powder Diffraction Standards (JCPDS) database was utilized. The composition and purity of the samples were determined on an FEI Nova 230 high resolution scanning electron microscope (FEI Company, U.S.A.) with an UltraDry EDS detector (Thermo Scientific, U.S.A.). Transmission electron microscopy (TEM) was performed on a TF-20 transmission electron microscope in order to confirm the crystal structure. Rietveld refinement utilizing *Maud* software was carried out to determine the cell parameters.[34–38] The hardness of each

sample was determined using a MicroMet 2103 Vickers microhardness tester (Buehler Ltd, U.S.A.). Fifteen indents of the following force loading were made in random areas of the sample: 0.49, 0.98, 1.96, 2.94 and 4.9 N (low to high, respectively). The length of the diagonals were measured using a high resolution optical microscope (Zeiss Axiotech 100HD, Carl Zeiss Vision GmbH, Germany) with 500x magnification, and Vickers hardness was calculated using Equation 2.1:

$$H_v = \frac{1854.4F}{a^2} \quad (2.1)$$

where *F* is the loading force applied in Newtons (N) and *a* is the average of the length of the two diagonals of each indent in micrometers.

Densities for the 50/50% solid solutions were calculated from powder XRD unit cell data and elemental composition from EDS.

Oxidation resistance was determined via thermogravimetric analysis utilizing a Pyris Diamond TGA/DTA unit (TG-DTA, Perkin-Elmer Instruments, U.S.A.). The following heating/cooling profile was used: heating in air from 25 to 200 ^{o}C (at 20 ^{o}C/min), holding at 200 ^{o}C for 30 minutes, heating from 200 to 1000 ^{o}C (at 2 ^{o}C/min), holding at 1000 ^{o}C for 120 minutes, cooling 1000 to 25 ^{o}C (at 5 ^{o}C/min).

RESULTS AND DISCUSSION

To determine and establish the composition and phase purity of mixed MB_{12} solid solutions, powder X-ray diffraction (PXRD) and energy-dispersive X-ray spectroscopy (EDS) analyses were performed. Figure 2-2 shows PXRD in the 5 - 50^{o} 2Θ for the three solid solutions: $Zr_{1-x}Y_xB_{12}$ (x = 0.05, 0.25, 0.50, 0.75 and 0.95), $Zr_{1-y}Sc_yB_{12}$ and $Y_{1-y}Sc_yB_{12}$ (y = 0.05, 0.25, 0.50, 0.75, 0.80, 0.85,

0.90 and 0.95). PXRD data for the β-rhombohedral boron doping phase of Sc (ScB_{50}, $R\bar{3}m$) and YB_{66} ($Fm\bar{3}c$) (Figure 2-3) compared to the reference patterns from JCPDS (Joint Committee for Powder Diffraction Standards) can be seen in Figure 2-4. EDS data and hardness are discussed later in this section (Figures 2-5 and Figure 2-6).

The three dodecaborides, ZrB_{12}, YB_{12} and ScB_{12}, are completely soluble in each other as binary metal substituted phases: $Zr_{1-x}Y_xB_{12}$, $Zr_{1-x}Sc_xB_{12}$ and $Y_{1-x}Sc_xB_{12}$. Samples with YB_{12} contain YB_{66} as a minor phase, while ScB_{12} samples contain ScB_{50} (Figure 2-3 and 2-4). ZrB_{12} and YB_{12} form an essentially perfect solid solution (Figure 2-2 and Table 2-1), which follows Vegard's Law within experimental error. This can be attributed to the fact that both of these dodecaborides have the cubic-UB_{12} ($Fm\bar{3}m$) structure, the electronegativities of the metals are similar, and the differences in their radii are within the 15% set by the Vegard's Law rules.[39] On the other hand, ScB_{12} possesses a tetragonal-ScB_{12} structure. This results in $Zr_{1-x}Sc_xB_{12}$ and $Y_{1-x}Sc_xB_{12}$ solid solutions having a solid-state phase transition[25] at ~ 90-95 at. % Sc (Figure 2-2 and Table 2-2). In addition, $Zr_{1-x}Sc_xB_{12}$ solid solutions were previously shown to undergo a temperature induced phase transition.[26] Unit cell parameters for cubic (FCC) and body-centered tetragonal (BCT) syngonies as well as the phase composition as determined by EDS are presented in Tables 2-1 and 2-2. Figure 2-3 shows the SEM images and elemental maps for the hardest compositions of the mixed metal dodecaborides: $Zr_{0.5}Y_{0.5}B_{12}$, $Zr_{0.5}Sc_{0.5}B_{12}$ and $Y_{0.5}Sc_{0.5}B_{12}$. For $Zr_{0.5}Y_{0.5}B_{12}$, both Zr and Y can be observed in the metal dodecaboride phase. In contrast, for the Sc containing dodecaboride solid solutions, $Zr_{0.5}Sc_{0.5}B_{12}$ and $Y_{0.5}Sc_{0.5}B_{12}$, while Zr and Y can be seen primarily in the dodecaboride phase, Sc can be seen both in the dodecaboride phase as well as in boron rich areas (as ScB_{50}).

After establishing the purity of the samples, Vickers hardness testing (under a load of 0.49 – 4.9 N) was carried out, the results of which are shown in Figure 2-6. High covalent bond density of the dodecaborides may be the reason that both pure MB_{12} as well as their mixed metal solid solutions are superhard ($H_v \geq 40$ GPa). For the $Zr_{1-x}Y_xB_{12}$ solid solution, at the composition of Y = 50 at. %, the hardness maximizes at 45.8 ± 1.3 GPa for a loading of 0.49 N, compared to 40.4 ± 1.8 GPa for pure ZrB_{12} (compared to a literature value of 39 GPa)[30,40] and 40.9 ± 1.6 GPa for pure YB_{12} (compared to a literature value of 42 GPa).[30] We speculate that the 14% increase in hardness here is due to a combination of both intrinsic factors (solid solution hardening) where incorporating atoms of different sizes (Zr: r_{at} = 1.55 Å, $r_{CN = 12}$ = 1.603 Å; Y: r_{at} = 1.80 Å, $r_{CN = 12}$ = 1.801 Å)[41,42] produces strain at a local scale and dislocation propagation is therefore hindered; as well as extrinsic factors (due to sample morphology, microstructure and the presence of boron rich phases). $Zr_{1-x}Y_xB_{12}$ solid solutions contain the YB_{66} phase, which in contrast to ScB_{50}, is not a β-rhombohedral boron doping phase, but a separate Y-B phase. YB_{66} ($Fm\bar{3}c$, Figure 2-3) contains 1584 boron atoms and 24 Y atoms and is superhard (40.4 ± 1.8 GPa at 0.49 N), potentially providing some extrinsic hardening for these samples.[28,43,44]

For the $Zr_{1-x}Sc_xB_{12}$ solid solution, the hardness increases to 48.0 ± 2.1 GPa at a composition of 50 at% Sc, compared to 40.4 ± 1.8 GPa for pure ZrB_{12} and 41.7 ± 2.2 GPa for pure ScB_{12}. This hardness increase can again be attributed to a combination of intrinsic (solid solution hardening), since at this composition ($Zr_{0.5}Sc_{0.5}B_{12}$) ScB_{12} is stabilized in the cubic structural type as well as extrinsic factors. The hardness of the solid solutions richer in Sc ($x \geq 0.5$) are harder than the corresponding samples richer in Zr ($x \leq 0.5$); this may be attributed to the fact that $Zr_{1-x}Sc_xB_{12}$ undergoes a cubic to tetragonal phase transition at 90-95 at. % Sc. This is similar to the martensitic transformation in steel, where the unit cell transforms from a cubic to a body-centered tetragonal

lattice through a diffusionless transformation. Solid solutions richer in Sc also contain the ScB_{50} phase (Figure 2-3), which is a solid solution of Sc in β-rhombohedral boron. This phase, like most metal boron doping phases, is superhard ($H_v \geq 40$ GPa) at 42.1 ± 2.2 GPa at 0.49 N, providing some extrinsic hardening.[45,46]

For the $Y_{1-x}Sc_xB_{12}$ solid solution, a hardness peak can be observed at 50 at. % Sc. The hardness increases to 45.2 ± 2.1 GPa compared to 40.9 ± 1.6 GPa for pure YB_{12} and 41.7 ± 2.2 GPa for pure ScB_{12}. Similarly to $Zr_{1-x}Sc_xB_{12}$, the hardness increase of $Y_{1-x}Sc_xB_{12}$ can be attributed to solid-solution hardnening as well as the presence of secondary boron rich phase, ScB_{50} phase, which is superhard ($H_v \geq 40$ GPa at 0.5 N of applied loading). A cubic to tetragonal phase transition occurs at 90-95 at. % Sc for this solid solution.

In order to determine the cell parameters, Rietveld refinement was carried out using *Maud* software (Tables 2-1 and 2-2).[34–38] For $Zr_{1-x}Y_xB_{12}$ the lattice parameter (a) of the cubic cell changed from 7.412 Å for pure ZrB_{12} to 7.505 Å for pure YB_{12} (Figure 2-2 and Table 2-1). The change and gradual increase of the cell parameters confirms that a solid solution has been formed. In order to check the composition of the $Zr_{1-x}Y_xB_{12}$ phase, EDS analysis was performed (Table 2-1). This analysis further confirmed the nearly perfect solid solution formation over all range of concentrations of Zr and Y in $Zr_{1-x}Y_xB_{12}$. As both of the parent dodecaborides (ZrB_{12} and YB_{12}) are of the cubic-UB_{12} ($Fm\bar{3}m$) structural type, this system has no solid-state phase transformation.

For $Zr_{1-x}Sc_xB_{12}$ and $Y_{1-x}Sc_xB_{12}$ solid solutions, not only can a change in the lattice parameters be observed indicative of the formation of a solid solution (Tables 2-2 and 2-3), but a solid state phase transition between the cubic-UB_{12} ($Fm\bar{3}m$) and tetragonal-ScB_{12} (*I4/mmm*) lattice types can be found as well. The phase transition occurs at ~90-95 at. % Sc for $Zr_{1-x}Sc_xB_{12}$ and $Y_{1-x}Sc_xB_{12}$ solid

solutions. A face-centered-cubic (FCC) to body-centered tetragonal (BCT) transition can be imagined if two FCC unit cells are positioned such that they share a face. Thus, the shared face-centered positions of the cubic cells become the body-centered positions of the tetragonal cell; the cubic *a* lattice parameter then becomes the tetragonal *c* lattice parameter, while the tetragonal *a* lattice parameter is composed of the cubic face diagonals and equals the cubic parameter *a* times $\frac{\sqrt{2}}{2}$. By refining the structural model to fit the data in the cubic and tetragonal unit cells over the whole range of solid solutions, we found that the values of the cubic *a* and tetragonal *c* lattice parameters stay essentially the same, within error, for low concentrations of scandium and diverges as they approach pure ScB_{12}. Therefore, at small concentrations of a secondary metal (5-10 at. %), one can speculate that the structure of the resulting mixed dodecaboride with scandium keeps the pure ScB_{12} tetragonal unit cell, whereas with the addition of more secondary metal, the unit cell stabilizes into the cubic-UB_{12} structure. To provide evidence for this speculation, a TEM image of showing the tetragonal diffraction pattern for $Zr_{0.05}Sc_{0.95}B_{12}$ can be seen in Supplemental Information section, Figure 2-7.

Analyzing the crystal structure of ZrB_{12} (ICSD 23861), YB_{12} (ICSD 23860) and ScB_{12} (ICSD 68028), one observes that tetragonal-ScB_{12} has shorter metal-B bonds, while having longer B-B bonds than other cubic metal dodecaborides. This leads to not only a distortion of the cuboctahedron boron cages, but also to stronger metal-boron bonds in tetragonal-ScB_{12}. Addition of a secondary transition metal in ScB_{12} allows for the alleviation of the cuboctahedral distortion and as a consequence stabilizes $M_{1-x}Sc_xB_{12}$ solid solution in the cubic structural type.

Metal dodecaboride samples exhibit interesting colors, ranging from violet for ZrB_{12} to light blue for YB_{12} and iceberg blue for ScB_{12}. The colors are a result of charge-transfer from the metal atoms

to the network of boron cuboctahedron cages.[16,17] Figure 2-8 shows the colors of solid solution samples of the mixed metal dodecaborides taken using an optical microscope. The color change is most pronounced for the $Zr_{1-x}Y_xB_{12}$ solid solution, which goes from violet for ZrB_{12} to light blue for YB_{12}. The color changes for $Zr_{1-x}Sc_xB_{12}$ and $Y_{1-x}Sc_xB_{12}$ are less pronounced due to the similarities of the shades of blue of YB_{12} and ScB_{12}.

Analysing the thermal stability data from TGA for the hardest solid solutions of ZrB_{12}, YB_{12} and ScB_{12}, one observes that the oxidation resistances for $Zr_{0.5}Y_{0.5}B_{12}$, $Zr_{0.5}Sc_{0.5}B_{12}$ and $Y_{0.5}Sc_{0.5}B_{12}$ are comparable to their parent compounds (Figure 2-9). Whereas, the oxidation resistances for ZrB_{12}, YB_{12} and ScB_{12} are ~610 ^oC, ~715 ^oC and ~685 ^oC, respectively, the mixed dodecaboride solid solutions are stable up until ~630 ^oC, ~685 ^oC and ~695 ^oC, respectively. This high oxidation resistance suggests that dodecaborides could be a promising replacement for the current industrial standard, tungsten carbide, which oxidizes at ~400 ^oC.[47] Furthermore, the densities for the hardest compositions are low, owing to their high boron content. X-ray densities of $Zr_{0.5}Y_{0.5}B_{12}$ (3.52 g/cm^3), $Zr_{0.5}Sc_{0.5}B_{12}$ (3.32 g/cm^3), and $Y_{0.5}Sc_{0.5}B_{12}$ (3.18 g/cm^3) show that they are as light, if not lighter than diamond (3.52 g/cm^3). The low density, superhardness and enhanced oxidation resistance makes metal dodecaborides an interesting choice as potential materials for cutting and machining or as lightweight protective coatings.

CONCLUSIONS

Mixed metal dodecaboride solid solutions of ZrB_{12}, YB_{12} and ScB_{12} have been examined in some detail. $Zr_{1-x}Sc_xB_{12}$ and $Y_{1-x}Sc_xB_{12}$ were found to have an FCC to BCT solid state phase transition, while $Zr_{1-x}Y_xB_{12}$ formed a nearly perfect solid solution, closely following Vegard's Law. All three solid solutions exhibit a hardness increase for the 50/50 at. % metal composition, attributed to solid

solution hardening. Moreover, $Zr_{0.5}Y_{0.5}B_{12}$, $Zr_{0.5}Sc_{0.5}B_{12}$ and $Y_{0.5}Sc_{0.5}B_{12}$ solid solutions show a substantial increase in oxidation resistance to ~630 ^{o}C, ~685 ^{o}C and ~695 ^{o}C, respectively, compared to other superhard metal borides (e.g. ~400 ^{o}C for WB_4) and the traditional cutting tool material WC (~400 ^{o}C). In addition, $Zr_{0.5}Y_{0.5}B_{12}$, $Zr_{0.5}Sc_{0.5}B_{12}$ and $Y_{0.5}Sc_{0.5}B_{12}$, have relatively low densities, 3.52, 3.32 and 3.18 g/cm^3, respectively, comparable to or lower than that of diamond (3.52 g/cm^3), and significantly lower than other superhard borides such as ReB_2 (12.67 g/cm^3)[13] and WB_4 (8.40 g/cm^3)[13] and the traditional cutting tool material WC (15.77 g/m^3)[13], making them of potential interest as materials for cutting and machining and as lightweight protective coatings.

ACKNOWLEDGEMENTS

We thank the National Science Foundation Division of Materials Research, Grant DMR-1506860 (R.B.K.) and the National Science Foundation DGE-0654431 Fellowship program (M.T.Y.) for financial support. We also thank Professor Benjamin M. Wu of the UCLA Department of Bioengineering for the use of his micro-indentation system. We would also like to thank Rebecca L. Li, Wai H. Mak, and Emily P. Nguyen for useful discussions.

Table 2-1. Composition[a] and Unit Cell Data[b] for $Zr_{1-x}Y_xB_{12}$[c]

Compound	Concentration of Y in ZrB_{12} (at.% Y)[a]	Cubic ($Fm\bar{3}m$)	
		a (Å)[b]	a (Å)[d]
ZrB_{12}	-	7.412(2)	7.412
$Zr_{0.95}Y_{0.05}B_{12}$	2.91 (0.10)	7.418(3)	7.417
$Zr_{0.75}Y_{0.25}B_{12}$	20.29 (0.12)	7.438(4)	7.435
$Zr_{0.50}Y_{0.50}B_{12}$	47.81 (0.55)	7.454(3)	7.459
$Zr_{0.25}Y_{0.75}B_{12}$	70.89 (0.46)	7.481(6)	7.482
$Zr_{0.05}Y_{0.95}B_{12}$	91.24 (0.41)	7.502(3)	7.500
YB_{12}	-	7.505(4)	7.505

[a]calculated from EDS analysis; errors are given in brackets
[b]from cell refinement using *Maud*; errors are given in brackets
[c]x = 0.00, 0.05, 0.25, 0.50, 0.75, 0.95 and 1.00
[d]calculated using Vegard's Law

Table 2-2. Composition[a] and Unit Cell Data[b] for $Zr_{1-y}Sc_yB_{12}$[c] and $Y_{1-y}Sc_yB_{12}$[c]

Compound	Concentration of Sc in ZrB_{12} (at.% Sc)[a]	Cubic ($Fm\bar{3}m$)	Tetragonal (*I4/mmm*)		Compound	Concentration of Sc in YB_{12} (at.% Sc)[a]	Cubic ($Fm\bar{3}m$)	Tetragonal (*I4/mmm*)	
		a (Å)[b]	a (Å)[b]	c (Å)[b]			a (Å)[b]	a (Å)[b]	c (Å)[b]
ZrB_{12}	-	7.412(2)	-	-	YB_{12}	-	7.505(4)	-	-
$Zr_{0.95}Sc_{0.05}B_{12}$	2.20 (0.09)	7.412(4)	5.241(2)	7.411(3)	$Y_{0.95}Sc_{0.05}B_{12}$	4.36 (0.17)	7.504(3)	5.306(2)	7.503(3)
$Zr_{0.75}Sc_{0.25}B_{12}$	15.14 (0.16)	7.410(3)	5.240(3)	7.410(4)	$Y_{0.75}Sc_{0.25}B_{12}$	26.45 (0.22)	7.486(2)	5.292(3)	7.486(2)
$Zr_{0.50}Sc_{0.50}B_{12}$	38.66 (0.28)	7.408(3)	5.237(4)	7.408(5)	$Y_{0.50}Sc_{0.50}B_{12}$	40.57 (0.28)	7.486(2)	5.291(4)	7.486(3)
$Zr_{0.25}Sc_{0.75}B_{12}$	65.16 (0.39)	7.405(4)	5.235(2)	7.405(4)	$Y_{0.25}Sc_{0.75}B_{12}$	65.79 (0.23)	7.455(3)	5.272(2)	7.452(4)
$Zr_{0.20}Sc_{0.80}B_{12}$	67.49 (0.26)	7.403(2)	5.234(5)	7.402(3)	$Y_{0.20}Sc_{0.80}B_{12}$	67.40 (0.31)	7.448(4)	5.255(5)	7.449(5)
$Zr_{0.15}Sc_{0.85}B_{12}$	87.17 (0.33)	7.402(5)	5.233(3)	7.393(3)	$Y_{0.15}Sc_{0.85}B_{12}$	73.90 (0.30)	7.442(5)	5.247(5)	7.439(5)
$Zr_{0.10}Sc_{0.90}B_{12}$	90.51 (0.69)	7.398(3)	5.233(4)	7.389(4)	$Y_{0.10}Sc_{0.90}B_{12}$	81.03 (0.39)	7.428(6)	5.243(3)	7.426(6)
$Zr_{0.05}Sc_{0.95}B_{12}$	94.97 (0.44)	7.395(3)	5.232(3)	7.385(3)	$Y_{0.05}Sc_{0.95}B_{12}$	92.38 (0.30)	7.402(5)	5.235(2)	7.389(3)
ScB_{12}	-	-	5.232(3)	7.361(4)	ScB_{12}	-	-	5.232(3)	7.361(4)

[a]calculated from EDS analysis; errors are given in brackets
[b]from cell refinement using *Maud*; errors are given in brackets
[c]y = 0.00, 0.05, 0.25, 0.50, 0.75, 0.80, 0.85, 0.90, 0.95 and 1.00

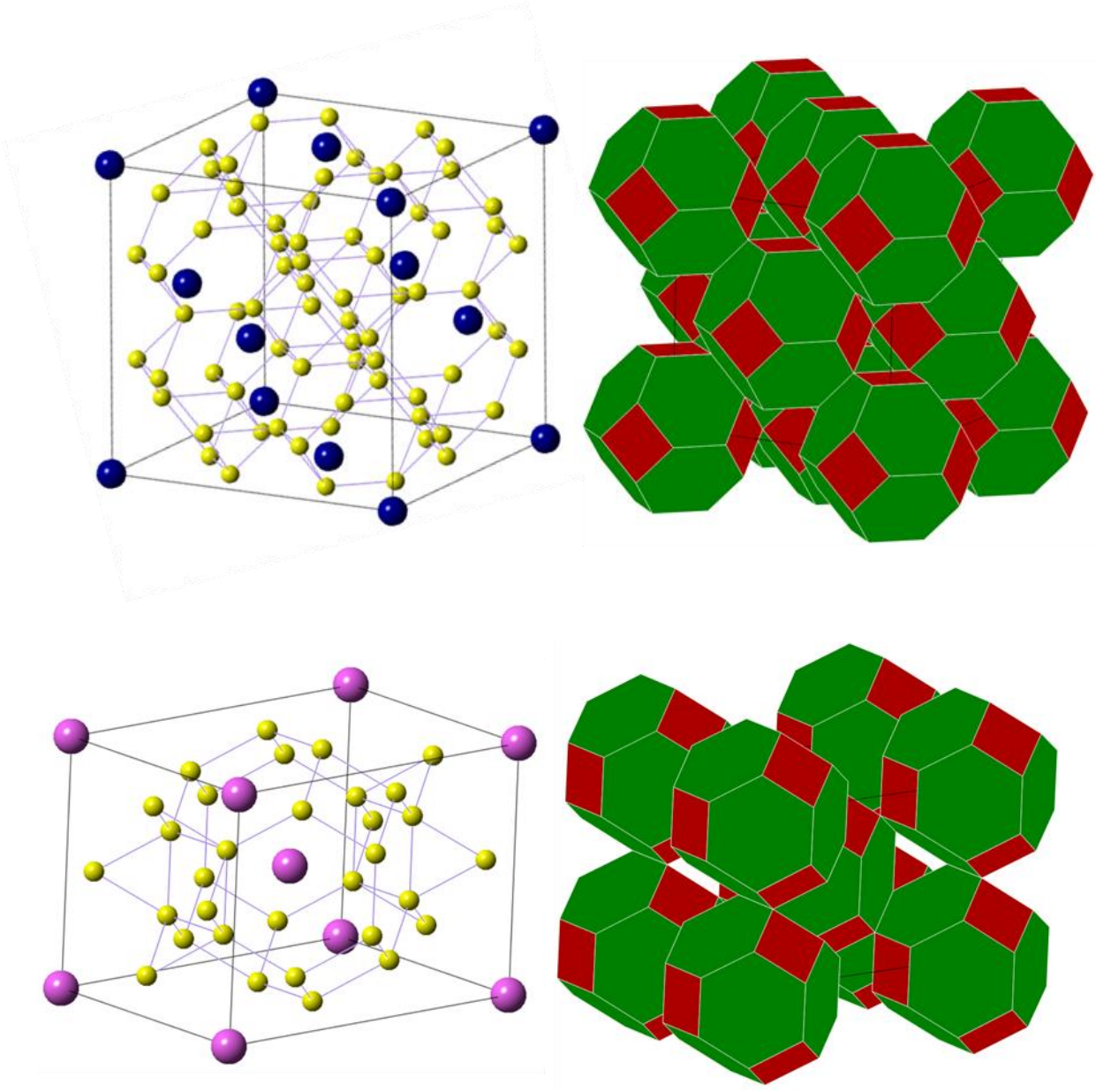

Figure 1-1. (Top left) The unit cell of the cubic-UB_{12} dodecaboride structure type: metal atoms are in blue, B atoms in yellow, (top right) cubic-UB_{12} polyhedra model: face-centered cubic (FCC) lattice of 24 boron atom cuboctahedra boron cages surrounding 12-coordinate metal atoms; (bottom left) The unit cell of the tetragonal-ScB_{12} dodecaboride structure type: metal atoms are in magenta, B atoms in yellow, (bottom right) tetragonal-ScB_{12} polyhedra model: body-centered tetragonal (BCT) lattice of 24 boron atom cuboctahedra boron cages surrounding 12-coordinate metal atoms; Note, while 24 borons surround each metal atom, each metal atom is equidistant from 12 B-B bonds, making it 12-coordinate.

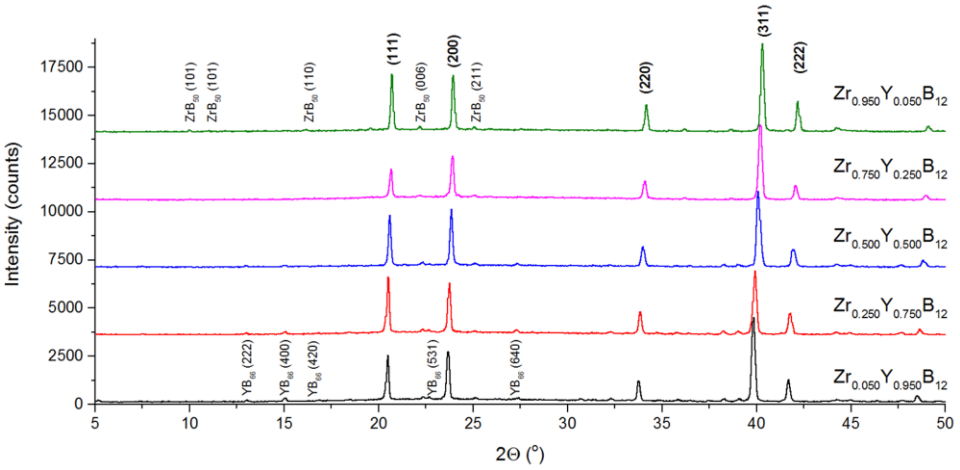

(a)

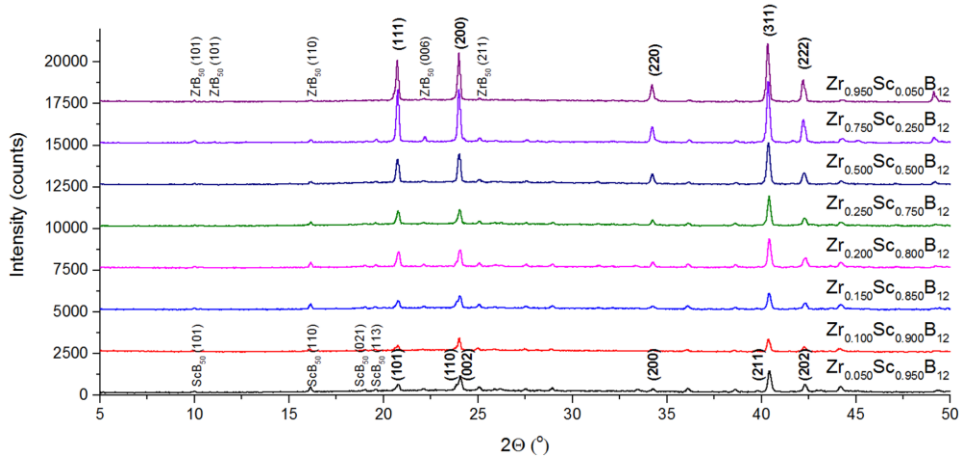

(b)

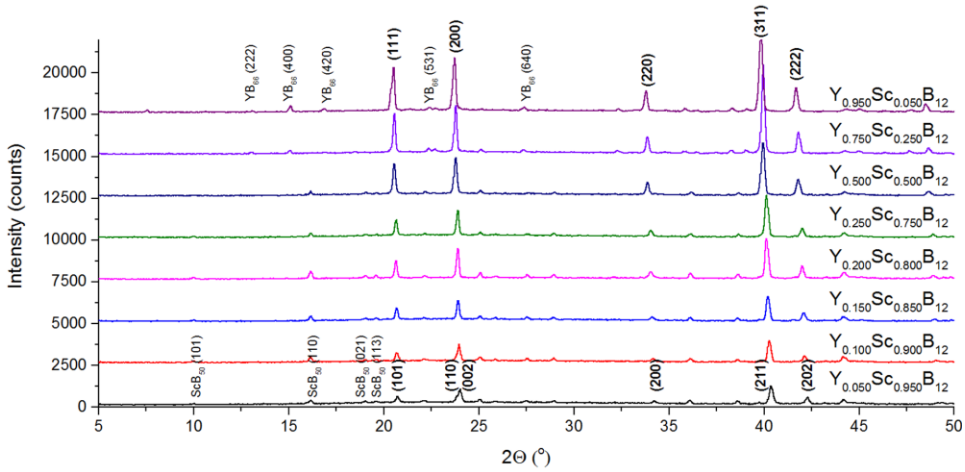

(c)

Figure 2-2. Powder XRD patterns of: (a) $Zr_{1-x}Y_xB_{12}$ (x = 0.00, 0.05, 0.25, 0.50, 0.75, 0.95 and 1.00); (b) $Zr_{1-y}Sc_yB_{12}$; and (c) $Y_{1-y}Sc_yB_{12}$ (y = 0.00, 0.05, 0.25, 0.50, 0.75, 0.80, 0.85, 0.90, 0.95 and 1.00).

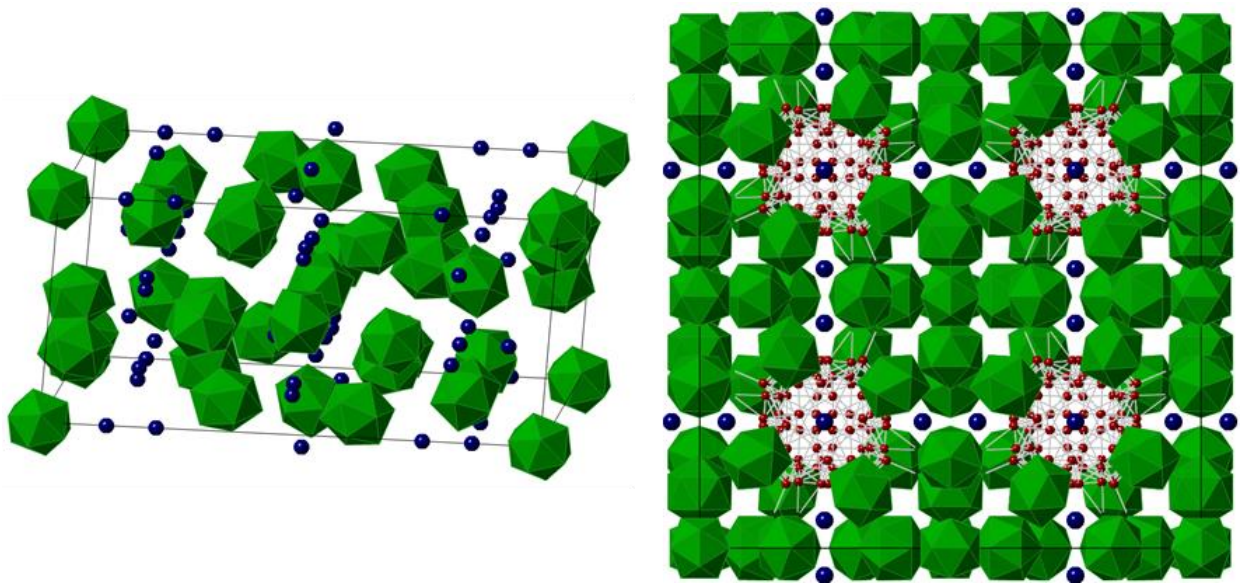

Figure 2-3. (Left) crystal structure of ScB_{50}, known as the β-rhombohedral boron doping phase of scandium (Inorganic Crystal Structure Database (ICSD) 2204, space group $R\bar{3}m$), showing characteristic boron icosahedra; (Right) crystal structure of YB_{66} (ICSD 23186, space group $Fm\bar{3}c$). (Boron atoms, which are part of B_{12} clusters are shown as green icosahedra, other boron atoms are in dark red, scandium atoms are in violet, yttrium atoms are in teal).

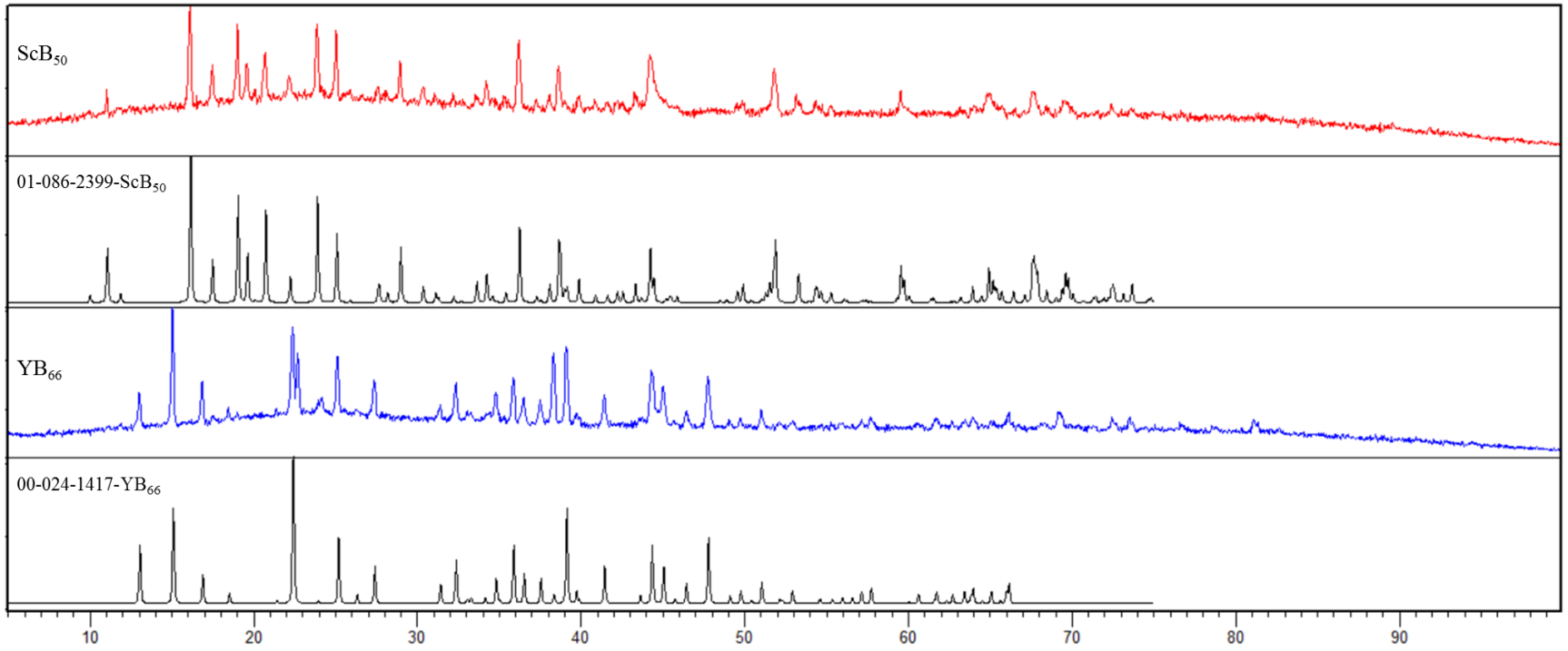

Figure 2-4. Powder XRD patterns of ScB_{50} (JCPDS 01-086-2399) and YB_{66} (JCPDS 00-024-1417).

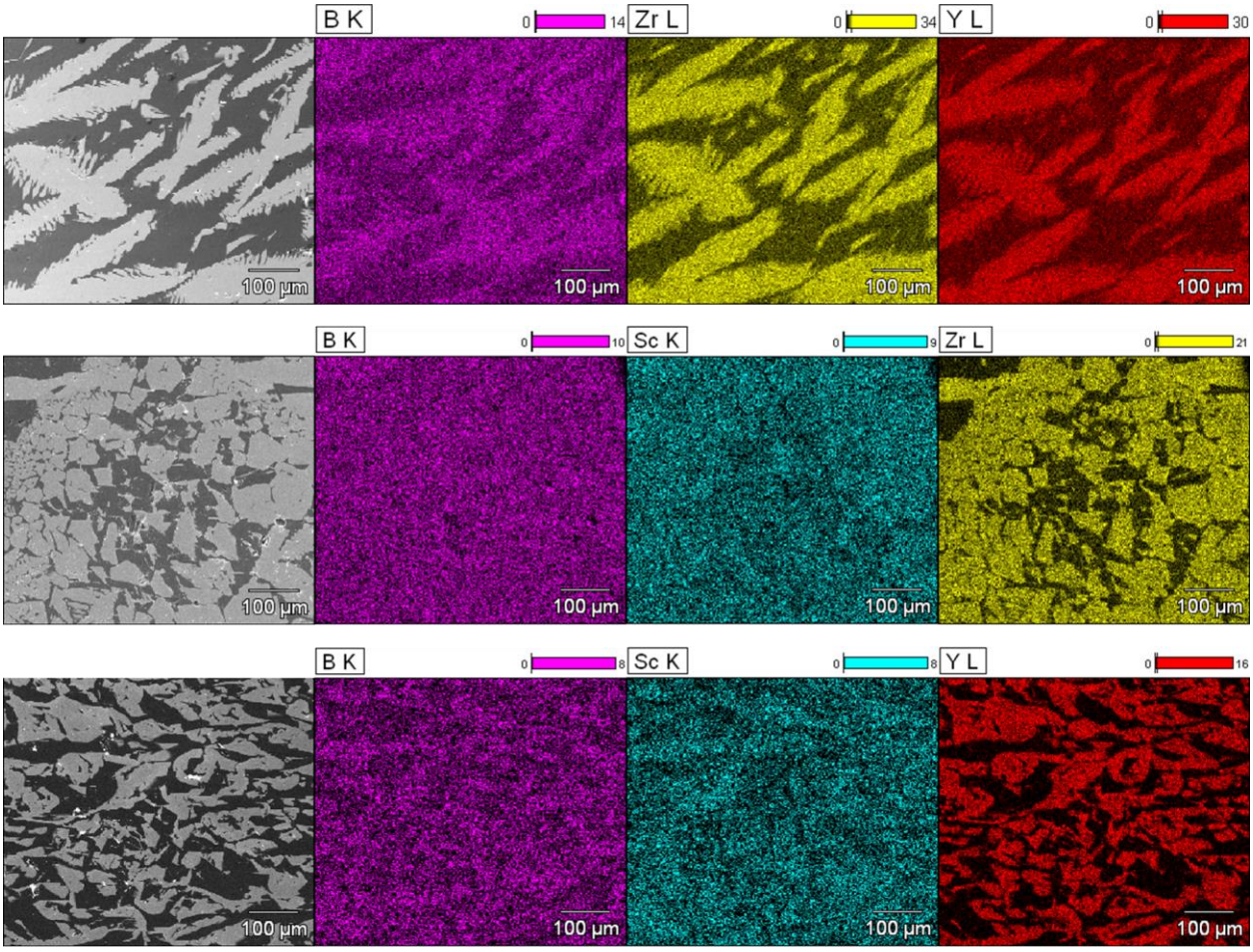

Figure 2-5. SEM images and elemental maps for boron (K line), scandium (K line), yttrium (L line), zirconium (L line) for mixed metal dodecaboride solid-solutions: (top) $Zr_{0.5}Y_{0.5}B_{12}$, (middle) $Zr_{0.5}Sc_{0.5}B_{12}$, (bottom) $Y_{0.5}Sc_{0.5}B_{12}$. For $Zr_{0.5}Y_{0.5}B_{12}$ both zirconium and yttrium can be observed in the metal dodecaboride phase. In contrast, for the scandium containing dodecaboride solid solutions, $Zr_{0.5}Sc_{0.5}B_{12}$ and $Y_{0.5}Sc_{0.5}B_{12}$, while yttrium can be seen primarily in the dodecaboride phase, scandium can be seen both in dodecaboride phase as well as in boron rich areas (as ScB_{50}). The thick horizontal bars represent the intensity as a color legend.

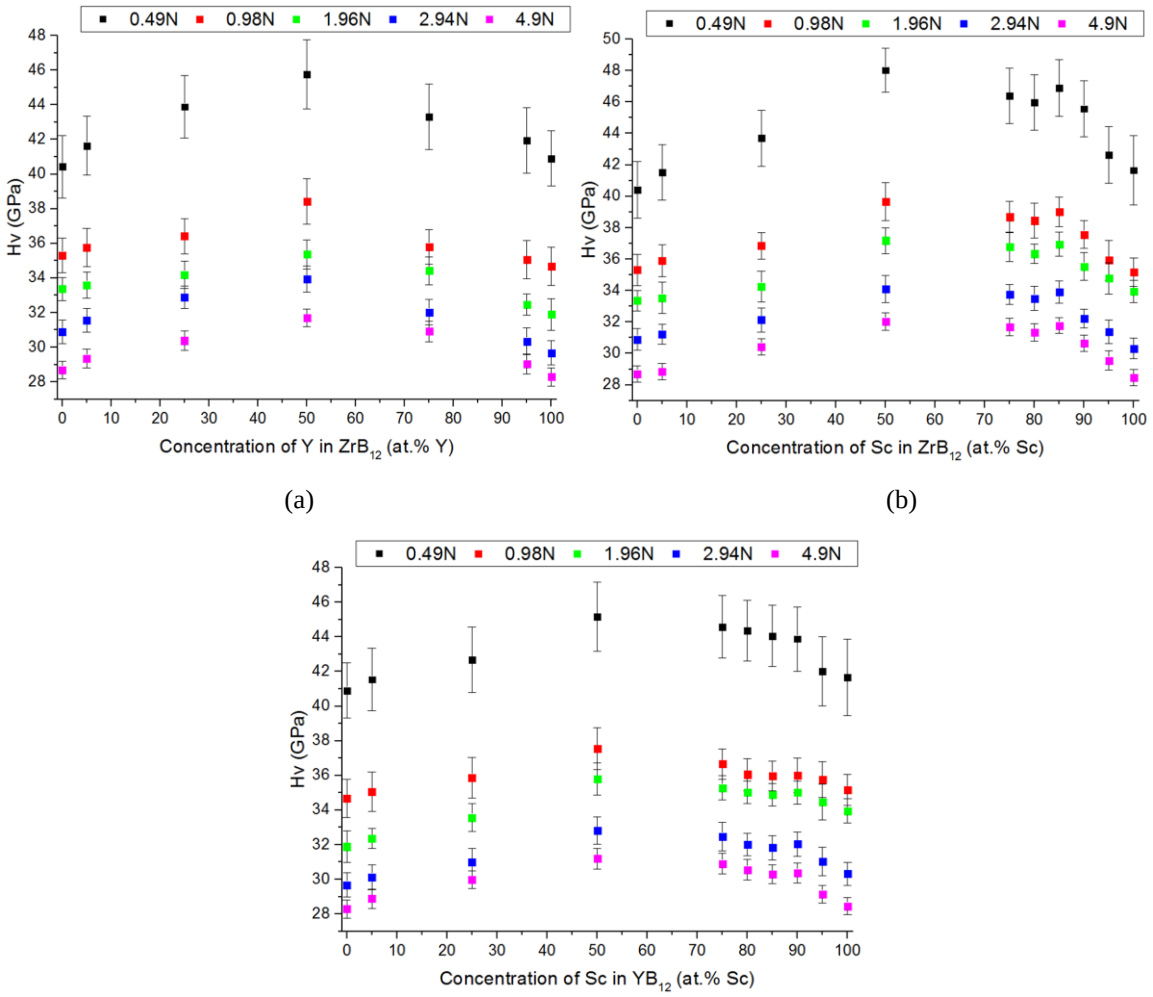

Figure 2-6. Vickers microindentation hardness of: (a) $Zr_{1-x}Y_xB_{12}$ (x = 0.00, 0.05, 0.25, 0.50, 0.75, 0.95 and 1.00); (b) $Zr_{1-y}Sc_yB_{12}$; and (c) $Y_{1-y}Sc_yB_{12}$ (y = 0.00, 0.05, 0.25, 0.50, 0.75, 0.80, 0.85, 0.90, 0.95 and 1.00) under loads of 0.49 N (low) to 4.9 N (high).

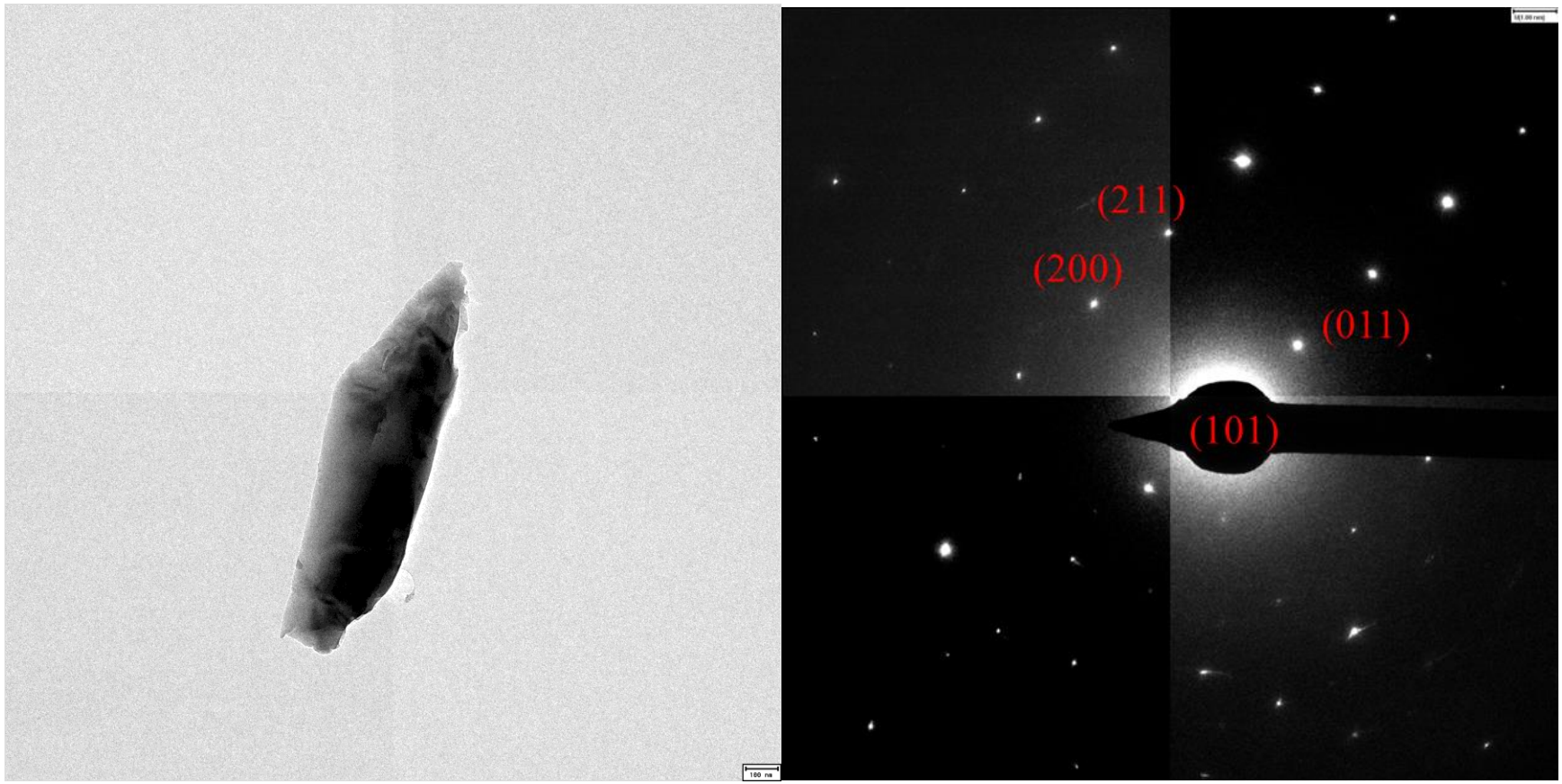

Figure 2-7. (Left) Transmission electron microscopy (TEM) image of a grain of $Zr_{0.05}Sc_{0.95}B_{12}$ (scale bar = 100 nm); (Right) electron diffraction image showing a tetragonal unit cell (scale bar = 1/1.0 nm).

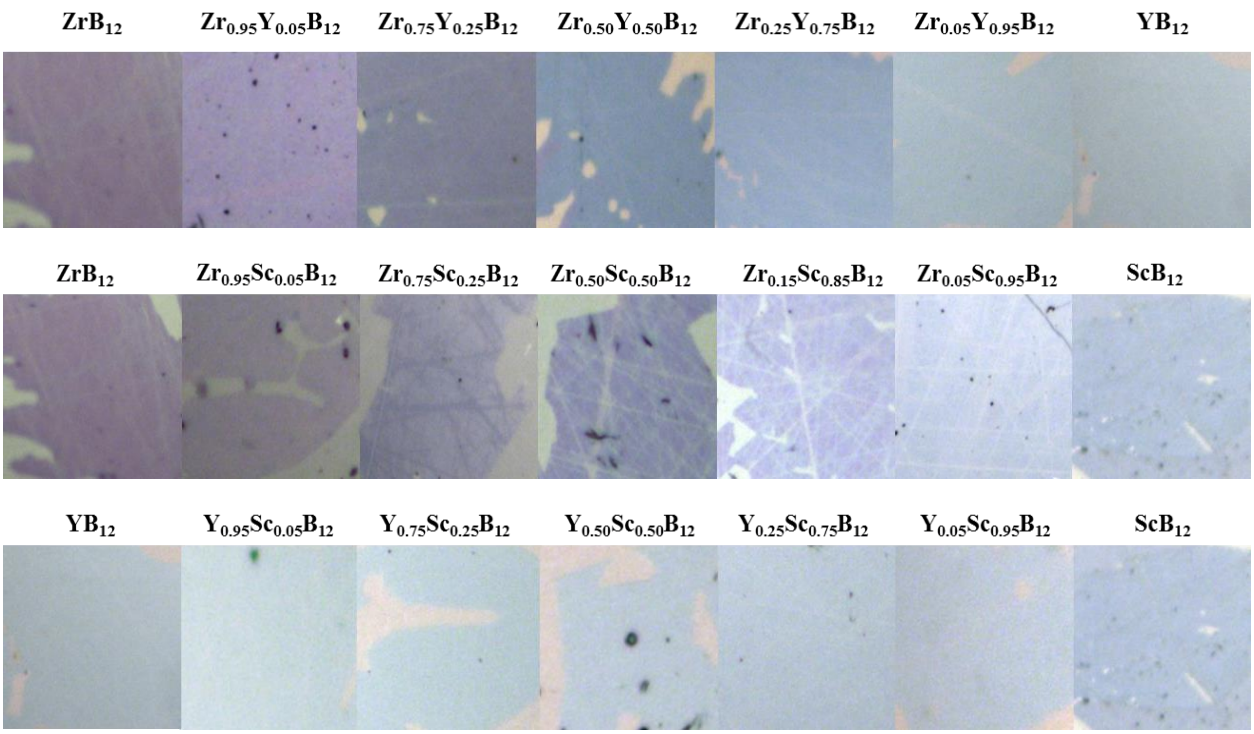

Figure 2-8. Optical microscopy images of the polished samples. A color change of the dodecaboride phase can be directly observed using a light microscope going from pure ZrB_{12} (violet) to YB_{12} (light-blue) and ScB_{12} (iceberg blue) phase. The color change is less pronounced for the $ZrScB_{12}$ and $YScB_{12}$ solid solutions.

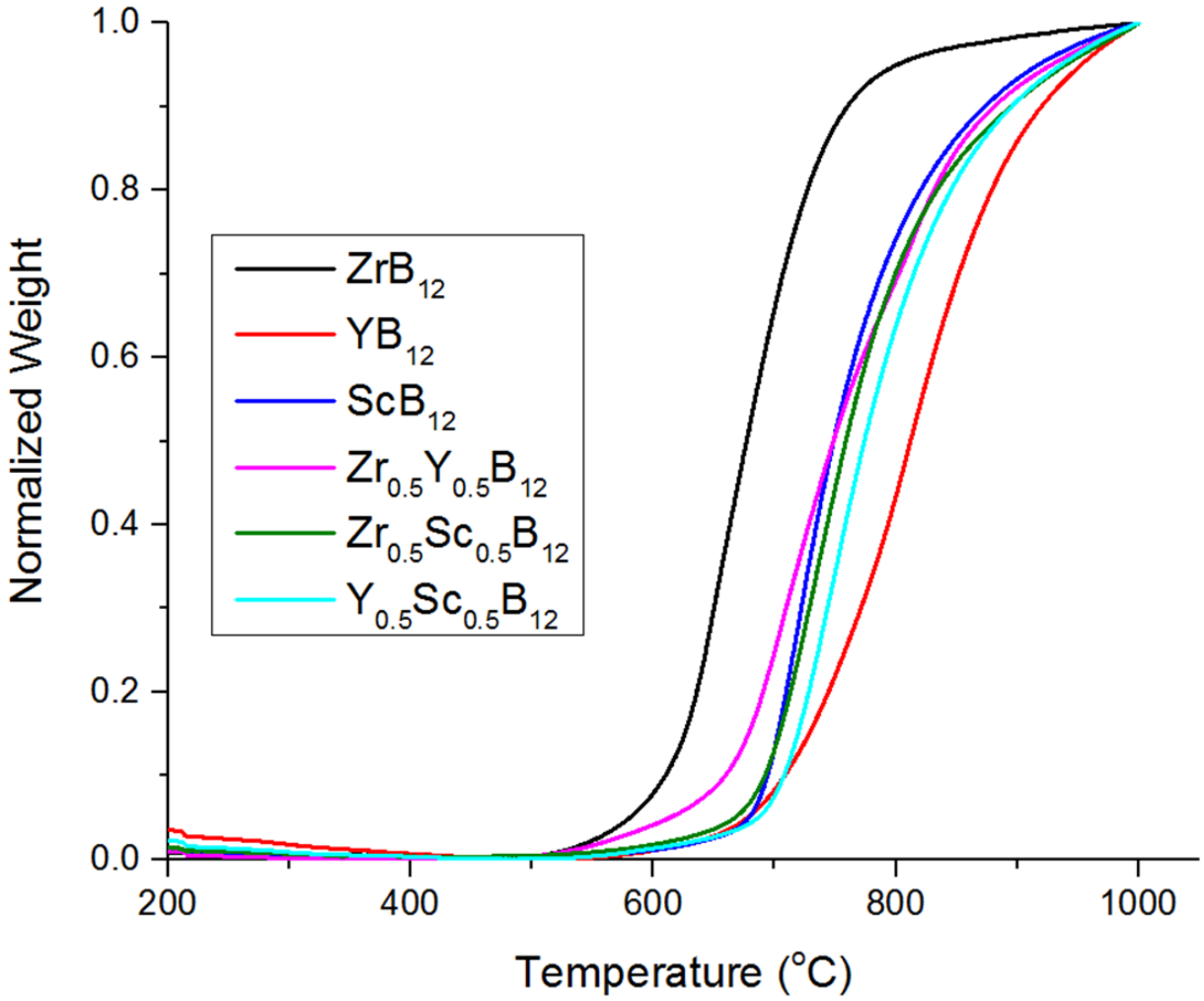

Figure 2-9. Thermal stability of pure ZrB_{12}, YB_{12} and ScB_{12} and the hardest solid solutions of mixed metal dodecaborides as measured by thermal gravimetric analysis in air. These data show that $Zr_{0.5}Y_{0.5}B_{12}$, $Zr_{0.5}Sc_{0.5}B_{12}$ and $Y_{0.5}Sc_{0.5}B_{12}$ are stable up to ~630 ^{o}C, ~685 ^{o}C and ~695 ^{o}C, respectively (using the extrapolated oxidation onset), compared to ~610 ^{o}C for pure ZrB_{12}, ~715^{o}C for pure YB_{12} and ~685 ^{o}C pure ScB_{12}.

REFERENCES

1. Mohammadi, R. & Kaner, R. B. *Superhard Materials*. *Encyclopedia of Inorganic and Bioinorganic Chemistry* (R.A. Scott ed., John Wiley and Sons, Inc., 2012).

2. Chung, H.-Y. *et al.* Synthesis of Ultra-Incompressible Superhard Rhenium Diboride at Ambient Pressure. *Science (80-.).* **316,** 436–439 (2007).

3. Chung, H.-Y. *et al.* Response to Comment on 'Synthesis of Ultra-Incompressible Superhard Rhenium Diboride at Ambient Pressure'. *Science (80-.).* **318,** 1550 (2007).

4. Knappschneider, A. *et al.* Possible superhardness of CrB4. *Inorg. Chem.* **52,** 540–542 (2013).

5. Mohammadi, R. *et al.* Tungsten tetraboride, an inexpensive superhard material. *Proc. Natl. Acad. Sci. U. S. A.* **108,** 10958–10962 (2011).

6. Yeung, M. T. *et al.* Superhard Monoborides: Hardness Enhancement through Alloying in W1−xTaxB. *Adv. Mater.* 6993–6998 (2016). doi:10.1002/adma.201601187

7. Yeung, M. T., Mohammadi, R. & Kaner, R. B. Ultraincompressible, Superhard Materials. *Annu. Rev. Mater. Res.* **46,** 465–485 (2016).

8. Wang, M., Li, Y., Cui, T., Ma, Y. & Zou, G. Origin of hardness in WB4 and its implications for ReB 4, TaB4, MoB4, TcB4, and OsB 4. *Appl. Phys. Lett.* **93,** 1–4 (2008).

9. Liang, Y., Gou, Y., Yuan, X., Zhong, Z. & Zhang, W. Unexpectedly hard and highly stable WB3 with a noncompact structure. *Chem. Phys. Lett.* **580,** 48–52 (2013).

10. Liang, Y., Yuan, X. & Zhang, W. Thermodynamic identification of tungsten borides.

Phys. Rev. B - Condens. Matter Mater. Phys. **83,** 2–5 (2011).

11. Gou, H., Li, Z., Wang, L. M., Lian, J. & Wang, Y. Peculiar structure and tensile strength of WB4: Nonstoichiometric origin. *AIP Adv.* **2,** (2012).

12. Albert, B. & Hillebrecht, H. Boron: Elementary challenge for experimenters and theoreticians. *Angew. Chemie - Int. Ed.* **48,** 8640–8668 (2009).

13. Samsonov, G. V. & Vinitskii, I. M. *Refractory compounds [in Russian]*. (Atomizdat, 1975).

14. Samsonov, G. V., Markovskii, L. Y., Zhigach, A. F. & Valyashko, M. G. *Boron, Its Compounds and Alloys [in Russian]*. (House of the Academy of the Sciences Ukrainian SSR, 1960).

15. Schmechel, R. & Werheit, H. Correlation between structural defects and electronic properties of icosahedral boron-rich solids. *J. Phys. Condens. Matter* **11,** 6803–6813 (1999).

16. Werheit, H. Present knowledge of electronic properties and charge transport of icosahedral boron-rich solids. *J. Phys. Conf. Ser.* **176,** (2009).

17. Werheit, H. *et al.* Raman scattering and isotopic phonon effects in dodecaborides. *J. Phys. Condens. Matter* **23,** (2011).

18. Werheit, H. Are there bipolarons in icosahedral boron-rich solids? *J. Phys. Condens. Matter* **19,** (2007).

19. Matthias, A. B. T. *et al.* Superconductivity and Antiferromagnetism in Boron-Rich Lattices Author(s): B. T. Matthias, T. H. Geballe, K. Andres, E. Corenzwit, G. W. Hull

and J. P. Maita Source: *Science (80-.).* **159,** 530 (1968).

20. La Placa, S., Binder, I. & Post, B. Binary dodecaborides. *J. Inorg. Nucl. Chem.* **18,** 113–117 (1961).

21. Matkovich, V. I., Economy, J., Giese, R. F. & Barrett, R. The structure of metallic dodecarborides. *Acta Crystallogr.* **19,** 1056–1058 (1965).

22. Lyutaya, M. D. & Akinina, Z. S. Chemical and Thermal Stability of Scandium Borides. *Inorg. Mater.* **1,** 1039–1043 (1965).

23. Bruskov, V. A. & Zavalii, L. V. Crystal Structure of ScB12. *Izv. Akad. Nauk SSSR, Neorg. Mater.* **24,** 506–507 (1988).

24. Renosto, S. T. *et al.* Superconductivity in the Th0.93Zr0.07B12 compound with UB12 prototype structure. *Phys. Lett. A* **379,** 2498–2501 (2015).

25. Paderno, Y. & Shitsevalova, N. Stabilization of cubic scandium dodecaboride. *J. Alloys Compd.* **219,** 119–123 (1995).

26. Hamada, K. *et al.* Phase transition in the Zr1-xScxB12 system. *Phys. Rev. B* **48,** 6892–6898 (1993).

27. Mar, R. W. & Stout, N. D. High Temperature Enthalpies of Binary Dodecaborides. *J. Chem. Phys.* **57,** 5342–5349 (1972).

28. Akopov, G., Yeung, M. T., Turner, C. L., Li, R. L. & Kaner, R. B. Stabilization of HfB12 in Y1−xHfxB12 under Ambient Pressure. *Inorg. Chem.* **55,** 5051–5055 (2016).

29. Cannon, J. F. & Farnsworth, P. B. High pressure syntheses of ThB12 and HfB12. *J. Less-*

Common Met. **92,** 359–368 (1983).

30. Odintsov, V. V. Hardness of metal dodecaborides of UB12 structure type [in Russian]. *Inorg. Chem. USSR* **10,** 366–367 (1974).

31. Portnoi, K. I., Romashov, V. M. & Burobina, L. N. Constitution diagram of the system Zirconium-Boron. *Sov. Powder Met. Met. Ceram.* **7,** 68–71 (1970).

32. Akopov, G., Yeung, M. T., Turner, C. L., Mohammadi, R. & Kaner, R. B. Extrinsic hardening of superhard tungsten tetraboride alloys with group 4 transition metals. *J. Am. Chem. Soc.* **138,** 5714–5721 (2016).

33. Paderno, Y. B. *et al.* Zirconium dodecaboride-based cutting material. *Powder Metall. Met. Ceram.* **43,** 546–548 (2004).

34. Lutterotti, L., Matthies, S., Wenk, H. R., Schultz, A. S. & Richardson, J. W. Combined texture and structure analysis of deformed limestone from time-of-flight neutron diffraction spectra. *J. Appl. Phys.* **81,** 594–600 (1997).

35. Lutterotti, L., Bortolotti, M., Ischia, G., Lonardelli, I. & Wenk, H. R. Rietveld texture analysis from diffraction images. *Zeitschrift fur Krist. Suppl.* **1,** 125–130 (2007).

36. Lutterotti, L., Chateigner, D., Ferrari, S. & Ricote, J. Texture, residual stress and structural analysis of thin films using a combined X-ray analysis. *Thin Solid Films* **450,** 34–41 (2004).

37. Lutterotti, L. Total pattern fitting for the combined size-strain-stress-texture determination in thin film diffraction. *Nucl. Instruments Methods Phys. Res. Sect. B Beam Interact. with Mater. Atoms* **268,** 334–340 (2010).

38. Lutterotti, L. Maud Rev. 2.55. *Maud Rev. 2.55, Univ. Trento-Italy, Dep. Ind. Eng. Trento, Italy* (2015).

39. Kittel, C. *Introduction to Solid State Physics*. (John Wiley & Sons, 2005).

40. Kuzenkova, M.A., Kislyi, P. S. Preparation of Zirconium diboride. *Powder Metall.* **12,** 966–969 (1965).

41. Slater, J. C. Atomic Radii in Crystals. *J. Chem. Phys.* **41,** 3199–3204 (1964).

42. Teatum, E., Waber, J., Gschneidner, K. *Compilation of calculated data useful in predicting metallurgical behavior of the elements in binary alloy systems*. (1960).

43. Richards, S. M. & Kaspar, J. S. The crystal structure of YB66. *Acta Crystallogr. Sect. B Struct. Crystallogr. Cryst. Chem.* **25,** 237–251 (1969).

44. Lundström, T. Borides: Solid-state Chemistry. in *Encyclopedia of Inorganic Chemistry* 481–494 (2006).

45. Callmer, B. A Single-Crystal Diffractometry Boron Investigation of Scandium in beta-rhombohedral boron. *J. Solid State Chem.* **23,** 391–398 (1978).

46. Carlsson, J. O. & Lundström, T. The solution hardening of β-rhombohedral boron. *J. Less-Common Met.* **22,** 317–320 (1970).

47. Mohammadi, R. *et al.* Enhancing the Hardness of Superhard Transition-Metal Borides: Molybdenum-Doped Tungsten Tetraboride. *Chem. Mater.* **28,** 632–637 (2016).

CHAPTER 3. AMBIENT PRESSURE SYNTHESIS OF HIGH PRESSURE MB_{12} PHASES: STABILIZATION OF HfB_{12} IN $Y_{1-x}Hf_xB_{12}$

ABSTRACT

Alloys of metal dodecaborides – YB_{12} with HfB_{12} – were prepared via arc-melting in order to stabilize the metastable HfB_{12} high-pressure phase under ambient pressure. Previously, HfB_{12} had only been synthesized under high-pressure (6.5 GPa). Powder X-ray diffraction (XRD) and energy-dispersive X-ray spectroscopy (EDS) were used to confirm the purity and phase composition of the prepared samples. The solubility limit for HfB_{12} in $Y_{1-x}Hf_xB_{12}$ (cubic UB_{12} structure type) was determined to be ~35 at.% Hf by XRD and EDS analysis. The value of the cubic unit cell parameter (*a*) changed from 7.505 Å (pure YB_{12}) to 7.454 Å across the solid solution range. Vicker's hardness increased from 40.9 ± 1.6 GPa for pure YB_{12} to 45.0 ± 1.9 GPa under an applied load of 0.49 N for the $Y_{1-x}Hf_xB_{12}$ solid solution composition with ~28 at.% Hf, suggesting both solid solution hardening and extrinsic hardening due to the formation of secondary phases of hafnium.

INTRODUCTION

Among the different types of borides, dodecaborides constitute a remarkable class of isotropic compounds that have so far only been studied for their electronic and magnetic properties.[1–7]

Several transition metals (*e.g.* Zr, Sc, Y), lanthanides (*e.g.* Lu, Tm, Er, Ho and Dy) and actinides (*e.g.* U) can form the dodecaboride phase.[8,9] Most dodecaborides have the cubic UB_{12} structure (space group Fm-3m), except scandium which adopts a tetragonal ScB_{12} lattice type (space group I4/mmm).[8] In the cubic UB_{12} structure of dodecaborides, the metal atoms form a face centered cubic lattice, each surrounded by a 24-atom cuboctahedron boron cage, with each boron atom being bonded to 5 other boron atoms and 2 metal atoms (Figure 3-1).[8,10] Each metal atom can be considered 12-coordinate, since the metal is equidistant from the center of 12 B-B bonds.

Due to their highly symmetrical structure, metal dodecaborides could potentially possess superior mechanical properties, such as superhardness (H_v > 40 GPa). Previous design rules for superhard metal borides (WB_4 and ReB_2)[11,12] have relied on a high valence density metal (for high incompressibility) and a high density of covalent bonds (to prevent slip). Metal dodecaborides exemplify these attributes; moreover, their high isotropy maximizes metal-boron bonding which possess increased electron-electron repulsions resulting in stiffer bonds. Since axes along metal-boron bonds can be comparable to or even stiffer than diamond,[13,14] the mechanical properties of metal dodecaborides could provide an excellent model to understand the role of metal-boron bonding in stiffness and incompressibility.

The main requirement for the formation of the metal dodecaboride phase is the narrow size range of the metal atom in a 12-coordinate environment. The metal must fit into the cuboctahedron boron cage, with the largest atom capable of doing so being yttrium (r_{at} = 1.80 Å, $r_{CN = 12}$ = 1.801 Å)[8,15] and the smallest being zirconium (r_{at} = 1.55 Å, $r_{CN = 12}$ = 1.603 Å).[8,15] Although hafnium has virtually the same atomic radius as zirconium (1.55 Å for both) due to the lanthanide contraction, this size will differ depending on the coordination environment. In a 12-coordination structure, hafnium has a metallic radius of 1.580 Å, which is below the lower metal size threshold capable of

accommodating a boron cuboctahedron cage.[10] This narrow range in metallic radii is reflected in the unit cell: the lattice parameters for metal dodecaborides generally fit between 7.4 Å < *a* < 7.5 Å (*e.g.* a_{ZrB12} = 7.408 Å, a_{UB12} = 7.473 Å, a_{YB12} = 7.500 Å).[10]

HfB_{12} was previously made by Cannon and Farnsworth using high pressure (6.5 GPa), as a minor product in the synthesis of HfB_2.[10] The high pressure synthesis of HfB_{12} uses the difference in incompressibility between hafnium metal and the boron network: under applied pressure the boron cage size is reduced and the apparent size of the metal atom is increased, thus allowing the formation of the HfB_{12} phase. In this way, the "apparent" lattice parameters will fit within the narrow size range. Attempts to synthesize HfB_{12} at ambient pressure have proved unsuccessful.[10,16] Here, we report the stabilization of the HfB_{12} phase in systems with ZrB_{12}, ScB_{12} and YB_{12}. The three metal dodecaborides explored in this study are: Zr (1.55 Å),[15] the smallest transition metal capable of forming such a phase, Sc (1.65 Å),[15] an intermediate-sized transition metal, and Y (1.80 Å),[15] the largest transition metal capable of forming a dodecaboride.

EXPERIMENTAL PROCEDURE

The synthesis of $Zr_{1-x}Hf_xB_{12}$, $Sc_{1-x}Hf_xB_{12}$ and $Y_{1-x}Hf_xB_{12}$ (x = 0.00, 0.05, 0.25, 0.50, 0.75, 0.95) alloys were carried out using high-purity metal and boron powders: amorphous boron (99+%, Strem Chemicals, U.S.A.), zirconium (99.5%, Strem Chemicals, U.S.A.), hafnium (99.8%, Materion, U.S.A.), scandium (99.9%, Sigma-Aldrich, U.S.A.) and yttrium (99.9%, Strem Chemicals, U.S.A.). The metals and boron were kept at a minimum 1:20 molar ratio in order to prevent the formation of lower boride phases. The weighed mixtures of powders were homogenized in an agate mortar and pestle and pressed into pellets using an applied load of 10

tons on a hydraulic press (Carver). The samples were prepared through arc-melting ($I \geq 70$ amps, t = 1-2 mins) under an ultra-high purity argon atmosphere.

The samples synthesized in the arc-melter were cut into two equal parts on a diamond saw (Ameritool Inc., U.S.A.). One part was used for powder X-ray diffraction (PXRD) analysis and therefore was crushed into a -325 mesh ($\leq$ 45 μm) powder using a tool steel Plattner-style diamond crusher. The other part of the cut sample was used for energy-dispersive X-ray spectroscopy (EDS) analysis and Vicker's hardness measurements. Each sample was put into an epoxy capsule utilizing an epoxy/hardener set (Allied High Tech Products Inc., U.S.A.). An optically flat surface was achieved on a semi-automated polisher (South Bay Technology Inc., U.S.A.), using the following abrasives: SiC discs of 120 - 1200 grit sizes (Allied High Tech Products Inc., U.S.A.) and 30 - 1 micron particle diamond films (South Bay Technology Inc., U.S.A.).

Powder X-ray diffraction (XRD) was performed on a Bruker D8 Discover Powder X-ray Diffractometer (Bruker Corporation, Germany) utilizing a Cu Kα X-ray beam (λ = 1.5418 Å) in the 5-100° 2θ range with a scan speed of 0.1055°/sec, time per step of 0.3 sec and step size of 0.0353°. The Joint Committee on Powder Diffraction Standards (JCPDS) database was used to determine the phases present in the powder X-ray diffraction data. The composition and purity analysis of the optically flat samples were performed on an UltraDry EDS detector (Thermo Scientific, U.S.A.) attached to a FEI Nova 230 high-resolution scanning electron microscope (FEI Company, U.S.A.). The cell parameters were determined with Rietveld using *Maud* software.[17–21]

Polished samples were further subject to Vicker's hardness measurements on a MicroMet 2103 Vickers microhardness tester (Buehler Ltd, U.S.A.) with a pyramidal diamond indenter tip. 15 indents were made using 0.49, 0.98, 1.96, 2.94 and 4.9 N of force load each, from low to high

respectively, and were performed in random areas of the sample. Then, using a high resolution optical microscope (Zeiss Axiotech 100HD, Carl Zeiss Vision GmbH, Germany) with 500x magnification, the length of the diagonals of each indent was determined. Vicker's hardness was calculated using Equation 3.1:

$$H_v = \frac{1854.4F}{a^2} \quad (3.1)$$

where F is the loading force applied in Newtons (N) and a is the average of the length of the two diagonals of each indent in micrometers.

RESULTS AND DISCUSSION

Powder X-ray diffraction (XRD) and energy-dispersive X-ray spectroscopy (EDS) analysis were performed in order to determine the purity and phase composition of the samples. Figure 3-2 shows the XRD data for the alloy $Y_{1-x}Hf_xB_{12}$ (a_{YB12} = 7.505 Å). Stabilization of HfB_{12} in the $Sc_{1-x}Hf_xB_{12}$ (a_{ScB12} = 7.383 Å) or $Zr_{1-x}Hf_xB_{12}$ (a_{ZrB12} = 7.412 Å) systems proved to be unsuccessful (see the powder XRD, Figure 3-3), suggesting that unit cell size plays a critical role in the stabilization process. Data from EDS and hardness measurements of $Y_{1-x}Hf_xB_{12}$ are discussed later in this section.

The spectra of the alloy of Hf and YB_{12} ($Y_{1-x}Hf_xB_{12}$, where x = 0.00, 0.05, 0.25, 0.50, 0.75 and 0.95) are presented in Figure 3-2. The solubility limit of Hf in YB_{12} is below 75 at.% Hf. Above 50 at.% Hf peaks corresponding to HfB_{50}, known as the β-rhombohedral boron doping phase of hafnium (JCPDS 01-086-2400), can be observed. At 75 at.% Hf, a secondary phase of hafnium, HfB_2 (JCPDS 01-089-3651) appears. The calculated cell parameters, as well as dodecaboride phase metal composition data are presented in Table 3-1.

After the phase purity of the samples was confirmed, Vicker's hardness testing (under loads of 0.49 to 4.9 N) was perfomed and the results are shown in Figure 3-4. All compositions of $Y_{1-x}Hf_xB_{12}$ (x = 0.05 – 0.75) are superhard ($H_v \geq 40$ GPa) under a load of 0.49 N; this can be attributed to the high covalent bond density found in the dodecaborides.

For the $Y_{1-x}Hf_xB_{12}$ alloy at the nominal concentration of 50 at.% Hf, the hardness increased to 45.0 ± 1.9 GPa under an applied load of 0.49 N, compared to 40.9 ± 1.6 GPa for pure YB_{12}.[22] The increase in hardness could potentially be attributed to solid solution hardening as the limit of solubility has been reached. In solid solutions, by substituting atoms of various sizes, localized strain is generated which pins the propagation of discolations. The decrease in hardness at 75 at.% Hf can be attributed to the formation of an AlB_2-type HfB_2 structure due to excess hafnium in the sample. As an AlB_2-type structure, HfB_2 posseses layers that are prone to slipping, resulting in a softer composite. However, it should be noted that $Hf_{0.75}Y_{0.25}B_{12}$ is still harder than pure YB_{12}. This may be due to the additional presence of a boron doping phase of hafnium and YB_{66} which have a hardness of ~40 GPa at 0.49 N, an increase of 6 GPa over the hardness of crystalline β-rhombohedral boron (34.2 GPa at 0.49 N).[16,23–25]

Elemental maps and an SEM image of a sample of the $Y_{0.75}Hf_{0.25}B_{12}$ alloy are presented in Figure 3-5. The presence of both hafnium and yttrium can be seen in the dodecaboride phases, while the boron rich areas correspond to the cubic YB_{66} phase (cubic, Fm-3c structure, a = 23.44 Å, Inorganic Crystal Structure Database, ICSD #23186).

Cell refinements were performed using *Maud* software.[17–20] The cubic cell parameter (a) changed from 7.505 Å for pure YB_{12} to 7.454 Å for $Y_{0.05}Hf_{0.95}B_{12}$ (compared to 7.377 Å for pure HfB_{12} synthesized under high pressure).[10] This decrease in cell parameter suggests that a solid solution

between HfB_{12} and YB_{12} has formed at least until the solubility limit of Hf in YB_{12} is reached. The composition of the dodecaboride phase was determined by both back-calculation from XRD cell refinement using Vegard's Law[26] and EDS analysis; the results are summarized in Table 3-1. Both methods produce values that are in good agreement and suggest that the maximum solubility of Hf in YB_{12} is ~35 at.% Hf, with excess hafnium doping β-rhombohedral boron to form HfB_{50}, and then producing HfB_2 with a further increase in the concentration of hafnium (Figure 3-2).

Surprisingly, further confirmation that an intimate solid-solution has formed can be found directly upon visual inspection. All dodecaborides exhibit a color, ranging from light blue for YB_{12} and ScB_{12} to violet for ZrB_{12}. The color is due to charge-transfer between the metal atoms and the cuboctahedron boron-cage network.[3,4] Figure 3-6 shows the change in color of the dodecaboride phase on going from pure YB_{12} (light-blue) to $Y_{0.25}Hf_{0.75}B_{12}$ (blue-violet). The color change is similar to the change observed in the $Zr_{1-x}Y_xB_{12}$ system,[27] suggesting that pure HfB_{12} is violet, analogous to ZrB_{12}.

Figure 3-7 (top) shows a plot of refined cell data from XRD for samples of $Y_{1-x}Hf_xB_{12}$ (x = 0.00, 0.05, 0.25, 0.50, 0.75 and 0.95) and cell data calculated from Vegard's Law versus nominal composition. Figure 3-7 (bottom) shows a plot of refined cell data from XRD for samples of $Y_{1-x}Hf_xB_{12}$ and data caclulated from Vegard's Law versus the dodecaboride phase composition from EDS analysis up to the Hf solubility limit in $YHfB_{12}$. The graph shows an excellent correlation of the cell parameters up to the solubility limit for hafnium in YB_{12} (~35 at.% Hf).

CONCLUSIONS

The high-pressure cubic HfB_{12} dodecaboride phase was successfully stabilized in the $Y_{1-x}Hf_xB_{12}$ system (a_{YB12} = 7.505 Å) under ambient pressure. The maximum solubility of hafnium in $Y_{1-x}Hf_xB_{12}$

was determined to be ~35 at.% Hf based on energy dispersive X-ray spectroscopy and unit cell refinement using powder X-ray diffraction. HfB_{12} could not be stabilized in either the $Sc_{1-x}Hf_xB_{12}$ (a_{ScB12} = 7.383 Å) or $Zr_{1-x}Hf_xB_{12}$ (a_{ZrB12} = 7.412 Å) alloy systems, suggesting that unit cell size plays a central role in the stabilization process. The alloy system $Y_{1-x}Hf_xB_{12}$ showed characteristics of a solid solution between HfB_{12} and YB_{12} as the cubic unit cell parameter (*a*) changed from 7.505 Å for pure YB_{12} to 7.454 Å across the solid solution range (compared to 7.377 Å for pure HfB_{12}).[10] $Y_{1-x}Hf_xB_{12}$ solid solutions exhibit the color change expected for the dodecaboride phase going from pure YB_{12} (light-blue) to $Y_{0.25}Hf_{0.75}B_{12}$ (blue-violet). Finally, the Vicker's hardness values of $Y_{1-x}Hf_xB_{12}$ alloys were measured under an applied load of 0.49 N. The hardness increased from 40.9 ± 1.6 GPa for pure YB_{12} to 45.0 ± 1.9 GPa with ~28 at.% Hf.[22] The increase in hardness can be attributed to the solid solution hardening as the limit of solubility is reached in addition to the formation of HfB_{50}, the β-rhombohedral boron doping phase of hafnium (H_v ~ 40 GPa at 0.49 N) due to excess hafnium in the sample.[16,23,24]

ACKNOWLEDGEMENTS

We thank the National Science Foundation Division of Materials Research, Grant DMR-1506860 (R.B.K.) and the National Science Foundation DGE-0654431 Fellowship program (M.T.Y.) for financial support. We also thank Professor Benjamin M. Wu of the UCLA Department of Bioengineering for the use of his micro-indentation system, and Professor Sarah Tolbert for helpful discussions.

Table 3-1. Compositions[a] and Unit Cell Data[b] for $Y_{1-x}Hf_xB_{12}$[c]

Compound	at.% Hf (nominal composition)	a, Å	at.% Hf (XRD)	Vegard's Law	at.% Hf (EDS)	Vegard's Law (EDS)
YB_{12}	0.00	7.505	0.00	7.505	0.00	7.505
$Y_{0.95}Hf_{0.05}B_{12}$	5.00	7.502	2.34	7.499	2.75	7.501
$Y_{0.75}Hf_{0.25}B_{12}$	25.00	7.483	17.19	7.473	12.18	7.489
$Y_{0.50}Hf_{0.50}B_{12}$	50.00	7.464	32.03	7.441	27.66	7.470
$Y_{0.25}Hf_{0.75}B_{12}$	75.00	7.458	36.72	7.409	33.01	7.463
$Y_{0.05}Hf_{0.95}B_{12}$	95.00	7.454	-	7.383	-	-
HfB_{12}[10]	100.0	7.377[10]	100.0	7.377[10]	-	-

[a]calculated from XRD data using Vegard's Law[26] and from EDS analysis
[b]from *Maud*[17–20]
[c]x = 0.00, 0.05, 0.25, 0.50, 0.75 and 0.95

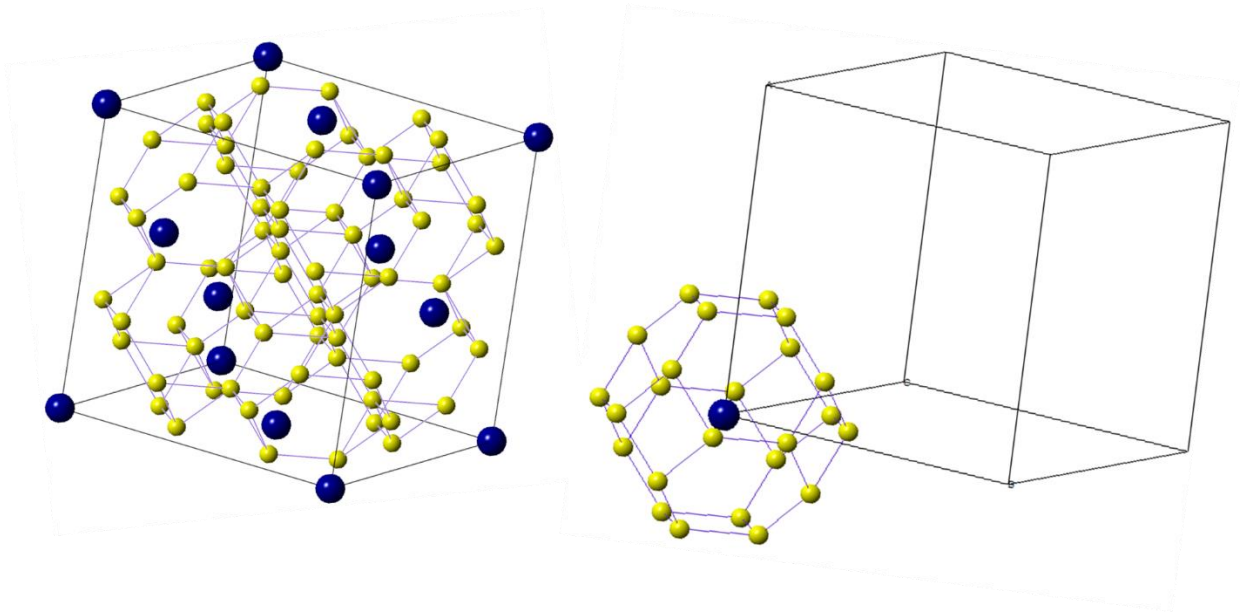

Figure 3-1. (Left) The unit cell of the cubic MB_{12} dodecaboride structure type: metal atoms are in blue, B atoms in yellow, (right) cuboctahedron boron cage surrounding a single 12-coordinate metal atom, the metal atoms occupy all face centered positions in the cubic cell. Note, while 24 borons surround each metal atom, it is equidistant from 12 B-B bonds, making it 12-coordinate.

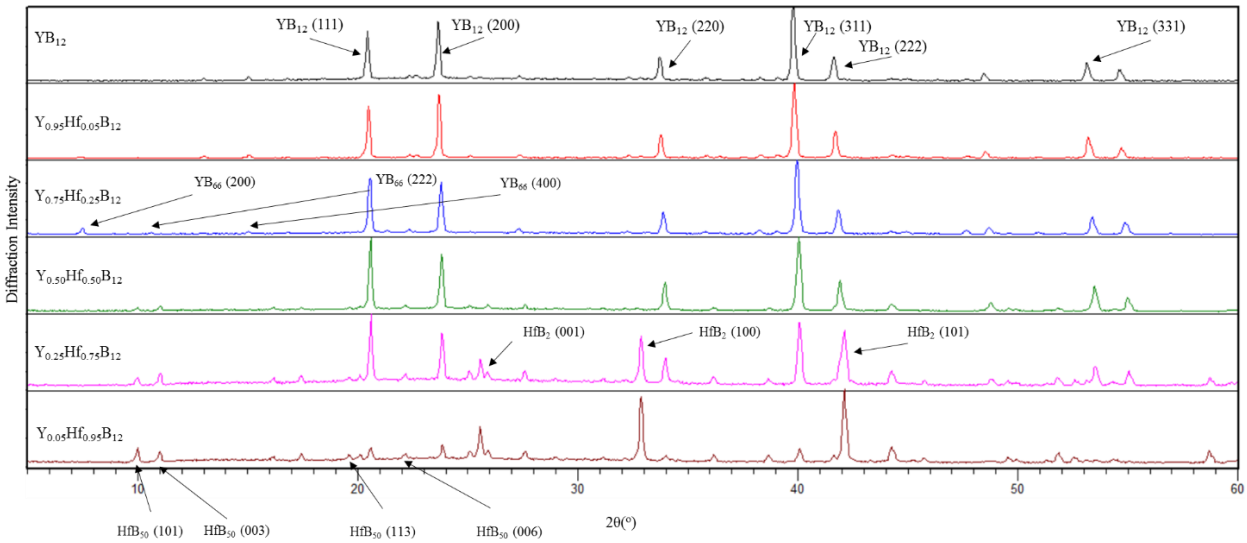

Figure 3-2. Powder XRD patterns of $Y_{1-x}Hf_xB_{12}$, where x = 0.00, 0.05, 0.25, 0.50, 0.75 and 0.95. The solubility limit of Hf in YB_{12} is below 50 at.% Hf (nominal composition). At 50 at.% Hf, peaks corresponding to HfB_{50} (β-rhombohedral boron doping phase of hafnium, JCPDS 01-086-2400) can be observed. At 75 at.% Hf, a secondary phase of HfB_2 (JCPDS 01-089-3651) appears.

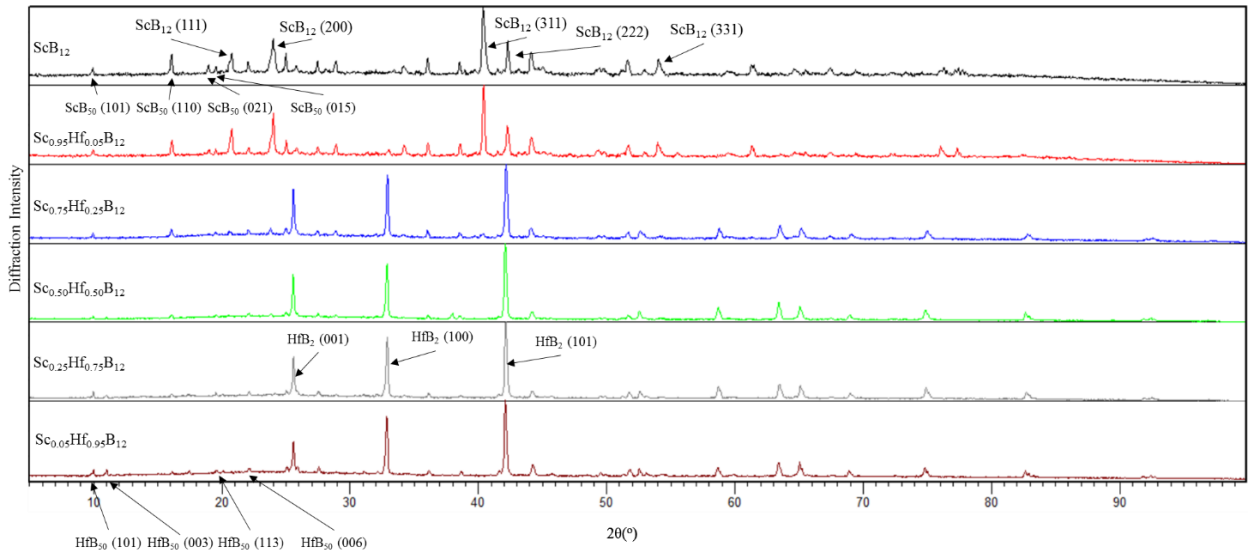

(a)

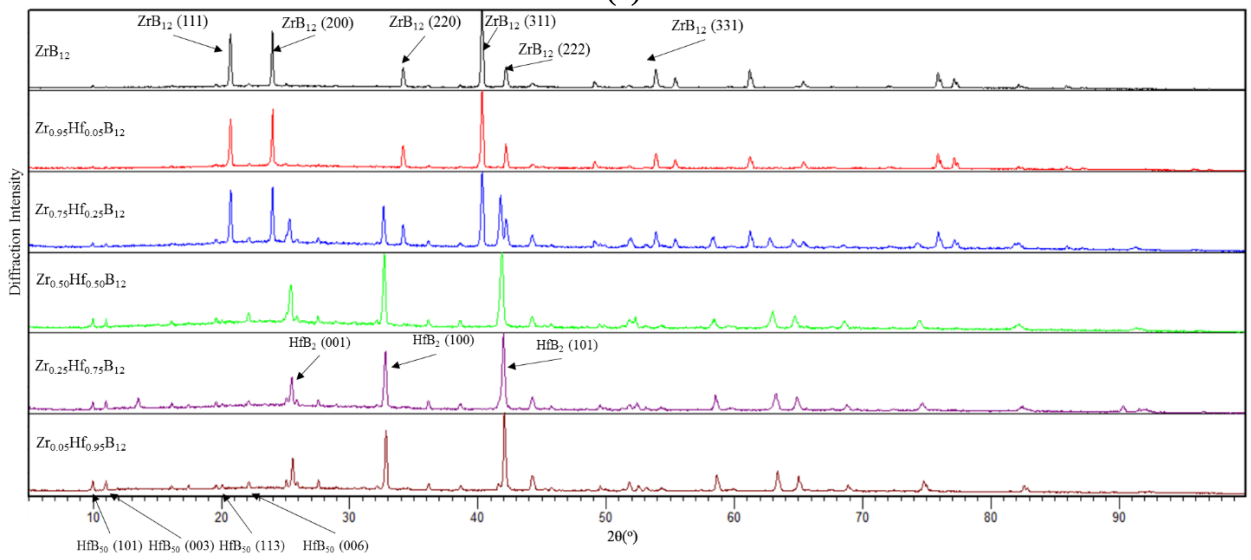

(b)

Figure 3-3. Powder XRD patterns of alloys of (a) $Sc_{1-x}Hf_xB_{12}$ and (b) $Zr_{1-x}Hf_xB_{12}$, where x = 0.00, 0.05, 0.25, 0.50, 0.75 and 0.95. For (a) peaks corresponding to a dodecaboride phase disappear at 25 at.%Hf (nominal composition), with the major phase being HfB_2 (JCPDS 01-089-3651); for (b) peaks corresponding to a dodecaboride phase disappear at 50 at.%Hf (nominal composition), with the major phase being HfB_2 (JCPDS 01-089-3651).

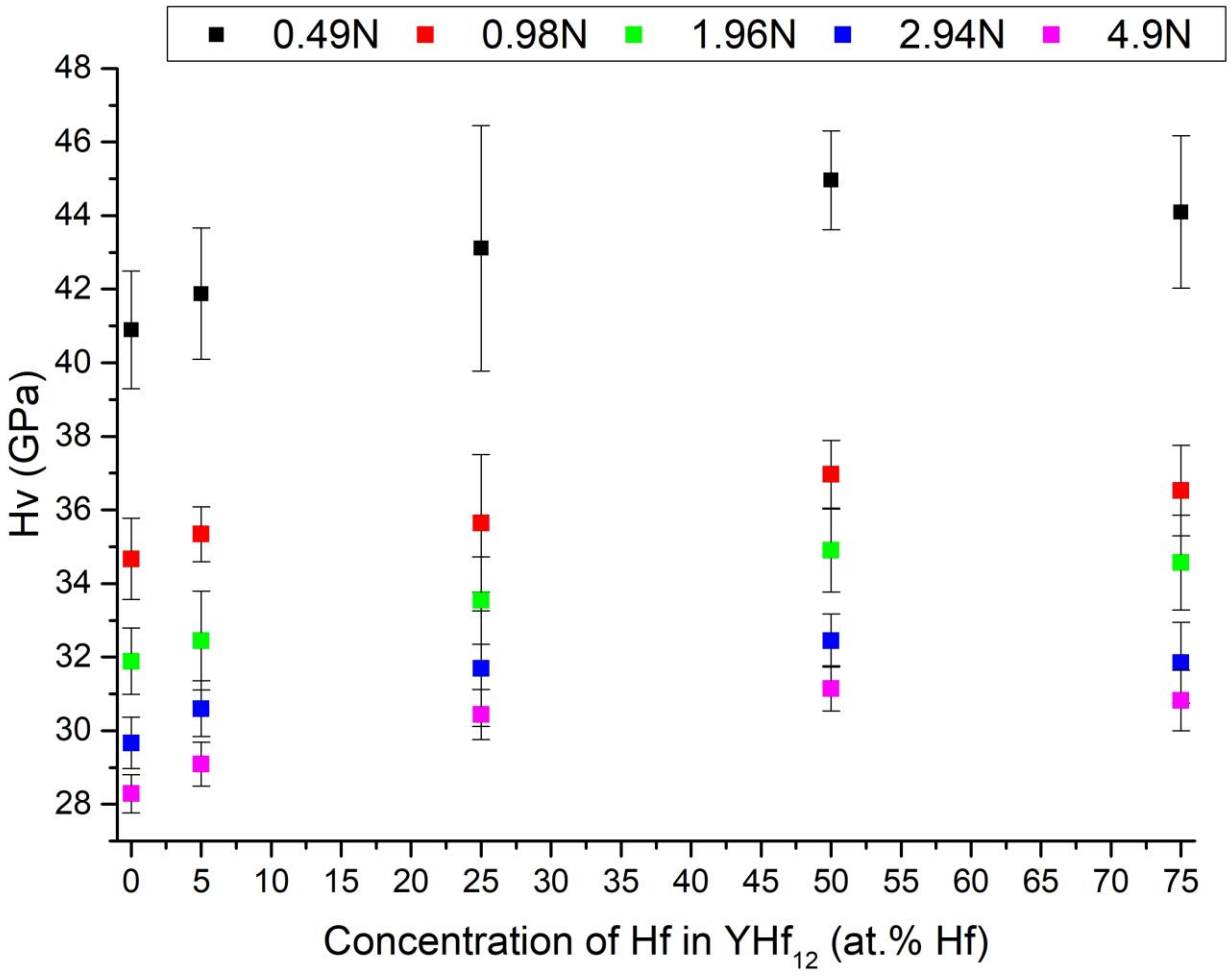

Figure 3-4. Vickers microindentation hardness (H_v) of $Y_{1-x}Hf_xB_{12}$ (x = 0.00, 0.05, 0.25, 0.50 and 0.75) with loads varying from 0.49 (low load) to 4.9 N (high load).

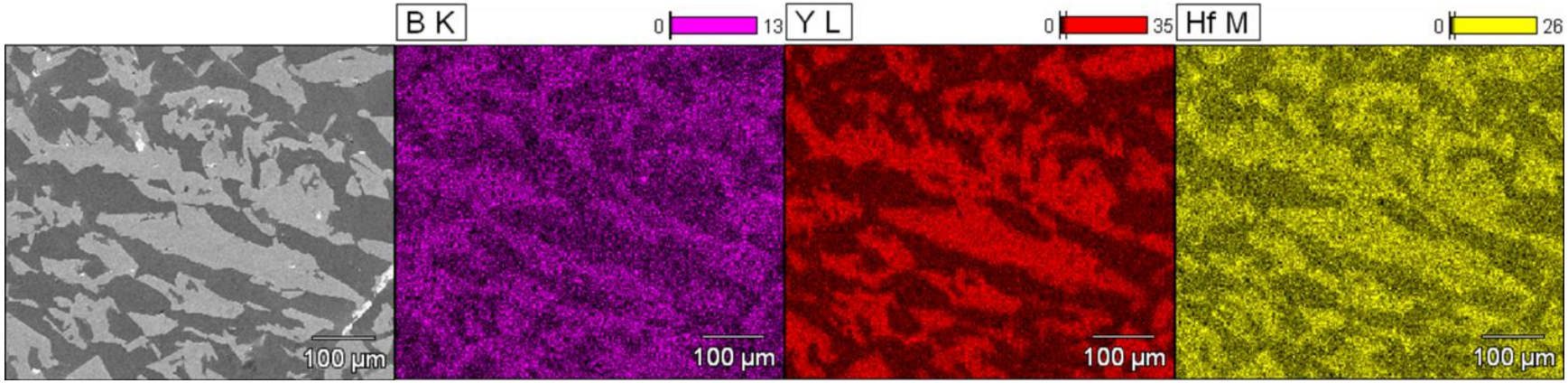

Figure 3-5. SEM images and elemental maps for boron (K line), yttrium (L line) and hafnium (M line) for the $Y_{0.75}Hf_{0.25}B_{12}$ solid solution showing the presence of yttrium and hafnium in the dodecaboride phase. The boron rich areas correspond to YB_{66} (cubic, $Fm\bar{3}c$ structure, a = 23.44 Å, ICSD 23186). The thick horizontal bars represent the intensity as a color legend.

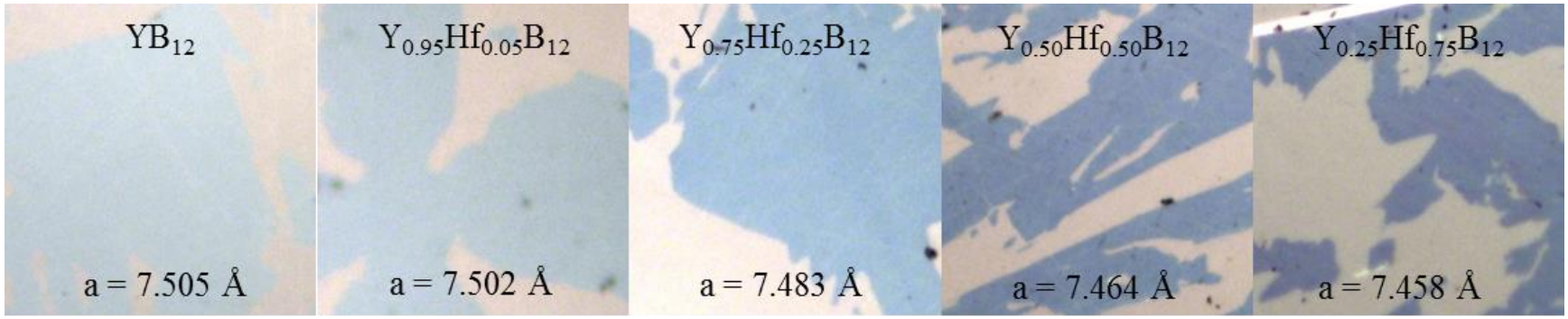

Figure 3-6. A color change of the dodecaboride phase can be directly observed using a light microscope going from pure YB_{12} (light-blue) to $Y_{0.25}Hf_{0.75}B_{12}$ (blue-violet) phase. The color change is similar to the change observed in the $Zr_{1-x}Y_xB_{12}$ system, suggesting that pure HfB_{12} is violet in color similar to ZrB_{12}. The white area in the $Y_{0.25}Hf_{0.75}B_{12}$ sample is HfB_2.

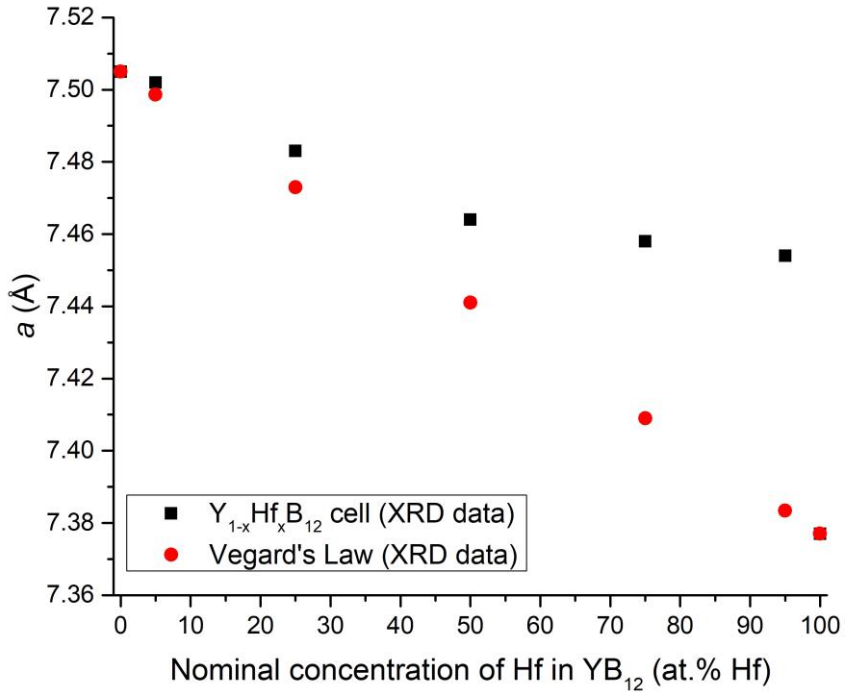

(a)

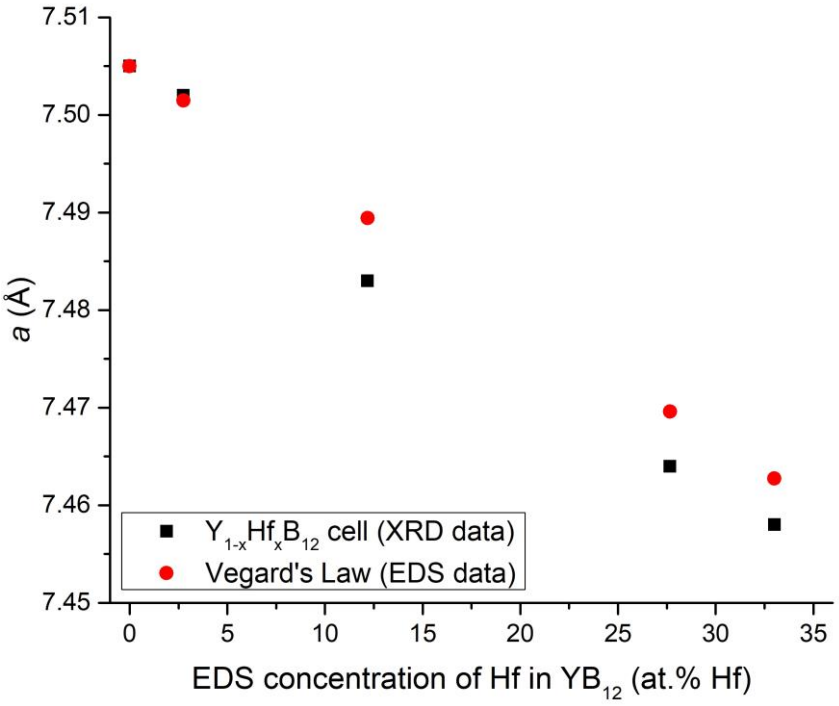

(b)

Figure 3-7. (a) Plot of refined cell data from XRD for samples of $Y_{1-x}Hf_xB_{12}$ (x = 0.00, 0.05, 0.25, 0.50, 0.75 and 0.95) and cell data calculated from Vegard's Law versus nominal composition; (b) plot of refined cell data for samples of $Y_{1-x}Hf_xB_{12}$ and data calculated from Vegard's Law versus composition of the dodecaboride phase, determined from EDS analysis up to the Hf solubility limit in $YHfB_{12}$.

REFERENCES

1. Samsonov, G. V. & Vinitskii, I. M. *Refractory compounds [in Russian]*. (Atomizdat, 1975).

2. Schmechel, R. & Werheit, H. Correlation between structural defects and electronic properties of icosahedral boron-rich solids. *J. Phys. Condens. Matter* **11,** 6803–6813 (1999).

3. Werheit, H. *et al.* Raman scattering and isotopic phonon effects in dodecaborides. *J. Phys. Condens. Matter* **23,** (2011).

4. Werheit, H. Present knowledge of electronic properties and charge transport of icosahedral boron-rich solids. *J. Phys. Conf. Ser.* **176,** (2009).

5. Werheit, H. Are there bipolarons in icosahedral boron-rich solids? *J. Phys. Condens. Matter* **19,** (2007).

6. Matthias, A. B. T. *et al.* Superconductivity and Antiferromagnetism in Boron-Rich Lattices Author(s): B. T. Matthias, T. H. Geballe, K. Andres, E. Corenzwit, G. W. Hull and J. P. Maita Source: *Science (80-.).* **159,** 530 (1968).

7. Samsonov, G. V., Markovskii, L. Y., Zhigach, A. F. & Valyashko, M. G. *Boron, Its Compounds and Alloys [in Russian]*. (House of the Academy of the Sciences Ukrainian SSR, 1960).

8. La Placa, S., Binder, I. & Post, B. Binary dodecaborides. *J. Inorg. Nucl. Chem.* **18,** 113–117 (1961).

9. Matkovich, V. I., Economy, J., Giese, R. F. & Barrett, R. The structure of metallic

dodecarborides. *Acta Crystallogr.* **19,** 1056–1058 (1965).

10. Cannon, J. F. & Farnsworth, P. B. High pressure syntheses of ThB12 and HfB12. *J. Less-Common Met.* **92,** 359–368 (1983).

11. Mohammadi, R. *et al.* Toward inexpensive superhard materials: Tungsten tetraboride-based solid solutions. *J. Am. Chem. Soc.* **134,** 20660–20668 (2012).

12. Chung, H.-Y. *et al.* Synthesis of Ultra-Incompressible Superhard Rhenium Diboride at Ambient Pressure. *Science (80-.).* **316,** 436–439 (2007).

13. Mohammadi, R. *et al.* Tungsten tetraboride, an inexpensive superhard material. *Proc. Natl. Acad. Sci. U. S. A.* **108,** 10958–10962 (2011).

14. Cumberland, R. W. *et al.* Osmium diboride, an ultra-incompressible, hard material. *J. Am. Chem. Soc.* **127,** 7264–7265 (2005).

15. Slater, J. C. Atomic Radii in Crystals. *J. Chem. Phys.* **41,** 3199–3204 (1964).

16. Portnoi, K. I., Romashov, V. M., Romanovich, I. V., Levinskii, Y. V. & Prokof'ev, S. A. Phase diagram of the system Hf-B. *Inorg. Mater.* **7,** 1769–1772 (1971).

17. Lutterotti, L., Matthies, S., Wenk, H. R., Schultz, A. S. & Richardson, J. W. Combined texture and structure analysis of deformed limestone from time-of-flight neutron diffraction spectra. *J. Appl. Phys.* **81,** 594–600 (1997).

18. Lutterotti, L., Chateigner, D., Ferrari, S. & Ricote, J. Texture, residual stress and structural analysis of thin films using a combined X-ray analysis. *Thin Solid Films* **450,** 34–41 (2004).

19. Lutterotti, L., Bortolotti, M., Ischia, G., Lonardelli, I. & Wenk, H. R. Rietveld texture analysis from diffraction images. *Zeitschrift fur Krist. Suppl.* **1,** 125–130 (2007).

20. Lutterotti, L. Total pattern fitting for the combined size-strain-stress-texture determination in thin film diffraction. *Nucl. Instruments Methods Phys. Res. Sect. B Beam Interact. with Mater. Atoms* **268,** 334–340 (2010).

21. Lutterotti, L. Maud Rev. 2.55. *Maud Rev. 2.55, Univ. Trento-Italy, Dep. Ind. Eng. Trento, Italy* (2015).

22. Odintsov, V. V. Hardness of metal dodecaborides of UB12 structure type [in Russian]. *Inorg. Chem. USSR* **10,** 366–367 (1974).

23. Carlsson, J. O. & Lundström, T. The solution hardening of β-rhombohedral boron. *J. Less-Common Met.* **22,** 317–320 (1970).

24. Andersson, S. & Lundström, T. The solubility of chromium in β-rhombohedral boron as determined in CrB_{41} by single-crystal diffractometry. *J. Solid State Chem.* **2,** 603–611 (1970).

25. Spear, K.E., Solovyov, G. I. High Boron Content Rare-Earth Borides. in *Solid State Chemistry: Proceedings, Volume 13* (ed. Roth, R. S.) 597 (Institute of Materials Research National Bureau of Standards, 1972).

26. Vegard, L. Die Konstitution der Mischkristalle und die Raumfullung der Atome. *Zeitschrift fur Phys.* **5,** 17–26 (1921).

27. Mar, R. W. & Stout, N. D. High Temperature Enthalpies of Binary Dodecaborides. *J. Chem. Phys.* **57,** 5342–5349 (1972).

CHAPTER 4. STABILIZATION OF LnB_{12} (Ln = Gd, Sm, Nd AND Pr) IN $Zr_{1-X}Ln_XB_{12}$ UNDER AMBIENT PRESSURE

"Reprinted (adapted) with permission from (Akopov, G.; Sobell, Z.C.; Yeung, M. T.; Kaner, R. B. "Stabilization of LnB_{12} (Ln = Gd, Sm, Nd, and Pr) in $Zr_{1-x}Ln_xB_{12}$ under Ambient Pressure" *Inorg. Chem.* 2016, 55 (23), 12419-12426 DOI: 10.1021/acs.inorgchem.6b02311). Copyright (2016) American Chemical Society."

ABSTRACT

We report ambient pressure stabilization of a previously synthesized high-pressure (6.5 GPa) phase, GdB_{12}, in a $Zr_{1-x}Gd_xB_{12}$ solid solution (with ~54 at. % Gd solubility, as determined by both powder X-ray diffraction and energy-dispersive spectroscopy). Limited solubilities of Sm (~15 at. % Sm), Nd (~7 at. % Nd) and Pr (~4 at. % Pr) in ZrB_{12} were also achieved. Previous attempts at preparing these rare-earth borides were unsuccessful even under high pressure. Based on insights provided from the unit cell sizes observed via solid solutions, at least 6.5 GPa of pressure would be needed to synthesize these rare-earth borides since Sm, Nd and Pr atomic radii are larger than that of Gd. The solid-solution formation for $Zr_{1-x}Gd_xB_{12}$ and $Zr_{1-x}Sm_xB_{12}$ can be seen in the change of the unit cell of each of the solid solutions relative to their pure parent compounds as well as in the change of color of the respective alloys. For $Zr_{0.45}Gd_{0.55}B_{12}$ and $Zr_{0.70}Sm_{0.30}B_{12}$, the cubic unit cell parameter (*a*) reached a value of 7.453 Å and 7.428 Å, respectively, compared to 7.412 Å for pure ZrB_{12}.

INTRODUCTION

Boride chemistry is rich, with many transition metals and main group elements capable to forming a range of boron compounds with stoichiometries ranging from sub-borides (M_4B, M_2B)[1] to mono- (MB),[2,3] di- (MB_2),[4–6] tetra- (MB_4),[7–10] hexa- (MB_6),[11–15] dodeca- (MB_{12})[16–18] and hectoborides

(MB_{66}).[19–21] As the boron bonds in these compounds pervade the crystal lattice, the mechanical properties are wholly dependent on the arrangement of boron.

The structure of metal dodecaborides can be described as a 3D network of edge-sharing 24 boron atoms with metal-encapsulating boron cuboctahedra arranged in a FCC (face-centered cubic-UB_{12} structure, $Fm\bar{3}m$) or a BCT (body-centered tetragonal-ScB_{12}, *I4/mmm*) lattice (Figure 4-1).[16] Many metals can form stable dodecaboride phases: transition metals (Sc, Zr and Y), lanthanides (Tb, Dy, Ho, Er, Tm, Yb and Lu) and actinides (U, Pu, Np).[16,18] While the majority of dodecaborides exhibit the cubic-UB_{12} structure, only scandium possesses its own tetragonal-ScB_{12} structural type.[16] Metal dodecaborides and their solid solutions have been studied for their excellent mechanical, thermal, electronic, and magnetic properties.[17,19,20,22–29]

The size of a metal atom in a 12-coordinate environment places limitations on which atoms can fit inside a boron cuboctahedral environment and form a metal dodecaboride. All metal dodecaborides, stable under ambient pressure, have metal atoms with sizes intermediate between zirconium (r_{at} = 1.55 Å, $r_{CN=12}$ = 1.603 Å)[16,30] and yttrium (r_{at} = 1.80 Å, $r_{CN=12}$ = 1.801 Å)[16,30], the smallest and largest metal atoms, respectively, capable of forming a stable transition metal dodecaboride. Therefore, this size requirement results in the stable dodecaboride lattice parameter lying between 7.408 Å (ZrB_{12})[31] and 7.500 Å (YB_{12}).[31]

Dodecaborides where the metal cation lies outside the range of stability (HfB_{12}, GdB_{12} and ThB_{12}) requires pressures upwards of 6.5 GPa.[31,32] These phases have metal atoms either smaller than zirconium (Hf, r_{at} = 1.55 Å, $r_{CN=12}$ = 1.580Å)[16,30] and thus incapable of accommodating the boron cuboctahedron cage, or larger that yttrium, resulting in a unit cell far exceeding the size of the YB_{12} cell (a = 7.524 Å for GdB_{12} and a = 7.612 Å for ThB_{12}).[31,32] The broad applicability of high-pressure synthesis for dodecaborides of all sizes comes from differences in incompressibility

between the metal atom and the boron network. For HfB_{12}, hafnium is more incompressible than the boron network; thus, the boron network shrinks in size under applied pressure, increasing the effective size of the hafnium atom.[31] For GdB_{12} and ThB_{12} the effect is reversed, with the effective size of the metal atom shrinking due to the increased compressibility of gadolinium and thorium atoms when compared to the boron network.[31]

Stabilization of high-pressure phases under ambient pressure gives the opportunity to study the properties of such unstable phases without the need for difficult synthesis conditions. So far two high-pressure dodecaboride phases have been stabilized in a solid solution with another stable metal dodecaboride: ThB_{12} was stabilized in the $ZrThB_{12}$ matrix[33], while HfB_{12} was stabilized in the $YHfB_{12}$ matrix.[34] The rules for stabilization are that a "smaller" atom size and unit cell dodecaboride can stabilize a "larger" one, e.g. $ZrThB_{12}$, and the converse, $YHfB_{12}$.

Here, we report the stabilization of the high-pressure phase of GdB_{12} in a matrix of ZrB_{12}, with a solubility of Gd in ZrB_{12} reaching ~54 at.% Gd, along with select properties. In addition, we report the stabilizations with limited solubilities (below 15%) of previously un-synthesized SmB_{12}, NdB_{12} and PrB_{12} in ZrB_{12} matrices, demonstrating a decrease in solubility with increasing size of the secondary metal.

EXPERIMENTAL PROCEDURE

Pellets of $Zr_{1-x}Gd_xB_{12}$, $Zr_{1-x}Sm_xB_{12}$, $Zr_{1-x}Pr_xB_{12}$, and $Zr_{1-x}Nd_xB_{12}$ (x = 0.05, 0.25, 0.50, 0.75 and 0.95) were prepared using high-purity metal and boron powders: amorphous boron (99+%, Strem Chemicals, USA), gadolinium (99%, Sigma-Aldrich, USA), zirconium (99.5%, Strem Chemicals, USA), samarium (Strem Chemicals, 99.9%), praseodymium (99.9%, Strem Chemicals, USA), and neodymium (99.8%, Strem Chemicals, USA). The metal to boron ratio was kept at a minimum of 1:20 to prevent the formation of lower borides (MB_6) as they are the ambient pressure most stable

boride phases of Gd, Sm, Nd, and Pr. The weighed mixtures were homogenized in vials in a vortex mixer for ~1 minute, then consolidated in a hydraulic press (Carver) under ~10 tons before being arc melted (I > 70 amps, T = 1 - 2 min) under a high purity argon atmosphere.

The resultant pellets were broken into 2 - 4 pieces by gently tapping using a tool steel Plattner-style diamond crusher. Half of the pieces were crushed using the aforementioned tool steel Plattner-style diamond crusher to −325 mesh (⩽ 45 μm) powder for powder XRD. PXRD was performed on a Bruker D8 Discover powder X-ray diffractometer (Bruker Corporation, Germany) utilizing a CuKα X-ray beam (λ = 1.5418 Å) in the 5 - 100° 2θ range with a scan speed of 0.1055°/s, time per step of 0.3 s. The phases analyzed were cross-referenced against the Joint Committee on Powder Diffraction Standards (JCPDS) database. *Maud* software was used to perform the unit cell refinements.[35–39]

One piece was encapsulated in an epoxy/hardener set (Allied High Tech Products Inc., USA) to be polished to an optically flat finish on a semi-automated polisher (Southbay Technology Inc., USA) using both silicon carbide abrasive disks of 120 - 1200 grit (Allied High Tech Products Inc., USA) and 30 - 1 μm particle-size diamond films (Southbay Technology Inc., USA).

The polished samples were analyzed using an UltraDry EDS detector (Thermo Scientific, USA) attached to an FEI Nova 230 high-resolution scanning electron microscope (FEI Company, USA). Vickers hardness testing was performed using a MicroMet 2103 Vickers microhardness tester (Buehler Ltd., USA) with a pyramidal diamond indenter tip. 15 indents were made at applied loadings of 0.49, 0.98, 1.96 each, and a minimum of 10 indents were made at loadings of 2.94 and 4.9 N each, and were performed in random areas of the sample. A high resolution optical microscope (Zeiss Axiotech 100HD, Carl Zeiss Vision GmbH, Germany) with 500x magnification was used to measure the length of the diagonals of each indent. Vicker's hardness was calculated

using Equation 4.1:

$$H_v = \frac{1854.4F}{a^2} \quad (4.1)$$

where F is the loading force applied in Newtons (N) and a is the average of the length of the two diagonals of each indent in micrometers.

Thermogravimetric analysis utilizing a Pyris Diamond TGA/DTA unit (TG-DTA, Perkin-Elmer Instruments, U.S.A.) was used to determine oxidation resistance. The profile used for heating and cooling in air was as follows: heat from 25 to 200 °C (at 20 °C/min), hold at 200 °C for 30 minutes, heat from 200 to 1000 °C (at 2 °C/min), hold at 1000 C for 120 minutes, cool 1000 to 25 °C (at 5 °C/min).

RESULTS AND DISCUSSION

Phase determination and sample purity was determined using powder X-ray diffraction (PXRD) and energy-dispersive X-ray spectroscopy (EDS). PXRD data (2Θ = 5 - 50°) for $Zr_{1-x}Gd_xB_{12}$, $Zr_{1-x}Sm_xB_{12}$, $Zr_{1-x}Nd_xB_{12}$ and $Zr_{1-x}Pr_xB_{12}$ solutions are shown in Figure 4-2. EDS data for $Zr_{1-x}Gd_xB_{12}$, $Zr_{1-x}Sm_xB_{12}$, $Zr_{1-x}Nd_xB_{12}$ and $Zr_{1-x}Pr_xB_{12}$ (Figure 4-3), hardness (Figure 4-4) and thermogravimetric analysis (Figure 4-6) data for $Zr_{0.5}Gd_{0.5}B_{12}$ are discussed in detail later in this section. Unit cell parameters and compositions for $Zr_{1-x}Gd_xB_{12}$, $Zr_{1-x}Sm_xB_{12}$, $Zr_{1-x}Nd_xB_{12}$ and $Zr_{1-x}Pr_xB_{12}$ alloys are provided in Tables 4-1 and 4-2.

For $Zr_{1-x}Gd_xB_{12}$, the solubility limit of Gd in ZrB_{12} is ~54 at.% Gd, whereas for $Zr_{1-x}Sm_xB_{12}$, the solubility limit of Sm in ZrB_{12} is ~15 at.% Sm. For $Zr_{1-x}Nd_xB_{12}$, the solubility limit of Nd in ZrB_{12} is ~7 at.% Nd and for $Zr_{1-x}Pr_xB_{12}$, the solubility limit of Pr in ZrB_{12} is ~15 at.% Pr. The above solubilities were determined by powder XRD and EDS analyses. Past the solubility limit of Gd, Sm, Nd and Pr in ZrB_{12}, the amount of the respective hexaboride (MB_6) phases, which are the highest stable borides, increase (Figure 4-2). As metal dodecaborides are typically formed along

the tie line of an incongruently melting phase,[40–42] they are accompanied by a lower boride (MB_2 or MB_6) at metal to boron ratio of ~1:12, and higher borides (MB_{50} and MB_{66}) at larger metal to boron ratios 1:20. Cell parameters determined for each of the solid solution compositions as well as the metal composition for $Zr_{1-x}Gd_xB_{12}$ and $Zr_{1-x}Sm_xB_{12}$ are given in Table 4-1. Note that the solubility of the secondary metal (Sm - Pr) in ZrB_{12} decreases with increasing size of said metal, which is in good agreement with the size requirements for the metal dodecaboride formation as discussed above.

Vickers hardness testing from 0.49 N (low load) to 4.9 N (high load) was perfomed on samples of $Zr_{1-x}Gd_xB_{12}$ (x = 0.05, 0.25 and 0.50) after the composition and purity of each was established. The hardness of $Zr_{1-x}Gd_xB_{12}$ solid solutions did not change (within the measurement error) remaining at around ~40 GPa at 0.49 N, similar to the parent ZrB_{12} (40.4 ± 1.8 GPa).[17]

Elemental maps and SEM images of selected samples of $Zr_{1-x}Gd_xB_{12}$, $Zr_{1-x}Sm_xB_{12}$, $Zr_{1-x}Nd_xB_{12}$ and $Zr_{1-x}Pr_xB_{12}$ alloys (x = 0.55, 0.30, 0.25 and 0.25 respectively) are presented in Figure 4-3. For the $Zr_{0.45}Gd_{0.55}B_{12}$ solid solution, the presence of zirconium and gadolinium can be seen in the dodecaboride phase. The boron rich areas correspond to a higher boride phase GdB_{66} (cubic, $Fm\bar{3}c$ structure, a = 23.449 Å, ICSD 614306). The $Zr_{0.70}Sm_{0.30}B_{12}$ solid solution shows the presence of zirconium and samarium in the dodecaboride phase. Here, the samarium rich areas correspond to SmB_6 (cubic, $Pm\bar{3}m$ structure, a = 4.133 Å, ICSD 194196), and the boron rich areas correspond to the higher boride phase SmB_{66} (cubic, $Fm\bar{3}c$ structure, a = 23.468 Å). The $Zr_{0.75}Nd_{0.25}B_{12}$ and $Zr_{0.75}Pr_{0.25}B_{12}$ solid solutions show the presence of both zirconium and the secondary metals, neodymium and praseodymium, respectively, in the dodecaboride phase. The neodymium rich areas correspond to NdB_6 (cubic, $Pm\bar{3}m$ structure, a = 4.127 Å, ICSD 614931), while the praseodymium rich areas correspond to PrB_6 (cubic, $Pm\bar{3}m$ structure, a = 4.123 Å, ICSD 615183).

In the samples containing Nd and Zr, the boron rich areas correspond to the higher boride phase NdB_{66} (cubic, $Fm\bar{3}c$ structure, a = 23.476 Å) and ZrB_{50} (rhombohedral, $R\bar{3}m$ structure, a = 10.932 Å, c = 23.849 Å), respectively. For praseodymium, however, the metal rich areas correspond to PrB_6 (cubic, $Pm\bar{3}m$ structure, a = 4.123 Å, ICSD 615183), while the boron rich areas correspond to the higher boride phase ZrB_{50} (rhombohedral, $R\bar{3}m$ structure, a = 10.932 Å, c = 23.849 Å) as the PrB_{66} phase does not exist.[43]

Maud software was used to perform the unit cell refinements.[35–39] For $Zr_{1-x}Gd_xB_{12}$, the cubic unit cell parameter (a) reached a value of 7.453 Å for the alloy with 55 nominal at.% Gd, compared to 7.412 Å and 7.524 Å (value from high-pressure – 6.5 GPa – synthesis)[32] for pure ZrB_{12} and GdB_{12}, respectively. The change in the unit cell suggests the formation of a solid solution between GdB_{12} and ZrB_{12}. As more Gd is present in the alloy, the GdB_6 phase concentration increases, as it is the ambient pressure stable boride phase.

EDS analysis and calculations using Vegard's Law[44] were used to determine the solubility limit of Gd in ZrB_{12} (Table 4-1). Both methods gave a value ~54 at.% Gd in ZrB_{12}; the excess Gd formed the boron rich GdB_{66} and ZrB_{50} phase. For $Zr_{1-x}Sm_xB_{12}$, the cubic unit cell parameter (a) reached a value of 7.428 Å for the alloy with 30 nominal at.% Sm, compared to 7.412 Å for pure ZrB_{12}. As the high pressure synthesis of SmB_{12} was not successful,[32] since it likely requires a pressure in excess of 6.5 GPa, there is no literature value for its unit cell. However, using the composition from EDS analysis and unit cell refinements, the unit cell for pure SmB_{12} can be determined through extrapolation – 7.543 Å. Still, the change in the unit cell suggests the formation of a solid solution between SmB_{12} and ZrB_{12}. As more Sm is present in the alloy, the SmB_6 phase concentration increases, as it is the ambient pressure stable boride phase for samarium.

For $Zr_{1-x}Nd_xB_{12}$ and $Zr_{1-x}Pr_xB_{12}$ there is a slight change in the unit cell parameter *(a)* compared to

the pure ZrB_{12}, corresponding to the limited solubilities of Nd and Pr in ZrB_{12}, 7 and 4 at. %, respectively. Similar to SmB_{12}, the high-pressure synthesis of NdB_{12} and PrB_{12} was unsuccessful[32]; therefore, it is not possible to compare the unit cells of the alloys with the unit cell of the pure compounds.

Another confimation of the solid solution formation of the dodecaboride phase can be directly observed using a light microscope (Figure 4-5) going from pure ZrB_{12} (violet) to $Zr_{0.45}Gd_{0.55}B_{12}$ (blue) and $Zr_{0.70}Sm_{0.30}B_{12}$ (blue-violet). The color change is due to the charge-transfer between the cuboctahedron boron cage network and the metal atoms. It also suggests that pure GdB_{12} and SmB_{12} should be blue, similar to YB_{12}, as Gd, Sm and Y are all in +3 oxidation states.[17,29,34] The dark blue phase observed in $Zr_{1-x}Sm_xB_{12}$ is SmB_6.

The thermal stability of the zirconium-gadolinium and zirconium-samarium borides was measured in air using thermogravimetric analysis (Figure 4-6). The $Zr_{0.5}Gd_{0.5}B_{12}$ sample is stable in air up to ~630 °C, while $Zr_{0.75}Sm_{0.25}B_{12}$ up to ~620 °C compared to ~610 °C for pure ZrB_{12}.[17]

CONCLUSIONS

We have successfully stabilized the high-pressure phase, GdB_{12},[32] in $Zr_{1-x}Gd_xB_{12}$ (with a ~54 at.% Gd solubility, as determied by PXRD and EDS) solid solutions under ambient pressure. In addition, limited solubilities of Sm, Nd and Pr (~15, ~7 and ~4 at. %, Sm, Nd and Pr, respectively) in ZrB_{12} was achieved. These phases were not previoulsy synthesized even under high pressure;[32] however, the limited solubility suggests that a synthesis pressure in excesss of 6.5 GPa is required as Sm, Nd, and Pr atomic radii are larger than that of Gd. The solid-solution formation for $Zr_{1-x}Gd_xB_{12}$ and $Zr_{1-x}Sm_xB_{12}$ can be seen in the change of the unit cell of each of the solid solutions relative to their pure parent compounds as well as in the change of color of the respective alloys.

ACKNOWLDGEMENTS

We thank the National Science Foundation Division of Materials Research, Grant DMR-1506860 (R.B.K.) and the National Science Foundation DGE-0654431 Fellowship program (M.T.Y.) for financial support. We also thank Professor Benjamin M. Wu of the UCLA Department of Bioengineering for the use of his micro-indentation system.

Table 4-1. Compositions[a] and Unit Cell Data[b] for $Zr_{1-x}Gd_xB_{12}$[c] and $Zr_{1-x}Sm_xB_{12}$[d]

Compound	a, Å	Vegard's Law	at.% Gd (EDS)	Compound	a, Å	at.% Sm (EDS)
ZrB_{12}	7.412(2)	7.412	-	ZrB_{12}	7.412(2)	-
$Zr_{0.95}Gd_{0.05}B_{12}$	7.420(3)	7.418	3.38 (0.23)	$Zr_{0.95}Sm_{0.05}B_{12}$	7.419(3)	2.93 (0.42)
$Zr_{0.75}Gd_{0.25}B_{12}$	7.444(3)	7.440	18.56 (0.31)	$Zr_{0.75}Sm_{0.25}B_{12}$	7.433(3)	14.94 (0.24)
$Zr_{0.50}Gd_{0.50}B_{12}$	7.464(2)	7.468	50.83 (0.80)	$Zr_{0.70}Sm_{0.30}B_{12}$	7.431(4)	13.99 (0.23)
$Zr_{0.45}Gd_{0.55}B_{12}$	7.468(2)	7.474	53.70 (0.64)	$Zr_{0.65}Sm_{0.35}B_{12}$	7.429(2)	-
$Zr_{0.35}Gd_{0.65}B_{12}$	7.453(2)	7.485	-	$Zr_{0.50}Sm_{0.50}B_{12}$	7.428(3)	-
$Zr_{0.25}Gd_{0.75}B_{12}$	-	7.496	-	$Zr_{0.25}Sm_{0.75}B_{12}$	-	-
$Zr_{0.05}Gd_{0.95}B_{12}$	-	7.518	-	$Zr_{0.05}Sm_{0.95}B_{12}$	-	-
GdB_{12}[32]	7.524[32]	7.524	-	SmB_{12}[e]	7.543[e]	-

[a]calculated from XRD data using Vegard's Law[44] and from EDS analysis, errors are given in brackets

[b]from *Maud*[35–39], errors are given in brackets

[c]x = 0.00, 0.05, 0.25, 0.50, 0.55, 0.65, 0.75 and 0.95

[d]x = 0.00, 0.05, 0.25, 0.30, 0.35, 0.50, 0.75 and 0.95

[e]there is no literature value for the SmB_{12} cell, as it has not yet been synthesized even under high pressure conditions,[32] it can, however, be extrapolated using the unit cell data and composition from EDS

Table 4-2. Compositions[a] and Unit Cell Data[b] for $Zr_{1-x}Nd_xB_{12}$[c] and $Zr_{1-x}Pr_xB_{12}$[c]

Compound	a, Å	at.% Nd (EDS)	Compound	a, Å	at.% Pr (EDS)
ZrB_{12}	7.412(2)	-	ZrB_{12}	7.412(2)	-
$Zr_{0.95}Nd_{0.05}B_{12}$	7.413(3)	1.76 (0.11)	$Zr_{0.95}Pr_{0.05}B_{12}$	7.415(2)	1.61 (0.22)
$Zr_{0.75}Nd_{0.25}B_{12}$	7.421(2)	7.17 (0.28)	$Zr_{0.75}Pr_{0.25}B_{12}$	7.418(4)	4.12 (0.27)
$Zr_{0.50}Nd_{0.50}B_{12}$	7.419(3)	-	$Zr_{0.50}Pr_{0.50}B_{12}$	7.418(3)	-
$Zr_{0.25}Nd_{0.75}B_{12}$	-	-	$Zr_{0.25}Pr_{0.75}B_{12}$	-	-
$Zr_{0.05}Nd_{0.95}B_{12}$	-	-	$Zr_{0.05}Pr_{0.95}B_{12}$	-	-
NdB_{12}[d]	-	-	PrB_{12}[d]	-	-

[a]calculated from XRD data using Vegard's Law[44] and from EDS analysis, errors are given in brackets

[b]from *Maud*,[35–39] errors are given in brackets

[c]x = 0.00, 0.05, 0.25, 0.50, 0.75 and 0.95

[d]there is no literature value for the NdB_{12} and PrB_{12} unit cells, as have not yet been synthesized even under high pressure conditions[32]

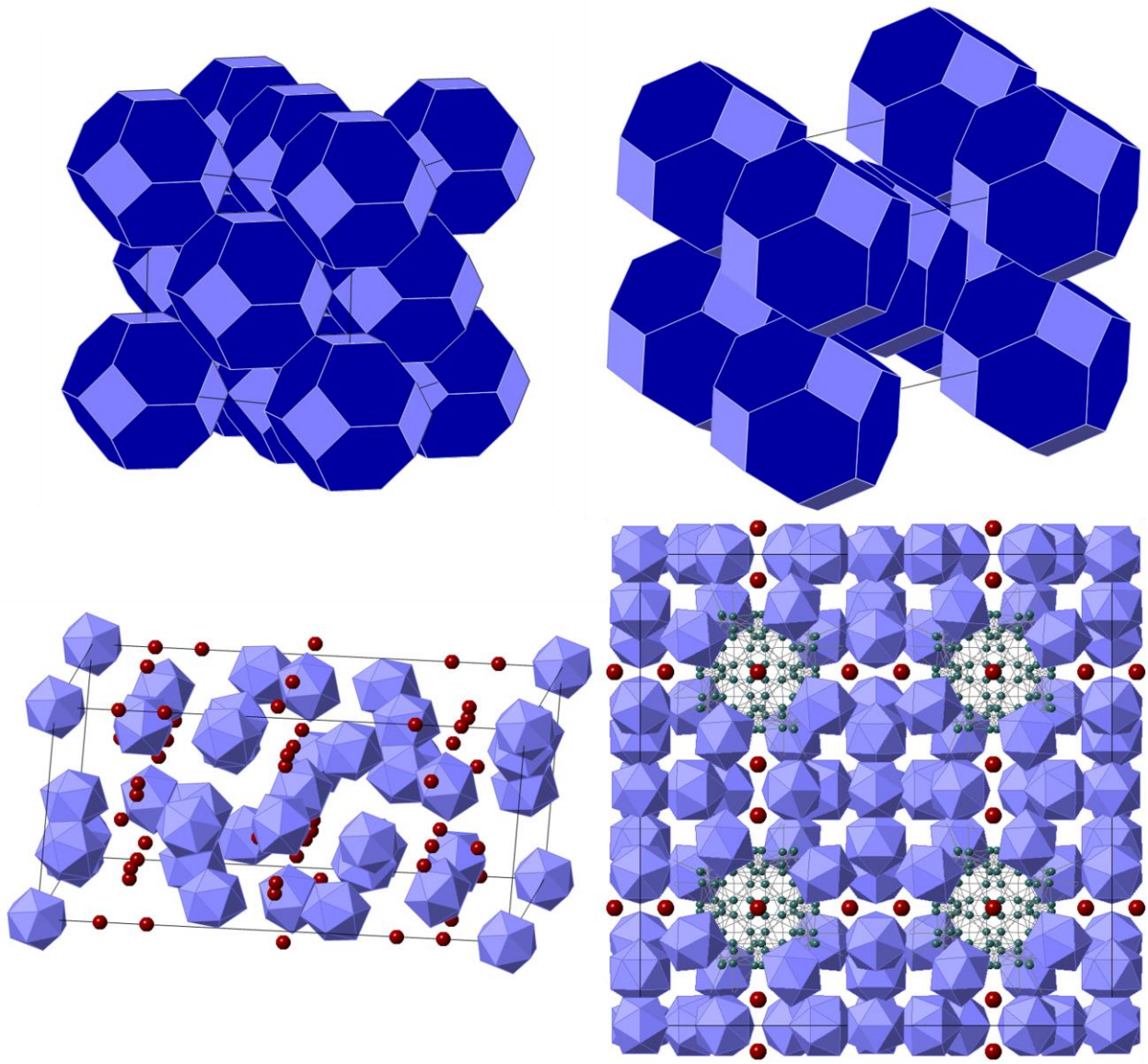

Figure 4-1. (Top left) Polyhedra model of the unit cell of a cubic-UB_{12} structural type metal dodecaboride: 24 boron atom cuboctahedra cages (square faces shown in red, hexagonal face in green) are arranged in a FCC lattice, with a 12- coordinate metal atom in the center of each cage; (top right) polyhedra model of the unit cell of a tetragonal-ScB_{12} structural type metal dodecaboride: 24 boron atom cuboctahedra cages (square faces shown in red, hexagonal facein green) are arranged in a BCT lattice, with a 12-coordinate metal atom in the center of each cage; Note, metals are considered 12-coordinate since 12 boron-boron bonds are equidistant from each metal atom in the 24 boron atom cuboctahedron cage; (bottom left) polyhedra model of the unit cell of a rhombohedral-MB_{50} structural type (solid solution of a metal in β-rhombohedral boron): boron atoms are arranged in B_{12} icosahedral units (shown in green), metal atoms are in blue; (bottom right) polyhedra model of the unit cell of a cubic-YB_{66} structural type metal boride: boron atoms are arranged in B_{12} icosahedral units (shown in green), boron atoms not forming icosahedra are in red, metal atoms are in blue.

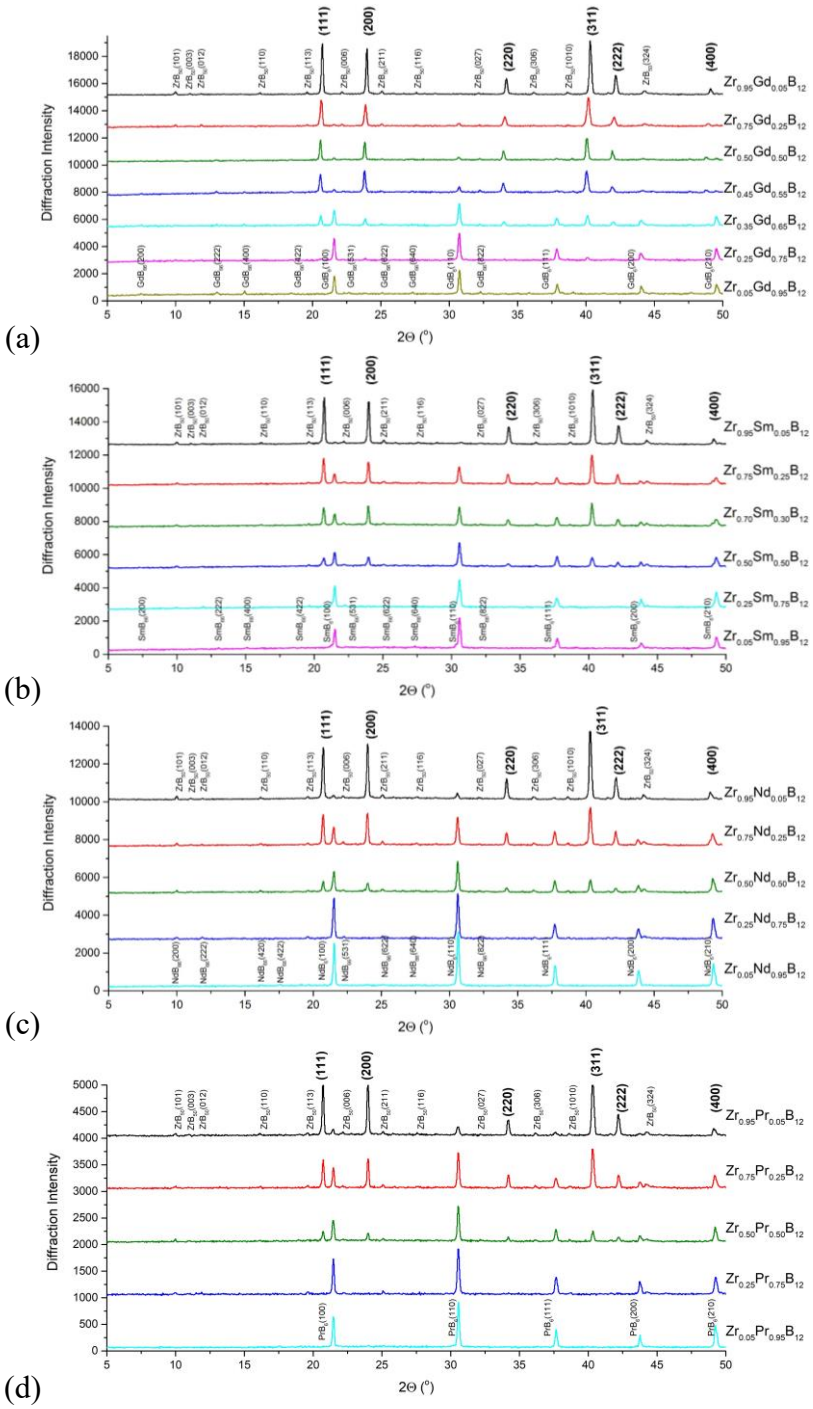

Figure 4-2. Powder XRD patterns of: (a) $Zr_{1-x}Gd_xB_{12}$, where x = 0.05, 0.25, 0.50, 0.55, 0.65, 0.75 and 0.95. The solubility limit of Gd in ZrB_{12} is ~54 at.% Gd; (b) $Zr_{1-x}Sm_xB_{12}$, where x = 0.05, 0.25, 0.30, 0.50, 0.75 and 0.95. The solubility limit of Sm in ZrB_{12} is ~15 at.% Sm; (c) $Zr_{1-x}Nd_xB_{12}$, where x = 0.05, 0.25, 0.50, 0.75 and 0.95. The solubility limit of Nd in ZrB_{12} is ~7 at.% Nd; (d) $Zr_{1-x}Pr_xB_{12}$, where x = 0.05, 0.25, 0.50, 0.75 and 0.95. The solubility limit of Pr in ZrB_{12} is ~4 at.% Pr. With increasing concentration of Gd, Sm, Nd and Pr, the MB_{12} phase concentration decreases while MB_6 increases. ZrB_{50} and MB_{66} are present at larger metal to boron ratios (i.e. 1:20).

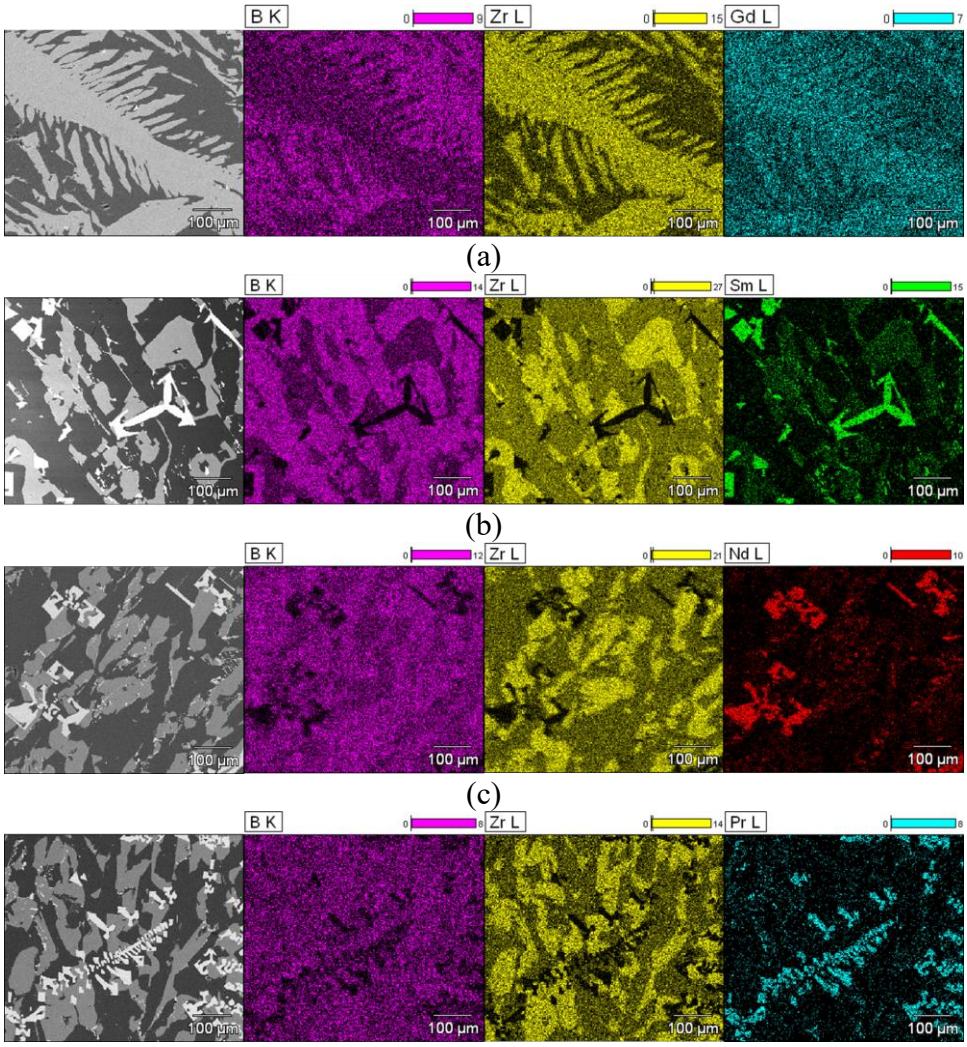

Figure 4-3. Elemental maps for boron (K line), Zr (L line) and Gd, Sm, Nd and Pr (L lines) of: (a) the $Zr_{0.45}Gd_{0.55}B_{12}$ solid solution showing the presence of Zr and Gd in the dodecaboride phase. The boron rich areas correspond to a higher boride phase GdB_{66} (cubic, $Fm\bar{3}c$ structure, a = 23.449 Å, ICSD (Inorganic Crystal Structure Database) 614306); (b) the $Zr_{0.70}Sm_{0.30}B_{12}$ solid solution showing the presence of Zr and Sm in the dodecaboride phase. The Sm rich areas correspond to SmB_6 (cubic, $Pm\bar{3}m$ structure, a = 4.133 Å, ICSD 194196), while the boron rich areas correspond to a higher boride phase SmB_{66} (cubic, $Fm\bar{3}c$ structure, a = 23.468 Å). (c) the $Zr_{0.75}Nd_{0.25}B_{12}$ solid solution showing the presence of Zr and Nd in the dodecaboride phase. The Nd rich areas correspond to NdB_6 (cubic, $Pm\bar{3}m$ structure, a = 4.127 Å, ICSD 614931), while the boron rich areas correspond to a higher boride phase NdB_{66} (cubic, $Fm\bar{3}c$ structure, a = 23.476 Å) and ZrB_{50} (rhombohedral, $R\bar{3}m$ structure, a = 10.932 Å, c = 23.849 Å); (d) the $Zr_{0.75}Pr_{0.25}B_{12}$ solid solution showing the presence of Zr and Pr in the dodecaboride phase. The Pr rich areas correspond to PrB_6 (cubic, $Pm\bar{3}m$ structure, a = 4.123 Å, ICSD 615183), while the boron rich areas correspond to a higher boride phase ZrB_{50} (rhombohedral, $R\bar{3}m$ structure, a = 10.932 Å, c = 23.849 Å). The thick horizontal bars represent the intensity as a color legend.

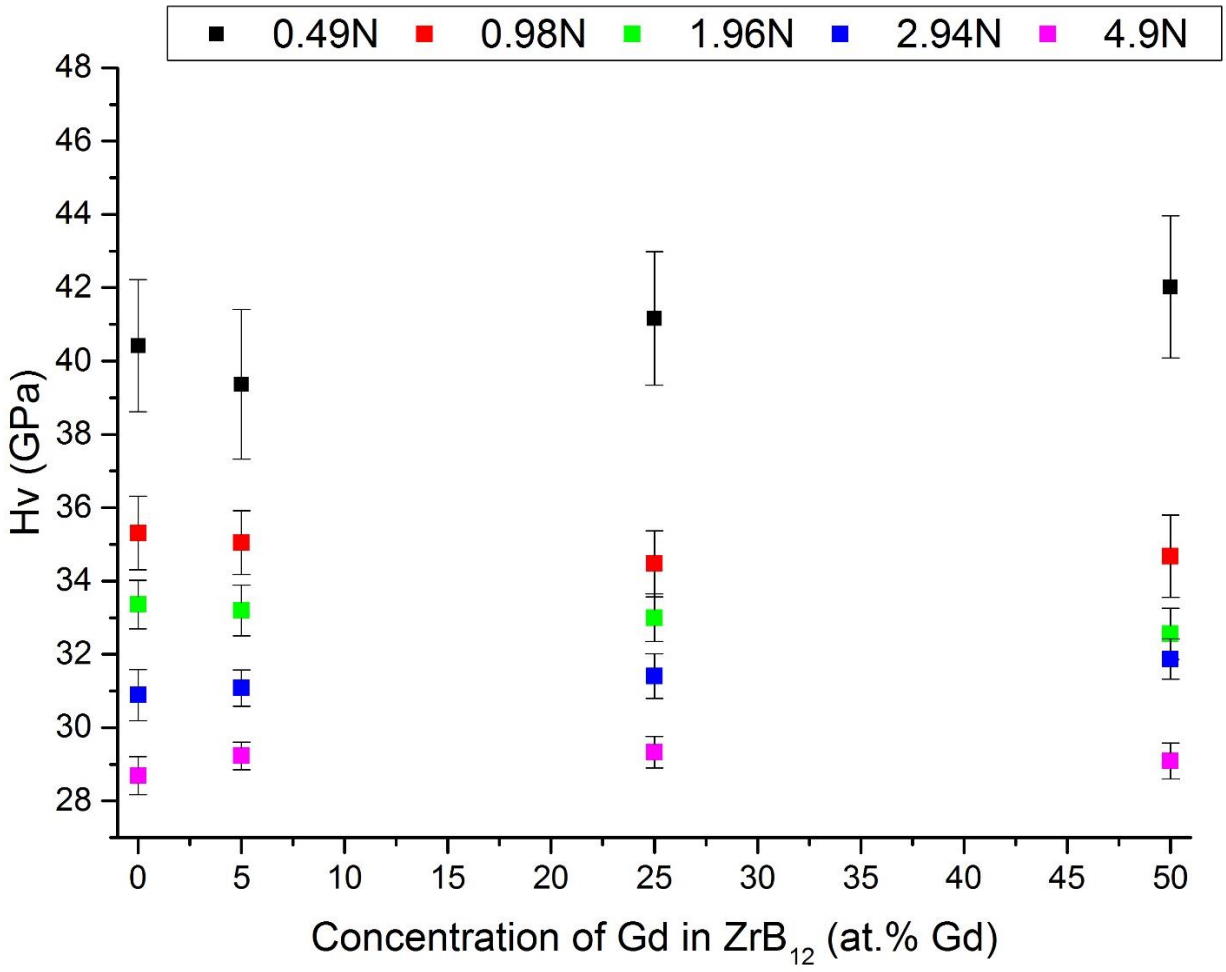

Figure 4-4. Vickers microindentation hardness (H_v) of $Zr_{1-x}Gd_xB_{12}$ (x = 0.05, 0.25 and 0.50) with loads varying from 0.49 (low load) to 4.9 N (high load). Hardness for ZrB_{12} was taken from reference.[17]

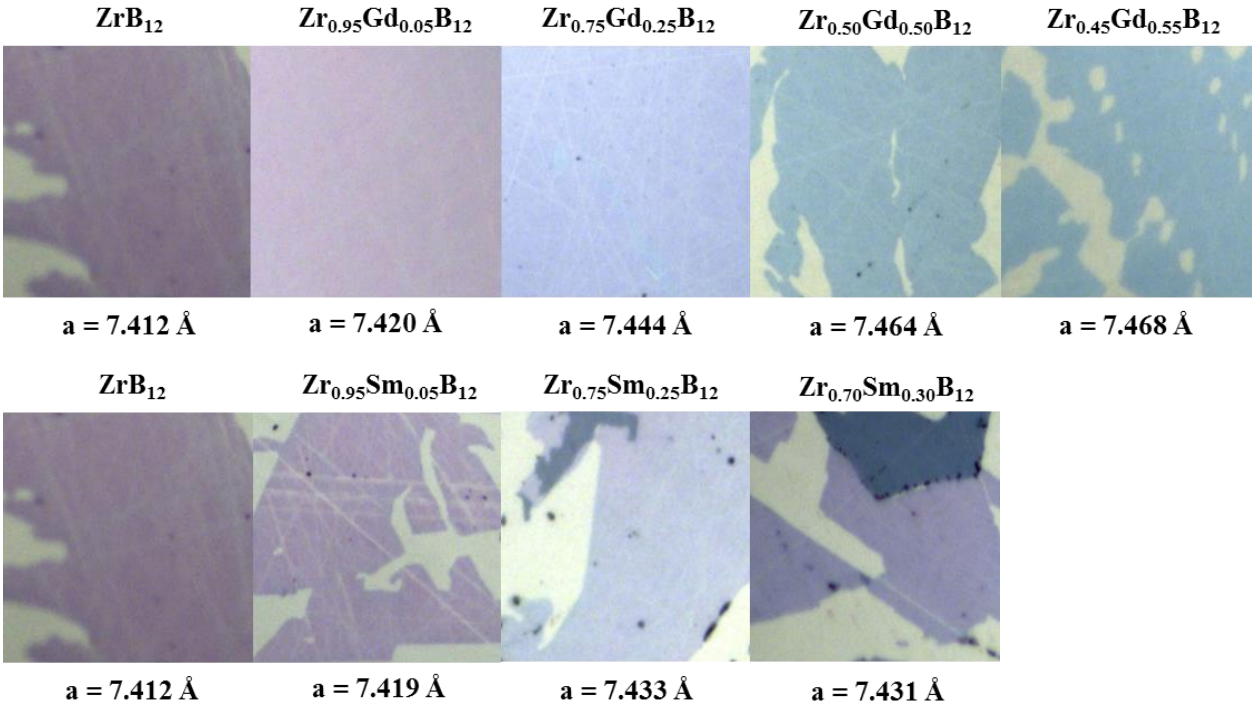

Figure 4-5. A color change of the dodecaboride phase can be directly observed using a light microscope going from pure ZrB_{12} (violet) to $Zr_{0.45}Gd_{0.55}B_{12}$ (blue) and $Zr_{0.70}Sm_{0.30}B_{12}$ (blue-violet) phases. The color change suggests that pure GdB_{12} and SmB_{12} are blue, similar to YB_{12}, as Gd, Sm and Y are all in +3 oxidation states.[29] The dark blue phase in $Zr_{1-x}Sm_xB_{12}$ is SmB_6.

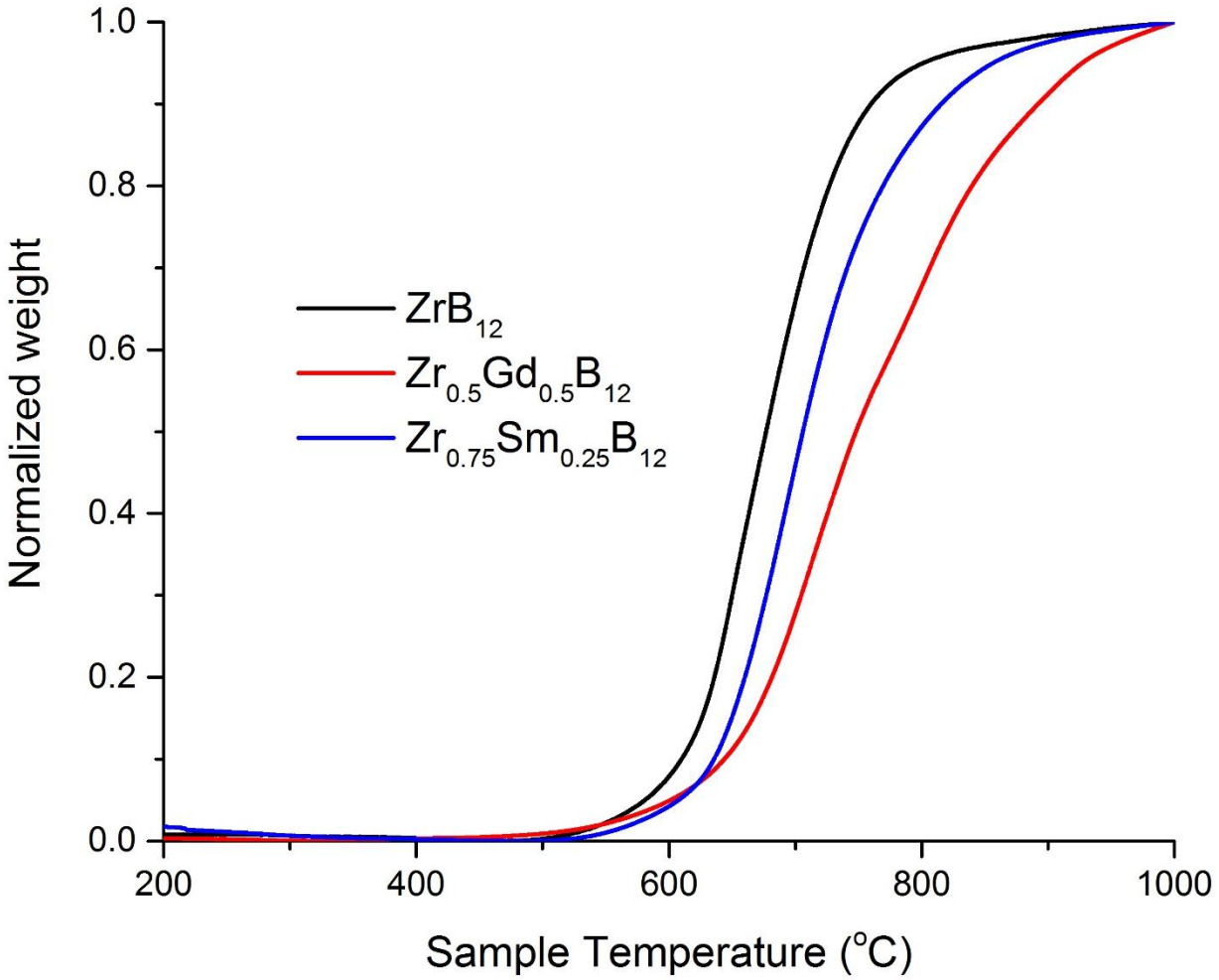

Figure 4-6. Thermal stability of pure ZrB_{12}, $Zr_{0.5}Gd_{0.5}B_{12}$ and $Zr_{0.75}Sm_{0.25}B_{12}$ as measured by thermal gravimetric analysis in air. These data show that $Zr_{0.5}Gd_{0.5}B_{12}$ is stable up to ~630 °C, while $Zr_{0.75}Sm_{0.25}B_{12}$ up to ~620 °C compared to ~610 °C for pure ZrB_{12} (using extrapolated onset method).

REFERENCES

1. Tergenius, L. E. Refinement of the crystal structure of orthorhombic Mn2B (formerly denoted Mn4B). *J. Less-Common Met.* **82,** 335–340 (1981).
2. Yeung, M. T. *et al.* Superhard Monoborides: Hardness Enhancement through Alloying in W1−xTaxB. *Adv. Mater.* 6993–6998 (2016). doi:10.1002/adma.201601187
3. Yeung, M. T. *et al.* Superhard W0.5Ta0.5B nanowires prepared under ambient pressure. *Appl. Phys. Lett.* **109,** 203107 (2016).
4. Levine, J. B. *et al.* Preparation and properties of metallic, superhard rhenium diboride crystals. *J. Am. Chem. Soc.* **130,** 16953–8 (2008).
5. Chung, H.-Y. *et al.* Synthesis of Ultra-Incompressible Superhard Rhenium Diboride at Ambient Pressure. *Science (80-.).* **316,** 436–439 (2007).
6. Whittaker, M. L. & Cutler, R. A. Effect of synthesis atmosphere, wetting, and compaction on the purity of AlB2. *J. Solid State Chem.* **201,** 93–100 (2013).
7. Akopov, G., Yeung, M. T., Turner, C. L., Mohammadi, R. & Kaner, R. B. Extrinsic hardening of superhard tungsten tetraboride alloys with group 4 transition metals. *J. Am. Chem. Soc.* **138,** 5714–5721 (2016).
8. Mohammadi, R. *et al.* Toward inexpensive superhard materials: Tungsten tetraboride-based solid solutions. *J. Am. Chem. Soc.* **134,** 20660–20668 (2012).
9. Knappschneider, A. *et al.* Manganese Tetraboride, MnB4: High-Temperature Crystal Structure, p–n Transition, 55Mn NMR Spectroscopy, Solid Solutions, and Mechanical Properties. *Chem. – A Eur. J.* **21,** 8177–8181 (2015).

10. Knappschneider, A., Litterscheid, C., Kurzman, J., Seshadri, R. & Albert, B. Crystal structure refinement and bonding patterns of CrB4: A boron-rich boride with a framework of tetrahedrally coordinated B atoms. *Inorg. Chem.* **50,** 10540–10542 (2011).

11. Mordovin, O. A. & Timofeeva, E. N. Rare-earth Element Hexaborides. *Russ. J. Inorg. Chem.* **13,** 1627–1629 (1968).

12. Dytchak, Y. I. Thermal oscillation of atoms of some metal hexaborides [in Russian]. *Izv. Vyzov. Fiz.* **1,** 154–156 (1973).

13. Timofeeva, I. I. & Timofeeva, E. N. Physicochemical properties of lanthanide hexaborides. *Inorg. Mater.* **4,** 1559–1561 (1968).

14. Zhitomirsky, M. E., Rice, T. M. & Anisimov, V. I. Magnetic properties: Ferromagnetism in the hexaborides. *Nature* **402,** 251–253 (1999).

15. Kim, D. J., Xia, J. & Fisk, Z. Topological surface state in the Kondo insulator samarium hexaboride. *Nat Mater* **13,** 466–470 (2014).

16. La Placa, S., Binder, I. & Post, B. Binary dodecaborides. *J. Inorg. Nucl. Chem.* **18,** 113–117 (1961).

17. Akopov, G., Yeung, M. T., Sobell, Z. C., Turner, C. L. & Kaner, R. B. Superhard Mixed Metal Dodecaborides. *Chem. Mater.* **28,** 6605–6612 (2016).

18. Matkovich, V. I., Economy, J., Giese, R. F. & Barrett, R. The structure of metallic dodecarborides. *Acta Crystallogr.* **19,** 1056–1058 (1965).

19. Samsonov, G. V. & Vinitskii, I. M. *Refractory compounds [in Russian]*. (Atomizdat, 1975).

20. Samsonov, G. V., Markovskii, L. Y., Zhigach, A. F. & Valyashko, M. G. *Boron, Its Compounds and Alloys [in Russian]*. (House of the Academy of the Sciences Ukrainian

SSR, 1960).

21. Lundström, T. Borides: Solid-state Chemistry. in *Encyclopedia of Inorganic Chemistry* 481–494 (2006).

22. Schmechel, R. & Werheit, H. Correlation between structural defects and electronic properties of icosahedral boron-rich solids. *J. Phys. Condens. Matter* **11,** 6803–6813 (1999).

23. Werheit, H. *et al.* Raman scattering and isotopic phonon effects in dodecaborides. *J. Phys. Condens. Matter* **23,** (2011).

24. Werheit, H. Present knowledge of electronic properties and charge transport of icosahedral boron-rich solids. *J. Phys. Conf. Ser.* **176,** (2009).

25. Werheit, H. Are there bipolarons in icosahedral boron-rich solids? *J. Phys. Condens. Matter* **19,** (2007).

26. Matthias, A. B. T. *et al.* Superconductivity and Antiferromagnetism in Boron-Rich Lattices. *Science (80-.).* **159,** 530 (1968).

27. Paderno, Y. B., Odintsov, V. V., Timofeeva, I. I. & Klochkov, L. A. Thermal expansion of metal dodecaborides. *High Temp.* **9,** 175–177 (1971).

28. Odintsov, V. V. Hardness of metal dodecaborides of UB12 structure type [in Russian]. *Inorg. Chem. USSR* **10,** 366–367 (1974).

29. Mar, R. W. & Stout, N. D. High Temperature Enthalpies of Binary Dodecaborides. *J. Chem. Phys.* **57,** 5342–5349 (1972).

30. Slater, J. C. Atomic Radii in Crystals. *J. Chem. Phys.* **41,** 3199–3204 (1964).

31. Cannon, J. F. & Farnsworth, P. B. High pressure syntheses of ThB12 and HfB12. *J. Less-Common Met.* **92,** 359–368 (1983).

32. Cannon, J. F., Cannon, D. M. & Tracy Hall, H. High pressure syntheses of SmB2 and GdB12. *J. Less-Common Met.* **56,** 83–90 (1977).

33. Renosto, S. T. *et al.* Superconductivity in the Th0.93Zr0.07B12 compound with UB12 prototype structure. *Phys. Lett. A* **379,** 2498–2501 (2015).

34. Akopov, G., Yeung, M. T., Turner, C. L., Li, R. L. & Kaner, R. B. Stabilization of HfB12 in Y1−xHfxB12 under Ambient Pressure. *Inorg. Chem.* **55,** 5051–5055 (2016).

35. Lutterotti, L., Chateigner, D., Ferrari, S. & Ricote, J. Texture, residual stress and structural analysis of thin films using a combined X-ray analysis. *Thin Solid Films* **450,** 34–41 (2004).

36. Lutterotti, L. Maud Rev. 2.55. *Maud Rev. 2.55, Univ. Trento-Italy, Dep. Ind. Eng. Trento, Italy* (2015).

37. Lutterotti, L. Total pattern fitting for the combined size-strain-stress-texture determination in thin film diffraction. *Nucl. Instruments Methods Phys. Res. Sect. B Beam Interact. with Mater. Atoms* **268,** 334–340 (2010).

38. Lutterotti, L., Matthies, S., Wenk, H. R., Schultz, A. S. & Richardson, J. W. Combined texture and structure analysis of deformed limestone from time-of-flight neutron diffraction spectra. *J. Appl. Phys.* **81,** 594–600 (1997).

39. Lutterotti, L., Bortolotti, M., Ischia, G., Lonardelli, I. & Wenk, H. R. Rietveld texture analysis from diffraction images. *Zeitschrift fur Krist. Suppl.* **1,** 125–130 (2007).

40. Liao, P. K., Spear, K. E. & Schlesinger, M. E. The B-Gd (Boron-Gadolinium) System. **17,** 330–334 (1996).

41. Liao, P. K. & Spear, K. E. B-Pm (Boron-Promethium). in *Binary Alloy Phase Diagrams, Vol 1* (ed. Massalski, T. B.) 517–520 (ASM International, 1990).

42. Liao, P. K. & Spear, K. E. The B-Nd (Boron-Neodymium) System. *J. Phase Equilib.* **17,** 335–339 (1996).

43. Liao, P. K. & Spear, K. E. B-Pr (Boron-Praseodymium). in *Binary Alloy Phase Diagrams, Vol 1* (ed. Massalski, T. B.) 519–522 (ASM International, 1990).

44. Vegard, L. Die Konstitution der Mischkristalle und die Raumfullung der Atome. *Zeitschrift fur Phys.* **5,** 17–26 (1921).

CHAPTER 5. INVESTIGATION OF TERNARY METAL DODECABORIDES ($(M_1M_2M_3)B_{12}$ (M_1, M_2 AND M_3 = Zr, Y, Hf AND Gd)

Reproduced from Akopov, G.; Roh, I.; Sobell, Z.C.; Yeung, M. T.; Kaner, R. B. "Investigation of Ternary Metal Dodecaborides $(M_1M_2M_3)B_{12}$ (M_1, M_2 and M_3 = Zr, Y, Hf and Gd)" *Dalton Trans.* **2018**, 47, 6683-6691with permission from The Royal Society of Chemistry.

ABSTRACT

Samples of metal borides with a nominal composition of $((M_1)_{(1-x-z)}(M_2)_{(x)}(M_3)_{(z)})$: 20B (M_1, M_2 and M_3 = Zr, Y, Hf and Gd) were prepared by arc-melting and studied for phase composition (using powder X-ray diffraction (PXRD) and energy dispersive X-ray spectroscopy (EDS)) and mechanical properties (Vickers hardness). Ternary metal dodecaborides phases were successfully synthesized for the majority of compositions, including stabilization of two high-pressure (6.5 GPa) phases (cubic-*UB_{12}* structure), HfB_{12} and GdB_{12}, in $(Zr_{1-x-z}Hf_xGd_z)$: 20B and $(Y_{1-x-z}Hf_xGd_z)$: 20B nominal alloy compositions. Unit cell refinement for the samples showed solid solution formation in most cases. Vickers hardness measurements indicated that most samples possess enhanced hardness in comparison to their parent phases, with the alloy $(Zr_{0.50}Y_{0.25}Gd_{0.25})$: 20B having a hardness of 46.9 ± 2.4 GPa compared to 41.3 ± 1.1 and 41.6 ± 1.3 GPa for alloy compositions of 1.0 Zr : 20B and 1.0 Y : 20B, respectively, at 0.49 N of applied load. Using the data from this manuscript as well as previous work, pseudo-ternary phase diagrams (at a constant boron content) have been constructed.

INTRODUCTION

Metal borides possess a host of remarkable thermal[1,2], optical, electronic and magnetic[1,3,4] properties. This wide range of attributes is matched by a comparable variety of boride structures:[1,2,5–9] from sub-borides (M_4B)[10] and tetraborides (MB_4)[11–13] to dodecaborides (MB_{12})[14–

[17] and even higher borides (MB_{50} and MB_{66})[18,19]. Owing to boron's propensity to catenate, the higher borides possess extended boron networks, which results in prodigious mechanical properties.[20]

Amongst these higher borides, metal dodecaborides[14] (MB_{12}) comprise a remarkable class of isotropic compounds, with interesting properties, such as superconductivity[21] and superhardness.[15,22] Metal dodecaborides crystallize in two structures which differ solely by the arrangement of their boron cuboctahedra: cubic-UB_{12} ($Fm\bar{3}m$) and tetragonal-ScB_{12} (*I4/mmm*) (Figure 5-1). For the cubic structure, the 24 boron atom cuboctahedron cages surrounding each metal atom are arranged in a face-centered cubic (FCC) lattice, while the tetragonal structure has a body-centered cubic (BCT) arrangement. The main criterion for the formation of metal dodecaborides of the cubic-UB_{12} structure under ambient pressure is the size of the metal, or more precisely, its radius in a 12 coordinate environment, with the smallest metal being zirconium (1.603 Å[23]) and largest yttrium (1.801 Å[23]). When the size of the metal deviates from this range even by a very small margin, like in the case of hafnium (1.580 Å[23]), the MB_{12} phase becomes unstable. However, it can be synthesized either under high pressure (6.5 GPa)[23] or stabilized in an alloy with a stable dodecaboride ($Y_{1-x}Hf_xB_{12}$).[17] The same is true for metals larger than yttrium (e.g. Gd, Sm, Nd, Pr and Th), they can either be synthesized under high pressure (e.g. ThB_{12} and GdB_{12})[24] or stabilized in a matrix with a stable dodecaboride ($Zr_{1-x}Th_xB_{12}$[21], $Zr_{1-x}Gd_xB_{12}$, $Zr_{1-x}Sm_xB_{12}$, $Zr_{1-x}Nd_xB_{12}$ and $Zr_{1-x}Pr_xB_{12}$[16]).

In both cases, the ambient pressure stabilization worked based on the following principle: a "smaller atom dodecaboride" being stabilized in a framework formed by a "larger atom dodecaboride" ($Y_{1-x}Hf_xB_{12}$) and vice versa ($Zr_{1-x}Gd_xB_{12}$) so that the final composition's lattice parameters fit within the region of dodecaboride formation. Stabilization and synthesis of high

pressure phases under ambient pressure gives an easy avenue to study their properties. As the lattice parameters of high pressure HfB_{12} are too large (and likewise for high pressure GdB_{12} too small), it is interesting to study whether these high-pressure phases can stabilize each other under ambient pressure as well as their behavior in ternary metal dodecaboride systems. Furthermore, the stabilization of HfB_{12} and GdB_{12} in the same compound has the additional advantage of solid solution strengthening, where dislocation propagation is pinned by localized strain. This is a technique that had been tried with other dodecaborides.[21,25,26] The greater size difference between Gd and Hf should create the aforementioned micro-strain, which could significantly improve the mechanical properties and hardness.

In this manuscript we have synthesized four ternary boride systems with the following nominal compositions: $(Zr_{1-x-z}Hf_xGd_z) : 20B$, $(Y_{1-x-z}Hf_xGd_z) : 20B$, $(Zr_{1-x-z}Hf_xY_z) : 20B$, $(Zr_{1-x-z}Y_xGd_z) : 20B$ and studied their phase composition and mechanical properties. We discovered that a ternary metal dodecaboride phase forms in most cases. Remarkably, it is possible to stabilize both high pressure phases (HfB_{12} and GdB_{12}) in the matrixes of $Zr_{1-x-z}Hf_xGd_zB_{12}$ and $Y_{1-x-z}Hf_xGd_zB_{12}$. A remarkable hardness increase of greater than 10% is observed in the alloy $(Zr_{0.50}Y_{0.25}Gd_{0.25}) : 20B$ when compared to its parent compounds.

EXPERIMENTAL PROCEDURE

Pellets of the following nominal compositions: $(Zr_{1-x-z}Hf_xGd_z) : 20B$, $(Y_{1-x-z}Hf_xGd_z) : 20B$, $(Zr_{1-x-z}Hf_xY_z) : 20B$, $(Zr_{1-x-z}Y_xGd_z) : 20B$ (x and z = 0.25, 0.33 and 0.5), $(Hf_{1-x}Gd_x) : 20B$, (x = 0.05, 0.25, 0.50, 0.75 and 0.95), and $(Y_{1-x}Gd_x) : 20B$ (x = 0.05, 0.25, 0.50, 0.70, 0.75 and 0.95), were prepared from high-purity metal and boron powders: amorphous boron (99+%, Strem Chemicals, USA), gadolinium (99%, Sigma-Aldrich, USA), zirconium (99.5%, Strem Chemicals, USA), yttrium (Strem Chemicals, 99.9%), hafnium (99.9%, Strem Chemicals, USA). A metal to boron molar ratio

of at least 1 : 20 was used to suppress the formation of lower borides (HfB_2, ZrB_2, GdB_6, and YB_6) and promote the formation of dodecaboride phases (MB_{12}). The weighed mixtures were homogenized with a vortex mixer for ~1 minute, then pressed in a hydraulic press (Carver) under ~10 tons before being arc melted (I > 70 amps, T = 1 - 2 min) under a high purity Ar atmosphere to prevent oxidation.

Subsequent ingots were then gently fractured into 2 - 4 pieces using a tool steel Plattner-style diamond crusher. For powder XRD, about half of each sample was crushed using the aforementioned tool steel Plattner-style diamond crusher into a −325 mesh (⩽ 45 μm) powder. PXRD was performed on a Bruker D8 Discover powder X-ray diffractometer (Bruker Corporation, Germany) utilizing a CuKα X-ray beam (λ = 1.5418 Å) in the 5 - 100° 2θ range with a scan speed of 0.1055°/s, time per step of 0.3 s. The phases analyzed were cross-referenced against the Joint Committee on Powder Diffraction Standards (JCPDS) database. *Maud* software was used to perform the unit cell refinements.[27–31]

The remaining ingots were encapsulated in an epoxy/hardener set (Allied High Tech Products Inc., USA), and then polished to an optically flat finish on a semi-automated polisher (Southbay Technology Inc., USA) using both silicon carbide abrasive disks of 120 - 1200 grit (Allied High Tech Products Inc., USA) and 30 - 1 μm particle-size diamond films (Southbay Technology Inc., USA).

The polished samples' morphology was analyzed using an UltraDry EDS detector (Thermo Scientific, USA) and an FEI Nova 230 high-resolution scanning electron microscope (FEI Company, USA). Vickers hardness testing was performed using a MicroMet 2103 Vickers microhardness tester (Buehler Ltd., USA) with a pyramidal diamond indenter tip. 15 indents were made at applied loads of 0.49, 0.98, 1.96 N each, and a minimum of 10 indents were made at

loadings of 2.94 and 4.9 N each, and were performed in random areas of the sample. A high resolution optical microscope (Zeiss Axiotech 100HD, Carl Zeiss Vision GmbH, Germany) with 500x magnification was used to measure the length of the diagonals of each indent. Vicker's hardness (H_v) was calculated using Equation 5.1:

$$H_v = \frac{1854.4\,F}{a^2} \tag{5.1}$$

where F is the loading force applied in Newtons (N) and a is the average of the length of the two diagonals of each indent in micrometers.

RESULTS AND DISCUSSION

Powder X-ray diffraction (PXRD) and energy-dispersive X-ray spectroscopy (EDS) were used to determine the purity and phase composition of the samples. Since the primary goal of this work was to study the formation of metal dodecaborides, all samples were prepared with a metal to boron ratios of 1 to 20 in order to promote the formation of higher boride phases (MB_{12}) and suppress the formation of lower borides (MB_2 and MB_6). Samples that were prepared with a stoichiometric amount of boron resulted in a larger proportion of lower borides in the samples.

We first prepared a solid solution between high pressure HfB_{12} and GdB_{12} by arc melting from the elements at ambient pressure. Figure 5-2 shows the PXRD spectra for alloys with nominal composition of $(Hf_{1-x}Gd_x) : 20B$ (x = 0.05, 0.25, 0.50, 0.75, 0.95) in the 2Θ range of 5 – 50°. Figure 5-3 shows the PXRD spectra for alloys with a nominal composition of $(Zr_{1-x-z}Hf_xGd_z) : 20B$, $(Y_{1-x-z}Hf_xGd_z) : 20B$, $(Zr_{1-x-z}Hf_xY_z) : 20B$, $(Zr_{1-x-z}Y_xGd_z) : 20B$ (x and z = 0.25, 0.33 and 0.50, the points were chosen in order to probe the entire ternary metal phase field) in the 2Θ range of 5 – 50°. Table 5-1 lists the values of the cubic unit cell parameters, metal concentration in the ternary dodecaboride phases and hardness values at varied applied loads of 0.49 – 4.9 N of force for the alloys with a nominal composition of $(Zr_{1-x-z}Hf_xGd_z) : 20B$, $(Y_{1-x-z}Hf_xGd_z) : 20B$, $(Zr_{1-x-z}Hf_xY_z) :$

20B, ($Zr_{1-x-z}Y_xGd_z$) : 20B (x and z = 0.25, 0.33 and 0.50). Figure 5-4 shows the SEM and EDS images for alloys with a nominal composition of ($Zr_{0.25}Hf_{0.50}Gd_{0.25}$) : 20B, ($Y_{0.50}Hf_{0.25}Gd_{0.25}$) : 20B, ($Zr_{0.50}Hf_{0.25}Y_{0.25}$) : 20B, ($Zr_{0.25}Y_{0.25}Gd_{0.50}$) : 20B. Figure 5-5 shows the pseudo-ternary phase diagrams (boron content kept constant at 20 boron equivalents). Finally, Figure 5-6 shows the optical images of the surfaces of the alloys with a nominal composition of ($Zr_{1-x-z}Hf_xGd_z$) : 20B, ($Y_{1-x-z}Hf_xGd_z$) : 20B, ($Zr_{1-x-z}Hf_xY_z$) : 20B, ($Zr_{1-x-z}Y_xGd_z$) : 20B (x and z = 0.25, 0.33 and 0.50).

Both HfB_{12}[23] and GdB_{12}[24] are high pressure phases (6.5 GPa) and can be stabilized by inserting the "smaller atom into a larger host atom dodecaboride matrix" ($Y_{1-x}Hf_xB_{12}$)[17] and vice versa ($Zr_{1-x}Gd_xB_{12}$)[16] using the principle outlined above. Thus, a hypothetical solid solution of $Hf_{1-x}Gd_xB_{12}$ should be stable as the larger Gd (1.801 Å)[23] will be compensated for by the smaller Hf (1.580 Å)[23]. However, when combined together in an alloy with a nominal composition of ($Hf_{1-x}Gd_x$) : 20B (Figure 5-2), it could be observed that no metal dodecaboride phase forms. The only phases present are diboride (HfB_2) and HfB_{50} (at higher concentrations of hafnium) and hexaboride (GdB_6) and GdB_{66} (at higher concentrations of gadolinium), with intermediate compositions having all of the aformentioned phases. This suggests that these two high pressure phases are unable to stabilize each other and might require a stable dodecaboride matrix in order to form at ambient pressure. Previous work had shown that HfB_{12} can be stabilized with YB_{12}, and GdB_{12} with ZrB_{12}. This is exactly what happens once Zr or Y are added to the composition, resulting in alloys with the following nominal compositions: ($Zr_{1-x-z}Hf_xGd_z$) : 20B, ($Y_{1-x-z}Hf_xGd_z$) : 20B (x and z = 0.25 and 0.50 (Figure 5-3).

In the case of ($Zr_{1-x-z}Hf_xGd_z$) : 20B (Figure 5-3a, Table 5-1), a ternary metal dodecaboride (MB_{12}) can be observed for all four compositions, with the alloys with nominal compositions of ($Zr_{0.33}Hf_{0.33}Gd_{0.33}$): 20B and ($Zr_{0.50}Hf_{0.25}Gd_{0.25}$): 20B, respectively, containing only the ternary

dodecaboride and a boron rich phase ($Hf_{1-x}Zr_xB_{50}$). The EDS analysis gives the following composition of the ternary dodecaboride: $Zr_{0.478}Hf_{0.155}Gd_{0.367}B_{12}$ and $Zr_{0.643}Hf_{0.104}Gd_{0.253}B_{12}$, respectively. Since ZrB_{12} is known to stabilize GdB_{12} and the $Zr_{1-x}Gd_xB_{12}$ solid solution exists until the concentration of gadolinium of 55 at.% Gd[16], but the solubility of HfB_{12} in ZrB_{12} is very limited,[17] we speculate that during the course of synthesis a meta-stable $Zr_{1-x}Gd_xB_{12}$ matrix forms first and then stabilizes HfB_{12} in it. A similar obervation can be made for the alloy with a nominal composition of $(Y_{1-x-z}Hf_xGd_z)$: 20B (Figure 5-3b, Table 5-1), where a ternary dodecaboride phase exists for three compositions. And since YB_{12} can stabilize HfB_{12} until a composition of $Y_{0.633}Hf_{0.367}B_{12}$, and solubility of GdB_{12} in YB_{12} is very limited, it could also be speculated that a $Y_{1-x}Hf_xB_{12}$ matrix forms first and then stabilizes GdB_{12} in it.

For the other compositions of $(Y_{1-x-z}Hf_xGd_z)$: 20B (Figure 5-3a, Table 5-1), secondary phases (di- and hexaborides, $Hf_{1-x}Zr_xB_2$ and $Gd_{1-x}Y_xB_6$) form, resulting from the excess amount of hafnium and gadolinium over the solubility limit in the ternary dodecaboride phases. In all cases, the main boride phases are accompanied by boron-rich phases ($Hf_{1-x}Zr_xB_{50}$ ($R\bar{3}m$)). For the other compositions of $(Y_{1-x-z}Hf_xGd_z)$: 20B (Figure 5-3b, Table 5-1), secondary phases (hexaborides, $Gd_{1-x}Y_xB_6$) form, resulting from the excess amount of gadolinium over the solubility limit in the ternary dodecaboride phases. The main boride phases are also accompanied by boron-rich phases (HfB_{50} ($R\bar{3}m$) and $Gd_{1-x}Y_xB_{66}$ ($Fm\bar{3}c$)). Only in the case of the alloy with a nominal composition of $(Y_{0.25}Hf_{0.25}Gd_{0.50})$: 20B, the main phase is a solid solution $Gd_{1-x}Y_xB_6$, resulting from a low amount of yttrium which is not enough to stabilize the ternary dodecaboride phase.

In the case of alloys with a nominal composition of $(Zr_{1-x-z}Hf_xY_z)$: 20B and $(Zr_{1-x-z}Y_xGd_z)$: 20B (Figure 5-3c-d, Table 5-1), the ternary metal dodecaboride is present at all compositions. Both zirconium and yttrium form stable dodecaborides (ZrB_{12} and YB_{12}) at ambient pressure, and thus,

are completely soluble in each other, forming the $Zr_{1-x}Y_xB_{12}$ solid solution at all compositions.[15] In both of these cases, the formation of ternary dodecaborides is highly favorable since for two out of three pairings of metals, the phases are either completely soluble ($Zr_{1-x}Y_xB_{12}$) or can be stabilized at ambient pressure ($Y_{1-x}Hf_xB_{12}$ and $Zr_{1-x}Gd_xB_{12}$, respectively). The secondary phases formed are diboride ($Hf_{1-x}Zr_xB_2$) for an alloy with a nominal composition of ($Zr_{0.25}Hf_{0.50}Y_{0.25}$) : 20B and hexaboride ($Gd_{1-x}Y_xB_6$) for an alloy with a nominal composition of ($Zr_{0.25}Y_{0.25}Gd_{0.50}$) : 20B.

Figure 5-4 shows the SEM and EDS elemental maps for alloys with a nominal composition of ($Zr_{0.25}Hf_{0.50}Gd_{0.25}$) : 20B, ($Y_{0.50}Hf_{0.25}Gd_{0.25}$) : 20B, ($Zr_{0.50}Hf_{0.25}Y_{0.25}$) : 20B, ($Zr_{0.25}Y_{0.25}Gd_{0.50}$) : 20B. For ($Y_{0.50}Hf_{0.25}Gd_{0.25}$) : 20B and ($Zr_{0.50}Hf_{0.25}Y_{0.25}$) : 20B a ternary metal dodecaboride phase can be observed, while for ($Zr_{0.25}Hf_{0.50}Gd_{0.25}$) : 20B and ($Zr_{0.25}Y_{0.25}Gd_{0.50}$) : 20B, lower boride phases (diborides and hexaborides, respectively) can be observed.

Based on the combined information from PXRD and EDS, one can construct limited composition pseudo-ternary (boron content is kept at a constant level of 20Boron equivalents) phase diagrams (Figure 5-5). ($Zr_{1-x-z}Hf_xGd_z$) : 20B, ($Y_{1-x-z}Hf_xGd_z$) : 20B, ($Zr_{1-x-z}Hf_xY_z$) : 20B, ($Zr_{1-x-z}Y_xGd_z$) : 20B, ($Hf_{1-x}Gd_x$) : 20B and ($Y_{1-x}Gd_x$) : 20B were analyzed in this manuscript, while data for other compositions were taken from previous publications: ($Zr_{1-x}Gd_x$) : 20B,[16] ($Zr_{1-x}Hf_x$) : 20B, ($Y_{1-x}Hf_x$) : 20B[17] and ($Zr_{1-x}Y_x$) : 20B.[15] Although there are known phase diagrams for binary systems: B-Zr,[32] B-Y,[33] B-Gd[34] and B-Hf,[35] and some ternary systems: B-Zr-Gd, B-Hf-Gd[36] and B-Zr-Hf,[37] they do not currently exist for some other systems: B-Zr-Y, B-Y-Hf and B-Y-Gd. Therefore, although there is only a limited number of data points for the ternary boride compositions, we feel that these pseudo-ternary phase diagrams might be a helpful starting point for a complete investigation of these systems (at a constant boron level) and elucidation of more precise phase

boundaries.

Figure 5-6 shows the optical images of the polished surfaces for: (a) ($Zr_{1-x-z}Hf_xGd_z$) : 20B; (b) ($Y_{1-x-z}Hf_xGd_z$) : 20B; (c) ($Zr_{1-x-z}Hf_xY_z$) : 20B; (d) ($Zr_{1-x-z}Y_xGd_z$) : 20B, where x and z = 0.25, 0.33 and 0.50. In all cases, the dodecaboride MB_{12} phases exhibit a color in the blue-violet range, while hexaboride MB_6 phases exhibit deep blue colors, diboride phases (white streaks) are colorless, whereas other areas correspond to the boron rich (also colorless) phases: MB_{50} (for Zr and Hf) and MB_{66} (for Y and Gd). For hexa- and dodecaborides the blue color is due to the metals in +3 oxidation states (Y and Gd), while the violet color is due to the metals in +4 oxidation states (Zr and Hf).[38] The color range can be used as another proof of the formation of ternary dodecaboride solid solutions for most of the aformentioned alloys.

The mechanical properties of the alloys were investigated using Vickers hardness testing (Table 5-1), in hopes that the varying metal radii will result in significant solid solution hardening. In most cases of the ternary boride alloys, the hardest compositions correspond to the samples which are majority Zr or Y or at the point in the middle of the ternary metal "phase field": $Zr_{0.50}Hf_{0.25}Gd_{0.25}$: 20B, $Y_{0.50}Hf_{0.25}Gd_{0.25}$: 20B, $Zr_{0.50}Y_{0.25}Gd_{0.25}$: 20B; $Zr_{0.33}Hf_{0.33}Gd_{0.33}$: 20B, $Y_{0.33}Hf_{0.33}Gd_{0.33}$: 20B, $Zr_{0.33}Hf_{0.33}Y_{0.33}$: 20B, $Zr_{0.33}Y_{0.33}Gd_{0.33}$: 20B. In all of these cases, the phases are harder than their "pure parent" phases. The hardest compound is $Zr_{0.50}Y_{0.25}Gd_{0.25}$: 20B nominal alloy composition having a hardness of 46.9 ± 2.4 GPa compared to 41.3 ± 1.1 and 41.6 ± 1.3 GPa for alloy compositions of 1.0 Zr : 20B and 1.0 Y : 20B, respectively, at 0.49 N of applied load. It can be speculated that in all of these cases the hardness increase is due to a combination of solid-solution hardening and the differences in metal valence and atomic size.[15–17]

CONCLUSIONS

In this manuscript, we have successfully synthesized ternary metal alloys with nominal

compositions of $(Zr_{1-x-z}Hf_xGd_z)$: 20B, $(Y_{1-x-z}Hf_xGd_z)$: 20B, $(Zr_{1-x-z}Hf_xY_z)$: 20B, $(Zr_{1-x-z}Y_xGd_z)$: 20B (x and z = 0.25, 0.33 and 0.5). It was discovered that for most of the compositions, a ternary metal dodecaboride phase (MB_{12}) forms. The hardness of all the compounds was measured, with the hardest composition being $Zr_{0.50}Y_{0.25}Gd_{0.25}$: 20B nominal alloy composition having a hardness of 46.9 ± 2.4 GPa at 0.49 N of applied load. This value is 10% higher than it two parents 1.0 Zr : 20B and 1.0 Y : 20B. Using the data from this manuscript and previous research, pseudo-ternary phase diagrams (with a constant boron content) have been created. Although, there is a limited amount of data points for the ternary boride compositions, these pseudo-ternary phase diagrams might be a helpful starting point for a complete investigation of these systems (at a constant boron level) and elucidation of more precise phase boundaries.

ACKNOWLDGEMENTS

We thank the National Science Foundation Division of Materials Research, Grant DMR-1506860 (R.B.K.) for financial support.

Table 5-1. Unit Cell Data and Compositions for $(Zr_{1-x-z}Hf_xGd_z)$: 20B, $(Y_{1-x-z}Hf_xGd_z)$: 20B, $(Zr_{1-x-z}Hf_xY_z)$: 20B, $(Zr_{1-x-z}Y_xGd_z)$: 20B.

Nominal Composition	MB_{12} Cubic Cell (Å)			Metal Concentration (EDS)[c] (at.% metal)			Vickers Hardness (GPa)[d]									
							0.49 N		0.98 N		1.96 N		2.98 N		4.9 N	
	a_{nom}[a]	a_{XRD}[b]	a_{EDS}[a]	M_1	M_2	M_3										
$Zr_{0.33}Hf_{0.33}Gd_{0.33}$: 20B	7.362	7.458(2)	7.446	47.78	15.54	36.68	42.1	2.3	35.4	1.1	33.3	0.7	32.0	0.9	29.4	1.0
$Zr_{0.50}Hf_{0.25}Gd_{0.25}$: 20B	7.429	7.448(3)	7.434	64.29	10.38	25.33	43.7	1.8	36.9	1.2	34.3	1.6	31.8	0.9	29.4	1.2
$Zr_{0.25}Hf_{0.50}Gd_{0.25}$: 20B	7.422	7.454(2)	7.448	49.94	12.35	37.71	41.9	1.6	33.9	1.2	31.5	1.5	30.2	0.8	28.1	0.7
$Zr_{0.25}Hf_{0.25}Gd_{0.50}$: 20B	7.458	7.453(5)	7.445	41.08	21.17	37.74	42.4	3.5	36.5	1.4	33.7	1.9	32.3	1.6	30.2	1.4
$Y_{0.33}Hf_{0.33}Gd_{0.33}$: 20B	7.394	7.484(4)	7.488	57.04	16.79	26.17	44.8	2.0	34.6	1.3	32.0	1.8	30.9	1.3	28.5	1.8
$Y_{0.50}Hf_{0.25}Gd_{0.25}$: 20B	7.478	7.488(3)	7.480	64.85	21.73	13.42	43.2	2.0	37.4	1.5	33.8	1.5	31.9	1.7	30.8	0.7
$Y_{0.25}Hf_{0.50}Gd_{0.25}$: 20B	7.446	7.472(3)	7.474	44.62	28.13	27.25	43.2	2.8	35.9	2.1	33.3	2.1	31.8	1.9	28.6	1.2
$Y_{0.25}Hf_{0.25}Gd_{0.50}$: 20B	7.483	N/A	N/A	N/A	N/A	N/A	37.6	4.0	30.9	1.8	27.1	1.0	25.7	1.8	25.4	1.8
$Zr_{0.33}Hf_{0.33}Y_{0.33}$: 20B	7.357	7.442(1)	7.445	43.88	14.61	41.51	45.2	2.6	35.0	1.6	32.3	1.3	30.9	1.3	29.9	0.5
$Zr_{0.50}Hf_{0.25}Y_{0.25}$: 20B	7.427	7.460(1)	7.437	59.35	10.01	30.63	42.0	2.8	36.4	2.1	31.6	1.4	29.6	1.6	29.5	0.8
$Zr_{0.25}Hf_{0.50}Y_{0.25}$: 20B	7.418	7.435(3)	7.460	32.19	11.48	56.33	44.2	2.8	35.5	1.7	33.0	1.7	31.9	1.6	29.3	1.3
$Zr_{0.25}Hf_{0.25}Y_{0.50}$: 20B	7.450	7.436(4)	7.450	32.52	19.35	48.12	41.9	2.9	33.8	1.4	30.4	1.3	29.9	1.2	29.2	1.0
$Zr_{0.33}Y_{0.33}Gd_{0.33}$: 20B	7.406	7.480(6)	7.472	40.83	35.21	23.97	42.1	2.6	33.4	1.8	31.9	1.2	30.2	1.0	27.5	0.4
$Zr_{0.50}Y_{0.25}Gd_{0.25}$: 20B	7.463	7.460(2)	7.453	59.48	24.26	16.27	46.9	2.4	35.1	1.0	32.2	1.7	30.6	1.3	28.7	1.3
$Zr_{0.25}Y_{0.50}Gd_{0.25}$: 20B	7.487	7.486(3)	7.477	33.72	50.18	16.09	41.1	1.9	33.5	1.7	30.8	1.1	29.3	0.8	28.0	0.7
$Zr_{0.25}Y_{0.25}Gd_{0.50}$: 20B	7.491	7.480(3)	7.465	49.16	20.17	30.67	42.1	2.5	36.0	1.9	32.9	1.6	31.1	1.5	29.3	1.5
1.0 Zr : 20B	7.408	7.412(2)	-	-	-	-	41.3	1.1	34.9	0.5	33.6	0.7	31.3	0.6	29.6	0.7
1.0 Y : 20B	7.500	7.505(4)	-	-	-	-	41.6	1.3	34.4	1.3	32.7	1.1	30.5	0.8	28.5	0.7
$Y_{0.25}Hf_{0.75}$: 20B[e]	7.409	7.458(3)	7.463	66.99	33.01	-	44.1	1.7	36.5	1.2	34.6	0.8	31.9	0.7	30.8	0.7
$Zr_{0.50}Gd_{0.50}$: 20B[e]	7.468	7.464(2)	7.469	49.17	50.83	-	42.1	1.9	34.7	1.1	32.6	0.7	31.9	0.6	29.1	0.5

[a]calculated from nominal and EDS metal compositions using Vegard's Law[39]; [b]from *Maud*[27–31], errors are given in brackets ($a(ZrB_{12})$ = 7.408 Å, $a(YB_{12})$ = 7.500 Å, $a(GdB_{12})$ = 7.524 Å, $a(HfB_{12})$ = 7.377 Å);[14,23,24] [c]errors for EDS values of metal compositions are within ±2.0 at.%, M_1 = Zr or Y, M_2 = Hf or Y, M_3 = Y or Gd; [d]errors for hardness are given next to the hardness values; [e]since both HfB_{12} ad GdB_{12} are high pressure phases, these solid solutions are the closest representation of the properties of these high pressure phases.[16,17]

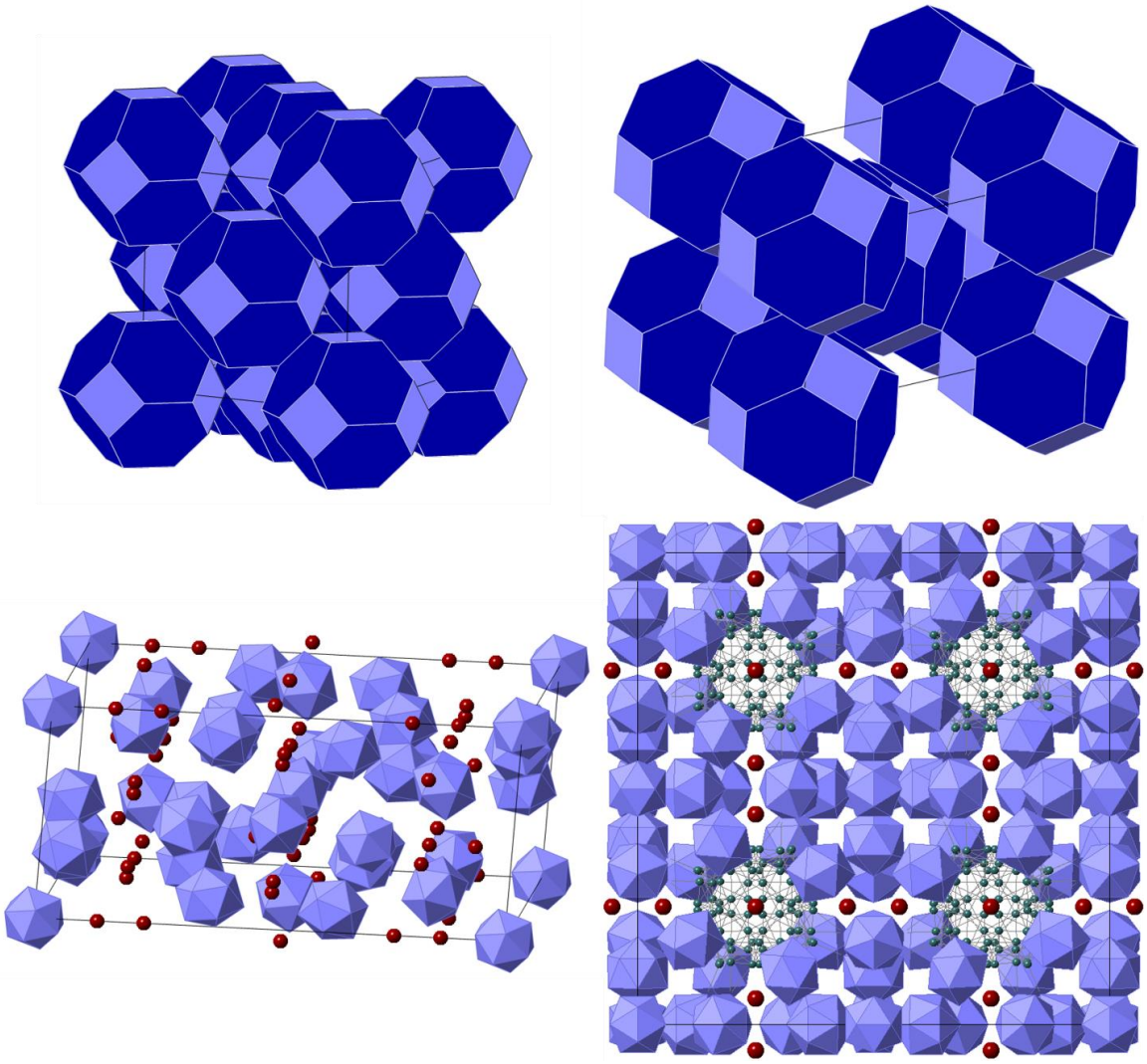

Figure 5-1. (Top left) Polyhedra model of the unit cell of a cubic-UB_{12} (ZrB_{12}, $Fm\bar{3}m$, ICSD 409635)[40] structural type metal dodecaboride: 24 boron atom cuboctahedra cages (square faces shown in red, hexagonal face in green) are arranged in a FCC lattice, with a 12 - coordinate metal atom in the center of each cage; (top right) polyhedra model of the unit cell of a tetragonal-ScB_{12} (ScB_{12}, I4/mmm, ICSD 615424)[41] structural type metal dodecaboride: 24 boron atom cuboctahedra cages (square faces shown in red, hexagonal faces in green) are arranged in a BCT lattice, with a 12-coordinate metal atom in the center of each cage; Note, metals are considered 12-coordinate since 12 boron-boron bonds are equidistant from each metal atom in the 24 boron atom cuboctahedron cage; (bottom left) polyhedra model of the unit cell of a rhombohedral-MB_{50} ($R\bar{3}m$, ICSD 40396)[42] structural type (solid solution of a metal in β-rhombohedral boron): boron atoms are arranged in B_{12} icosahedral units (shown in green), metal atoms are in blue; (bottom right) polyhedra model of the unit cell of a cubic-YB_{66} ($Fm\bar{3}c$, ICSD 23186)[18] structural type metal boride: boron atoms are arranged in B_{12} icosahedral units (shown in green), boron atoms not forming icosahedra are in red, metal atoms are in blue. "Reprinted (adapted) with permission from (Akopov, G., Sobell, Z.C., Yeung, M.T., and Kaner, R.B. *Inorganic Chemistry* 2016 *55* (23), 12419-12426 DOI: 10.1021/acs.inorgchem.6b02311). Copyright (2016) American Chemical Society."

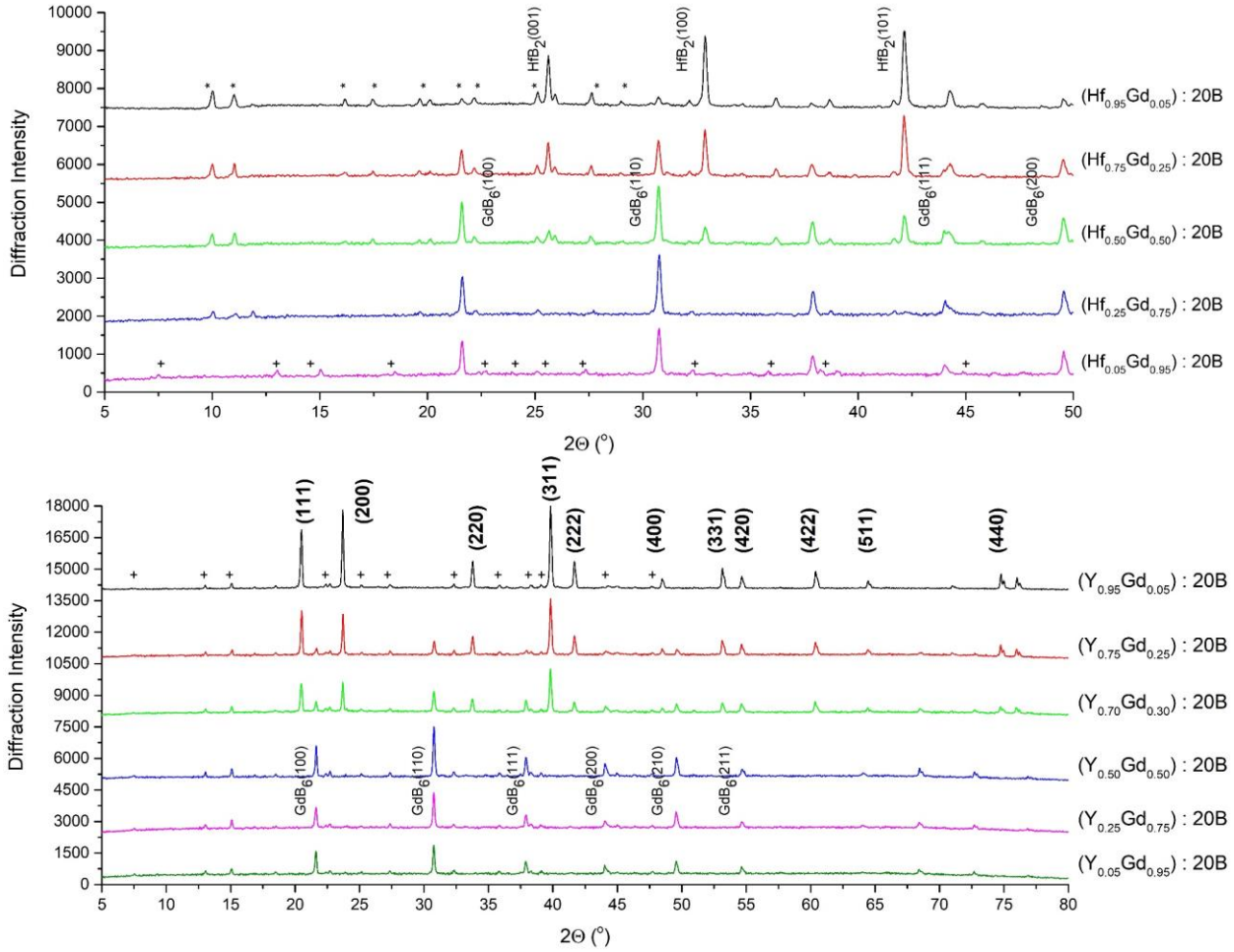

(b)

Figure 5-2. Powder XRD patterns of: (a) $(Hf_{1-x}Gd_x)$: 20 B, where x = 0.05, 0.25, 0.50, 0.75 and 0.95. The dodecaboride MB_{12} phase does not form for any composition of this alloy. The diboride (HfB_2, P6/mmm, JCPDS 03-065-3387) phase forms at higher concentrations of hafnium, while the hexaboride (GdB_6, $Pm\bar{3}m$, JCPDS 03-065-1826) phase forms for higher concentrations of gadolinium; (b) $(Y_{1-x}Gd_x)$: 20 B, where x = 0.05, 0.25, 0.50, 0.70, 0.75 and 0.95. The dodecaboride MB_{12} phase disappears for compositions of this alloy greater than 30 at.% Gd, with the hexaboride (GdB_6, $Pm\bar{3}m$, JCPDS 03-065-1826) phase forming at higher concentrations of gadolinium. (*) indicates the boron rich phase - solid solution of hafnium in β-rhombohedral boron (HfB_{50}, $R\bar{3}m$, JCPDS 01-086-2400), while (+) indicates GdB_{66} ($Fm\bar{3}c$, JCPDS 00-024-1256).

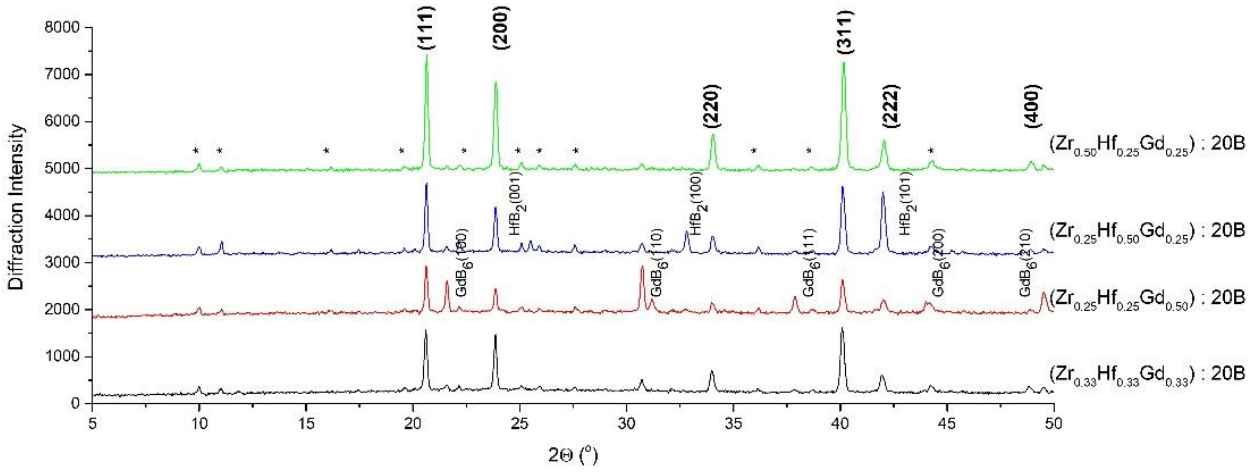
Diffraction Intensity
2Θ (°)
(111)
(200)
(220)
(311)
(222)
(400)
HfB2(001)
HfB2(100)
HfB2(101)
GdB6(100)
GdB6(110)
GdB6(111)
GdB6(200)
GdB6(210)
(Zr0.50Hf0.25Gd0.25) : 20B
(Zr0.25Hf0.50Gd0.25) : 20B
(Zr0.25Hf0.25Gd0.50) : 20B
(Zr0.33Hf0.33Gd0.33) : 20B

(a)

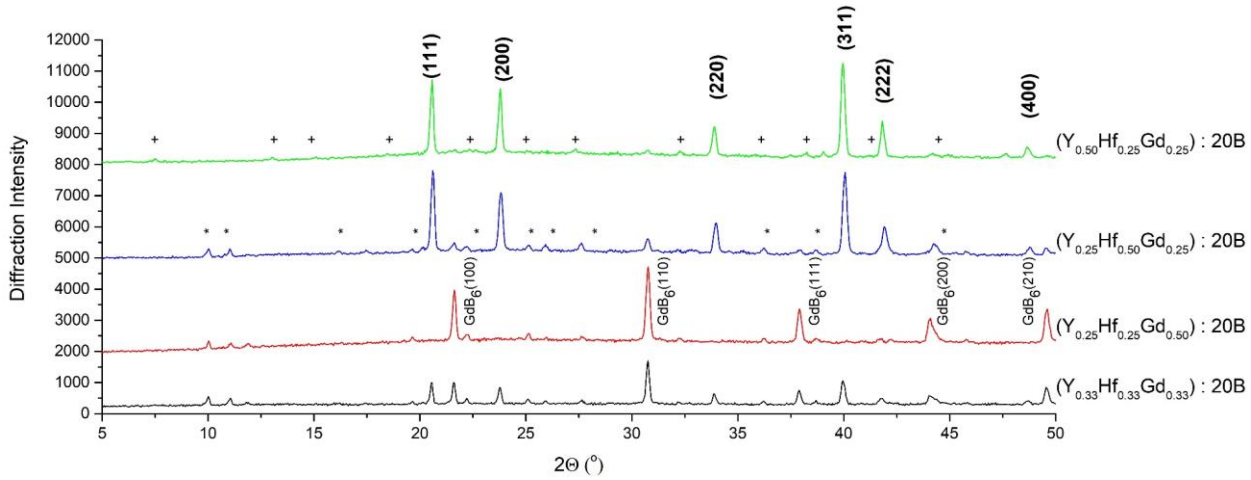
Diffraction Intensity
2Θ (°)
(111)
(200)
(220)
(311)
(222)
(400)
GdB6(100)
GdB6(110)
GdB6(111)
GdB6(200)
GdB6(210)
(Y0.50Hf0.25Gd0.25) : 20B
(Y0.25Hf0.50Gd0.25) : 20B
(Y0.25Hf0.25Gd0.50) : 20B
(Y0.33Hf0.33Gd0.33) : 20B

(b)

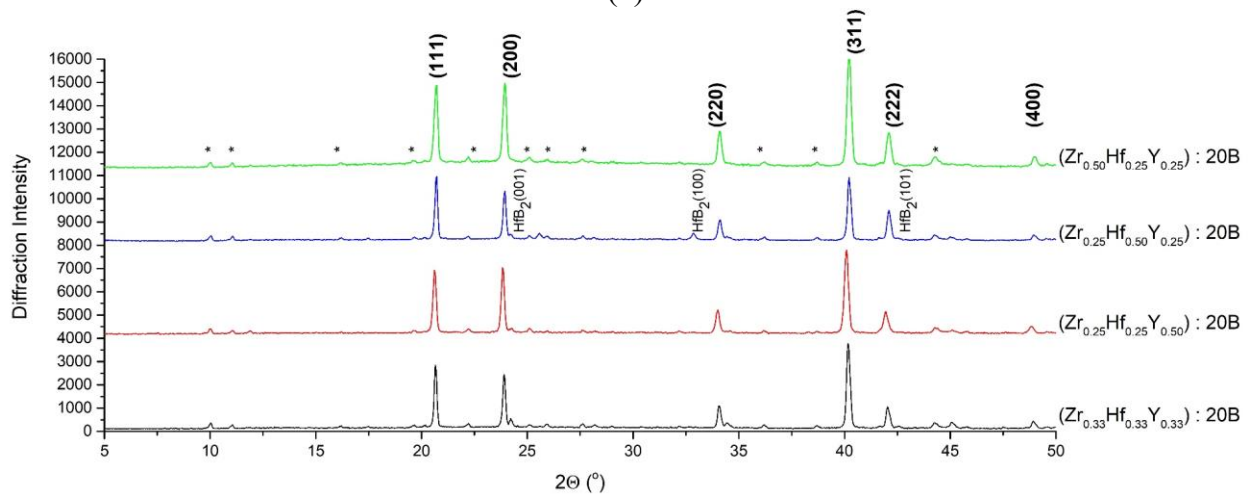
Diffraction Intensity
2Θ (°)
(111)
(200)
(220)
(311)
(222)
(400)
HfB2(001)
HfB2(100)
HfB2(101)
(Zr0.50Hf0.25Y0.25) : 20B
(Zr0.25Hf0.50Y0.25) : 20B
(Zr0.25Hf0.25Y0.50) : 20B
(Zr0.33Hf0.33Y0.33) : 20B

(c)

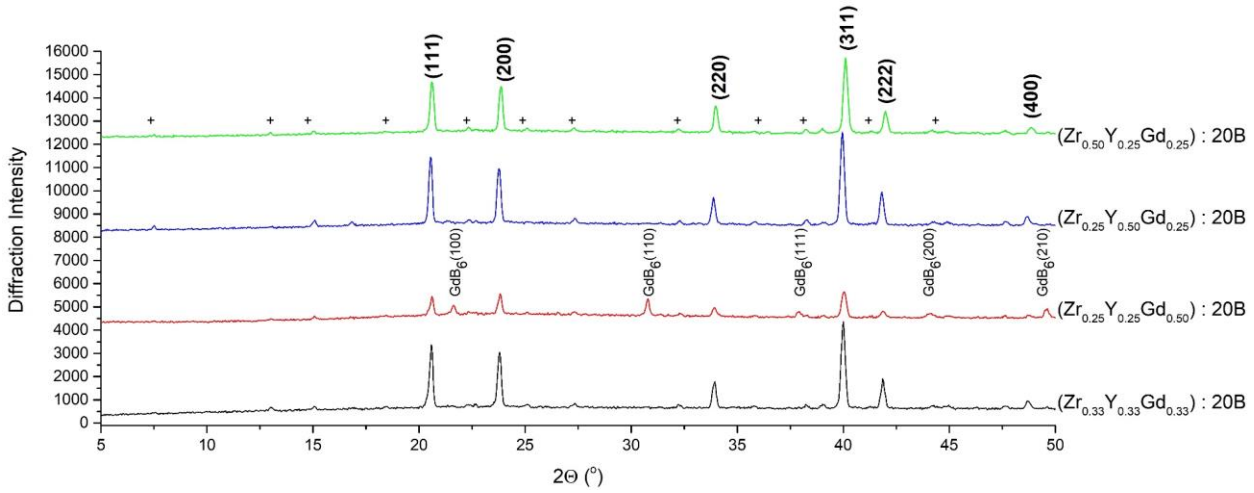

(d)

Figure 5-3. Powder XRD patterns of: (a) ($Zr_{1-x-z}Hf_xGd_z$) : 20B, where x and z = 0.25, 0.33 and 0.50. The ternary dodecaboride MB_{12} phase can be observed for all 4 compositions, the binary diboride MB_2 phase ($Hf_{1-x}Zr_xB_2$ solid solution) can be observed for $Zr_{0.25}Hf_{0.50}Gd_{0.25}$: 20B, while the hexaboride MB_6 phase (GdB_6) can be observed for all phases except for $Zr_{0.50}Hf_{0.25}Gd_{0.25}$: 20B; (b) ($Y_{1-x-z}Hf_xGd_z$) : 20B, where x and z = 0.25, 0.33 and 0.50. The ternary dodecaboride MB_{12} phase can be observed for all compositions, except for $Y_{0.25}Hf_{0.25}Gd_{0.50}$: 20B, while the binary hexaboride MB_6 phase ($Gd_{1-x}Y_xB_6$ solid solution) can be observed for all compositions except for $Y_{0.50}Hf_{0.25}Gd_{0.25}$: 20B; (c) ($Zr_{1-x-z}Hf_xY_z$) : 20B, where x and z = 0.25, 0.33 and 0.50. The ternary dodecaboride MB_{12} phase can be observed for all 4 compositions, the binary diboride MB_2 phase ($Hf_{1-x}Zr_xB_2$ solid solution) can be observed for $Zr_{0.25}Hf_{0.50}Y_{0.25}$: 20B, while the hexaboride MB_6 phase (YB_6) can be observed for all phases except for $Zr_{0.50}Hf_{0.25}Y_{0.25}$: 20B; (d) ($Zr_{1-x-z}Y_xGd_z$) : 20B, where x and z = 0.25, 0.33 and 0.50. The ternary dodecaboride MB_{12} phase can be observed for all 4 compositions, the binary hexaboride MB_6 phase ($Gd_{1-x}Y_xB_6$ solid solution) can be observed for $Zr_{0.25}Y_{0.25}Gd_{0.50}$: 20B. For all cases: (*) define the boron rich phase - solid solution of hafnium-zirconium in β-rhombohedral boron ($Hf_{1-x}Zr_xB_{50}$), both $R\bar{3}m$, JCPDS 01-086-2400 and 03-065-2184, respectively); while (+) define GdB_{66} and YB_{66} or their solid solutions (both $Fm\bar{3}c$, JCPDS 00-024-1256 and 01-073-0759, respectively). The peaks were assigned using: HfB_2, *P6/mmm*, JCPDS 03-065-3387, GdB_6, $Pm\bar{3}m$, JCPDS 03-065-1826 and ZrB_{12}, $Fm\bar{3}m$, JCPDS 03-065-3100.

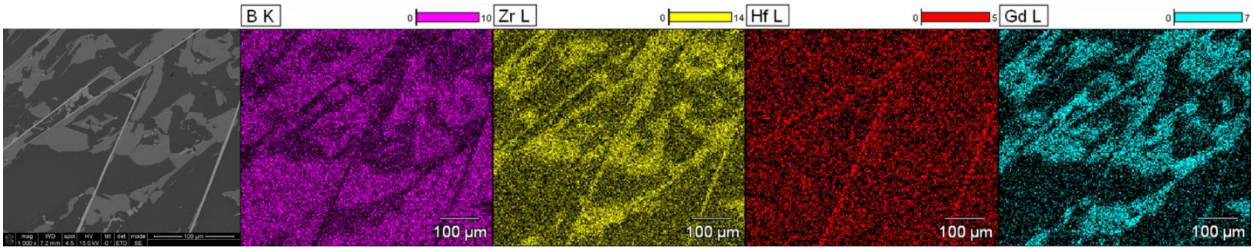

(a)

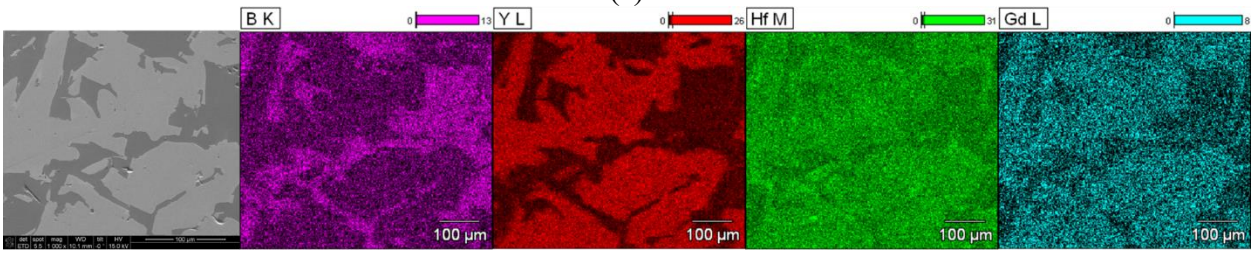

(b)

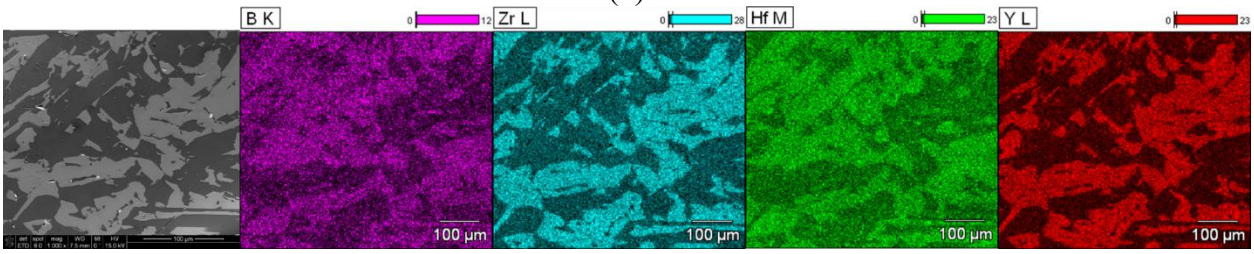

(c)

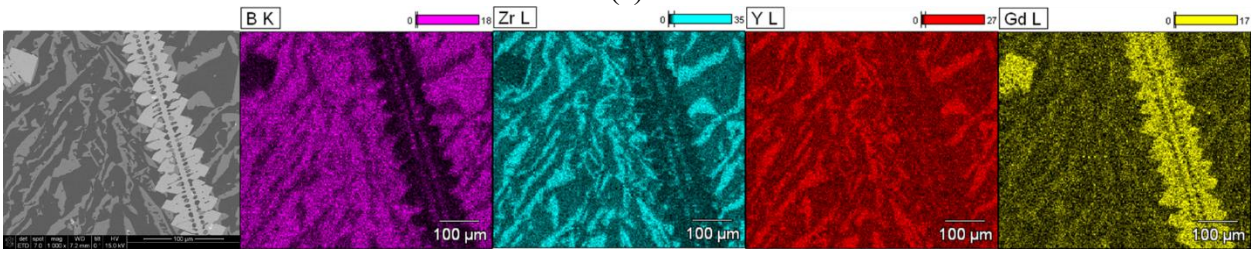

(d)

Figure 5-4. Elemental maps for boron (K line), zirconium, yttrium, gadolinium (L lines) and hafnium (M line) of: (a) the $Zr_{0.25}Hf_{0.50}Gd_{0.25}$: 20B, dodecaboride MB_{12} as well as $Zr_{1-x}Hf_xB_2$ solid solution phases; (b) $Y_{0.50}Hf_{0.25}Gd_{0.25}$: 20B, dodecaboride MB_{12} phase; (c) $Zr_{0.50}Hf_{0.25}Y_{0.25}$: 20B, dodecaboride MB_{12} phase; (d) $Zr_{0.25}Y_{0.50}Gd_{0.25}$: 20B, dodecaboride MB_{12} as well as hexaboride GdB_6 phases. The thick horizontal bars represent the intensity as a color legend. The SEM images were taken at a magnification of 1000x, while the EDS images at 500x, the scale bars are 100 µm in all cases.

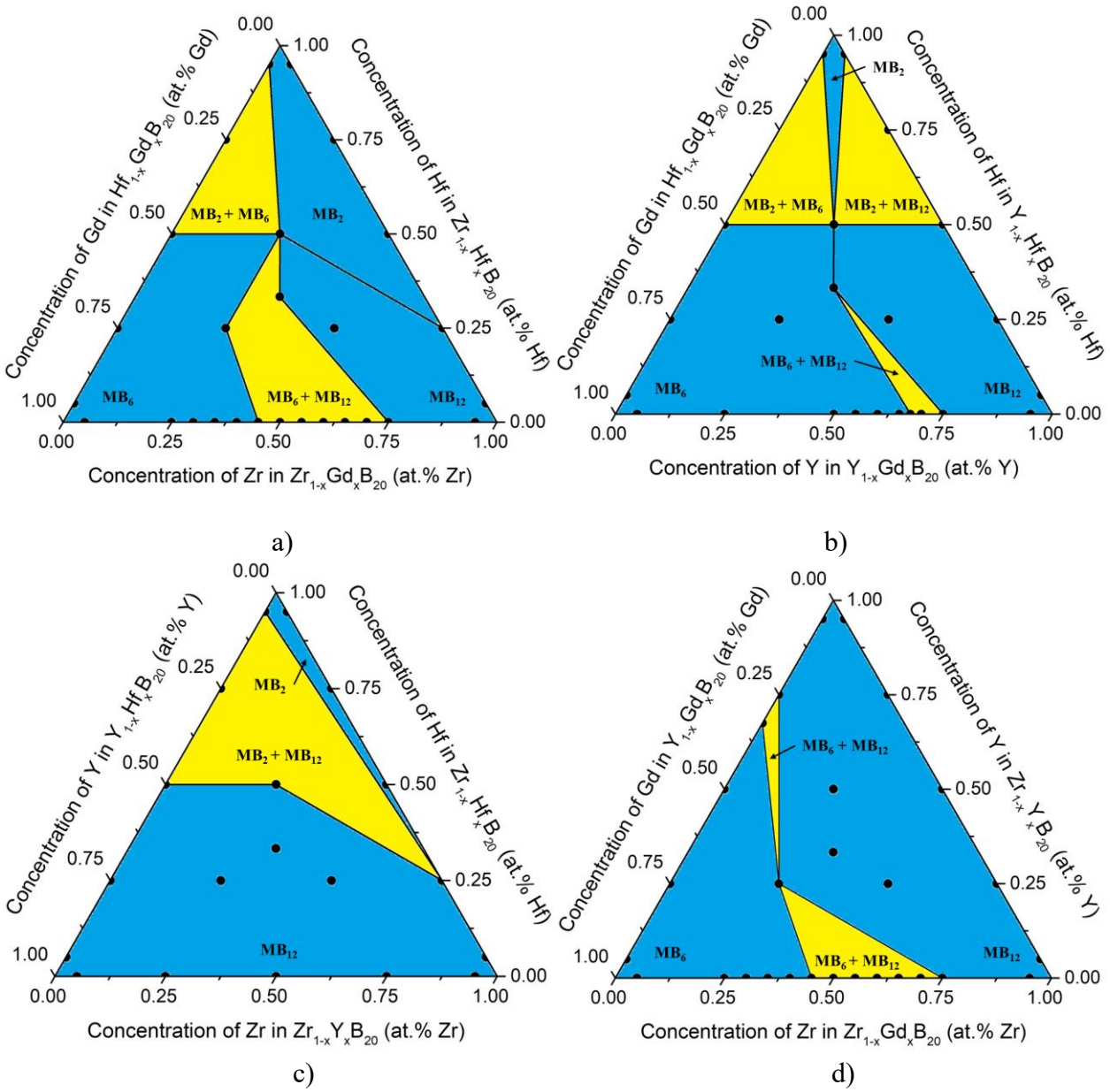

Figure 5-5. Pseudo-ternary phase diagrams (limited compositions, metal to boron ratio is kept constant at 1 : 20) for: (a) $(Zr_{1-x-z}Hf_xGd_z) : 20B$; (b) $(Y_{1-x-z}Hf_xGd_z) : 20B$; (c) $(Zr_{1-x-z}Hf_xY_z) : 20B$; (d) $(Zr_{1-x-z}Y_xGd_z) : 20B$. In all cases x and z = 0.25, 0.33 and 0.50; black dots correspond to the analyzed compositions; the blue regions correspond to compositions with single boride phases, while yellow regions to compositions with two distinct boride phases. MB_{12} corresponds to ternary dodecaborides of Zr, Y, Hf and Gd; MB_2 to binary diborides $(Hf_{1-x}Zr_xB_2)$; and MB_6 to binary hexaborides $(Gd_{1-x}Y_xB_6)$. Due to the excess of boron in the samples, in all cases the main boride phases are accompanied by boron rich phases and their solid solutions: MB_{50} (for Zr and Hf) and MB_{66} (for Y and Gd). $(Zr_{1-x-z}Hf_xGd_z) : 20B$, $(Y_{1-x-z}Hf_xGd_z) : 20B$, $(Zr_{1-x-z}Hf_xY_z) : 20B$, $(Zr_{1-x-z}Y_xGd_z) : 20B$, $(Hf_{1-x}Gd_x) : 20B$ and $(Y_{1-x}Gd_x) : 20B$ were analyzed in this manuscript, while data for other compositions were taken from previous publications: $(Zr_{1-x}Gd_x) : 20B$,[16] $(Zr_{1-x}Hf_x) : 20B$, $(Y_{1-x}Hf_x) : 20B$[17] and $(Zr_{1-x}Y_x) : 20B$.[15]

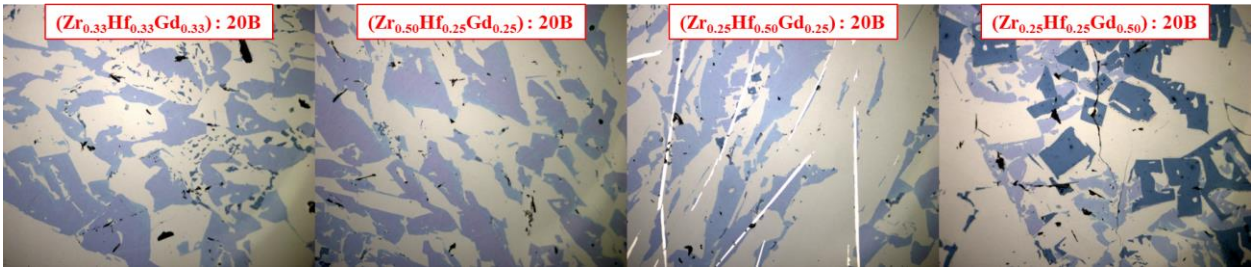

(a)

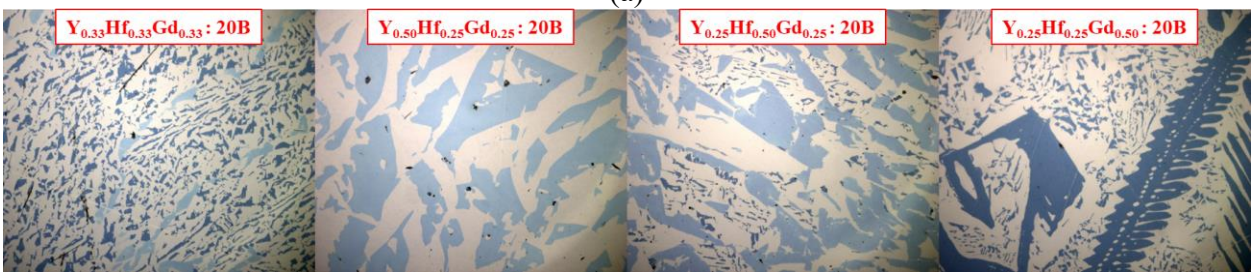

(b)

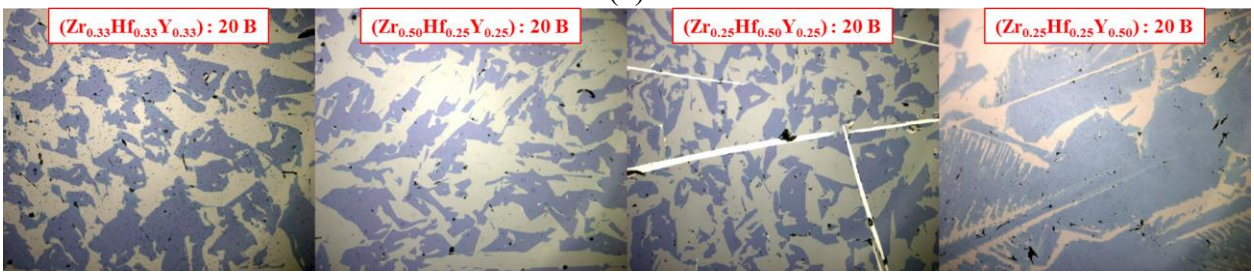

(c)

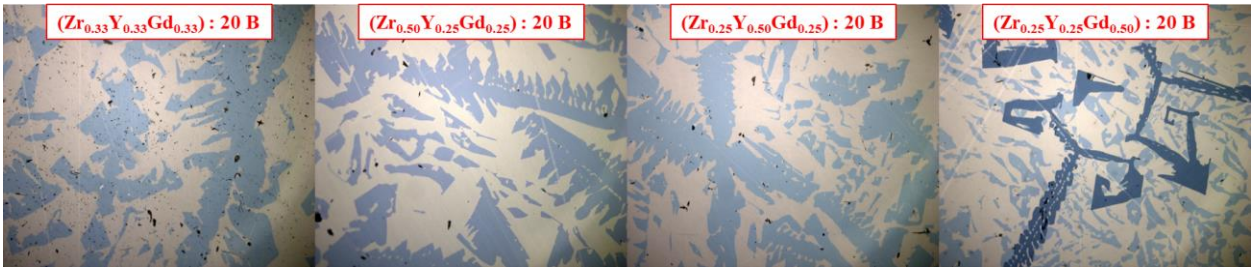

(d)

Figure 5-6. Optical images of the polished surfaces for: (a) $(Zr_{1-x-z}Hf_xGd_z)$: 20B; (b) $(Y_{1-x-z}Hf_xGd_z)$: 20B; (c) $(Zr_{1-x-z}Hf_xY_z)$: 20B; (d) $(Zr_{1-x-z}Y_xGd_z)$: 20B, where x and z = 0.25, 0.33 and 0.50. In all cases the dodecaboride MB_{12} phases exhibit a color from the blue-violet range, hexaboride MB_6 phases exhibit a deep blue color, diboride phases (white streaks) are colorless, while other areas correspond to the boron rich (also colorless) phases: MB_{50} (for Zr and Hf) and MB_{66} (for Y and Gd). For hexa- and dodecaborides the blue color is due to the metals in +3 oxidation states (Y and Gd), while the violet color is due to the metals in +4 oxidation states (Zr and Hf).[38]

REFERENCES

1. Samsonov, G. V., Markovskii, L. Y., Zhigach, A. F. & Valyashko, M. G. *Boron, Its Compounds and Alloys [in Russian]*. (House of the Academy of the Sciences Ukrainian SSR, 1960).
2. Samsonov, G. V., Serebriakova, T. I. & Neronov, V. A. *Borides [in Russian]*. (Atomizdat, 1975).
3. Scheifers, J. P., Zhang, Y. & Fokwa, B. P. T. Boron: Enabling Exciting Metal-Rich Structures and Magnetic Properties. *Acc. Chem. Res.* **50,** 2317–2325 (2017).
4. Buschow, K. H. J. Magnetic Properties of Borides. in *Boron and Refractory Borides* (ed. Matkovich, V. I.) 494–515 (Springer Berlin Heidelberg, 1977). doi:10.1007/978-3-642-66620-9_26
5. Akopov, G., Yeung, M. T. & Kaner, R. B. Rediscovering the Crystal Chemistry of Borides. *Adv. Mater.* **29,** (2017).
6. Samsonov, G. V. *Refractory compounds of metals with nonmetals [in Russian]*. (Metallurgiya, 1964).
7. Albert, B. & Hillebrecht, H. Boron: Elementary challenge for experimenters and theoreticians. *Angew. Chemie - Int. Ed.* **48,** 8640–8668 (2009).
8. Fokwa, B. P. T. Borides: Solid-State Chemistry. *Encycl. Inorg. Bioinorg. Chem.* 1–14 (2014). doi:10.1002/9781119951438.eibc0022.pub2
9. Lundström, T. Borides: Solid-state Chemistry. in *Encyclopedia of Inorganic Chemistry* 481–494 (2006).
10. Tergenius, L. E. Refinement of the crystal structure of orthorhombic Mn2B (formerly denoted Mn4B). *J. Less-Common Met.* **82,** 335–340 (1981).

11. Bodrova, L. G., Koval'chenko, M. S. & Serebryakova, T. I. Preparation of tungsten tetraboride. *Sov. Powder Metall. Met. Ceram.* **13,** 1–3 (1974).

12. Akopov, G. *et al.* Effects of Variable Boron Concentration on the Properties of Superhard Tungsten Tetraboride. *J. Am. Chem. Soc.* **139,** 17120–17127 (2017).

13. Akopov, G., Yeung, M. T., Turner, C. L., Mohammadi, R. & Kaner, R. B. Extrinsic hardening of superhard tungsten tetraboride alloys with group 4 transition metals. *J. Am. Chem. Soc.* **138,** 5714–5721 (2016).

14. La Placa, S., Binder, I. & Post, B. Binary dodecaborides. *J. Inorg. Nucl. Chem.* **18,** 113–117 (1961).

15. Akopov, G., Yeung, M. T., Sobell, Z. C., Turner, C. L. & Kaner, R. B. Superhard Mixed Metal Dodecaborides. *Chem. Mater.* **28,** 6605–6612 (2016).

16. Akopov, G., Sobell, Z. C. C., Yeung, M. T. T. & Kaner, R. B. B. Stabilization of LnB12 (Ln = Gd, Sm, Nd, and Pr) in Zr1−xLnxB12 under Ambient Pressure. *Inorg. Chem.* **55,** 12419–12426 (2016).

17. Akopov, G., Yeung, M. T., Turner, C. L., Li, R. L. & Kaner, R. B. Stabilization of HfB12 in Y1-xHfxB12 under Ambient Pressure. *Inorg. Chem.* **55,** 5051–5055 (2016).

18. Richards, S. M. & Kaspar, J. S. The crystal structure of YB66. *Acta Crystallogr. Sect. B Struct. Crystallogr. Cryst. Chem.* **25,** 237–251 (1969).

19. Crespo, A. J., Tergenius, L. E. & Lundstrom, T. The solid solution of 4d, 5d and some p elements in beta-rhombohedral boron. *J. Less-Common Met.* **77,** 147–150 (1981).

20. Yeung, M. T., Mohammadi, R. & Kaner, R. B. Ultraincompressible, Superhard Materials. *Annu. Rev. Mater. Res.* **46,** 465–485 (2016).

21. Renosto, S. T. *et al.* Superconductivity in the Th0.93Zr0.07B12 compound with UB12

prototype structure. *Phys. Lett. A* **379,** 2498–2501 (2015).

22. Odintsov, V. V. Hardness of metal dodecaborides of UB12 structure type [in Russian]. *Inorg. Chem. USSR* **10,** 366–367 (1974).

23. Cannon, J. F. & Farnsworth, P. B. High pressure syntheses of ThB12 and HfB12. *J. Less-Common Met.* **92,** 359–368 (1983).

24. Cannon, J. F., Cannon, D. M. & Tracy Hall, H. High pressure syntheses of SmB2 and GdB12. *J. Less-Common Met.* **56,** 83–90 (1977).

25. Akopov, G., Sobell, Z. C., Yeung, M. T. & Kaner, R. B. Stabilization of LnB_{12} (Ln = Gd, Sm, Nd, and Pr) in $Zr_{1-x}Ln_xB_{12}$ under Ambient Pressure. *Inorg. Chem.* **55,** 12419–12426 (2016).

26. Akopov, G., Yeung, M. T., Turner, C. L., Li, R. L. & Kaner, R. B. Stabilization of HfB12 in Y1−xHfxB12 under Ambient Pressure. *Inorg. Chem.* **55,** 5051–5055 (2016).

27. Lutterotti, L., Chateigner, D., Ferrari, S. & Ricote, J. Texture, residual stress and structural analysis of thin films using a combined X-ray analysis. *Thin Solid Films* **450,** 34–41 (2004).

28. Lutterotti, L. Maud Rev. 2.55. *Maud Rev. 2.55, Univ. Trento-Italy, Dep. Ind. Eng. Trento, Italy* (2015).

29. Lutterotti, L. Total pattern fitting for the combined size-strain-stress-texture determination in thin film diffraction. *Nucl. Instruments Methods Phys. Res. Sect. B Beam Interact. with Mater. Atoms* **268,** 334–340 (2010).

30. Lutterotti, L., Matthies, S., Wenk, H. R., Schultz, A. S. & Richardson, J. W. Combined texture and structure analysis of deformed limestone from time-of-flight neutron diffraction spectra. *J. Appl. Phys.* **81,** 594–600 (1997).

31. Lutterotti, L., Bortolotti, M., Ischia, G., Lonardelli, I. & Wenk, H. R. Rietveld texture analysis from diffraction images. *Zeitschrift fur Krist. Suppl.* **1,** 125–130 (2007).

32. Portnoi, K. I., Romashev, V. M. & Burobina, L. N. Constitution Diagram of the System Zirconium-Boron. *Powder Metall. Met. Ceram.* **7,** 68–71 (1970).

33. Liao, P. K. & Spear, K. E. The B-Y (boron-yttrium) system. *J. Phase Equilibria* **16,** 521–524 (1995).

34. Liao, P. K., Spear, K. E. & Schlesinger, M. E. The B-Gd (Boron-Gadolinium) System. **17,** 330–334 (1996).

35. Portnoi, K. I., Romashov, V. M., Romanovich, I. V., Levinskii, Y. V. & Prokof'ev, S. A. Phase diagram of the system Hf-B. *Inorg. Mater.* **7,** 1769–1772 (1971).

36. Chaban, N. F. & Kuz'ma, Y. B. {Ti, Zr, Hf}-Gd-B Systems. *Sov. Powder Metall. Met. Ceram.* **17,** 592–593 (1978).

37. Rudy, E. Zr-Hf-B System. *Comp. Phase Diagr. Data, Ternary Phase Equilib. TM-B-C-Si, AFML-Tr-65-2, Part V* 562–581 (1969).

38. Mar, R. W. & Stout, N. D. High Temperature Enthalpies of Binary Dodecaborides. *J. Chem. Phys.* **57,** 5342–5349 (1972).

39. Vegard, L. Die Konstitution der Mischkristalle und die Raumfullung der Atome. *Zeitschrift fur Phys.* **5,** 17–26 (1921).

40. Leithe-Jasper, A., Sato, A. & Tanaka, T. Refinement of the crystal structure of zirconium dodecaboride, ZrB 12, at 140 K and 293 K. *Zeitschrift fur Krist. - New Cryst. Struct.* **217,** 319–320 (2002).

41. Callmer, B. A Single-Crystal Diffractometry Boron Investigation of Scandium in beta-rhombohedral boron. *J. Solid State Chem.* **23,** 391–398 (1978).

42. Slack, G. A., Hejna, C. I., Garbauskas, M. & Kasper, J. S. X-ray study of transition-metal dopants in beta-boron. *J. Solid State Chem.* **76,** 64–86 (1988).

CHAPTER 6. EXTRINSIC HARDENING OF SUPERHARD TUNGSTEN TETRABORIDE ALLOYS WITH GROUP 4 TRANSITION METALS

ABSTRACT

Alloys of tungsten tetraboride (WB_4) with the group 4 transition metals, titanium (Ti), zirconium (Zr) and hafnium (Hf) of different concentrations (0-50 at.% on a metals basis) were synthesized by arc-melting in order to study their mechanical properties. The phase composition and purity of the as-synthesized samples were confirmed using powder X-ray Diffraction (XRD) and Energy Dispersive X-ray Spectroscopy (EDS). The solubility limit as determined by XRD is 20 at.% for Ti, 10 at.% for Zr and 8 at.% for Hf. Vickers indentation measurements of WB_4 alloys with 8 at.% Ti, 8 at.% Zr and 6 at.% Hf, gave hardness values, H_v, of 50.9 ± 2.2, 55.9 ± 2.7 and 51.6 ± 2.8 GPa, respectively, compared to 43.3 GPa for pure WB_4 under an applied load of 0.49 N. Each of the aforementioned compositions are considered superhard (H_v > 40 GPa), likely due to extrinsic hardening that plays a key role in these superhard metal borides. Furthermore, these materials exhibit a significantly reduced indentation size effect, which can be seen in the plateauing hardness values for the $W_{1-x}Zr_xB_4$ alloy. In addition, $W_{0.92}Zr_{0.08}B_4$, a product of spinoidal decomposition, possesses nanostructured grains and enhanced grain hardening. The hardness of $W_{0.92}Zr_{0.08}B_4$ is 34.7 ± 0.65 GPa under an applied load of 4.9 N, the highest value obtained for any superhard metal at this relatively high loading. In addition, the WB_4 alloys with Ti, Zr and Hf showed a substantially

increased oxidation resistance up to ~460 °C, ~510 °C and ~490 °C, respectively, compared to ~400 °C for pure WB_4.

INTRODUCTION

Diamond is the hardest mineral because of its structure. The high density of carbon atoms produces ultra-incompressibility, while the large number of short covalent bonds gives rise to its extreme shear modulus. Together, these attributes make natural diamond superhard; as such, diamond is commonly used in the oil industry for cutting and drilling. Unfortunately, both natural diamond, due to its limited supply, and synthetic diamond, due to the high pressure and high temperature needed for its synthesis, are expensive. Diamond cutting tools cannot be used to cut ferrous metals such as steel due to the formation of brittle carbides. Therefore, most cutting tools are made out of less expensive materials such as tungsten carbide (WC). Since WC is a hard metal, it can be readily cut and shaped using electric discharge machining. However, WC is not that hard (H_v = 25 GPa)[1] so the development of superhard metals (H_v > 40 GPa) is becoming an increasingly important area for exploration.

The primary focus for the development of superhard metals to date has been on new compositions and crystal structures. Metal borides represent an interesting class of covalent, yet metallic compounds, with a wide range of mechanical, thermal and electronic properties.[2–5] These compounds exhibit a variety of crystal lattices with different arrangements of boron atoms, ranging from isolated borons ($Cr_2B_{(rhomb)}$) to boron networks ($TaB_{2(hex)}$) to a boron backbone ($UB_{12(cub)}$, $YB_{66(cub)}$).[2,3] While intrinsically related structural and mechanical properties[1] are fundamental to the development of such materials, there is a strong possibility that overall hardness can be dramatically enhanced following a completely orthogonal approach, i.e. through extrinsic effects.

More intriguingly, all of these new borides are metallic; meaning that unlike natural diamond, conventional metallurgical techniques such as dispersion, precipitation, or grain boundary hardening can be used to strengthen them.

Among the different borides, tungsten tetraboride (WB_4, $P6_3/mmc$, Inorganic Crystal Structure Database, ICSD #291124) represents a very interesting system due to its unique defect structure, which allows for hosting a wide variety of other transition metals in its lattice to form alloys (Figure 6-1).[6–9] Previous work has shown that adding different transition metals can dramatically increase the hardness and mechanical properties of WB_4 alloys, which intrinsically is already superhard (Vickers hardness $H_v \geq 40$ GPa).[7,8,10]

Here, we report on WB_4 alloys with Ti, Zr and Hf, and how changes and differences in structure and grain morphology affect the hardness and thermal stability. Likely mechanisms behind the changes in properties are provided in each case. In this way, we demonstrate that unlike diamond, superhard metal borides are metals, for which conventional hardening mechanisms are applicable even in the superhard regime.

EXPERIMENTAL PROCEDURE

In order to prepare samples of WB_4 and its alloys with Ti, Zr and Hf, powders of high-purity were used: tungsten (99.95%, Strem Chemicals, U.S.A.), amorphous boron (99+%, Strem Chemicals, U.S.A.), titanium (99%, Johnson Matthey Chemical Products, U.S.A.), zirconium (99.5%, Strem Chemicals, U.S.A.) and hafnium (99.8%, Materion, U.S.A.). The molar ratios of tungsten to boron was kept at 1:12 in order to prevent the formation of secondary boride phases of tungsten (*e.g.* WB_2).[8,11] The powders of the appropriate metals were weighed according to the calculated values for each sample of the alloys of WB_4 with Ti, Zr and Hf: $W_xTi_{1-x}B_4$, $W_xZr_{1-x}B_4$ and $W_xHf_{1-x}B_4$ (x

= 0.0 - 0.5). To ensure that each mixture was homogeneous, the powders were then thoroughly mixed in an agate mortar using a pestle. The sample mixtures were then pressed into pellets using a hydraulic press (Carver) with an applied load of 10 tons. The pressed samples were then placed into an arc-melter chamber on top of a water-cooled copper hearth and arc-melted in an argon atmosphere using a current of 70 amps for 1-2 minutes.

In order to carry out further analysis, each arc-melted sample was cut into two halves using a diamond saw (Ameritool Inc., U.S.A.). The first half was crushed using a tool steel Plattner-style diamond crusher into a fine sub 40-micron powder and used for powder XRD analysis. The second half was prepared for hardness measurements and EDS analysis by encapsulation in epoxy using an epoxy/hardener set (Allied High Tech Products Inc., U.S.A.). The samples were polished to an optically flat surface using a polishing station (South Bay Technology Inc., U.S.A.) and silicon carbide papers of 120 - 1200 grit sizes (Allied High Tech Products Inc., U.S.A.), followed by diamond films with particle sizes ranging from 30 to 1 micron (South Bay Technology Inc., U.S.A.).

The samples were then subjected to powder X-ray diffraction (PXRD) analysis and energy-dispersive X-ray spectroscopy (EDS) analysis in order to verify the composition and purity of the boride phases. Powder XRD analysis was carried out on the crushed powder samples using a Bruker D8 Discover Powder X-ray Diffractometer (Bruker Corporation, Germany). Powder XRD patterns were collected using a Cu Kα X-ray beam (λ = 1.5418 Å) in the 5-100° 2θ range with a step size of 0.0353°, scan speed of 0.1055°/sec and time per step of 0.3 sec. The collected patterns were then cross-referenced against the patterns in the database of the Joint Committee on Powder Diffraction Standards (JCPDS) to identify the phases present in the XRD patterns. The polished samples were checked for phase purity using an UltraDry EDS detector (Thermo Scientific,

U.S.A.) attached to a FEI Nova 230 high-resolution scanning electron microscope (FEI Company, U.S.A.).

Hardness measurements were performed on the polished samples using a MicroMet 2103 Vickers micro-hardness tester (Buehler Ltd, U.S.A.) with a pyramidal diamond indenter tip. Each sample was indented 20 times at randomly chosen spots with an applied load of 0.49, 0.98, 1.96, 2.94 and 4.9 N of force. In order to calculate the Vickers hardness values (H_v, in GPa) the diagonals of each indent were measured under a total magnification of 500x using a high-resolution optical microscope, Zeiss Axiotech 100HD (Carl Zeiss Vision GmbH, Germany) and the following formula was used (Equation 6.1):

$$H_v = \frac{1854.4F}{d^2} \tag{6.1}$$

where F is the applied load in Newtons (N) and *d* is the arithmetic average length of the diagonals of each indent in microns. The hardness values for all 20 indents for each respective loading were then averaged and plotted on hardness graphs (Figure 6-3a-c). All calculated average hardness values under each applied load of 0.49, 0.98, 1.96, 2.94 and 4.9 N have a standard deviation within 4.31, 3.45, 2.92, 2.03 and 1.41 GPa, respectively.

Thermogravimetric analysis was performed using a Pyris Diamond TGA/DTA unit (TG-DTA, Perkin-Elmer Instruments, U.S.A.). The samples were heated in an air from 25 to 200 °C at a rate of 20 °C/min, held at 200 °C for half an hour to remove any moisture, heated from 200 to 1000 °C at a rate of 2 °C/min, held at 1000 °C for two hours and then cooled from 1000 to 25 °C at a rate of 5 °C/min. In order to identify the resulting phase(s), XRD analysis was performed.

RESULTS AND DISCUSSION

The work here investigates the effects of group 4 transition metals (titanium, zirconium and hafnium) on the hardness and thermal stability of the resulting alloys formed with tungsten tetraboride: $W_xTi_{1-x}B_4$, $W_xZr_{1-x}B_4$ and $W_xHf_{1-x}B_4$, where x = 0.0 – 0.5. The relatively small atomic size of tungsten (W = 1.35 Å)[12] means that titanium (Ti = 1.40 Å)[12] is slightly larger than tungsten, while zirconium (Zr = 1.55 Å)[12] and hafnium (Hf = 1.55 Å)[12] are considerably larger. Thus, the effects of increasing atomic size mismatch on the mechanical properties can be studied. Moreover, the highest boride of titanium (TiB_2), zirconium (ZrB_{12}) and hafnium (HfB_2) vary, which is especially prominent in the case of the latter two metals. Although zirconium and hafnium should have similar atomic radii due to the lanthanide contraction[12], their atomic radii differ in a 12-coordinate environment (Hf = 1.580 Å, Zr = 1.603 Å), which results in only zirconium possessing a dodecaboride phase (ZrB_{12}).[13,14] This phase of boron represents a solid solution of hafnium in β-rhombohedral boron. The main difference between this phase and pure β-rhombohedral boron is the substitution of some of the boron icosahedra for Hf atoms. Note that the β-rhombohedral boron doping phase of hafnium (H_v ~ 40 GPa at 0.49 N)[15] which is significantly harder than pure β-rhombohedral boron (H_v ~ 34.2 GPa at 0.49 N),[16,17] can provide an additional extrinsic route to hardening the corresponding alloy of WB_4, since tungsten tetraboride requires excess boron in its synthesis in order to avoid the formation of a lower boride (WB_2).

In order to confirm the composition and purity of each sample, energy-dispersive X-ray spectroscopy (EDS) was utilized. Additionally, powder X-ray diffraction (XRD) was used to verify the composition and phase purity. Figures 6-2a-c show the powder XRD patterns respectively for the alloys $W_xTi_{1-x}B_4$, $W_xZr_{1-x}B_4$ and $W_xHf_{1-x}B_4$. Due to the stoichiometry used for the preparation of the samples, all of them contain some excess crystalline boron, which cannot be

observed with ordinary powder XRD. Therefore, EDS analysis was performed on polished samples of $W_xTi_{1-x}B_4$, $W_xZr_{1-x}B_4$ and $W_xHf_{1-x}B_4$, the results of which will be discussed in greater detail later in the paper.

Powder XRD patterns of the alloys of WB_4 and Ti ($W_xTi_{1-x}B_4$) are shown in Figure 6-2a. These patterns indicate that Ti is soluble in WB_4 at or below 20 at.%; at higher concentrations, a secondary phase, TiB_2 (JCPDS 01-075-0967) appears with its corresponding peaks. Note that peaks corresponding to WB_2 (JCPDS 01-073-1244) were not observed in any $W_xTi_{1-x}B_4$ samples.

Powder XRD patterns of the alloys of WB_4 and Zr ($W_xZr_{1-x}B_4$) are shown in Figure 6-2b. These patterns indicate that Zr is soluble in WB_4 at or below 10 at.%; at a concentration 20 at.% a Zr secondary phase, ZrB_{12} (JCPDS 03-065-7806) appears with its corresponding peaks. Diffraction peaks corresponding to WB_2 (JCPDS 01-073-1244) were observed at 40 at.% Zr for $W_xZr_{1-x}B_4$ samples.

Powder XRD patterns of the alloys of WB_4 and Hf ($W_xHf_{1-x}B_4$) are shown in Figure 6-2c. These patterns indicate that Hf is soluble in WB_4 at or below 8 at.%. At 10 at.% Hf, a secondary phase, HfB_{50} (β-rhombohedral boron doping phase of hafnium, JCPDS 01-086-2400) was observed. At 30 at.% Hf, HfB_2 (JCPDS 01-089-3651) appeared. Diffraction peaks corresponding to WB_2 (JCPDS 01-073-1244) were observed at 30 at.% Hf for $W_xHf_{1-x}B_4$ samples. The formation of ZrB_{12} and HfB_{50} is thermodynamically favorable, since they are the highest borides for Zr and Hf, respectively, given the stoichiometry used for the preparation of WB_4.[2]

After confirming the composition and purity of the samples using powder XRD and EDS, Vickers micro-indentation hardness measurements were performed on each of the samples under applied loads ranging from 0.49 to 4.9 N. The results of the hardness measurements are shown in Figures

6-3a-c. For the $W_xTi_{1-x}B_4$ alloy with 8 at.% Ti under a load of 0.49 N, the hardness increased to 50.9 ± 2.2 GPa from 43.3 ± 2.1 GPa[7] for pure WB_4 (corresponding to 0 at.% Ti on the graph). Upon increasing the concentration of Ti, the hardness decreased to 36.3 ± 1.7 GPa at 50 at.% Ti which can be attributed to the formation of TiB_2 as a secondary phase, since the solubility limit for Ti in WB_4 has been exceeded. Similar observations are seen in the measurements carried out under other loads (0.98, 1.94, 2.94, and 4.9 N).

For the $W_xZr_{1-x}B_4$ alloy with 8 at.% Zr under a load of 0.49 N, the hardness dramatically increased to 55.9 ± 2.7 GPa, followed by a decrease to 45.1 ± 2.6 GPa at 10 at.% Zr. Upon increasing the concentration of Zr, the hardness increased slightly to 46.9 ± 2.3 GPa at 20 at.% Zr, followed by a decrease to 42.6 ± 2.2 GPa at 30 at.% Zr and then increased to 45.6 ± 2.3 GPa at 50 at.% Zr, which can be attributed to the formation of a metal dodecaboride, ZrB_{12} (hardness of ~ 40 GPa at 0.49 N of force),[18] secondary phase and its competition with WB_4 at higher concentrations of zirconium.

For the $W_xHf_{1-x}B_4$ alloy with 4-6 at.% Hf under a load of 0.49 N, the hardness increased to 51.3 ± 2.9 GPa and 51.6 ± 2.8 GPa, respectively. The hardness then decreased to 42.2 ± 2.7 GPa at 10 at.% Hf and gradually increased to 45.4 ± 2.2 GPa at 50 at.% Hf, which can be attributed to exceeding the solubility limit of Hf in WB_4 and the formation of the β-rhombohedral boron doping phase of hafnium, HfB_{50}, thus hardening the excess boron. HfB_{50} has a hardness of ~40 GPa at 0.49 N compared to 34.2 GPa at 0.49 N for a sample of crystalline β-rhombohedral boron.[15–17]

The structure of WB_4 has been investigated over many years.[8,11] As established by G. Hägg, in order for higher metal borides (MB_4, MB_6, MB_{12}) to adopt a cubic or hexagonal structure, the ratio of the radius of a boron atom to the radius of a metal atom (Hägg's ratio) should not be above 0.59.[19] The Hägg's ratio for tungsten is $R_B/R_W = 0.63 > 0.59$, therefore, WB_4 cannot adopt a simple

cubic or hexagonal lattice.[3,19] Most recently Lech et al. demonstrated that the crystal structure of WB_4 not only contains partially filled tungsten sites (one-third of W atoms are systematically absent), but also boron trimer sites.[6] Therefore, this unique defect structure of WB_4 could be one of the causes of the hardening for the alloys of WB_4 with Ti, Zr and Hf (Figures 6-3a-c).[7] Since Ti, Zr and Hf are group IV elements, they have two less valence electrons than tungsten. With B occupying the systematic vacant sites of tungsten, the metal atoms can expand the number of boron vacancies.[7]

For the alloy of WB_4 with Ti ($W_xTi_{1-x}B_4$) at 8 at.% Ti, the valence electron difference in combination with the similar, yet slightly greater size of the Ti atom (1.40 Å, compared to 1.35 Å for W)[12] can explain the observed hardness increase. Titanium atoms occupy the positions devoid of tungsten atoms and the increase in observed hardness is therefore most likely due to solid-solution hardening. TiB_2 is considered the highest boride of Ti, however, titanium can go into a boron matrix and form the β-rhombohedral boron doping phase of titanium (TiB_{50}).[20] Due to the relatively smaller X-ray cross section of titanium (compared to tungsten), this phase does not appear in XRD; however, it can be seen using EDS (Figure 6-4). This can explain the smooth decrease in the hardness at Ti concentrations greater than 10 at.%. As the concentration of Ti increases, it starts to form a TiB_2 secondary phase. While TiB_2 is the hardest AlB_2-type diboride (hardness of 35 GPa at 0.49 N of force),[21] it is still softer than pure WB_4. This combined with the formation of a β-rhombohedral boron doping phase of titanium, TiB_{50} (hardness of 36.4 GPa at a load of 0.49 N)[17] provides no extrinsic hardening for the $W_xTi_{1-x}B_4$ alloy and therefore decreases the overall hardness. In addition, it should be noted that the TiB_2 phase is located in the tungsten rich areas of WB_4 and given the high melting temperature of this phase (3225 °C, compared to 2020 °C for WB_4),[20,22] we can conclude that TiB_2 precipitates out first from the melt and provides

a template pattern for the further precipitation of the WB_4 phase (Figure 6-4); this is known as precipitation hardening.

For the alloy of WB_4 with Zr ($W_xZr_{1-x}B_4$) at 8 at.% Zr, the valence electron difference and the metal size mismatch (Zr = 1.55 Å, W = 1.35 Å)[12] in combination with the drastic change in grain morphology (Figure 6-5) can provide a partial explanation for the sharp peak observed in hardness (Figure 6-3b). Similar to titanium, zirconium atoms can occupy the positions devoid of tungsten atoms and thus increase the hardness due to solid-solution hardening. In contrast to titanium, zirconium's highest boride phase is a metal dodecaboride ZrB_{12}.[20] Moreover, while Zr also possesses a β-rhombohedral boron doping phase (ZrB_{50}), this does not readily form due to the availability of the higher boride, ZrB_{12} (Figure 6-4).

Comparing the phase diagrams for the W-boron and Zr-boron systems, there is a similarity to the way both WB_4 and ZrB_{12} form.[22,23] Previous reports indicated that the formation of metal dodecaborides (MB_{12}) are very much dependent on the size of the metal atom in order to accommodate a cuboctahedron unit of boron atoms. Zirconium (1.55 Å)[12] and yttrium (1.80 Å)[12] are the smallest and largest metal atoms, respectively, capable of forming dodecaboride structures.[13,14] While tungsten (1.35 Å)[12] is too small to accommodate a cuboctahedron boron unit and form a dodecaboride, it can be proposed that that $W_xZr_{1-x}B_4$ alloy can form a metastable dodecaboride that decomposes into the hexagonal WB_4 structure at low concentrations of Zr. The optimal doping amount appears to be 8 at.% Zr in the $W_xZr_{1-x}B_4$ alloy as seen by the drastic change in morphology (Figure 6-5).[8,14]

Indeed, the morphology of the 8 at% Zr composition suggests that at high temperatures, the metastable dodecaboride is stabilized. When the arcing is terminated, the sample rapidly cools on

the hearth, and the metastable dodecaboride decomposes into two immiscible species: WB_4 and the β-rhombohedral boron doping phase of zirconium (ZrB_{50}); this is known as spinoidal decomposition.[24] Fortuitously, this results in nanostructured grains (Figure 6-5) and grain hardening. The high density of grain boundaries prevents dislocation propagation and increases the overall hardness of the composite. As such, $W_{0.92}Zr_{0.08}B_4$ (55.9 ± 2.7 GPa at 0.49 N) is 28% harder than its parent WB_4 (43.3 ± 2.1 GPa at 0.49 N). Similar changes in grain morphology and as a result increases in hardness can be expected for other transition metals capable of forming dodecaboride species: scandium and yttrium. Most promisingly, this suggests that decomposition of metastable phases can lead to new routes towards the nanostructuring of superhard grains.

Hardness changes at concentrations of zirconium greater than 10 at.% may be attributed to the following reasons: below 20 at.% zirconium, the ZrB_{12} secondary phase appears, which hardens the material through a dispersion-hardening mechanism. At higher concentrations of zirconium, both ZrB_{12} and WB_4 phases form, which are the highest borides of zirconium and tungsten respectively, and they compete with one another. The hardness of $W_xZr_{1-x}B_4$ gently increases as x approaches 50 at.% Zr and more ZrB_{12} is formed.

For the alloy of WB_4 with Hf ($W_xHf_{1-x}B_4$) at 4-6 at.% Hf, the valence electron difference and the metal size mismatch (Hf = 1.55 Å, W = 1.35 Å)[12] may provide an explanation for the broad hardness peak with hardness values increasing to 51.3 ± 2.9 and 51.6 ± 2.8 GPa at 0.49 N, respectively, compared to 43.3 ± 2.1 GPa at 0.49 N for pure WB_4 (Figure 6-3c). Similar to titanium and zirconium, hafnium atoms can occupy the positions of the missing tungsten atoms and the increase in hardness is therefore most likely due to solid-solution hardening. Similar to titanium, hafnium's highest boride phase is the diboride HfB_2; however, it also forms the β-rhombohedral boron doping phase of hafnium, HfB_{50}.[15] In contrast to TiB_{50}, hafnium has a large enough X-ray

cross-section for the HfB_{50} phase to appear in powder XRD spectrum (Figure 6-2c). Due to the lanthanide contraction, for most purposes zirconium and hafnium have essentially the same atomic radius (1.55 Å).[12] Thus, in contrast to zirconium, hafnium does not form a dodecaboride phase under ambient pressure; however, it can be synthesized with the application of 6.5 GPa of pressure.[13] This is due to the fact that in a 12-coordinate environment, zirconium and hafnium have different metallic radii: 1.603 and 1.580 Å, respectively.[13]

The HfB_{50} phase appears as a secondary phase at 10 at.% Hf (Figure 6-2c). Figure 6-7 shows the elemental maps of a sample of an alloy of WB_4 with 10 at.% Hf ($W_{0.90}Hf_{0.10}B_4$). Note that hafnium is present not only in the tungsten rich areas (showing the presence of Hf in the WB_4 lattice), but also in boron rich areas (forming HfB_{50}). As the concentration of hafnium increases, it extrinsically hardens WB_4 by hardening the excess crystalline boron (H_v = 34.2 GPa at 0.49 N)[16,17] (Figure 6-3c) through the formation of a β-rhombohedral boron doping phase of hafnium, HfB_{50}, (H_v ~ 40 GPa at 0.49 N).[15]

Table 6-1 compares the values of hardness for the hardest compositions of alloys of WB_4 with Ti, Zr and Hf with those of pure WB_4 and the hardest WB_4 alloy reported, $W_{0.93}Ta_{0.02}Cr_{0.05}B_4$.[7] Both $W_{0.93}Ta_{0.02}Cr_{0.05}B_4$ and $W_{0.92}Zr_{0.08}B_4$ have similar total secondary metal content, 7-8 at.%, and while $W_{0.92}Zr_{0.08}B_4$ is slightly softer than $W_{0.93}Ta_{0.02}Cr_{0.05}B_4$ at low load (0.49 N), it exhibits increased hardness values at higher loads, indicating a smaller influence of the indentation size effect due to the extremely fine surface morphology of this sample (Figure 6-5).

Oxidation resistance is an important parameter for materials used for cutting and machining tools. As such, in order to test the thermal stability of the samples of alloys of Ti, Zr and Hf with WB_4,

thermogravimetric analysis in air was performed on the samples with the compositions corresponding to the hardest alloys. Figure 6-6 summarizes the results.

The TGA data indicate that alloys of Ti, Zr and Hf with WB_4 have enhanced oxidation properties in comparison to pure WB_4 and the hardest tantalum-chromium alloys of WB_4 ($W_{0.93}Ta_{0.02}Cr_{0.05}B_4$). $W_{0.92}Ti_{0.08}B_4$, $W_{0.92}Zr_{0.08}B_4$ and $W_{0.94}Hf_{0.06}B_4$ are stable up to ~460 °C, ~510 °C and ~490 °C respectively, compared to ~400 °C for pure WB_4 and ~420 °C for $W_{0.93}Ta_{0.02}Cr_{0.05}B_4$. The products of oxidation are WO_3 and TiO_2 for $W_{0.92}Ti_{0.08}B_4$, WO_3 and ZrO_2 for $W_{0.92}Zr_{0.08}B_4$ and WO_3 and HfO_2 for $W_{0.94}Hf_{0.06}B_4$ samples, as determined by powder XRD analysis. Thus, an increase of about 100 °C in stability is observed for the hardest zirconium alloy of WB_4, which has a comparable hardness to that of $W_{0.93}Ta_{0.02}Cr_{0.05}B_4$.

CONCLUSIONS

Alloys of WB_4 with the group 4 transition metals (Ti, Zr and Hf) were synthesized and their hardness and thermal stability characterized. These alloys are interesting due to the higher boride phases they can form: metal dodecaboride and β-rhombohedral boron doping phases. Doping with 8% Ti ($W_{0.92}Ti_{0.08}B_4$), 8% Zr ($W_{0.92}Zr_{0.08}B_4$), 6% Hf ($W_{0.94}Hf_{0.06}B_4$) showed the highest values of hardness (at 0.49 N applied load) for their respective alloys: 50.9 ± 2.2, 55.9 ± 2.7 and 51.6 ± 2.8 GPa, compared to 43.3 ± 2.1 GPa for pure WB_4. Electronic effects from valence electron mismatch (4 electrons for Group 4 metals and 6 electrons for tungsten from Group 6) or atomic size mismatch (W = 1.35 Å, Ti = 1.40 Å, Zr = 1.55 Å, Hf = 1.55 Å)[12] are the likely cause of the increase in hardness at low concentrations of Ti, Zr and Hf. In addition, the alloys of WB_4 with zirconium and hafnium showed extrinsic hardening at higher concentrations of these transition metals. Alloys of WB_4 with zirconium showed drastic changes in the surface morphology of the corresponding

samples at <10 at.% Zr, likely due to the formation of a metastable Zr-W dodecaboride phase. This can be attributed to the formation of the hard metal dodecaboride phase (ZrB_{12}) for zirconium and hardening of the excess boron, through the formation of β-rhombohedral boron doping phase (HfB_{50}) for hafnium. In addition, the alloys of titanium, zirconium and hafnium with WB_4 showed increased oxidation resistance up to ~460 °C, ~510 °C and ~490 °C respectively, compared to ~400 °C for pure WB_4. By adding to WB_4 other metals with larger atomic radii than tungsten that possess different higher boride phases, such as YB_{66}[25] for yttrium and ScB_{19}[26] for scandium, their effects on the resulting alloys can be studied and other possible hardening mechanisms explored.

ACKNOWLEDGMENTS

We thank the National Science Foundation Division of Materials Research, Grant DMR-1506860 (R.B.K.), Virginia Commonwealth University Startup Grant 137422 (R.M.), and the National Science Foundation IGERT-MCTP Fellowship program (M.T.Y.) for financial support and Professor Benjamin M. Wu of the UCLA Department of Bioengineering for the use of the micro-indentation system in his laboratory.

Table 6-1. Vickers Microindentation Hardness Data for the Hardest Alloys of WB_4 with Ti, Zr and Hf [a]

Compound/Alloy	Applied Load (N)				
	0.49	0.98	1.96	2.94	4.9
WB_4	43.4	38.3	32.8	30.5	28.1
$W_{0.93}Ta_{0.02}Cr_{0.05}B_4$	57.3	44.1	38.2	34.8	31.7
$W_{0.92}Ti_{0.08}B_4$	50.9	39.9	36.2	34.5	32.5
$W_{0.92}Zr_{0.08}B_4$	55.9	42.9	39.8	35.9	34.7
$W_{0.94}Hf_{0.06}B_4$	51.6	40.2	35.1	33.7	32.3

[a]Hardness data for pure WB_4 and $W_{0.93}Ta_{0.02}Cr_{0.05}B_4$ alloy are presented for comparison.[7]

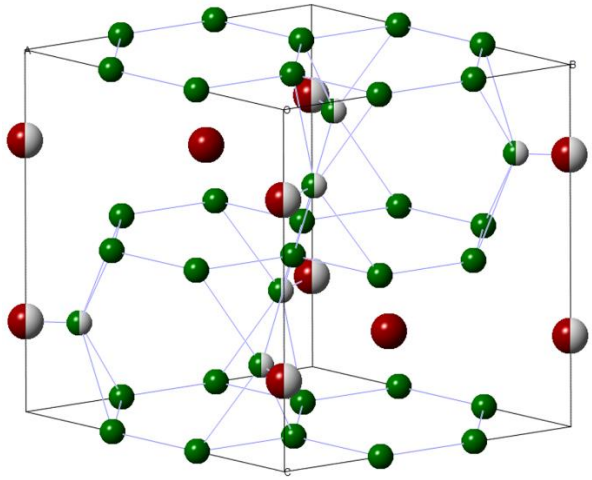

Figure 6-1. Crystal structure of tungsten tetraboride (WB_4, $P6_3/mmc$, Inorganic Crystal Structure Database, ICSD, 291124). Boron atoms are represented in green and tungsten atoms are shown in maroon; the half-filled atoms show partially occupied positions.

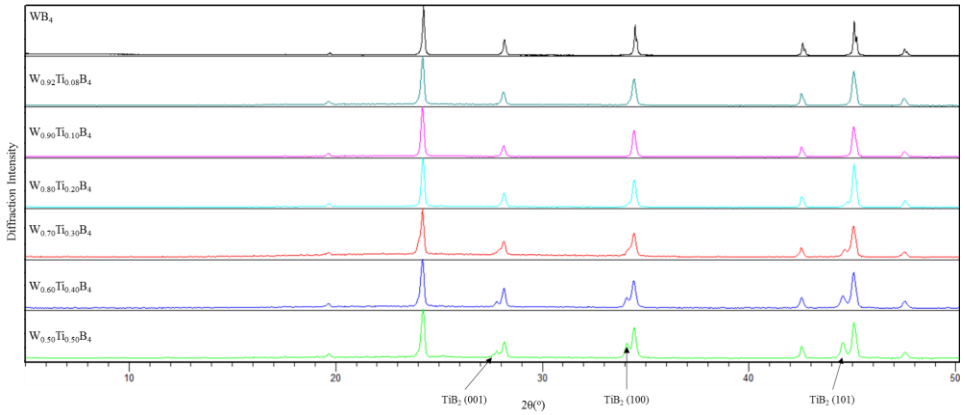

(a)

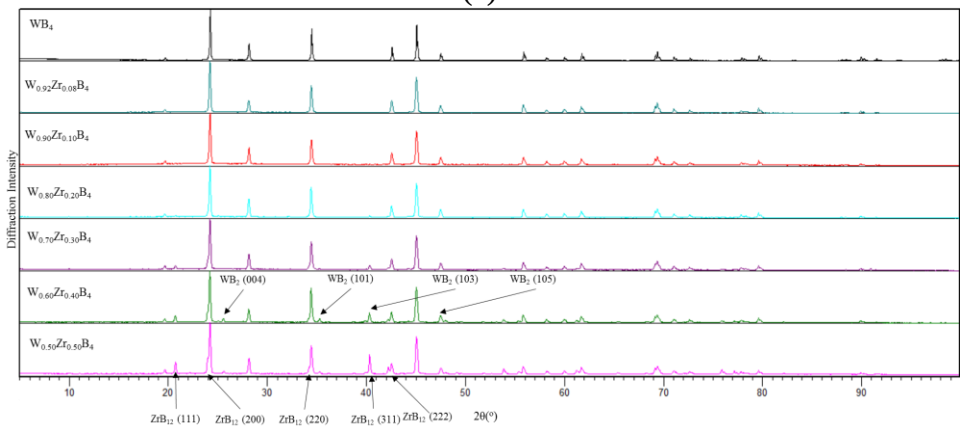

(b)

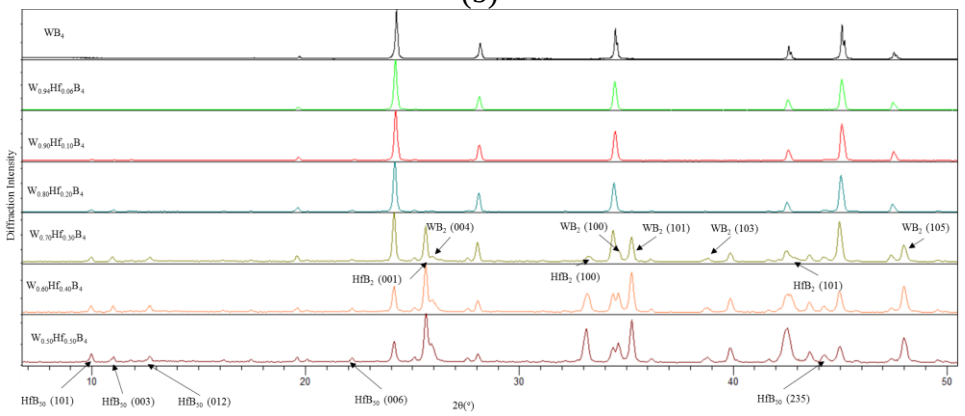

(c)

Figure 6-2. Powder XRD patterns of alloys of WB_4 with 2-50 at.% (a) Ti, (b) Zr and (c) Hf added on a metals basis. The top spectrum in each set is pure WB_4 (JCPDS 00-019-1373). The solubility limit is less than 20 at.% for Ti, 10 at.% for Zr and below 8 at.% for Hf. Above 20 at.% Ti, TiB_2 (JCPDS 01-075-0967), above 20 at.% Zr, ZrB_{12} (JCPDS 03-065-7806) and above 10 and 20 at.% Hf, HfB_{50} (β-rhombohedral boron doping phase of hafnium) and HfB_2 (JCPDS 01-086-2400 and 01-089-3651) appear, respectively, as secondary phases. In addition, peaks corresponding to WB_2 (JCPDS 01-073-1244) are observed at 40 at.% Zr and 30 at.% Hf.

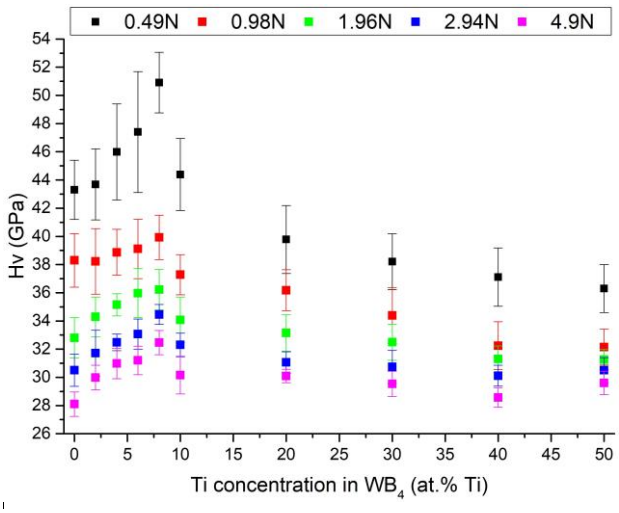

(a)

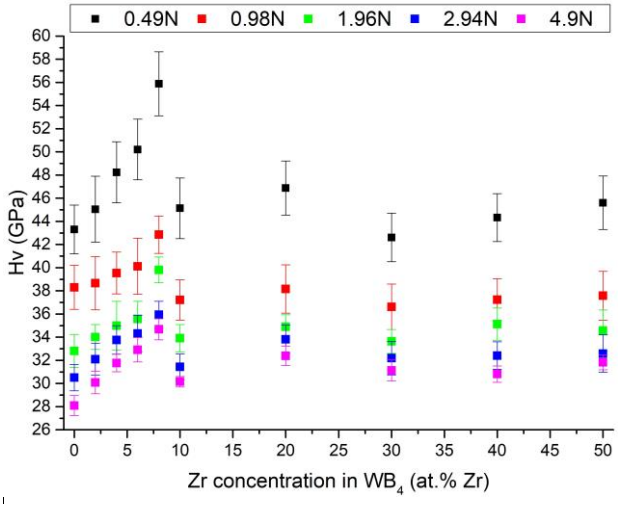

(b)

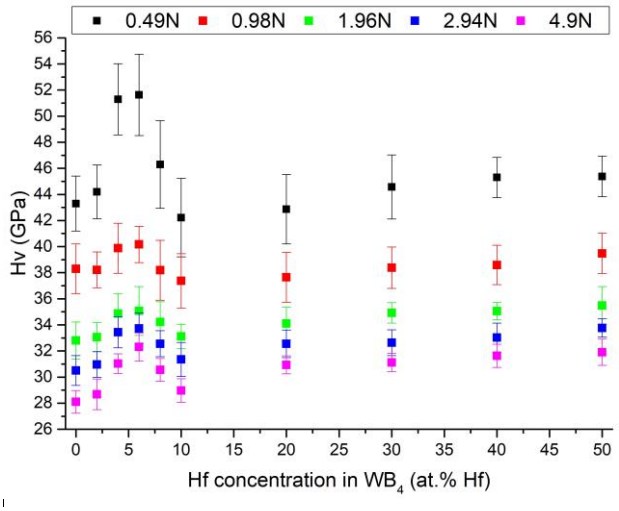

(c)

Figure 6-3. Vickers microindentation hardness of tungsten tetraboride alloys with (a) Ti, (b) Zr, and (c) Hf under 0.49 N (low) to 4.9 N (high) loads. The metal concentrations (x) in $W_{1-x}M_xB_4$ were changed by adding 2 - 50 at.% Ti, Zr, and Hf on a metals basis.

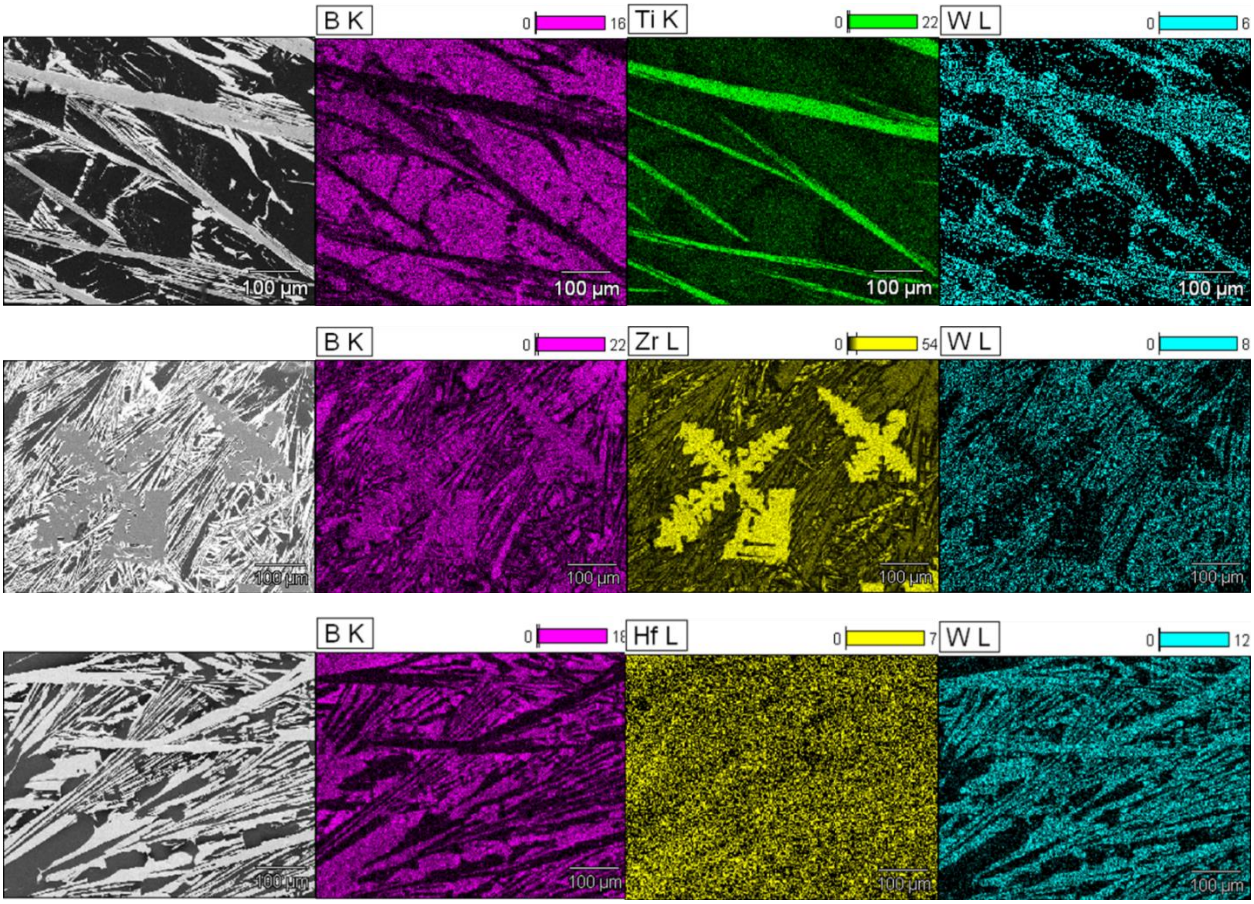

Figure 6-4. Elemental maps for boron (K line), titanium (K line), zirconium (L line), hafnium (L line) and tungsten (L line) for the $W_{0.50}Ti_{0.50}B_4$, $W_{0.50}Zr_{0.50}B_4$, $W_{0.90}Hf_{0.10}B_4$ alloys showing the presence of titanium in TiB_{50} (β-rhombohedral boron doping phase of titanium) corresponding to boron rich areas and TiB_2 in tungsten rich areas, presence of zirconium in ZrB_{12} and no formation of ZrB_{50}; and presence of hafnium in WB_4 as well as in the boron-rich phase.

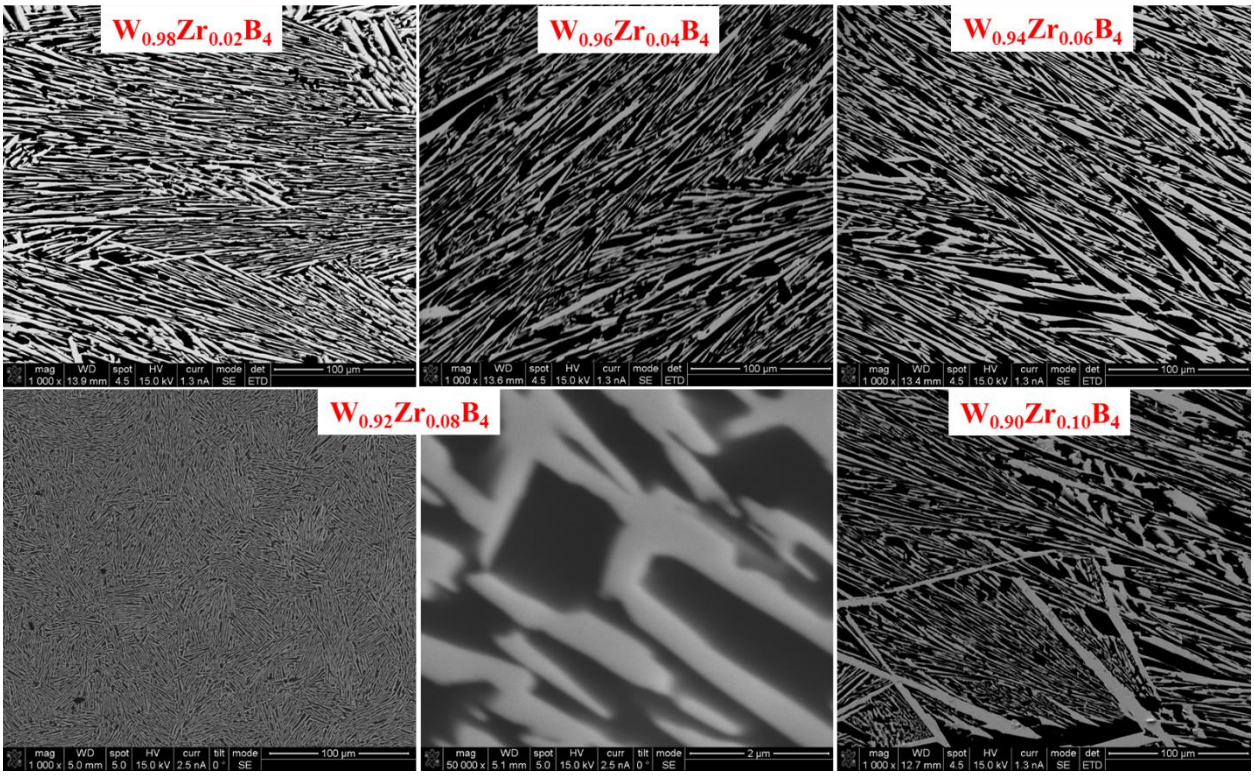

Figure 6-5. SEM images of the alloys of WB_4 with 2-10 at.% Zr taken at 1000x magnification and 50,000x for the hardest composition, $W_{0.92}Zr_{0.08}B_4$, showing changes in morphology. The drastic change of surface morphology at 8 at.% Zr can be attributed to a decomposition from a meta-stable W-Zr dodecaboride phase.

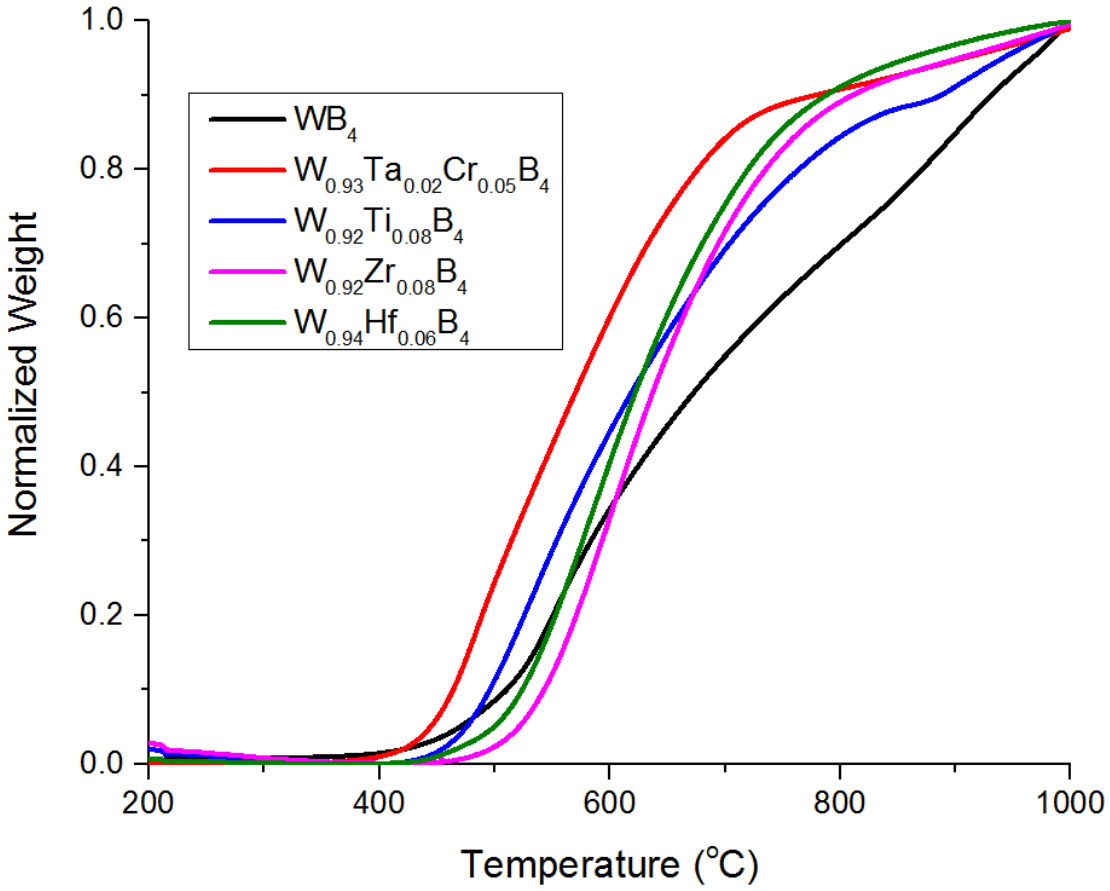

Figure 6-6. Thermal stability of the hardest tungsten tetraboride alloys with Ti, Zr and Hf as measured by thermal gravimetric analysis in air. The data for pure WB_4 and the hardest alloy $W_{0.93}Ta_{0.02}Cr_{0.05}B_4$ are given for comparison. These data show that $W_{0.92}Ti_{0.08}B_4$, $W_{0.92}Zr_{0.08}B_4$ and $W_{0.94}Hf_{0.06}B_4$ are stable up to ~460 °C, ~510 °C and ~490 °C, respectively (using the extrapolated oxidation onset), compared to ~400 °C for pure WB_4 and ~420 °C for the $W_{0.93}Ta_{0.02}Cr_{0.05}B_4$ alloy.

REFERENCES

1. Yeung, M. T., Mohammadi, R. & Kaner, R. B. Ultraincompressible, Superhard Materials. *Annu. Rev. Mater. Res.* **46,** 465–485 (2016).

2. Samsonov, G. V. *Borides [in Russian]*. (Atomizdat, 1975).

3. Samsonov, G.V., Markovskii, L. Y. *Boron, Its Compounds and Alloys [in Russian]*. (House of the Academy of the Sciences Ukrainian SSR, 1960).

4. Mohammadi, R. & Kaner, R. B. *Superhard Materials*. *Encyclopedia of Inorganic and Bioinorganic Chemistry* (R.A. Scott ed., John Wiley and Sons, Inc., 2012).

5. Kaner, R. B., Gilman, J. J. & Tolbert, S. H. Designing Superhard Materials. *Science (80-.).* **308,** 1268–1269 (2005).

6. Lech, A. T., Turner, C. L., Mohammadi, R., Tolbert, S. H. & Kaner, R. B. Structure of superhard tungsten tetraboride: A missing link between MB 2 and MB 12 higher borides. *Proc. Natl. Acad. Sci.* **112,** 3223–3228 (2015).

7. Mohammadi, R. *et al.* Toward inexpensive superhard materials: Tungsten tetraboride-based solid solutions. *J. Am. Chem. Soc.* **134,** 20660–20668 (2012).

8. Mohammadi, R. *et al.* Tungsten tetraboride, an inexpensive superhard material. *Proc. Natl. Acad. Sci. U. S. A.* **108,** 10958–10962 (2011).

9. Mohammadi, R. *et al.* Enhancing the Hardness of Superhard Transition-Metal Borides: Molybdenum-Doped Tungsten Tetraboride. *Chem. Mater.* **28,** 632–637 (2016).

10. Bodrova, L. G., Koval'chenko, M. S. & Serebryakova, T. I. Preparation of tungsten

tetraboride. *Sov. Powder Metall. Met. Ceram.* **13,** 1–3 (1974).

11. Romans, P. A. & Krug, M. P. Composition and crystallographic data for the highest boride of tungsten. *Acta Crystallogr.* **20,** 313–315 (1966).

12. Slater, J. C. Atomic Radii in Crystals. *J. Chem. Phys.* **41,** 3199–3204 (1964).

13. Cannon, J. F. & Farnsworth, P. B. High pressure syntheses of ThB12 and HfB12. *J. Less-Common Met.* **92,** 359–368 (1983).

14. La Placa, S., Binder, I. & Post, B. Binary dodecaborides. *J. Inorg. Nucl. Chem.* **18,** 113–117 (1961).

15. Portnoi, K. I., Romashov, V. M., Romanovich, I. V., Levinskii, Y. V. & Prokof'ev, S. A. Phase diagram of the system Hf-B. *Inorg. Mater.* **7,** 1769–1772 (1971).

16. Andersson, S. & Lundström, T. The solubility of chromium in β-rhombohedral boron as determined in CrB_{41} by single-crystal diffractometry. *J. Solid State Chem.* **2,** 603–611 (1970).

17. Carlsson, J. O. & Lundström, T. The solution hardening of β-rhombohedral boron. *J. Less-Common Met.* **22,** 317–320 (1970).

18. Kuzenkova, M.A., Kislyi, P. S. preparation of Zircoium diboride. *Powder Metall.* **12,** 966–969 (1965).

19. Hägg, G. No Title. *Z. Phys. Chem.* **B12,** (1931).

20. Murray J.L., Liao P.K., and S. K. E. B-Ti (BoronTitanium). *Bin. Alloy Phase Diagrams* **1,** 544–548 (1990).

21. Basu, B., Raju, G. B. & Suri, A. K. Processing and properties of monolithic TiB 2 based materials. *Int. Mater. Rev.* **51,** 352–374 (2006).

22. Duschanek, H., Rogl, P. ASM Alloy Phase Diagrams Critical Assessment and Thermodynamic Calculation of the Binary System BoronTungsten (B-W). *J. Phase Equilib.* **16,** 150–161 (1995).

23. Portnoi, K. I. Constitution diagram of the system zirconiumboron. *Sov. Powder Met. Met. Ceram.* **9,** 577–580 (1970).

24. Cahn, J. W. On spinodal decomposition. *Acta Metall.* **9,** 795–801 (1961).

25. Richards, S. M. & Kaspar, J. S. The crystal structure of YB66. *Acta Crystallogr. Sect. B Struct. Crystallogr. Cryst. Chem.* **25,** 237–251 (1969).

26. Tanaka, T., Okada, S. & Gurin, V. A new scandium boride: ScB19. *J. Alloys Compd.* **267,** 211–214 (1998).

CHAPTER 7. EFFECTS OF VARIABLE BORON CONCENTRATION ON THE PROPERTIES OF SUPERHARD TUNGSTEN TETRABORIDE

ABSTRACT

Tungsten tetraboride is an inexpensive, superhard material easily prepared at ambient pressure. Unfortunately, there are relatively few compounds in existence that crystallize in the same structure as tungsten tetraboride. Furthermore, the lack of data in the tetraboride phase space limits the discovery of any new superhard compounds that also possess high incompressibility and a 3-D boron network that withstands shear. Thus, the focus of the work here is to chemically probe the range of thermodynamically stable tetraboride compounds with respect to both the transition metal and the boron content. Tungsten tetraboride alloys with a variable concentration of boron were prepared by arc-melting and investigated for their mechanical properties and thermal stability. The purity and phase composition were confirmed by energy dispersive X-ray spectroscopy (EDS) and powder X-ray diffraction (PXRD). For variable boron WB_x, it was found that samples prepared with a metal to boron ratio of 1 : 11.6 to 1 : 9 have similar hardness values (~40 GPa at 0.49 N loading) as well as having a similar thermal oxidation temperature of ~455 °C. A nearly single phase compound was successfully stabilized with tantalum and prepared with a nearly stoichiometric amount of boron (4.5) as $W_{0.668}Ta_{0.332}B_{4.5}$. Therefore, the cost of production of WB_4 can be decreased while maintaining its remarkable properties. Insights from this work will help design future compounds stable in the adaptable tungsten tetraboride structure.

INTRODUCTION

Metal borides have been studied for over a century and possess a range of useful thermal,[1,2] electronic and magnetic[1,3,4] properties, as well as remarkable chemistries.[5,6] They have many potential applications simply because they have a wide range of possible structures and boron arrangements and,[7] ranging from sub-borides with isolated boron atoms (Cr_4B) to boron-rich phases built using B_{12} boron icosahedra (YB_{66}, HfB_{50}).[8,9]

Over the past decade, the boride community has discovered a few compounds possessing superior mechanical[9,10] properties. Perhaps one of the most studied borides that exist at the limit of materials strength are those that are superhard, possessing a Vickers hardness, H_v > 40 GPa. The first superhard metal boride discovered was rhenium diboride in 2007,[11,12] which is capable of scratching diamond, the hardest natural material known. However, the high cost of rhenium led to the discovery of a less expensive superhard boride, tungsten tetraboride, in 2011.[13] Since then there has been a concerted effort to discover new structural analogues of tungsten tetraboride. These new phases try to incorporate an incompressible form of tungsten (to raise the bulk modulus)[14] along with a 3-D boron network (to prevent shear).[15–17]

Fortunately, tungsten tetraboride (Figure 7-1) is a very adaptable structure; containing metal vacancies and voids,[18,19] it can accommodate metal atoms as interstitial dopants in addition to traditional substitutional doping. Substitutional doping in the form of alloying and solid-solution formation, can greatly enhance hardness through not only intrinsic, but also extrinsic effects.[13,14,20–22] Tungsten tetraboride is an incongruently melting phase, requiring excess boron in order to form by direct heating.[23] It is typically prepared using a W : B ratio of 1 : 12; and at this composition

the only products are tungsten tetraboride and β-rhombohedral boron;[24] otherwise, at lower metal to boron ratios, a lower tungsten diboride forms.[20,22]

Theoretical calculations have resulted in the prediction of numerous tetraborides.[25–35] This has resulted in claims of ReB_4, OsB_4, and TaB_4, all isostructural with tungsten tetraboride. Unfortunately, none of these compounds have yet to be experimentally prepared and it is quite probably that these compounds are not stable under equilibrium conditions. Furthermore, the lack of either positive or negative results prevents synergy between experimentalists searching for new structures, and theorists seeking verification.[36] Thus, the goal of our work here is to explore the phase space of stable tungsten tetraboride-like structures. To accomplish this, we will chemically probe the tetraboride structure with substituents of interest. Because the parent compound is stable, it will serve as a "scaffold" to crystallize any potential tetraboride analogues. We are excited to report some stabilization of the tetraboride phase without the need for excess boron. Furthermore, we study the thermal stability of these borides in air, and gauge the usefulness of this new family of borides. The work presented here partially validates some of the theoretical claims towards stable tetraborides, and we hope the positive and negative data will inspire new insights.

EXPERIMENTAL PROCEDURE

Alloys of WB_x with a variable boron content (x = 11.6, 10.5, 10.0, 9.5, 9.0, 8.5, 8.0, 7.0, 6.0 and 4.5), and alloys of WB_4 with Ta, Nb, V, Mo, Re and Cr were prepared using: tungsten (99.95%, Strem Chemicals, U.S.A.), amorphous boron (99+%, Strem Chemicals, U.S.A.), tantalum (99.9%, Materion, U.S.A.), niobium (99.8%, Strem Chemicals, U.S.A.), vanadium (99.5%, Strem Chemicals, U.S.A.), molybdenum (99.9%, Strem Chemicals, U.S.A.), rhenium (99.99%, Cerac Specialty Inorganics, now Materion), chromium (99.9%, Research Organics/Inorganics Chemical

Corp.). For these alloys of WB_4 the M : B ratio was kept at 1 : 4.5. For samples of 1-x W: x Ta : 4.5 B, 1-x W: x Nb : 4.5 B, 1-x W: x Mo : 4.5 B , 1-x W: x Re : 4.5 B and 1-x W: x Cr : 4.5 B, x = 0.083, 0.166, 0.250, 0.332, 0.415 and 0.500. For 1-y W: y V : 4.5 B, y = 0.166, 0.332, 0.500, 0.668 and 0.854.

Metal powders and boron in desired proportions were calculated, weighed and mixed with a pestle in an agate mortar to ensure homogeneity. The mixtures of powders were pressed into pellets under a 10-ton load using a hydraulic press (Carver). These cold-pressed pellets were then placed into an arc-melter chamber on top of a water-cooled copper hearth and arc-melted in an argon atmosphere using a current of I = 70 amps for t = 1 - 2 minutes.

Prepared samples were cut into two halves using a diamond saw (Ameritool Inc., U.S.A.). One half was used for powder X-ray diffraction analysis (PXRD) analysis and crushed into powder (< 40 μm) using a Plattner-style crusher. The other half was used for scanning electron microscopy (SEM) / energy dispersion spectroscopy (EDS) and Vickers hardness testing and was encapsulated into epoxy using an epoxy/hardener set (Allied High Tech Products Inc., U.S.A.).

To achieve an optically flat surface, the samples were polished using SiC papers (120 – 1200 grit sizes, Allied High Tech Products Inc., U.S.A.) and diamond films (30 to 1 micron particle sizes, South Bay Technology Inc., U.S.A.) on a semi-automated polishing station (South Bay Technology Inc., U.S.A.).

Purity and phase composition of the samples were established using PXRD and EDS techniques. PXRD was performed on a Bruker D8 Discover Powder X-ray Diffractometer (Bruker Corporation, Germany), using a Cu Kα X-ray beam (λ = 1.5418 Å) in the 5-100° 2θ range with a step size of 0.0353°, scan speed of 0.1055°/sec and time per step of 0.3 sec. The Joint Committee

on Powder Diffraction Standards (JCPDS) database was used to identify the phases present in the samples. The phase purity was further verified on the polished samples using an UltraDry EDS detector (Thermo Scientific, U.S.A.) attached to a FEI Nova 230 high-resolution scanning electron microscope (FEI Company, U.S.A.). *Maud* software was used to perform the unit cell refinements.[37–41]

Hardness measurements were done on polished samples using a load-cell type multi-Vickers hardness tester (Leco, U.S.A.) with a pyramidal diamond indenter tip. Under each applied load: 0.49, 0.98, 1.96, 2.94 and 4.9 N, 10 indents were made in randomly chosen spots on the sample surface. The lengths of the diagonals of the indents were measured using a high-resolution optical microscope, Zeiss Axiotech 100HD (Carl Zeiss Vision GmbH, Germany) with a 500x magnification. Vickers hardness values (H_v, in GPa) were calculated using the following formula (Equation 7.1) and the values of all 10 indents per load were averaged:

$$H_v = \frac{1854.4F}{d^2} \tag{7.1}$$

where d is the arithmetic average length of the diagonals of each indent in microns and F is the applied load in Newtons (N).

Density (ρ) measurements were performed utilizing a density determination kit (Mettler-Toledo, U.S.A.) by measuring the weights of the samples in air and in an auxiliary liquid (ethanol); the density was calculated using the following formula (Equation 7.2):

$$\rho = \frac{A}{A-B}(\rho_0 - \rho_L) + \rho_L \tag{7.2}$$

where A is the weight of the sample in air, B is the weight of the sample in the auxiliary liquid (ethanol), ρ_0 is the density of auxiliary liquid (ethanol – 0.789 g/cm^3), and ρ_L is the density of air (0.0012 g/cm^3).

A Pyris Diamond TGA/DTA unit (TG-DTA, Perkin-Elmer Instruments, U.S.A.) was utilized in order to perform the thermogravimetric analyses, each with the following heating profile: heat in air from 25 to 200 °C at a rate of 20 °C/min, hold at 200 °C for 30 minutes to remove any moisture, heat from 200 to 1000 °C at a rate of 2 °C/min, hold at 1000 °C for 2 hours and cool from 1000 to 25 °C at a rate of 5 °C/min. XRD analysis was then performed in order to identify the resulting phase(s).

RESULTS AND DISCUSSION

Here we investigate the effect of variable boron composition on the phase stability of tungsten tetraboride and its relation to both mechanical (hardness) and thermal (oxidation resistance) properties. In addition, we consider the possibility of stabilizing and forming a tungsten tetraboride type phase using a near-stoichiometric ratio of tungsten to boron by forming an alloy with metals that have a similar atomic size to W (1.35 Å): Ta (1.45 Å), Nb (1.45 Å), V (1.35 Å), Mo (1.45 Å), Cr (1.40 Å) and Re (1.35 Å).[42] By lowering the boron content below the traditional ratios used for synthesis, we will get a better grasp of which transition metals can actually sustain the desired structure.

The structure of tungsten tetraboride (Figure 7-1) has been under debate for many years, with several papers offering structures, which at first glance looked similar, but had some differences in the arrangement of the boron atoms in the unit cell (boron dimers vs. polyhedra).[18,43] We recently resolved this discrepancy through X-ray and neutron co-refinement, and find that the boron

backbone is most accurately described as a defective cuboctahedra while the W sites are only partially occupied (one-third of W atoms are systematically absent).[18,43] Tungsten tetraboride (*P6$_3$/mmc*) differs from other tetraboride families, such as: CrB_4 (*Immm*),[44] UB_4 (*P4/mbm*)[45,46] and MoB_4 (*P2$_1$/c*),[47,48] with only MoB_4 (*P6$_3$/mmc*)[49,50] belonging to a similar structure type. This can be explained by the fact that the value of Hägg's ratio (the ratio of the radius of a boron atom to the radius of a metal atom) for tungsten is 0.63, which is greater than 0.59 needed in order for the metal boride to adopt a simple cubic or hexagonal structure.[51] The unique structure of tungsten tetraboride allows it to accommodate metal atoms in vacancies in addition to ordinary substitution of metal (tungsten) positions, which enables alloys with other transition metals (Ti, Zr, Hf, Ta, Mo and Cr) to have enhanced mechanical properties (hardness) and oxidation resistance.[20,22,52] Therefore, in addition to accommodating the metals in the voids inside the structure (as well as substitute in tungsten positions in the case of $W_{1-x}Mo_xB_{4.5}$),[52] WB_4 can also form a traditional solid solution, and therefore, the Hume-Rothery rules (atomic radii difference, similarity of crystal structure, oxidation states and electronegativity) are fully applicable to these cases.[53]

The composition and purity of the samples were analyzed and verified using powder X-ray diffraction (PXRD). Figure 7-2 shows the powder XRD patterns for samples of WB_x with a variable nominal composition of boron (x = 4.5, 6.0, 7.0, 8.0, 8.5, 9.0, 9.5, 10.0, 10.5 and 11.6) in the 10 – 50° 2Θ range. Figure 7-3 shows the PXRD patterns for samples of (1-x) W: (x) Ta : 4.5 B (x = 0.083, 0.166, 0.250, 0.332, 0.415 and 0.500) in the 15 – 50° 2Θ range. Furthermore, full PXRD spectra in the 15 – 80° 2Θ range for samples of (1-x) W: (x) Ta : 4.5 B, (1-x) W: (x) Nb : 4.5 B, (1-x) W: (x) Mo : 4.5 B , (1-x) W: (x) Re : 4.5 B and (1-x) W: (x) Cr : 4.5 B (x = 0.083, 0.166, 0.250, 0.332, 0.415 and 0.500) and (1-y) W: (y) V : (4.5) B (y = 0.166, 0.332, 0.500, 0.834, 1.000) can be found in Figures 7-4 - 7-5.

PXRD data for WB_x with a variable boron composition can be found in Figure 7-2. These data show that the tungsten tetraboride phase (JCPDS 00-019-1373), is present at all tungsten to boron ratios. Moreover, WB_4 without any secondary tungsten-boron phases can be readily prepared with a W : B ratio of 1 : 11.6 to 1 : 9.0; however, due to the stoichiometry used, excess crystalline boron (β-rhombohedral boron)[54] will be present in the samples. A lower boride phase, tungsten diboride appears at W : B ratios of less than or equal to 1 : 11.6, as seen from the phase diagram; from the pXRD, the diboride peaks show at W : B ratios at 1 : 8.5 and lower. Analyzing the phase diagram for the tungsten-boron system,[19,23] it should be noted that since tungsten tetraboride is an incongruently melting phase and a peritectic decomposition product, it can coexist with excess boron upon cooling a melt of nominal composition W : B of 1 : 4; this also holds for other tetraborides (e.g. CrB_4).[44] Table 7-1 provides the unit cell data for WB_x, which indicates that for boron ratios of 11.6 down to 4.5 there are no significant changes in the lattice parameters for the tungsten tetraboride phase.

From our previous diffraction study, the stoichiometry of tungsten tetraboride from the unit cell is ~$WB_{4.5}$, and thus to probe the stability of theoretically predicted metal tetraboride phases, we kept the boron content fixed and substituted tungsten with other metals[25–35]. This will reveal which of the computationally predicted tetraborides are stable; plus, the presence of tungsten should help direct formation. Powder XRD data for the alloys of W with Ta, Nb and V prepared with a M : B = 1 : 4.5, are given in Figures 7-3. For $W_{1-x}Ta_xB_{4.5}$ (Figure 7-3), it can be seen that both tungsten tetraboride and tungsten diboride structure are present at low concentrations of Ta (below 25 at.% Ta), while the TaB_2 phase (JCPDS 03-065-3385) appears at higher concentrations of Ta (~58.5 at.% Ta). These phases are probably solid solutions with tantalum. However, at around 33.2 at.% Ta, no secondary, lower boride phases for either tungsten or tantalum are present, and the

remaining peaks correspond only to the tetraboride phase. The peaks are slightly broadened indicating that the structure is under stress as Ta does not appear to want to be in the *P6$_3$/mmc* crystal structure, since TaB_2 (*P6/mmm*)[55] is the highest boride known in that system.[56] Table 7-2 shows the unit cell data for alloys of (1-x) W: (x) Ta : 4.5 B. These data indicate the formation of a solid solution as can be seen in the change of the parameters of the hexagonal unit cell from *a* = 5.200 Å and *c* = 6.336 Å, to *a* = 5.242 Å and *c* = 6.417 Å.

As Ta is a group 5 transition metal that stabilizes the preparation of a WB_4 phase at low boron content, we next tested the role of size. For (1-x) W: (x) Nb : 4.5 B and (1-y) W: (y) V : 4.5 B (Figure 7-4) the behavior is similar, with samples with low concentrations of secondary metals (Nb and V) having peaks corresponding to tungsten tetraboride and tungsten diboride, in the case of Nb, and WB_4 in the case of V. However, both alloys form a lower boride phase, NbB_2 (*P6/mmm*, JCPDS 03-065-7540)[57] and VB_2 (*P6/mmm*, JCPDS 01-089-3927)[58] at higher concentrations of secondary metal (Nb and V). In the case of (1-x) W : (x) Nb : 4.5 B, the formation of the lower boride of niobium occurs while WB_2 is also present in the samples; for (1-y) W: (y) V : 4.5 B, VB_2 phase is formed almost immediately upon adding vanadium to WB_4; the small size of vanadium is unfavorable in the WB_4 structure, thus resulting in smaller values for the lattice parameters of VB_2 phase. These observations can be explained by the fact that although all three metals added are in the same group (group 5), thus possessing the same valence electron count, Ta is the only metal for which in addition to valence electron count, the atomic size difference and the overall chemical nature is the most similar to tungsten. This suggests that both valence electron count and atomic size is crucial.

PXRD for WB_4 with Mo is given in Figure 7-4a. For 1-x W: x Mo : 4.5 B, tungsten tetraboride forms at all concentrations of Mo; molybdenum also forms a tetraboride that belongs with to the

same structure type as WB_4, MoB_4 (*P6₃/mmc*, JCPDS 00-020-1236).[49,50] Tungsten diboride, WB_2 is also present at all concentrations of Mo, in addition, MoB_2 ($R\bar{3}m$, JCPDS 00-038-1460)[59,60] forms at ~50 at.% Mo. The fact that Mo is completely soluble in WB_4, forming a solid solution, due to having a tetraboride with the same crystal structure, may explain why there is no suppression of lower boride phases even though Mo is in the same group as W and has a similar atomic size to Ta.

PXRD for WB_4 with Re is given in Figure 7-4b. For (1-x) W : (x) Re : 4.5 B, tungsten tetraboride forms at concentrations of Re of 0 - 41.5 at.% Re. Tungsten diboride, WB_2, is present at concentrations of Re from 0 – 25.0 at.% Re, in addition, ReB_2 (*P6₃/mmc*, JCPDS 00-011-0581)[61] forms at all concentrations of rhenium. In this case, rhenium forms a very favorable, stable phase[62], ReB_2, and does not readily alloy with WB_4.

PXRD for WB_4 with Cr is given in Figure 7-4c. For $W_{1-x}Cr_xB_{4.5}$, tungsten tetraboride forms at concentrations of Cr from 0 - 41.5 at.% Cr. Tungsten diboride, WB_2 is present at concentrations of Cr from 0 – 41.5 at.% Cr, in addition, CrB_2 (*P6/mmm*, JCPDS 01-089-3533)[63] forms at concentrations of chromium from 25.0 – 50.0 at.% Cr. In this case, Cr can only form a diboride using a melt technique (such as arc-melting), while CrB_4 can only be formed by a non-melt/equilibrium technique (such as vapor transport[44]). However, analogous to the case of vanadium, due to the size of chromium (and the resulting small lattice parameters for CrB_2 compared to other metal diborides) it cannot be accommodated in the WB_4 structure and precipitates out as a separate phase.

Figure 7-6 presents SEM images of the surfaces of WB_4 samples with a variable boron composition from 11.6 down to 4.5. Note that while the overall decomposition patterns remain similar between

the samples, the areas corresponding to the metallic tetraboride phase (gray) become larger until a ratio of W : B = 1 : 8.5, which agrees with the decrease in the insulating boron phase. However, after that lower tungsten to boron ratios produce the lower boride phase, WB_2, which appears inside of the WB_4 grains as lighter gray areas, since WB_2 has a more metallic character than WB_4. Figure 7-7 shows close up SEM images and EDS maps of WB_x with a ratio of W : B = 1 : 4.5, showing the difference in contrast between WB_2 and WB_4 areas. The W map shows the tungsten "rich" areas corresponding to WB_2 and more tungsten "poor" areas corresponding to WB_4. This can be explained by the fact that WB_2 has a higher melting point than WB_4, 2365 °C versus 2020 °C[64], respectively, indicating that WB_2 forms first with WB_4 forming around the WB_2 "template", similar to WB_4 formation around TiB_2.[20]

Figure 7-8 shows the SEM image and elemental maps for $W_{0.668}Ta_{0.332}B_{4.5}$. Comparing the SEM/EDS images and maps for this alloy and for WB_x with a W : B ratio of 1 : 4.5 (Figure 7-7), it should be noted that the W-Ta boride is almost completely single phase (with the exception of some β-rhombohedral boron), with no lower borides present. This further verifies the formation of a "pure" WB_4-like phase; further optimization could likely totally eliminate the excess boron.

In addition, density measurements were performed on samples of WB_x with a variable boron content and the results are presented in Table 7-1. The XRD density of tungsten tetraboride is 8.4 g/cm^3, while the pycnometric density of W : B = 1 : 11.6 is 5.15 g/cm^3. This can be explained by the fact that WB_x has excess boron in the form of β-rhombohedral boron, with a density of 2.29 g/cm^3.[24] The density of WB_x with a variable boron content of 11.6 down to 4.5, increases from 5.15 to ~8.5 g/cm^3 due to not only reduction in the excess boron content, but also to the formation of a lower boride, WB_2, which has a density of 12.76 g/cm^3.[65]

Vickers micro-indentation hardness measurements of WB_x with a variable boron content were performed after establishing the composition and purity of the samples using PXRD and SEM/EDS. The samples were indented using applied loads of 0.49 N (50 gram-force, "low load") to 4.9 N (500 gram-force, "high load"). Figure 7-9 shows the hardness of WB_x with a variable boron composition. It can be seen that samples which only contain the WB_4 phase and excess β-rhombohedral boron (W : B = 1 : 11.6 to 1 : 9.0) have similar, within experimental error, hardness values of ~40 GPa at low load (50 gf), which makes it possible to prepare alloys and solid solutions of WB_4 using a lower nominal metal to boron ratio of 1 : 9.0 versus the traditional 1 : 12. It is likely that WB_2 is present in all samples below a W : B ratio of 1 : 11.6, and is thus responsible for the decreasing hardness. Depending on the application, this may result in better thermal conductivity properties, as the samples become more metallic with a lower concentration of the more insulating boron secondary phase. For samples with a W : B ratio of lower than 1 : 9.0, a decrease in hardness can be observed, from 41.2 ± 1.4 GPa to 30.8 ± 2.8 GPa at low load, which can be explained by the formation of the softer tungsten diboride phase (H_v for WB_2 is ~26 GPa),[23] which reduces the overall hardness of the sample. The decrease in hardness is less pronounced for "high loading" (500 gf), indicating that the hardness of the material approaching the asymptotic limit stays relatively constant, while the extrinsic hardness due to grain and surface morphology (at "low loading" - 50 gf) changes to a greater degree. The hardness of $W_{0.668}Ta_{0.332}B_4$ was measured to be 33.7 ± 2.2 GPa at low load, which although higher than that for WB_x with a W : B ratio of 1 : 4.5 (30.8 ± 2.8 GPa), is still lower than that of WB_x with W : B ratios from 1 : 9 to 1 : 11.6 (~40 GPa).

Figure 7-10 summarizes the thermogravimetric analysis performed in air on WB_x with W : B ratios from 1 : 9 to 1 : 11.6. Oxidation resistance is very important for cutting and machining materials

as it characterizes the long-term stability and performance of the materials. TGA analysis shows that both compositions of WB_x have similar oxidation resistance temperatures of ~455 °C (~450 °C for WB_x with a ratio of W : B = 11.6 and ~465 °C for a ratio of W : B = 1 : 9.0).

The oxidation resistance temperatures together with comparable hardness values (~40 GPa) suggests that these materials can be readily interchanged if less boron content is desired. The tungsten-boron system is interesting because excellent mechanical properties are found in a relatively low cost metal (tungsten) system. The existence of the $W_{0.668}Ta_{0.332}B_{4.5}$ alloy means that further optimization with less addition of a secondary metal is possible and perhaps less boron content may lead to a composition that will have a comparable hardness level to traditional WB_4 prepared with 11.6 boron equivalents.

CONCLUSIONS

Alloys of tungsten tetraboride with a variable metal to boron ratios of 1 : 11.6 down to 1 : 4.5 were synthesized and analyzed for their mechanical (hardness) and thermal oxidation properties. For the variable boron WB_x, it was found that both hardness and oxidation resistance remain constant for M : B = 1 : 11.6 – 1 : 9.0 (~40 GPa at low load and ~455 °C oxidation resistance), which makes it possible to prepare tungsten tetraboride with a lower number of boron equivalents. However, for low M : B ratios (below 1 : 8.5), the hardness quickly dropped to ~30 GPa at low load, due to the formation of the soft tungsten diboride phase. It was found that by adding a second metal (Ta), WB_4 could be stabilized with a nearly stoichiometric amount of boron (4.5) with no secondary phases. The resulting hardness of $W_{0.668}Ta_{0.332}B_{4.5}$ (M : B = 1 : 4.5) alloy although greater than that for $WB_{4.5}$ (33.7 ± 2.2 GPa at low load), is lower than that of "traditional" tungsten tetraboride (Table 7-3), prepared with more equivalents of boron (~40 GPa at low load). However, the

existence of a $W_{0.668}Ta_{0.332}B_{4.5}$ alloy means that further optimization (there is a somewhat linear dependence of boron content versus the addition of a secondary metal) with less addition of a secondary metal and perhaps more boron content may lead to a composition that will have a similar hardness level to traditional WB_4 prepared with 11.6 boron equivalents.

ACKNOWLEDGMENTS

This manuscript is dedicated in loving memory of Nino Manelashvili, the mother of lead author.

We thank the National Science Foundation Division of Materials Research, Grant DMR-1506860 (R.B.K.) for financial support.

Table 7-1. Unit Cell Data[a], Density[b], and % phase[c] for WB_x with a Variable Boron Composition

W : B	a (Å)	c (Å)	ρ (g/cm^3)	% β-B	% WB_2 / WB_4
1 : 11.6[b]	5.199(8)	6.329(9)	-	-	-

1 : 11.6	5.202(1)	6.341(1)	5.15[d]	44.42	55.78
1 : 11.0	5.201(3)	6.338(1)	5.38	-	-
1 : 10.5	5.202(3)	6.338(3)	5.44	48.28	51.72
1 : 10.0	5.203(5)	6.340(2)	5.69	-	-
1 : 9.5	5.201(1)	6.337(3)	5.73	43.15	56.85
1 : 9.0	5.201(2)	6.336(2)	6.12	42.95	57.05
1 : 8.5	5.201(4)	6.337(2)	6.29	36.18	63.82
1 : 8.0	5.203(4)	6.338(4)	6.82	34.89	65.11
1 : 7.0	5.200(2)	6.335(1)	7.51	32.81	67.19
1 : 6.0	5.202(1)	6.338(1)	7.94	30.53	69.47
1 : 4.5	5.200(1)	6.336(2)	8.46	21.50	78.50

[a]The standard deviations are given in brackets;
[b]Values for this unit cell were taken from Lech *et al.*;[18]
[c]Values calculated from area analysis of SEM images;
[d]Density of tungsten tetraboride phase from XRD is 8.40 g/cm^3.[65]

Table 7-2. Unit Cell Data for $WB_{4.5}$[a] and $W_{1-x}Ta_xB_{4.5}$[a,b]

Alloy	at.% Ta	a (Å)	c (Å)
$WB_{4.5}$	0.0	5.200(1)	6.336(2)
$W_{0.917}Ta_{0.083}B_{4.5}$	8.3	5.209(2)	6.353(3)
$W_{0.834}Ta_{0.166}B_{4.5}$	16.6	5.216(3)	6.365(2)
$W_{0.750}Ta_{0.250}B_{4.5}$	25.0	5.217(2)	6.365(4)
$W_{0.668}Ta_{0.332}B_{4.5}$	33.2	5.224(3)	6.377(4)
$W_{0.585}Ta_{0.415}B_{4.5}$	41.5	5.232(2)	6.398(3)
$W_{0.500}Ta_{0.500}B_{4.5}$	50.0	5.242(1)	6.417(2)

[a]The alloys were prepared with a W : B = 1 : 4.5;

[b]The standard deviations are given in brackets.

Table 7-3. Comparison of Various Superhard Materials

Composition	Vickers Hardness (GPa)	Load (N)
c-BN	47[a]	9.8
Diamond	85[a]	9.8
WB_4	46.2[b]	0.49
ReB_2	48[a]	0.49
$W_{0.668}Ta_{0.332}B_4$	33.7[c]	0.49

[a]Hardness values were taken from Mohammadi *et al*.;[66]
[b]Hardness value was take from Gu *et al*.;[67]
[c]Hardness value is from current work.

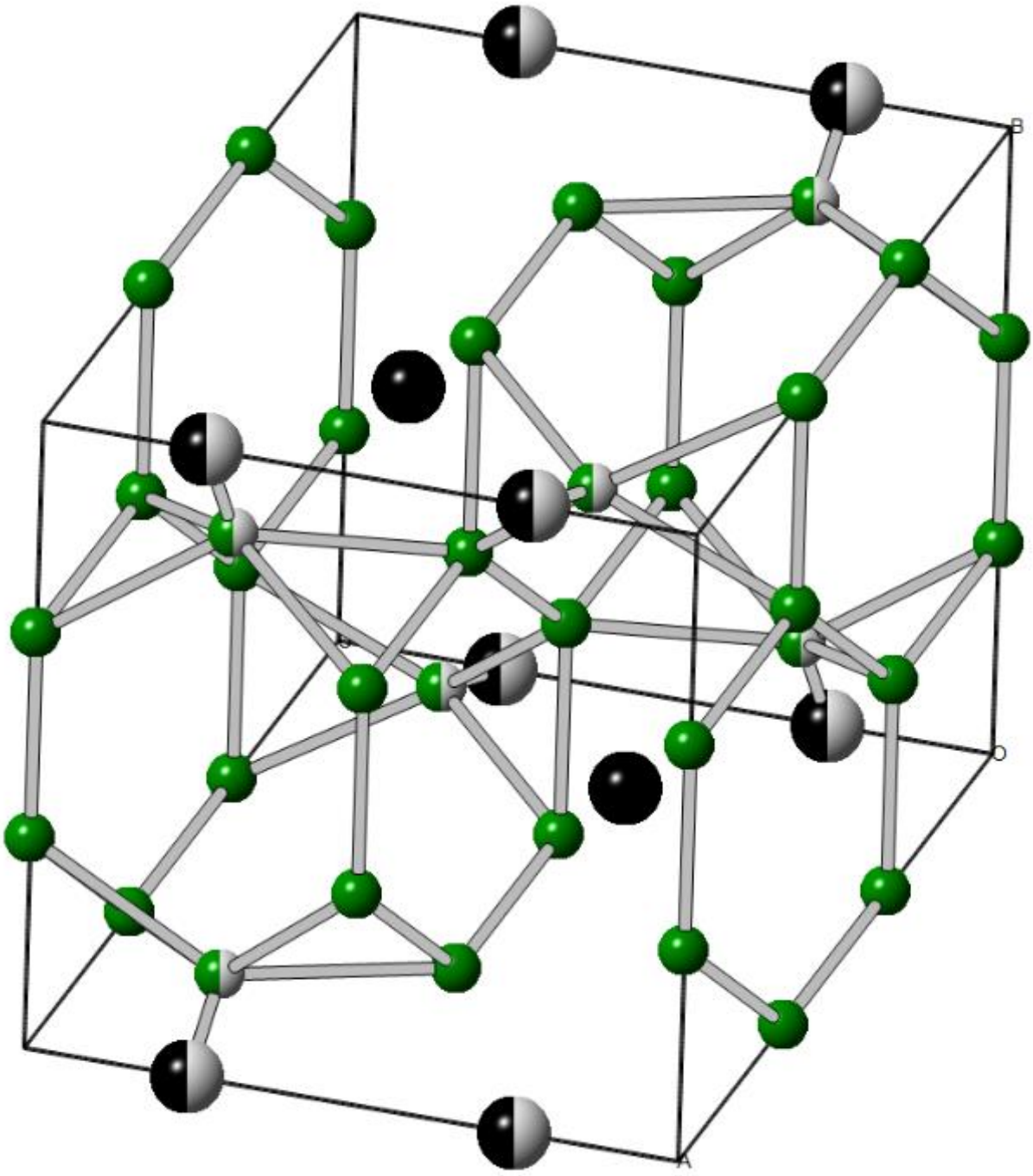

Figure 7-1. Tungsten tetraboride crystal structure (*P6₃/mmc*, ICSD (Inorganic Crystal Structure Database) 291124).[18] Tungsten atoms are shown in black, while boron atoms are in green; half-filled atoms depict partially occupied positions.

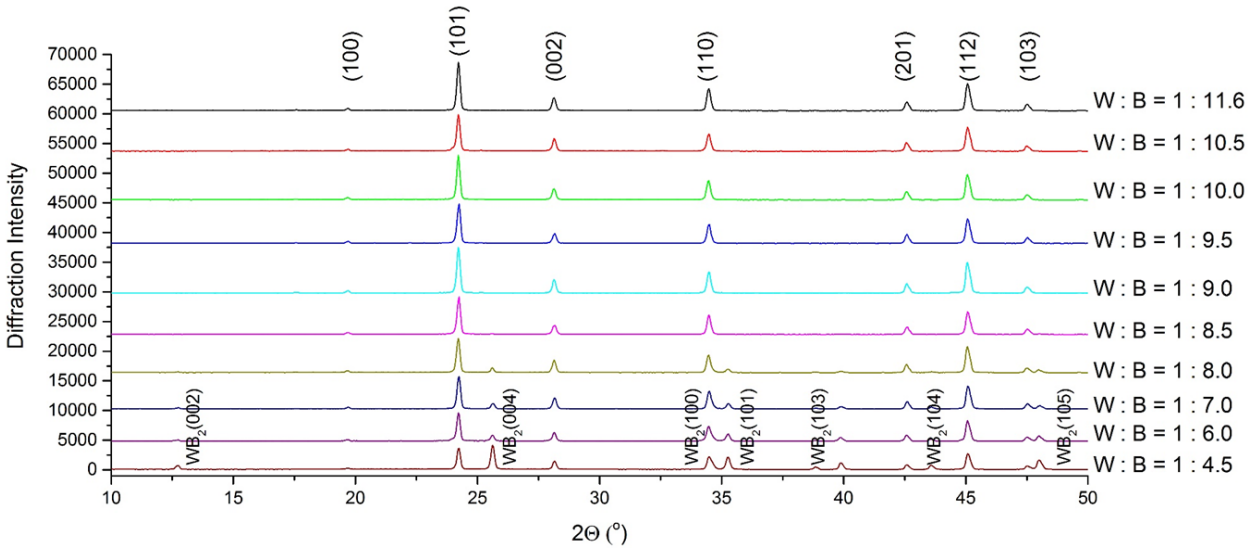

Figure 7-2. Powder XRD patterns (10 – 50° 2Θ) of alloys of WB_x with a variable boron content of 4.5 to 11.6. Tungsten tetraboride (JCPDS 00-019-1373), forms at all ratios of W : B; tungsten diboride, WB_2 (JCPDS 01-073-1244) appears below W : B ratio of 1 : 9.0.

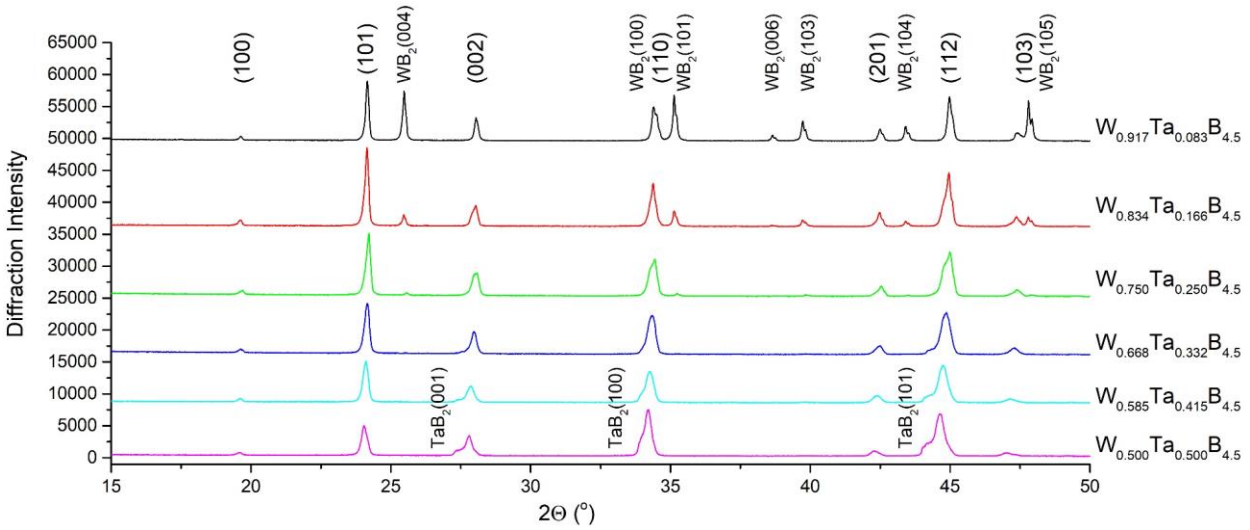

Figure 7-3. Powder XRD patterns (15 – 50° 2Θ) of alloys of (1-x) W : (x) Ta : 4.5 B. Tungsten tetraboride (JCPDS 00-019-1373), forms at all concentrations of Ta; tungsten diboride, WB_2 (JCPDS 01-073-1244) disappears at a tantalum content of 25 at.% Ta, visible TaB_2 (JCPDS 03-065-3385) peaks appear at a tantalum content of 50 at.% Ta. The sample with a composition of $W_{0.668}Ta_{0.332}B_{4.5}$ contains only WB_4 peaks.

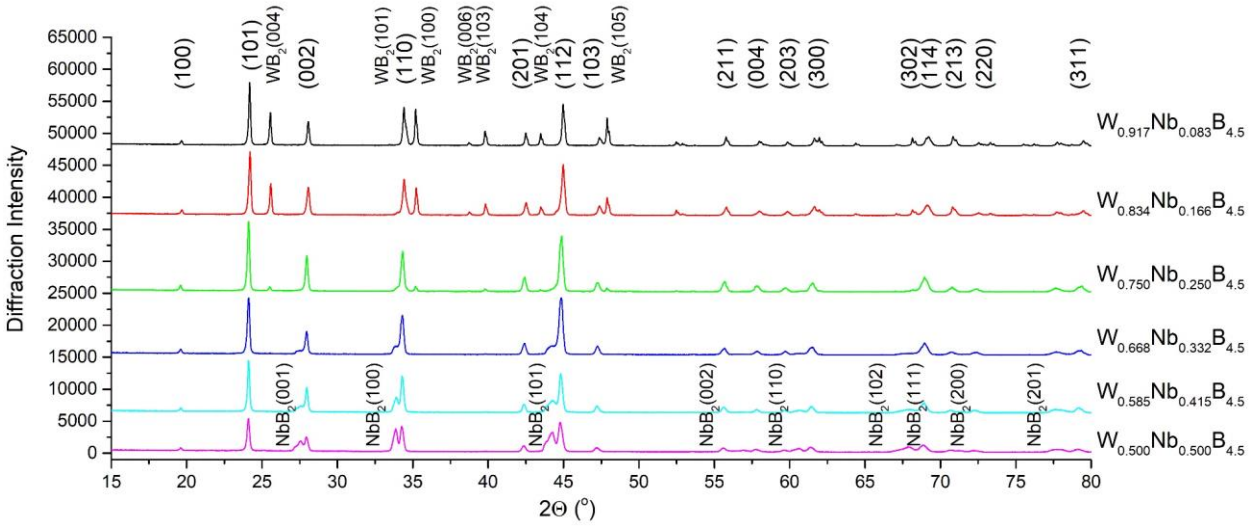

(a)

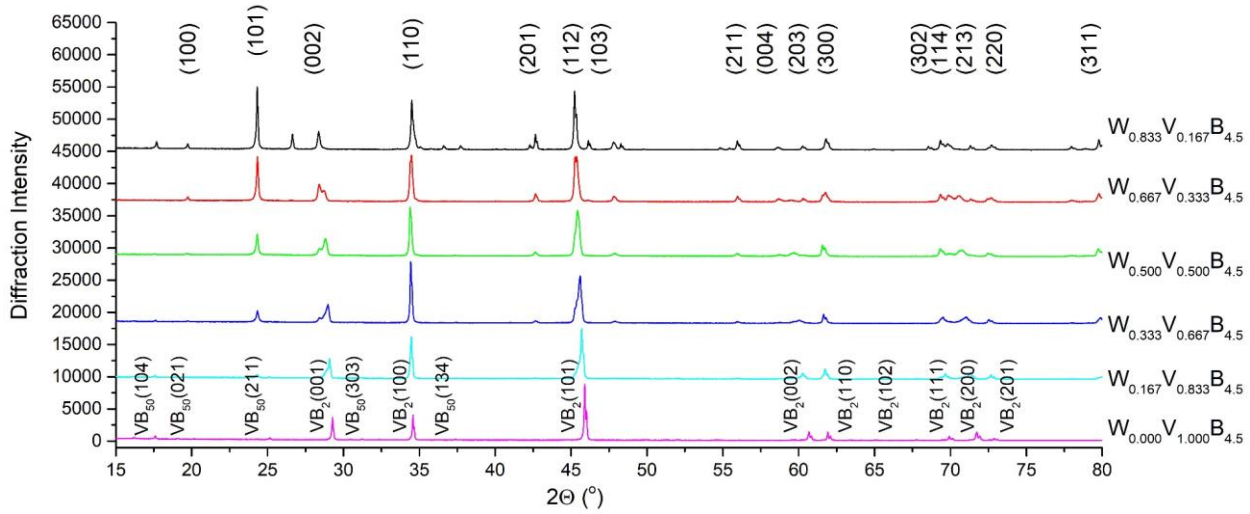

(b)

Figure 7-4. Powder XRD patterns (15 – 80° 2Θ) of alloys of (a) $W_{1-x}Nb_xB_{4.5}$, and (b) $W_{1-x}V_xB_{4.5}$. Tungsten tetraboride (JCPDS 00-019-1373), forms at all concentrations of Nb and V. For (a) tungsten diboride, WB_2 (JCPDS 01-073-1244) disappears at a niobium content of 33.2 at.% Nb, visible NbB_2 (JCPDS 03-065-7540) peaks appear at a niobium content of 33.2 at.% Nb. For (b) visible VB_2 (JCPDS 01-089-3927) peaks appear at a vanadium content of 33.3 at.% V.

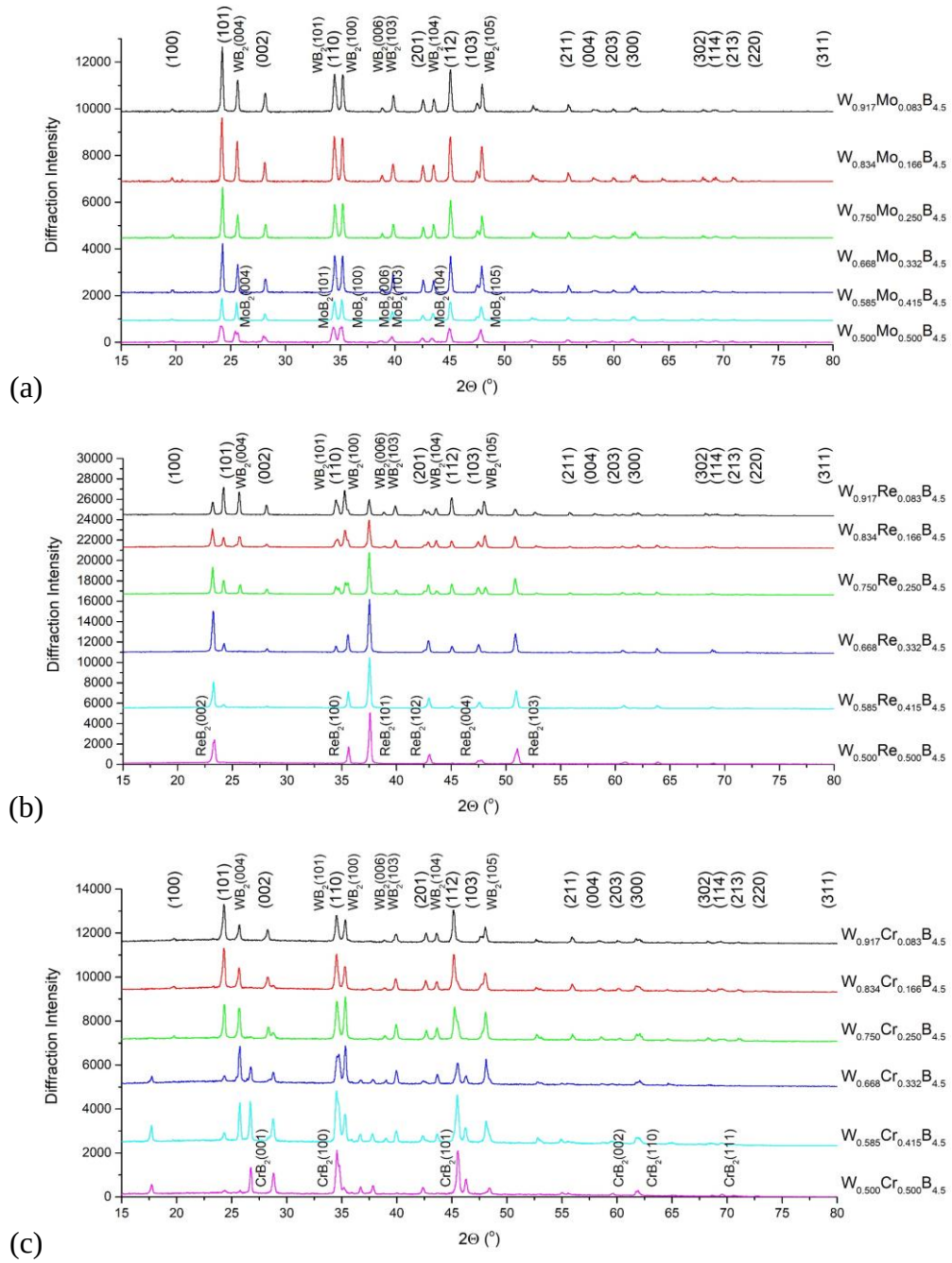

Figure 7-5. Powder XRD patterns (15 – 80° 2Θ) of alloys of (a) $W_{1-x}Mo_xB_{4.5}$, (b) $W_{1-x}Re_xB_{4.5}$ and (c) $W_{1-x}Cr_xB_{4.5}$. (a) WB_4 (JCPDS 00-019-1373), forms at all concentrations of Mo, as molybdenum also forms a tetraboride with a similar crystal structure, MoB_4 (JCPDS 00-020-1236). Tungsten diboride, WB_2 (JCPDS 01-073-1244) is present at all concentrations of Mo; MoB_2 (JCPDS 00-038-1460) forms at ~50 at.% Mo. (b) WB_4 (JCPDS 00-019-1373), forms at concentrations of Re from 0 – 41.5 at.% Re. WB_2 (JCPDS 01-073-1244) is present at concentrations of Re from 0 – 25.0 at.% Re; ReB_2 (JCPDS 00-011-0581) forms at all concentrations of Re. (c) WB_4 (JCPDS 00-019-1373), forms at concentrations of Cr from 0 – 41.5 at.% Cr. WB_2 (JCPDS 01-073-1244) is present at concentrations of Re from 0 – 41.5 at.% Cr; CrB_2 (JCPDS 01-089-3533) forms at all concentrations of Cr from 25 – 50 at.% Cr.

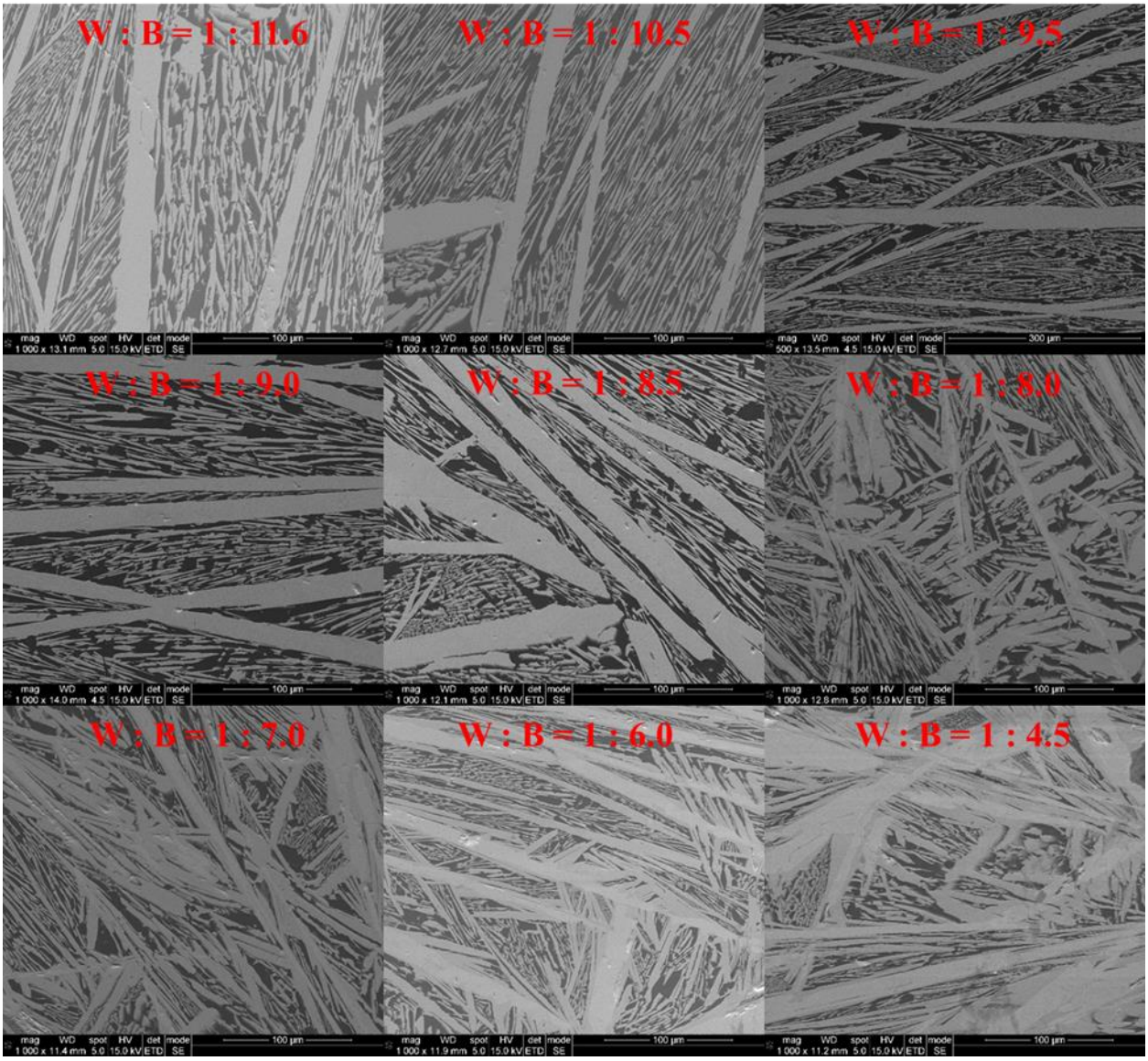

Figure 7-6. SEM images of surfaces of alloys of WB_x with a variable boron content from 4.5 to 11.6. Black areas correspond to boron, while gray areas correspond to metallic phases (tungsten tetra- and diborides). For samples with a W : B of more than 1 : 8.5, only tungten tetraboride and boron are present; for samples with W : B of less than 1 : 8.5, WB_2 (lighter gray areas) can be seen alongside tungten tetraboride. All images were taken at a magnification of 1000x and the scale bar in the images is 100 μm.

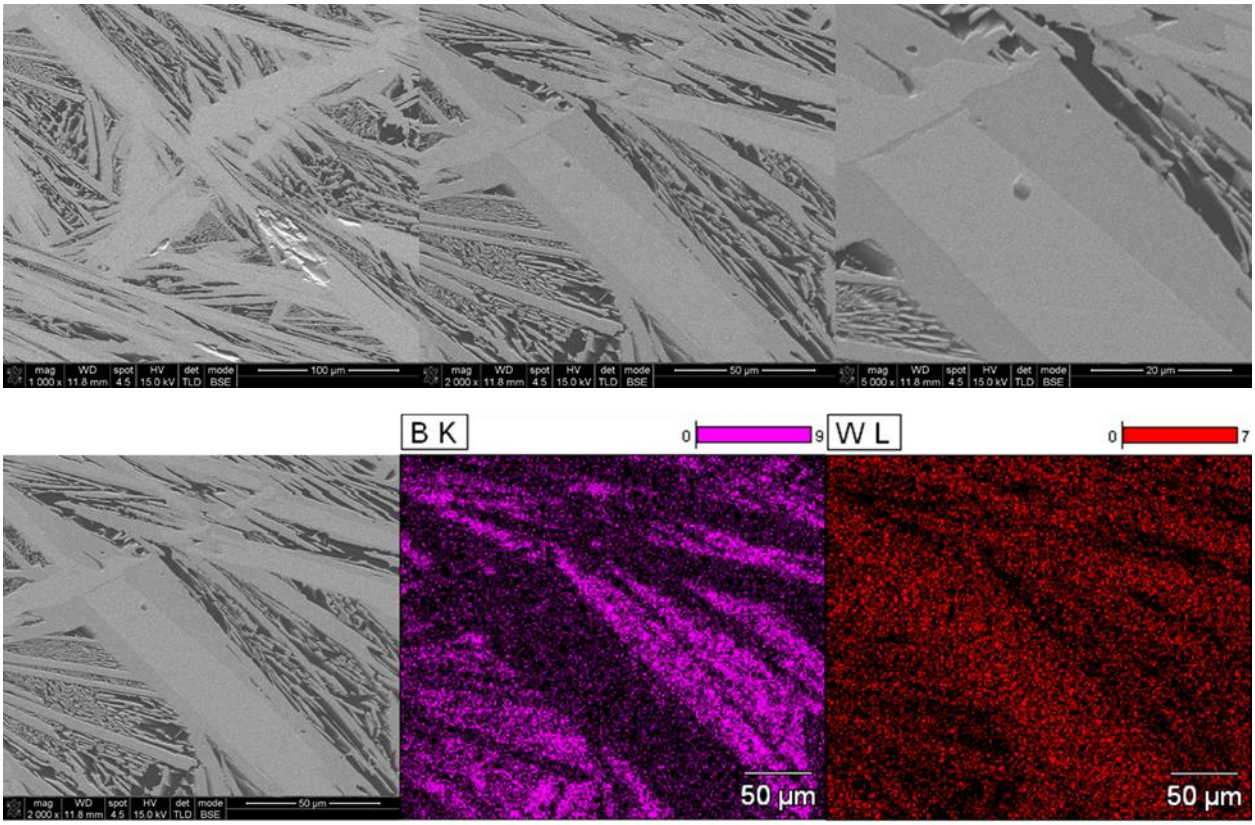

Figure 7-7. (Top) SEM images of surfaces of alloys of WB_x with a ratio of W : B = 1 : 4.5. Black areas correspond to boron, while gray areas correspond to metallic phases: tungten tetraboride (dark gray) and WB_2 (light gray). The images were taken at a magnification of 1000x (left), 2000x (Middle) and 5000x (right) and the scale bars in the images are 100, 50 and 20 µm, respectively. (Bottom) SEM image and EDS maps (boron K line and tungsten L line) for a sample of WB_x with a ratio of W : B = 1 : 4.5. Black areas correspond to crystalline β-rhombohedral boron (seen in B map). The W map shows the tungsten "rich" areas corresponding to WB_2 and more tungsten "poor" areas corresponding to tungten tetraboride. The image and maps were taken at 2000x magnification; the scale bar in the images is 50 µm.

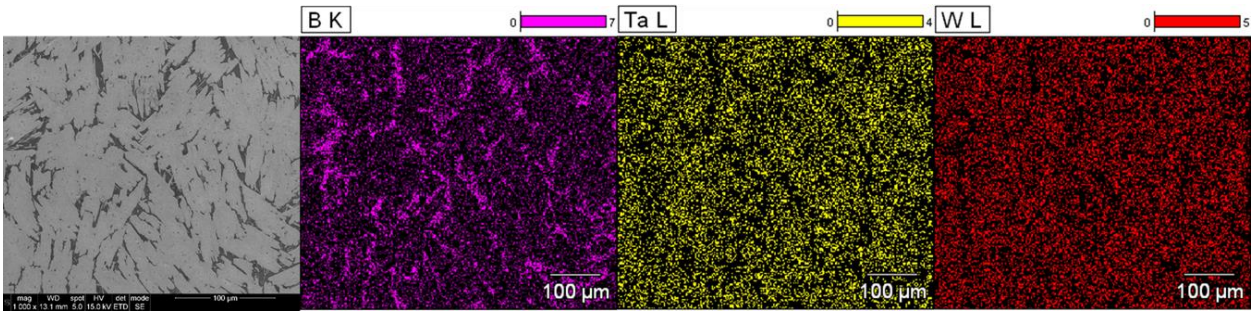

Figure 7-8. Elemental maps for boron (K line), tantalum (L line) and tungsten (L line) for the $W_{0.668}Ta_{0.332}B_{4.5}$ alloy, showing the presence of both tantalum and tungsten in the metal-boron phase; the boron rich areas are β-rhombohedral boron.

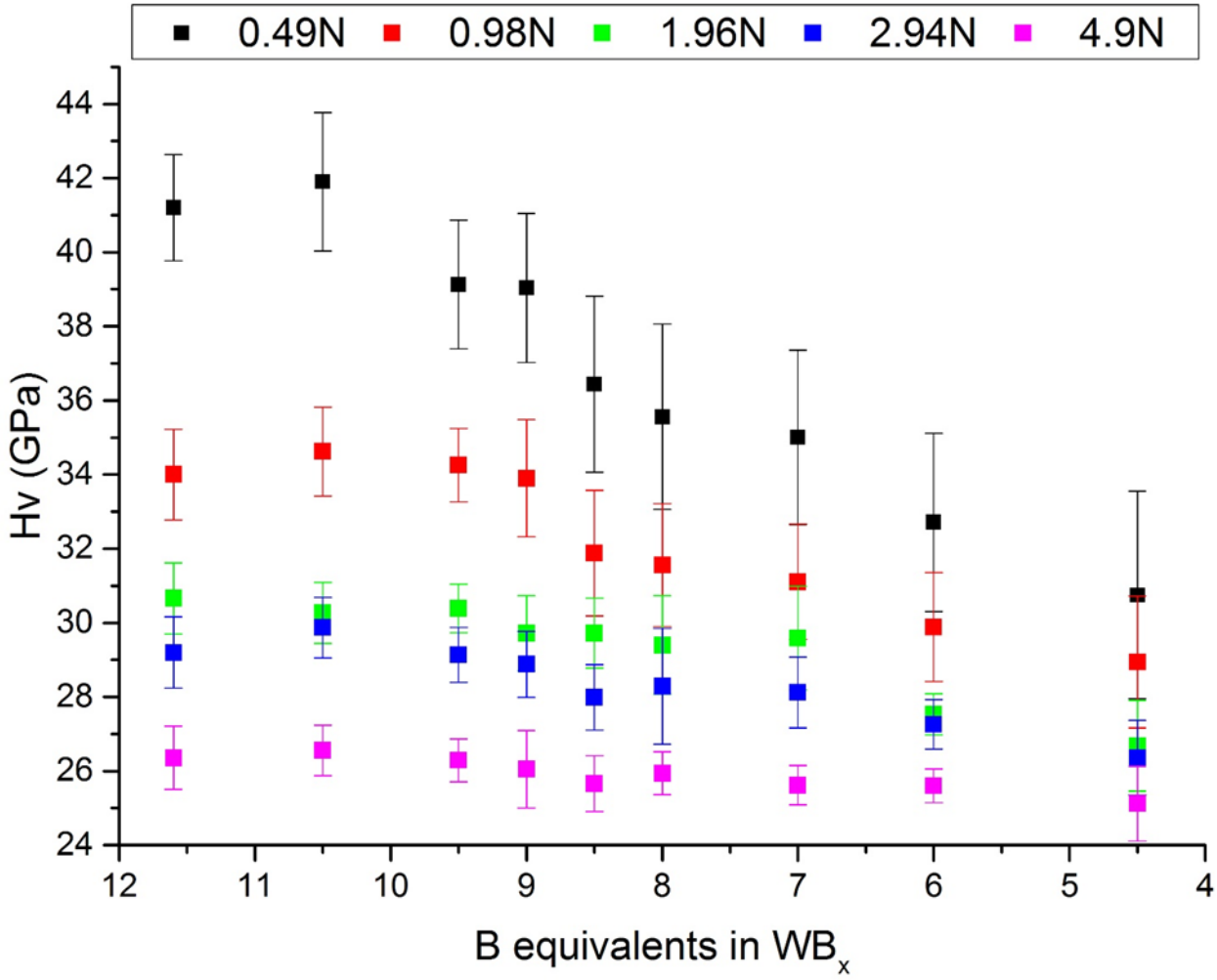

Figure 7-9. Vickers micro-indentation hardness of alloys of WB_x with a variable boron content of 4.5 to 11.6 under 0.49 N (50 gram-force, "low") to 4.9 N (500 gram-force, "high") loads. The hardness of tungsten tetraboride alloys prepared with a W : B ratio from 1 : 11.6 to 1 : 9.0, have a hardness of ~40 GPa.

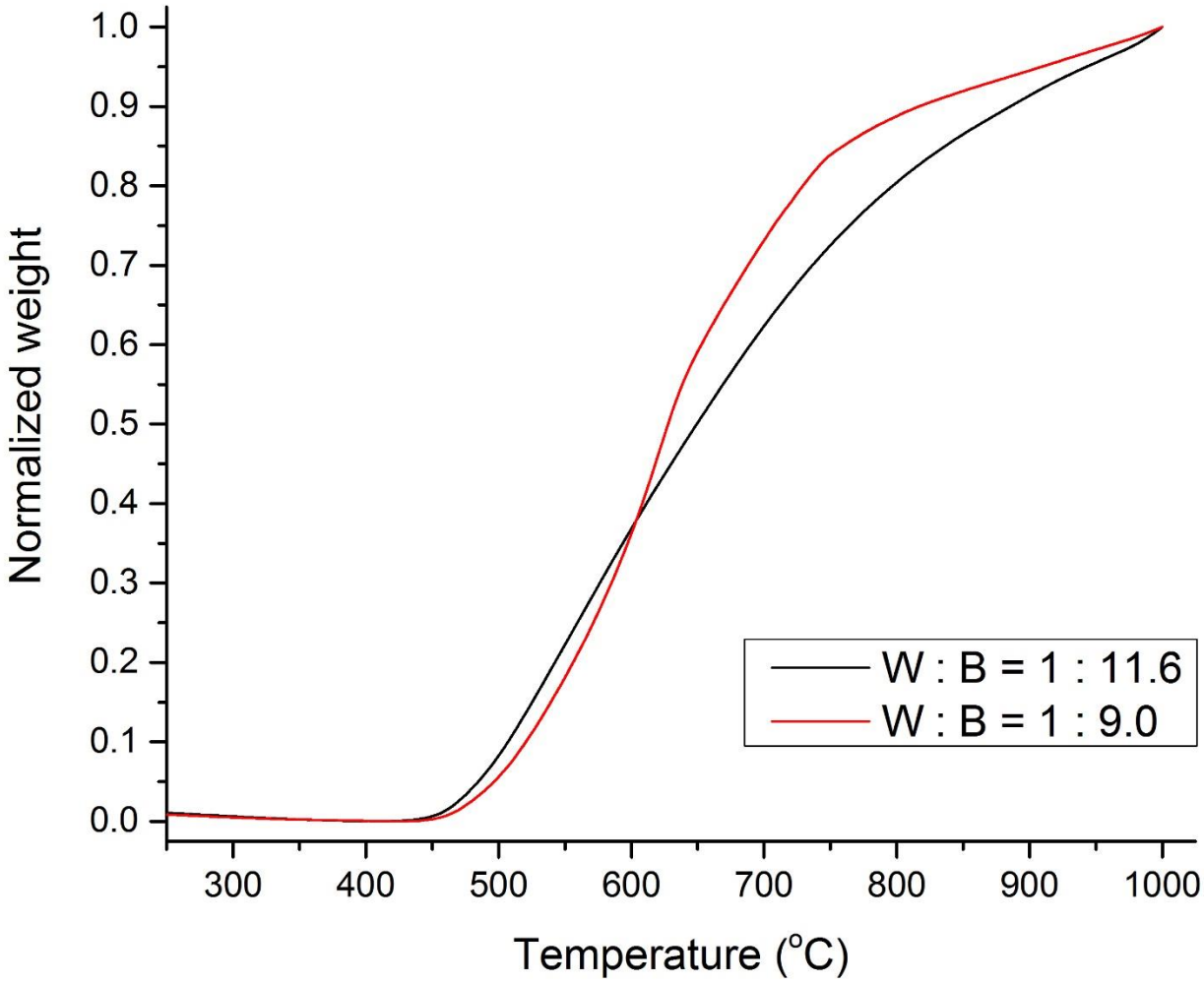

Figure 7-10. Thermal stability of tungsten tetraboride alloys prepared with a W : B ratio of 1 : 11.6 and 1 : 9.0, as measured by thermal gravimetric analysis in air. These data show that both of these alloys are stable to a temperature of ~455 °C, using the extrapolated onset method (~450 °C for WB_x with W : B = 11.6 and ~465 °C for W : B = 1 : 9.0).

REFERENCES

1. Samsonov, G. V., Markovskii, L. Y., Zhigach, A. F. & Valyashko, M. G. *Boron, Its Compounds and Alloys [in Russian]*. (House of the Academy of the Sciences Ukrainian SSR, 1960).

2. Samsonov, G. V., Serebriakova, T. I. & Neronov, V. A. *Borides [in Russian]*. (Atomizdat, 1975).

3. Buschow, K. H. J. Magnetic Properties of Borides. in *Boron and Refractory Borides* (ed. Matkovich, V. I.) 494–515 (Springer Berlin Heidelberg, 1977). doi:10.1007/978-3-642-66620-9_26

4. Scheifers, J. P., Zhang, Y. & Fokwa, B. P. T. Boron: Enabling Exciting Metal-Rich Structures and Magnetic Properties. *Acc. Chem. Res.* **50,** 2317–2325 (2017).

5. Lundström, T. Borides: Solid-state Chemistry. in *Encyclopedia of Inorganic Chemistry* 481–494 (2006).

6. Fokwa, B. P. T. Borides: Solid-State Chemistry. *Encycl. Inorg. Bioinorg. Chem.* 1–14 (2014). doi:10.1002/9781119951438.eibc0022.pub2

7. Albert, B. & Hillebrecht, H. Boron: Elementary challenge for experimenters and theoreticians. *Angew. Chemie - Int. Ed.* **48,** 8640–8668 (2009).

8. Kiessling, R., Samuelson, O., Lindstedt, G. & Kinell, P.-O. The Borides of Manganese. *Acta Chemica Scandinavica* **4,** 146–159 (1950).

9. Akopov, G., Yeung, M. T. & Kaner, R. B. Rediscovering the Crystal Chemistry of Borides. *Adv. Mater.* **29,** (2017).

10. Yeung, M. T., Mohammadi, R. & Kaner, R. B. Ultraincompressible, Superhard Materials.

Annu. Rev. Mater. Res. **46,** 465–485 (2016).

11. Chung, H.-Y. *et al.* Synthesis of Ultra-Incompressible Superhard Rhenium Diboride at Ambient Pressure. *Science (80-.).* **316,** 436–439 (2007).

12. Chung, H.-Y. *et al.* Response to Comment on 'Synthesis of Ultra-Incompressible Superhard Rhenium Diboride at Ambient Pressure'. *Science (80-.).* **318,** 1550 (2007).

13. Mohammadi, R. *et al.* Tungsten tetraboride, an inexpensive superhard material. *Proc. Natl. Acad. Sci. U. S. A.* **108,** 10958–10962 (2011).

14. Yeung, M. T. *et al.* Superhard Monoborides: Hardness Enhancement through Alloying in W1−xTaxB. *Adv. Mater.* 6993–6998 (2016). doi:10.1002/adma.201601187

15. Akopov, G., Yeung, M. T., Sobell, Z. C., Turner, C. L. & Kaner, R. B. Superhard Mixed Metal Dodecaborides. *Chem. Mater.* **28,** 6605–6612 (2016).

16. Akopov, G., Sobell, Z. C. C., Yeung, M. T. T. & Kaner, R. B. B. Stabilization of LnB12 (Ln = Gd, Sm, Nd, and Pr) in Zr1−xLnxB12 under Ambient Pressure. *Inorg. Chem.* **55,** 12419–12426 (2016).

17. Akopov, G., Yeung, M. T., Turner, C. L., Li, R. L. & Kaner, R. B. Stabilization of HfB12 in Y1-xHfxB12 under Ambient Pressure. *Inorg. Chem.* **55,** 5051–5055 (2016).

18. Lech, A. T., Turner, C. L., Mohammadi, R., Tolbert, S. H. & Kaner, R. B. Structure of superhard tungsten tetraboride: A missing link between MB 2 and MB 12 higher borides. *Proc. Natl. Acad. Sci.* **112,** 3223–3228 (2015).

19. Bodrova, L. G., Koval'chenko, M. S. & Serebryakova, T. I. Preparation of tungsten tetraboride. *Sov. Powder Metall. Met. Ceram.* **13,** 1–3 (1974).

20. Akopov, G., Yeung, M. T., Turner, C. L., Mohammadi, R. & Kaner, R. B. Extrinsic hardening of superhard tungsten tetraboride alloys with group 4 transition metals. *J. Am. Chem. Soc.* **138,** 5714–5721 (2016).

21. Yeung, M. T. *et al.* Superhard W0.5Ta0.5B nanowires prepared under ambient pressure. *Appl. Phys. Lett.* **109,** 203107 (2016).

22. Mohammadi, R. *et al.* Toward inexpensive superhard materials: Tungsten tetraboride-based solid solutions. *J. Am. Chem. Soc.* **134,** 20660–20668 (2012).

23. Portnoi, K. I., Romashev, V. M., Levinskii, Y. V. & Romanovich, I. V. Phase diagram of the system tungsten-boron. *Powder Metall.* **5,** 398–402 (1967).

24. Hoard, J. L., Sullenger, D. B., Kennard, C. H. L. & Hughes, R. E. The structure analysis of beta-rhombohedral boron. *J. Solid State Chem.* **1,** 268–277 (1970).

25. Zhang, X., Zhao, E. & Wu, Z. Prediction of new high pressure phase of TaB 3 : First-principles. *J. Alloy. Compd.* **632,** 37–43 (2015).

26. Yan, Q., Wang, Y. X., Wang, B., Yang, J. & Yang, G. The ground-state structure and physical properties of ReB3 and IrB3 predicted from first principles. *RSC Adv.* **5,** 25919–25928 (2015).

27. Wu, L. *et al.* Unraveling Stable Vanadium Tetraboride and Triboride by First- Principles Computations. *J. Phys. Chem. C* **119,** 21649–21657 (2015).

28. Zeiringer, I. *et al.* Crystal Structure of W(1-x)B3 and Phase Equilibria in the Boron-Rich Part of the Systems Mo-Rh-B and W- {Ru , Os , Rh , Ir , Ni , Pd , Pt }-B. *J. Phase Equilibria Diffus.* **35,** 384–395 (2014).

29. Liang, Y., Yuan, X., Fu, Z., Li, Y. & Zhong, Z. An unusual variation of stability and hardness in molybdenum borides. *Appl. Phys. Lett.* **101,** 1–6 (2012).

30. Zhang, M., Yan, H., Wei, Q. & Wang, H. Universal ground state hexagonal phases and mechanical properties of stoichiometric transition metal tetraborides: TMB4(TM =W, Tc, and Re). *Comput. Mater. Sci.* **68,** 371–378 (2013).

31. Wang, B., Wang, D. Y. & Xu, Y. A new hard phase of ReB 4 predicted from first principles. *J. Alloys Compd.* **573,** 20–26 (2013).

32. Online, V. A. *et al.* First-principles structural design of superhard material of ZrB 4. *Phys.Chem. Chem.Phys.* **15,** 20894–20899 (2013).

33. Liang, Y., Zhong, Z. & Zhang, W. A thermodynamic criterion for designing superhard transition-metal borides with ultimate boron content. *Comput. Mater. Sci.* **68,** 222–228 (2013).

34. Kotmool, K., Bovornratanaraks, T., Pinsook, U. & Ahuja, R. Superhard Semiconducting Phase of Osmium Tetraboride Stabilizing at 11 GPa. *J. Phys. Chem. C* **120,** 23165–23171 (2016).

35. Zhang, M., Yan, H., Wei, Q. & Zheng, B. Reinvestigation of Mechanical Properties and Shear-Induced Atomic Deformation of Tetragonal Superhard Semiconducting OsB 4. *J. Phys. Chem. C* **121,** 6290–6299 (2017).

36. Mansouri Tehrani, A., Ghadbeigi, L., Brgoch, J. & Sparks, T. D. Balancing Mechanical Properties and Sustainability in the Search for Superhard Materials. *Integr. Mater. Manuf. Innov.* **6,** 1–8 (2017).

37. Lutterotti, L. Maud Rev. 2.55. *Maud Rev. 2.55, Univ. Trento-Italy, Dep. Ind. Eng. Trento, Italy* (2015).

38. Lutterotti, L., Matthies, S., Wenk, H. R., Schultz, A. S. & Richardson, J. W. Combined texture and structure analysis of deformed limestone from time-of-flight neutron diffraction spectra. *J. Appl. Phys.* **81,** 594–600 (1997).

39. Lutterotti, L., Bortolotti, M., Ischia, G., Lonardelli, I. & Wenk, H. R. Rietveld texture analysis from diffraction images. *Zeitschrift fur Krist. Suppl.* **1,** 125–130 (2007).

40. Lutterotti, L. Total pattern fitting for the combined size-strain-stress-texture determination in thin film diffraction. *Nucl. Instruments Methods Phys. Res. Sect. B Beam Interact. with Mater. Atoms* **268,** 334–340 (2010).

41. Lutterotti, L., Chateigner, D., Ferrari, S. & Ricote, J. Texture, residual stress and structural analysis of thin films using a combined X-ray analysis. *Thin Solid Films* **450,** 34–41 (2004).

42. Slater, J. C. Atomic Radii in Crystals. *J. Chem. Phys.* **41,** 3199–3204 (1964).

43. Lundström, T. The structure of Ru2B3 and WB2.0 as etermined by single-crystal diffractometry, and some notes on the W-B system. *Ark. Kemi* **30,** 115–127 (1968).

44. Knappschneider, A., Litterscheid, C., Kurzman, J., Seshadri, R. & Albert, B. Crystal structure refinement and bonding patterns of CrB4: A boron-rich boride with a framework of tetrahedrally coordinated B atoms. *Inorg. Chem.* **50,** 10540–10542 (2011).

45. Zalkin, A. & Templeton, D. H. The crystal structures of CeB 4 ThB 4 and UB 4. *Acta Crystallogr.* **6,** 269–272 (1953).

46. Zalkin, A. & Templeton, D. H. The crystal structures of CeB4, ThB4 and UB4. *J. Chem. Phys.* **18,** 391 (1950).

47. Knappschneider, A. *et al.* Manganese Tetraboride, MnB4: High-Temperature Crystal Structure, p–n Transition, 55Mn NMR Spectroscopy, Solid Solutions, and Mechanical Properties. *Chem. – A Eur. J.* **21,** 8177–8181 (2015).

48. Knappschneider, A. *et al.* Peierls-distorted monoclinic MnB4 with a mn-Mn bond. *Angew. Chemie - Int. Ed.* **53,** 1684–1688 (2014).

49. Klesnar, H., Aselage, T. L., Morosin, B. & Kwei, G. H. The diboride compounds of molybdenum: MoB2−x and Mo2B5−y. *J. Alloys Compd.* **241,** 180–186 (1996).

50. Lundström, T. & Rosenberg, I. The crystal structure of the molybdenum boride Mo1-xB3. *J. Solid State Chem.* **6,** 299–305 (1973).

51. Hägg, G. Ubergangselementen in' binaren Sistem mit Bor, Kohlenstoff und Stickstoff. *Z. Phys. Chem.* **B12,** 33 (1931).

52. Mohammadi, R. *et al.* Enhancing the Hardness of Superhard Transition-Metal Borides: Molybdenum-Doped Tungsten Tetraboride. *Chem. Mater.* **28,** 632–637 (2016).

53. Kittel, C. *Introduction to Solid State Physics*. (John Wiley & Sons, 2005).

54. Slack, G. A., Hejna, C. I., Garbauskas, M. F. & Kasper, J. S. The crystal structure and density of β-rhombohedral boron. *J. Solid State Chem.* **76,** 52–63 (1988).

55. Okada, S., Kudou, K., Higashi, I. & Lundström, T. Single crystals of TaB, Ta5B6, Ta3B4 and TaB2, as obtained from high-temperature metal solutions, and their properties. *J. Cryst. Growth* **128,** 1120–1124 (1993).

56. Okamoto, H. Comment on B-Ta (boron-tantalum). *J. Phase Equilibria* **14,** 393–394 (1993).

57. Okada, S., Hamano, K., Lundström, T. & Higashi, I. Crystal growth of the new compound Nb2B3, and the borides NbB, Nb5B6, Nb3B4, and NbB2. *AIP Conf. Proc.* **231,** 456–459 (1991).

58. Spear, K. E., Liao, P. K. & Smith, J. F. B-V (Boron-Vanadium). in *Binary Alloy Phase Diagrams, Vol. 1* 551–554 (1990).

59. Frotscher, M. *et al.* M2B5 or M2B4? A Reinvestigation of the Mo/B and W/B System. *Zeitschrift für Anorg. und Allg. Chemie* **633,** 2626–2630 (2007).

60. Higashi, I., Takahashi, Y. & Okada, S. Crystal structure of MoB2. *J. Less-Common Met.* **123,** 277–283 (1986).

61. La Placa, S. J. & Post, B. The crystal structure of rhenium diboride. *Acta Crystallogr.* **15,** 97–99 (1962).

62. Portnoi, K. I. & Romashev, V. M. B-Re (Boron-Rhenium). in *Binary Alloy Phase Diagrams, Vol. 1* (ed. Massalski, T. B.) 525–526 (ASM International, 1990).

63. Portnoi, K. I., Romashov, V. M. & Romanovich, I. V. Diagram of state of the chromium-boron system. *Sov. Powder Metall. Met. Ceram.* **8,** 298–302 (1969).

64. Duschanek, H., Rogl, P. *et al.* Critical assessment and thermodynamic calculation of the binary system boron-tungsten (B-W). *J. Phase Equilibria* **16,** 150–161 (1995).

65. Kuz'ma, Y. B., Serebryakova, T. I. & Plakhina, A. M. The polymorphic transformation of W2B5. *Russ. J. Inorg. Chem.* **12,** 288–289 (1967).

66. Mohammadi, R. & Kaner, R. B. *Superhard Materials*. *Encyclopedia of Inorganic and Bioinorganic Chemistry* (R.A. Scott ed., John Wiley and Sons, Inc., 2012).

67. Gu, Q., Krauss, G. & Steurer, W. Transition Metal Borides: Superhard versus Ultra-incompressible. *Adv. Mater.* **20,** 3620–3626 (2008).

CHAPTER 8. EFFECTS OF DODECABORIDE-FORMING METALS ON THE PROPERTIES OF SUPERHARD TUNGSTEN TETRABORIDE

"Reprinted (adapted) with permission from (Akopov, G.; Yeung, M.T.; Roh, I.; Sobell, Z.C.; Yin, H.; Mak, W.H.; Khan, S.I.; Kaner, R. B. "Effects of Dodecaboride-Forming Metals on the Properties of Superhard Tungsten Tetraboride" *Chem. Mater.* **2018**, 30, 3559-3570 DOI: 10.1021/acs.chemmater.8b01464). Copyright (2018) American Chemical Society."

ABSTRACT

Tungsten tetraboride alloys with Y, Sc, Gd, Tb, Dy, Ho and Er were prepared by arc-melting and investigated for their thermal stability and mechanical properties. The phase composition and purity were confirmed by powder X-ray diffraction (PXRD) and energy dispersive X-ray spectroscopy (EDS). In all cases, except for Sc, a change to a "dendritic" morphology was observed; for alloys with Sc, the metal boride and boron grains became smaller; however, no patterning was observed. This shows that tuning the composition of the alloys of WB_4 with transition metals and lanthanides results in a modification of the morphology leading to patterning and smaller grains that enhance mechanical and thermal properties. For alloys of WB_4 with Y, Sc, Gd, Dy, Tb, Ho and Er, an increase in hardness to 50.2 ± 2.4, 48.9 ± 2.5, 48.0 ± 2.1, 46.3 ± 2.6, 48.5 ± 2.3, 46.4 ± 3.4, 47.2 ± 2.9 GPa at low load, respectively, compared to 41.2 ± 1.4 GPa for WB_4 is observed. Moreover, the alloys of WB_4 with Y, Sc and Gd showed an increase in oxidation resistance from ~450 °C for WB_4, to ~470 °C, ~525 °C and 465 °C, respectively.

INTRODUCTION

Metal borides are often used as structural materials simply because of their superior mechanical properties. Perhaps one defining feature of borides is their superhardness (defined as having a Vickers hardness, H_v, above 40 GPa) and ultra-incompressibility (defined as having a bulk

modulus above 300 GPa).[1–4] Rhenium diboride (ReB_2) is the first reported superhard transition metal boride,[1,2] however, due to the high price of rhenium metal, a search for less costly alternatives resulted in the discovery of tungsten tetraboride (WB_4) as an alternative.[3] Over the last few years, the field has prospered with more phases (alloys and solid-solutions) using: 1) elements analogous to tungsten, such as tantalum in metal monoborides (greatly increasing bulk modulus);[4] or 2) possessing a true 3D network of boron atoms (making the material more isotropic and preventing shear in the structure), as in metal dodecaborides, MB_{12}.[5–7]

The search for new superhard metals stands on the shoulders of boride crystallography. Metal borides come in a large variety of possible structures, primarily defined by the way the boron atoms are arranged: isolated boron atoms (e.g. Cr_4B), single and double chains (e.g. CrB and Ta_3B_4), networks of boron atoms (e.g. AlB_2, ReB_2, WB_4, ZrB_{12}), and structures based on boron icosahedra, B_{12} (e.g. ZrB_{50} and GdB_{66}).[8,9] Metal borides have a long and rich history spanning over a century; and numerous publications have demonstrated the many remarkable properties of these compounds summarized in the following review papers: boride chemistry,[9–11] structures,[12] electronic and magnetic,[13,14] thermal[13,15] and mechanical[9,16] properties.

Superhard tungsten tetraboride (WB_4, Figure 8-1) is crystallographically unique among borides, due to its "defect" structure, possessing both voids and metal vacancies.[17,18] Since WB_4 is based on a defective cubic dodecaboride structure, it can not only form traditional solid-solution compounds (accepting secondary metals as substitutional dopants), but can also accommodate interstitial dopants to form alloys. Both of these methods can lead to enhancement of mechanical properties for WB_4 and other borides, through both intrinsic (e.g. solid-solution hardening) and extrinsic (e.g. morphology modification) effects.[3,4,19–21]

As an incongruently melting phase, WB_4, is usually prepared with excess boron (W : B ~ 1 : 12) in order to prevent the formation of the softer lower boride (WB_2).[3,20,22] At this metal to boron ratio, WB_4 forms alongside β-rhombohedral boron ($R\bar{3}m$). However, due to the excess crystalline boron present, the size and shape of the grains can be controlled and fine tuning of properties can be accomplished.[20] Pure tungsten tetraboride cannot be prepared at the stoichiometric ratio of tungsten to boron, however, it can be stabilized by the addition of ~32 at. % Ta at W : B = 1 : 4.5, although, the structure appears to be under stress and its mechanical properties are hindered.[23]

By incorporating group 3 (Sc and Y) and lanthanide (Gd, Tb, Dy, Ho and Er) metals into WB_4 alloys and solid solutions, we hope to control morphology and as a result enhance hardness and thermal stability. However, Sc appears to behave completely different as compared to Y and the lanthanides, therefore, the papers will highlight these differences that Sc and other metals have on the properties of WB_4.

EXPERIMENTAL PROCEDURE

Alloys of WB_4 with Y, Sc, Gd, Tb, Dy, Ho and Er were prepared using: tungsten (99.95%, Strem Chemicals, U.S.A.), amorphous boron (99+%, Strem Chemicals, U.S.A.), yttrium (99.9%, Strem Chemicals, U.S.A.), scandium (99.9%, American Elements, U.S.A.), gadolinium (99.9%, Strem Chemicals, U.S.A.), terbium (99.9%, Strem Chemicals, U.S.A.), dysprosium (99.9%, Strem Chemicals, U.S.A.), holmium (99.9%, Strem Chemicals, U.S.A.) and erbium (99.9%, Strem Chemicals, U.S.A.). For these alloys the M : B ratio was kept at 1 : 11.6. For samples with a nominal composition of $(W_{1-x}Y_x)$: 11.6B, $(W_{1-x}Gd_x)$: 11.6B, $(W_{1-x}Tb_x)$: 11.6B, $(W_{1-x}Dy_x)$: 11.6B, $(W_{1-x}Ho_x)$: 11.6B, and $(W_{1-x}Er_x)$: 11.6B, x = 0.00, 0.02, 0.04, 0.06, 0.08, 0.10, 0.20, 0.30,

0.40, 0.50; and for the samples of ($W_{1-z}Sc_z$) : 11.6B, z = 0.00, 0.02, 0.04, 0.06, 0.08, 0.10, 0.20, 0.25, 0.30, 0.40, 0.50.

Boron and metal powders in appropriate ratios were mixed in an agate mortar with a pestle to ensure homogeneity. A hydraulic press (Carver) was used to press the mixtures of powders into pellets (ø1.27 cm (0.5 in)) under a 10-ton load. The pressed pellets were then placed into an arc-melting chamber on top of a water-cooled copper hearth and arc-melted in an Ar atmosphere using a current of 70 amps until molten (typically less than 1 - 2 minutes).

A plate-like single crystal of $ScB_{\sim 24}$ (scandium in the β-rhombohedral boron phase) was acquired serendipitously, having formed on the surface of one of the arced Sc-B samples upon cooling.

The prepared samples were separated into two halves using a diamond saw (Ameritool Inc., U.S.A.), with one half crushed into sub-40 μm powder for powder X-ray diffraction analysis (PXRD) using a Plattner-style crusher, while the other half was encapsulated into epoxy for scanning electron microscopy (SEM) / energy dispersion spectroscopy (EDS) and Vickers hardness testing using an epoxy/hardener set (Allied High Tech Products Inc., U.S.A.).

In order to polish the samples to an optically flat surface, SiC papers (120 – 1200 grit sizes, Allied High Tech Products Inc., U.S.A.) and diamond films with particle sizes ranging from 30 to 1 micron (South Bay Technology Inc., U.S.A.) were used on a semi-automated polishing station (South Bay Technology Inc., U.S.A.).

To establish the purity and phase composition of the samples, PXRD and EDS techniques were used. PXRD was performed on a Bruker D8 Discover Powder X-ray Diffractometer (Bruker Corporation, Germany) using a Cu Kα X-ray beam (λ = 1.5418 Å) in the 5 - 100° 2Θ range with a step size of 0.0353°, scan speed of 0.1055°/sec and time per step of 0.3 sec. The Joint Committee

on Powder Diffraction Standards (JCPDS) database was used to identify the phases present in the samples. *Maud* software was used to perform the unit cell refinements.[24–29] The phase purity was further verified on the polished samples using an UltraDry EDS detector (Thermo Scientific, U.S.A.) attached to a FEI Nova 230 high-resolution scanning electron microscope (FEI Company, U.S.A.).

In order to perform single crystal structure determination, a single crystal of scandium boride was mounted on a nylon loop using perfluoropolyether oil. A Bruker APEX-II CCD diffractometer (Bruker Corporation, Germany), with a Mo *Kα* X-ray beam (λ = 0.71073 Å) was used to collect the diffraction data. Unit cell determination and data refinement were carried out using the program Bruker SAINT. The structue was solved using SHELXS-97[30,31] and refined using SHELXL-2013.[32,33]

Hardness measurements were performed on polished samples using a load-cell type multi-Vickers hardness tester (Leco, U.S.A.) with a pyramidal diamond indenter tip. Under each applied load: 0.49, 0.98, 1.96, 2.94 and 4.9 N, 10 indents were made in randomly chosen spots on the sample surface. The lengths of the diagonals of the indents were measured using a high-resolution optical microscope, Zeiss Axiotech 100HD (Carl Zeiss Vision GmbH, Germany) with a 500x magnification. Vickers hardness values (H_v in GPa) were calculated using the following formula (Equation 8.1) and the values of all 10 indents per load were averaged:

$$H_v = \frac{1854.4F}{d^2} \tag{8.1}$$

where *d* is the arithmetic average length of the diagonals of each indent in microns and F is the applied load in Newtons (N).

Density (ρ) measurements were performed utilizing a density determination kit (Mettler-Toledo, U.S.A.) by measuring the weights of the samples in air and in an auxiliary liquid (ethanol); the density was calculated using the following formula (Equation 8.2):

$$\rho = \frac{A}{A-B}(\rho_0 - \rho_L) + \rho_L \qquad (8.2)$$

where *A* is the weight of the sample in air, *B* is the weight of the sample in the auxiliary liquid (ethanol), ρ_0 is the density of auxiliary liquid (ethanol – 0.789 g/cm^3), and ρ_L is the density of air (0.0012 g/cm^3).

A Pyris Diamond TGA/DTA unit (TG-DTA, Perkin-Elmer Instruments, U.S.A.) was utilized in order to perform the thermogravimetric analyses, each with the following heating profile: heat in air from 25 to 200 °C at a rate of 20 °C/min, hold at 200 °C for 30 minutes to remove any moisture, heat from 200 to 1000 °C at a rate of 2 °C/min, hold at 1000 °C for 2 hours and cool from 1000 to 25 °C at a rate of 5 °C/min. Oxidation resistance temperature was determined using extrapolated oxidation onset - temperature that denotes the temperature at which the weight loss begins. The extrapolated temperature onset (tangent to the part of the curve where there is no change in the slope gradient) is used because it is reproducible between TGA analysis on different instruments (ASTM E1131-08(2014); ISO 11358-1:2014).[34,35] XRD analysis was then performed in order to identify the resulting phase(s).

RESULTS AND DISCUSSION

Figure 8-2 shows a scheme depicting the phase formation in ($W_{1-x}M_x$) : 11.6B (M = Sc, Y, Gd, Tb, Dy, Ho and Er) alloys with the addition of different amounts of secondary metals. Figures 8-3, 8-4a-c, and 8-5a-c show the PXRD data for the alloy of W : 11.6B with Sc, Y, Gd and Tb, Dy,

Ho and Er in the 10 – 50° 2Θ range. Several other candidate metals were either unsuccessful in their alloying with W : 11.6B, such as La, Sm, Nd and Pr (large metal size relative to W), or were not used, due to hazards (Pm being radioactive) and/or their pyrophoric nature (Ce), and availability in pure form (oxides) or metal size (Eu, Yb and Lu).

It can be seen that Sc has several unique effects on ($W_{1-x}Sc_x$) : 11.6B alloys (Figure 8-3): it has the widest range of full solubility (≤ 0.20 at.% Sc) and in that it eventually suppresses the formation of tungsten tetraboride phase and promotes the formation of tungsten diboride (≥ 25 at.% Sc), and, moreover, Sc does not form its dodecaboride phase (ScB_{12}) or any other boride phase, except for the boron-rich $ScB_{24\text{-}28}$ ($R\bar{3}m$, JCPDS 01-071-0420; Figure 8-6, Cambridge Crystallographic Data Center (CCDC) 1565340),[36] which appears at ~40 at.% Sc. This mutual suppression of WB_4 and ScB_{12} phases by scandium and tungsten, respectively, can be explained by several factors. First, ScB_{12} (in pure form) forms a tetragonal structure (*I4/mmm*[36–39]), unlike all other MB_{12} phases;[39] this, together with the fact that the WB_4 structure can be derived from a cubic MB_{12} metastable phase,[18,20] could lead to the possible formation of scandium dodecaboride in the melt, thus suppressing the WB_4 phase. Second, scandium is known to form metal diboride phases, such as an AlB_2-type (*P6/mmm*) structure with tungsten, which could be highly favorable for the W-Sc-B ternary system and suppress the formation of higher borides (WB_4 and ScB_{12}).[40] On the other hand, Y and the lanthanides' behavior (Figures 8-4a-c and 8-5a-c) is similar in that the alloys possess some region of full solubility in ($W_{1-x}M_x$) : 11.6B (≤ 0.06 at.% for Y and Gd and ≤ 0.08 at.% for Tb, Dy, Ho and Er) and crystalline β-rhombohedral boron, followed by a region of equilibrium of a ($W_{1-x}M_x$) : 11.6B alloy with their highest boride (GdB_6 ($Pm\bar{3}m$) for Gd and MB_{12} phases ($Fm\bar{3}m$) for Tb, Dy, Ho and Er) and a boron-rich boride phase (MB_{66} ($Fm\bar{3}c$) in all cases). The behavior of yttrium and terbium is similar to that of zirconium (another dodecaboride forming

transition metal) in W : 11.6B.[20] Interestingly, tungsten diboride only forms in the case of Y and Tb, being absent in the cases of other lanthanides. This fact can be in part explained by analyzing the binary and M-B[41–47] and ternary W-M-B[40,48–50] phase diagrams. From these diagrams it can be speculated that $(W_{1-x}Y_x)$: 11.6B and $(W_{1-x}Tb_x)$: 11.6B alloys form a tungsten diboride phase, due to yttrium and terbium (being the only lanthanide) having a congruently melting diboride (YB_2 and TbB_2, *P6/mmm*), similar to the W-B system.[22,44,49]

Table 8-1 presents the data for the unit cell parameters for the alloys of WB_4 with secondary metals. It could be noted that while there is a marginal change in the value of the *a* lattice parameter, there a noticeable change in the value of the *c* lattice parameter. Tungsten tetraboride has a defect structure (Figure 8-1), which can accommodate metal atoms in the voids and vacancies as interstitial dopants. This could explain the lattice expansion (especially in the *c*-direction) due to the fact that all secondary metals used have a larger atomic radius than W (1.60 Å for Sc, 1.80 Å for Y and ~1.75 Å for lanthanides, compared to 1.35 Å for W).[51]

Density measurements were performed on W : 11.6B alloys with Sc, Y, Gd, Tb, Dy, Ho and Er (Figure 8-7). The general density trend is that the overall density of the $(W_{1-x}M_x)$: 11.6B alloy decreases with an increasing addition of a secondary metal, as all of those metals are less dense than tungsten. However, depending on the chemical nature of the secondary metal and its boride phases' melting points, the density of the samples may stay relatively constant (e.g. alloys with Dy and Ho) as more time is needed in order to melt the pressed sample pellet, and as such, more boron might evaporate during arc melting. However, as all of the samples (with the exception of alloys with a high content of Sc) contain a "pure" tungsten tetraboride phase, it could be stipulated that boron content never drops below 9.0 – 9.5 as that is the minimum amount of boron required to form WB_4, with an addition of no or a small amount of secondary metals.[23] It was shown that WB_4

prepared with a metal to boron ratio of 1 : 11.6 to 1 : 9.0, retains almost identical hardness and oxidation resistance properties.[23] The greatest change in density is for the Sc alloy, which changes from 5.15 g/cm^3 ("pure" tetraboride) to 3.94 g/cm^3 (at 50 at.% Sc), due to the low density of scandium (3.0 g/cm^3). This could be advantageous for more lightweight superhard materials and tools as this W-Sc-B alloy is ~24% lighter than "pure" tungsten tetraboride.

Figures 8-8, 8-9 and 8-10 show the SEM images and elemental maps for the alloys of W : 11.6B with Sc, Y, Gd, Tb, Dy, Ho and Er. For $(W_{0.75}Sc_{0.25})$: 11.6B, the elemental maps show the presence of both scandium and tungsten in the metal-boron phase, while the boron rich areas correspond to solid solutions of scandium in the β-rhombohedral boron phase (Figure 8-8).[36] On the other hand, for yttrium and the five lanthanides (Figures 8-9 and 8-10), the "metal-rich" (non-tungsten) areas correspond to the highest metal-boride formed: YB_{12}, GdB_6, TbB_{12}, DyB_{12}, HoB_{12} and ErB_{12}, as confirmed by PXRD data. Gadolinium has a cubic-*MB_{12}* type phase; however, it is a high-pressure phase[52] (similar to hafnium (HfB_{12}) and thorium (ThB_{12})),[53] and as such cannot be formed under ambient pressure conditions, except as part of a solid solution, e.g. $Zr_{1-x}Gd_xB_{12}$[7] (similar to $Y_{1-x}Hf_xB_{12}$).[6] As all the metals (Y and lanthanides) are in the +3 oxidation state,[54] the higher borides phases *MB_{12}* and *MB_6* (for Gd) exhibit color – different shades of blue; while +4 oxidation state metals[54] (Zr and Hf) form *MB_{12}* phases which are violet.

Figure 8-11 shows the SEM images for alloys of W : 11.6B with Sc, Y, Gd, Tb, Dy, Ho and Er indicating a change of morphology in the grains. For all cases, except for Tb and Sc, the change in morphology occurs at 8 – 10 at.% metal substitution; however, for Tb it occurs at 10 - 20 at.% Tb. In all cases the morphology and grain shape change from a "WB_4"-like structure to a structure having a "dendritic" pattern with noticeably smaller grain sizes forming along the sample cooling gradient (from the bottom to the top of the sample). The change in morphology coincides with an

increase in hardness for several of the secondary metal additions to WB_4 (as discussed below); however, this influence is not as dramatic as the morphology change in $(W_{0.92}Zr_{0.08})$: 11.6B, where a spinoidal decomposition causes the grains to become nanostructured.[20] For $(W_{1-x}Sc_x)$: 11.6B a change in morphology resulting in a decrease in the size of the metal-boride and boron grains occurs at 6 – 8 at.% Sc.

Figures 8-12, 8-13a-c and 8-14a-c show the results of the Vickers micro-indentation hardness measurements of W : 11.6B with Y, Sc, Gd, Tb, Dy, Ho and Er additions. The samples were indented using applied loads of 0.49 N (50 gram-force, i.e. "low load") to 4.9 N (500 gram-force, i.e. "high load"). All samples show an increase in hardness below 10 at.% secondary metal substitution that can be attributed to intrinsic ("doping" of vacant sites in WB_4 phase) and extrinsic (grain morphology) hardness increases in the WB_4 phase.[3,19,20] The intrinsic hardness can be ascribed to valence electron mismatch and atomic size differences between tungsten and Y, Sc and the lanthanides.[3,20]

For $(W_{1-x}Sc_x)$: 11.6B , the hardness increased from 41.2 ± 1.4 GPa at low load to 47.0 ± 1.9 GPa and 48.9 ± 2.5 GPa at 6 and 8 at.% Sc, respectively. Since the change in morphology for $(W_{1-x}Sc_x)$: 11.6B results in a decrease in the size of the metal-boride and boron grains, the increase in hardness can be attributed to both intrinsic and extrinsic effects. On the other hand, for $(W_{1-x}M_x)$: 11.6B with Y and the five lanthanides, the increase in hardness occurs in the 4 – 8 at.% range. For $(W_{1-x}Y_x)$: 11.6B , the hardness increased from 41.2 ± 1.4 GPa at low load to 50.2 ± 2.4 at 6 at.% Y; in addition, the hardness remained in the 48 – 49 GPa region for 4 – 8 at.% Y. This increase can be attributed primarily to an intrinsic effect – the filling of vacant sites in WB_4 by yttrium atoms. Similarly for $(W_{1-x}Gd_x)$: 11.6B, the hardness increased from 41.2 ± 1.4 GPa at low load to 48.0 ± 2.1 at 4 at.% Gd; in addition, the hardness remained in the 47 – 48 GPa region for 4 – 8

at.% Gd. For $(W_{1-x}Tb_x)$: 11.6B , the hardness increased from 41.2 ± 1.4 GPa at low load to 46.3 ± 2.6 at 6 at.% Tb, again this can be attributed to intrinsic effects. For $(W_{1-x}Dy_x)$: 11.6B , $(W_{1-x}Ho_x)$: 11.6B and $(W_{1-x}Er_x)$: 11.6B , the increase in hardness occurs in the 6 – 8 at.% range. For $W_{1-x}Dy_xB_4$, the hardness increased from 41.2 ± 1.4 GPa at low load to 48.5 ± 2.3 and 47.8 ± 2.4 at 6 and 8 at.% Dy, respectively, coinciding with the change to dendritic morphology (Figure 8-11). In $(W_{1-x}Ho_x)$: 11.6B , the hardness increased from 41.2 ± 1.4 GPa at low load to 46.5 ± 2.4 at 8 at.% Ho, again coinciding with the change in morphology. Finally, for $(W_{1-x}Er_x)$: 11.6B , the hardness increased from 41.2 ± 1.4 GPa at low load to 47.2 ± 2.9 and 45.8 ± 2.3 at 6 and 10 at.% Er, respectively; the second increase in hardness coincided with a change in morphology.

The alloys of W : 11.6B with Y, Sc and Gd showed an increase in oxidation resistance from ~450 °C for W : 11.6B, to ~470 °C, ~525 °C and 465 °C, respectively (Figure 8-15). Figure 8-16 shows a plot of oxidation resistance (°C) *vs.* Vickers hardness (GPa) at 0.49 N (50 gf) loading for select metal borides. Note that borides based on WB_4 tend to have higher hardness values, while borides not containing tungsten (MB_{12}) tend to have higher oxidation resistances, this is due to the fact that tungsten oxidizes before boron.

CONCLUSIONS

Alloys of W : 11.6B with group 3 transition metals (Sc and Y) and lanthanides (Gd, Tb, Dy, Ho and Er) were synthesized and analyzed for their mechanical (hardness) and thermal oxidation properties. For alloys of W : 11.6B with Y, Sc, Gd, Dy, Tb, Ho and Er, an increase in hardness to 50.2 ± 2.4, 48.9 ± 2.5, 48.0 ± 2.1, 46.3 ± 2.6, 48.5 ± 2.3, 46.4 ± 3.4, 47.2 ± 2.9 GPa at low load, respectively, was observed compared to 41.2 ± 1.4 GPa for W : 11.6B. In all cases, except for Sc, a change to a “dendritic” morphology was detected; for W : 11.6B with Sc, the metal boride and

boron grains became smaller; however, no patterning was observed. This shows that tuning the composition of the alloys of W : 11.6B with transition metals and lanthanides results in a modification of the morphology leading to patterning and smaller grains (nanosize grains)[20] that enhance mechanical and thermal properties. The alloys of W : 11.6B with Y, Sc and Gd showed an increase in oxidation resistance from ~450 °C for W : 11.6B, to ~470 °C, ~525 °C and 465 °C, respectively.

ACKNOWLEDGMENTS

We thank the National Science Foundation Division of Materials Research, Grant DMR-1506860 (R.B.K.) for financial support.

Table 8-1. Unit cell parameters for alloys of WB_4 with Y, Gd, Tb, Dy, Ho, Er and Sc[a]

x (at%)	$W_{1-x}Y_xB_4$		$W_{1-x}Gd_xB_4$		$W_{1-x}Tb_xB_4$		$W_{1-x}Dy_xB_4$		$W_{1-x}Ho_xB_4$		$W_{1-x}Er_xB_4$		x (at%)	$W_{1-x}Sc_xB_4$	
	a (Å)	c (Å)	a (Å)	c (Å)	a (Å)	c (Å)	a (Å)	c (Å)	a (Å)	c (Å)	a (Å)	c (Å)		a (Å)	c (Å)
0[b]	5.2087	6.3383	5.2087	6.3383	5.2087	6.3383	5.2087	6.3383	5.2087	6.3383	5.2087	6.3383	0	5.2087	6.3383
2	5.2051	6.3435	5.2043	6.3422	5.2042	6.3425	5.2087	6.3483	5.2036	6.3410	5.2049	6.3424	2	5.2042	6.3410
4	5.2040	6.3411	5.2041	6.3426	5.2016	6.3410	5.2030	6.3409	5.2026	6.3408	5.2042	6.3426	4	5.2033	6.3407
6	5.2026	6.3416	5.2025	6.3420	5.2032	6.3433	5.2033	6.3433	5.2023	6.3404	5.2037	6.3431	6	5.2055	6.3417
8	5.2024	6.3421	5.2027	6.3426	5.2026	6.3436	5.2023	6.3407	5.2009	6.3407	5.2029	6.3413	8	5.2036	6.3401
10	5.2014	6.3419	5.2006	6.3392	5.2014	6.3415	5.2024	6.3421	5.2043	6.3461	5.2017	6.3415	10	5.2046	6.3389
20	5.1994	6.3364	5.1991	6.3382	5.2011	6.3374	5.2013	6.3393	5.2011	6.3378	5.2012	6.3379	20	5.2040	6.3381
30	5.1998	6.3357	5.2005	6.3394	5.1996	6.3352	5.2020	6.3387	5.1997	6.3362	5.2020	6.3382	25	5.2035	6.3397
40	5.2001	6.3365	5.1994	6.3395	5.1998	6.3365	5.1997	6.3353	5.2010	6.3366	5.2004	6.3372	30	5.1989	6.3374
50	5.1991	6.3360	5.1996	6.3374	5.1999	6.3368	5.1982	6.3319	5.2024	6.2391	5.2013	6.3384	40	N/A	N/A

[a]from *Maud*[24–29]; [b]compare with literature values of lattice parameters of a = 5.1998(15), c = 6.3299(19) for WB_4[18]

Table 8-2. Details on the Data Collection and Structure Refinement of $ScB_{\sim 24}$[a]

Structure formula	$Sc_{12.59}B_{305.75}$ ($ScB_{\sim 24}$)
Crystal system/Space group	Rhombohedral / $R\bar{3}m$
Lattice parameters *a*, *b*, *c* (Å)	10.9640(8), 10.9640(8), 24.0838(13)
Formula units Z, Z'	6, 0
Cell volume ($Å^3$)	2507.3(4)
Calculated density (g/cm^3)	2.564
Temperature (K)	293(2)
Radiation/Wavelength (Å)	Mo K_α / 0.71073
Θ range (°)	2.31 – 30.69
Number of unique reflections/parameters	927 / 113
μ (mm^{-1}), Absorption correction	0.864, 0.62 – 0.74
Crystal Shape, size (mm^3), color	Plate, 0.06 x 0.02 x 0.01, Shiny black
R (unique reflections)	3.41%
wR2 (unique reflections)	9.06%

[a]Reference code - CCDC 1565340

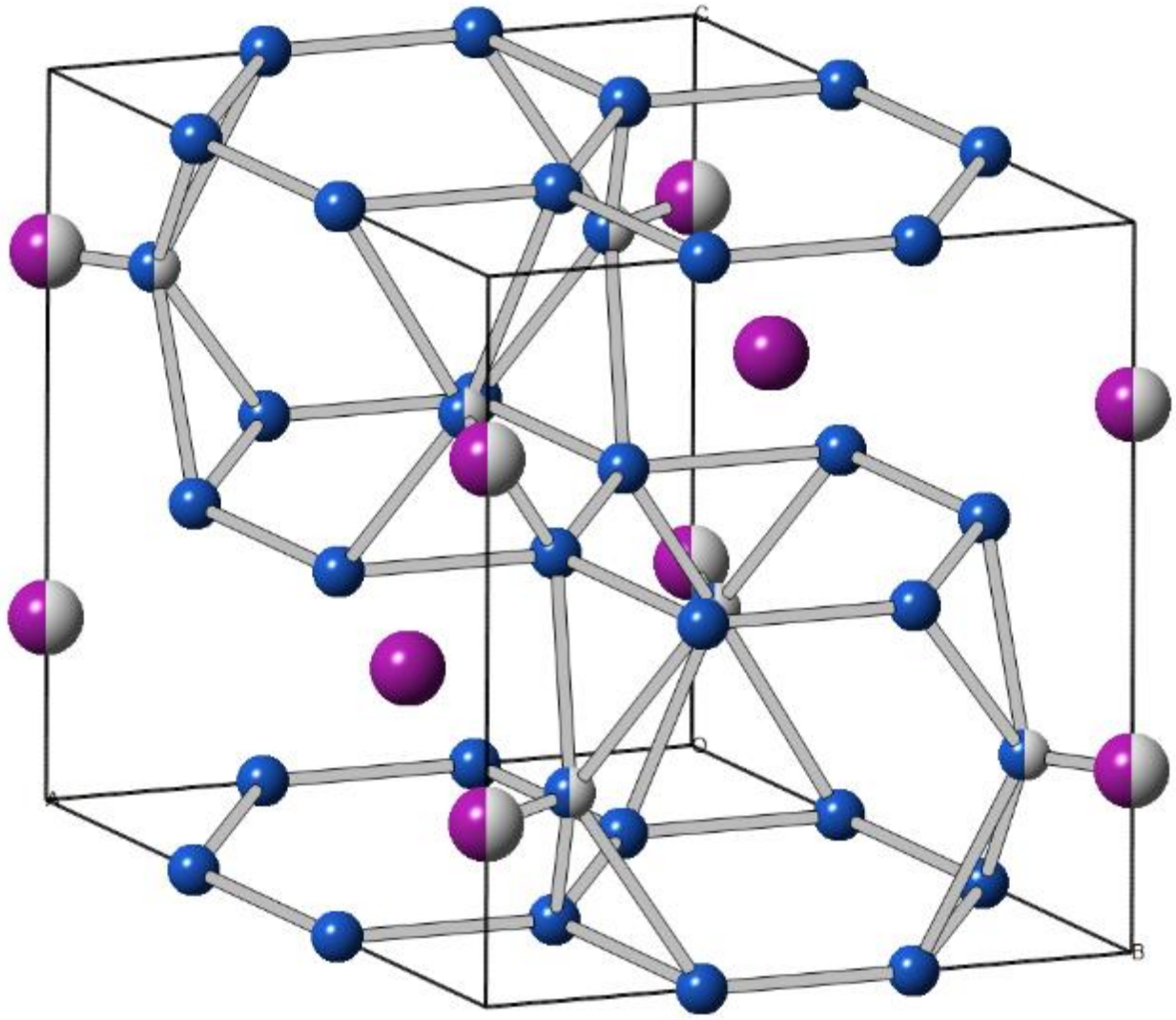

Figure 8-1. Crystal structure of WB_4 having the *P6₃/mmc* space group (ICSD (Inorganic Crystal Structure Database) 291124).[18] Tungsten atoms are shown in violet, while boron atoms are in blue; partially occupied positions are depicted by half-filled atoms.

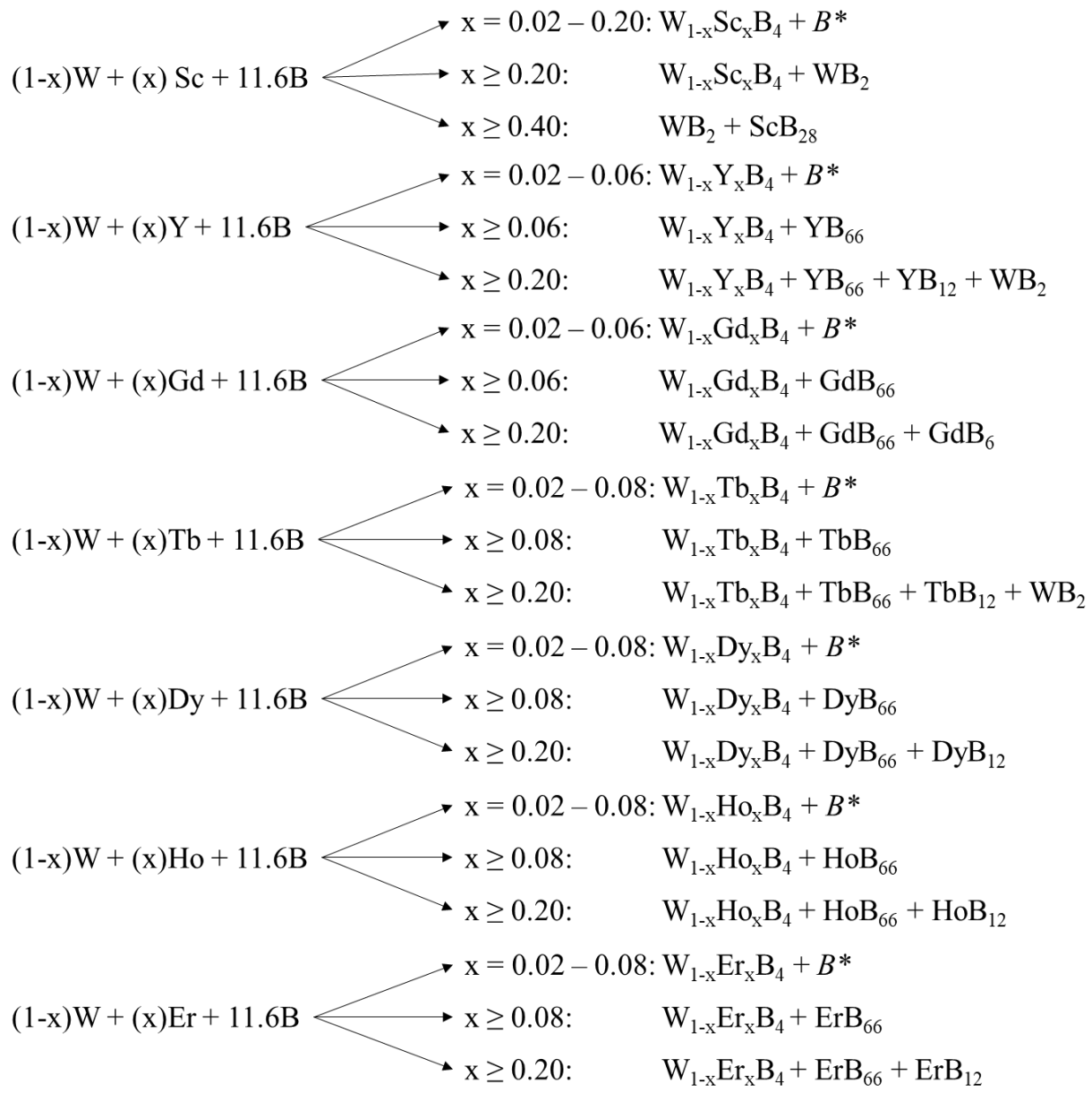

Figure 8-2. Phase formation based on the concentration (x = 0.0 – 0.5) of a secondary metal (Sc, Y, Gd, Tb, Dy, Ho and Er) added to a W : 11.6B alloy, showing regions of solid solution and multi-phase mixtures. *B** is crystalline β-rhombohedral boron.

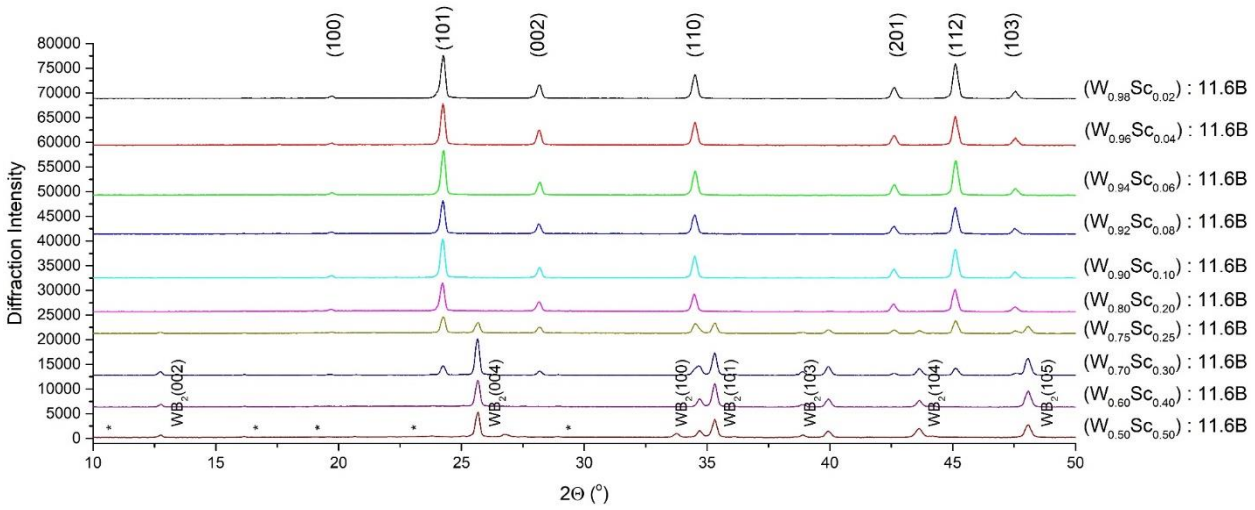

Figure 8-3. Powder XRD patterns (10 – 50° 2Θ) of alloys of nominal composition of $(W_{1-x}Sc_x)$: 11.6B. WB_4 (*P6₃/mmc*, JCPDS 00-019-1373) is present until 30 at.% Sc, while WB_2 appears at 25 at.% Sc. No ScB_{12} (*I4/mmm*) is present at any concentration of Sc; the peaks for the solid solution of scandium in β-rhombohedral boron, (*) ScB_{28} ($R\bar{3}m$, JCPDS 01-071-0420, Figure 8-6, CCDC 1565340), which are visible at ~40 at.% Sc.

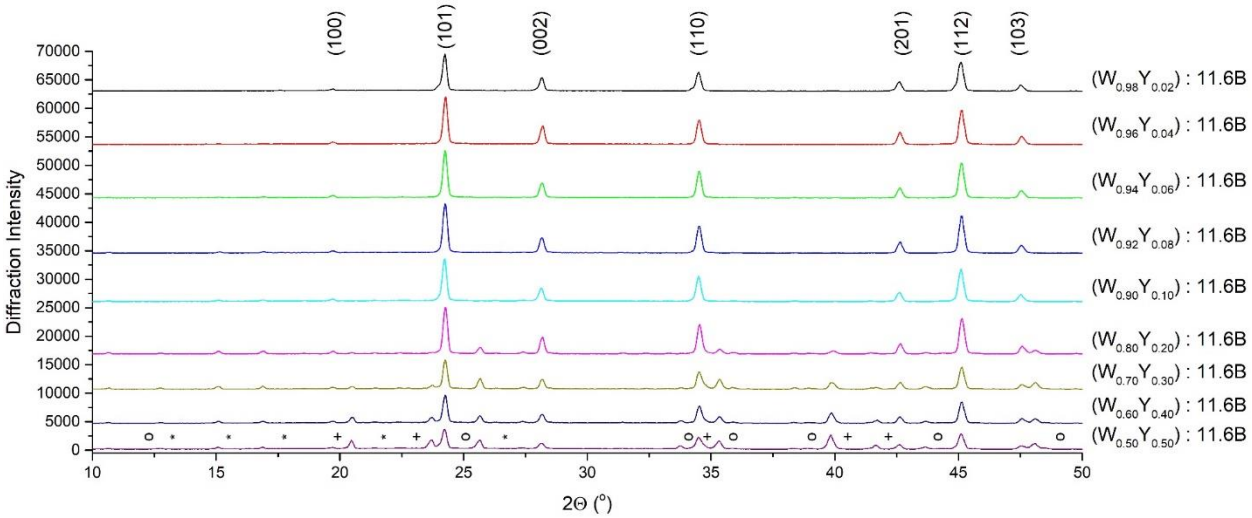
(100)
(101)
(002)
(110)
(201)
(112)
(103)
Diffraction Intensity
2Θ (°)
(W0.98Y0.02) : 11.6B
(W0.96Y0.04) : 11.6B
(W0.94Y0.06) : 11.6B
(W0.92Y0.08) : 11.6B
(W0.90Y0.10) : 11.6B
(W0.80Y0.20) : 11.6B
(W0.70Y0.30) : 11.6B
(W0.60Y0.40) : 11.6B
(W0.50Y0.50) : 11.6B

(a)

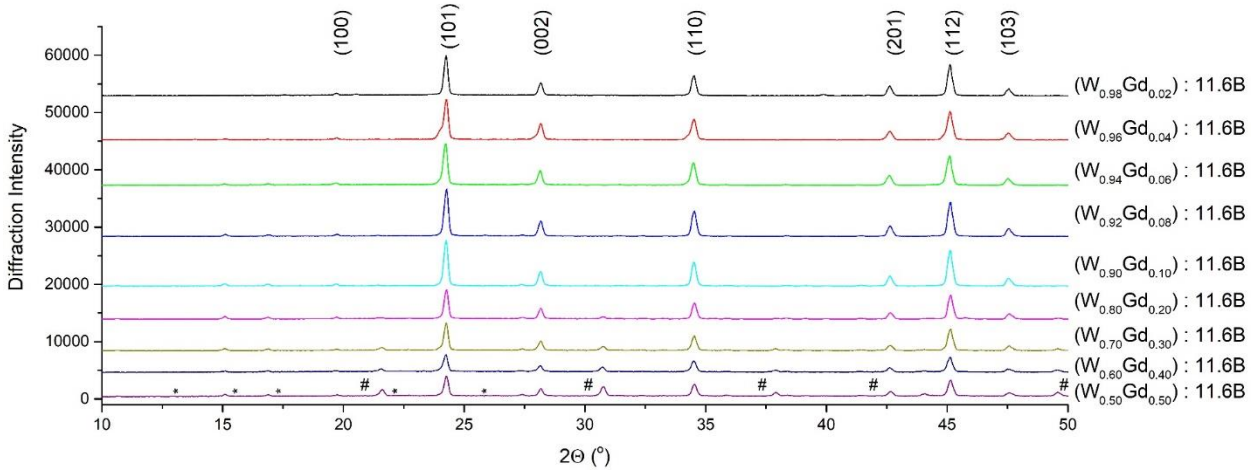
(100)
(101)
(002)
(110)
(201)
(112)
(103)
Diffraction Intensity
2Θ (°)
(W0.98Gd0.02) : 11.6B
(W0.96Gd0.04) : 11.6B
(W0.94Gd0.06) : 11.6B
(W0.92Gd0.08) : 11.6B
(W0.90Gd0.10) : 11.6B
(W0.80Gd0.20) : 11.6B
(W0.70Gd0.30) : 11.6B
(W0.60Gd0.40) : 11.6B
(W0.50Gd0.50) : 11.6B

(b)

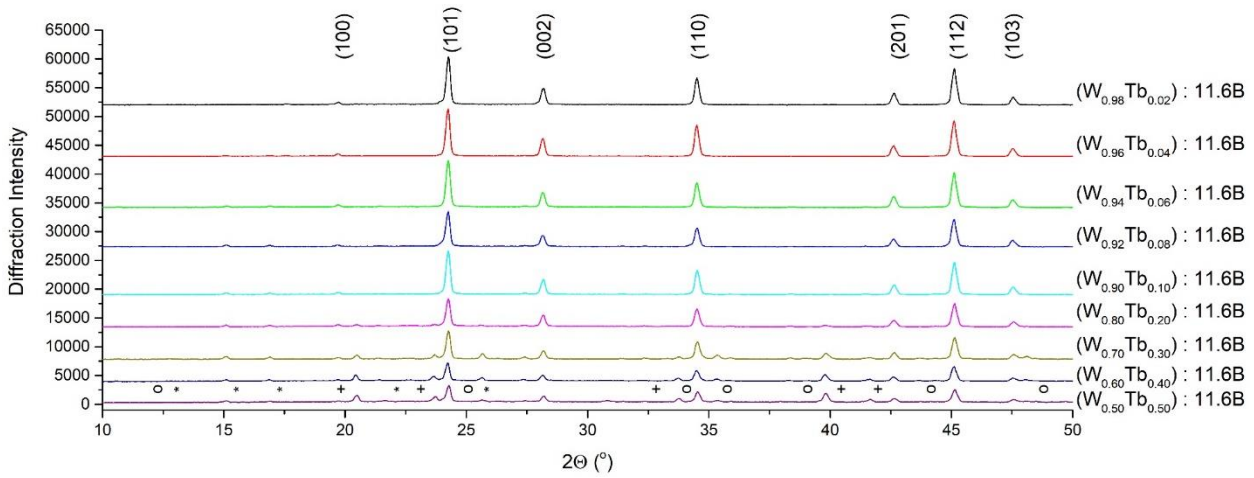

(c)

Figure 8-4. Powder XRD patterns (10 – 50° 2Θ) of alloys with a nominal composition of $(W_{1-x}M_x)$: 11.6B, where M is: (a) Y, (b) Gd and (c) Tb. (a) For $(W_{1-x}Y_x)$: 11.6B, WB_4 (*P6₃/mmc*, JCPDS 00-019-1373) peaks are present all concentrations of Y; higher boride phases (*) YB_{66} ($Fm\bar{3}c$, JCPDS 01-073-0759) and (+) YB_{12} ($Fm\bar{3}m$, JCPDS 01-073-1382) appear at 6 and 20 at.% Y, respectively. Tungsten diboride (o) (JCPDS 01-073-1244) appears at 20 at.% Y; (b) For $(W_{1-x}Gd_x)$: 11.6B, WB_4 peaks are present all concentrations of Gd; higher boride phases (*) GdB_{66} ($Fm\bar{3}c$, JCPDS 00-024-1256) and (#) GdB_6 ($Pm\bar{3}m$, JCPDS 03-065-1826) appear at 6 and 20 at.% Gd, respectively; (c) For $(W_{1-x}Tb_x)$: 11.6B, WB_4 (JCPDS 00-019-1373) peaks are present at all concentrations of Tb; higher boride phases (*) TbB_{66} ($Fm\bar{3}c$, JCPDS 00-025-0931) and (+) TbB_{12} ($Fm\bar{3}m$, JCPDS 00-029-1326) appear at 4 and 20 at.% Tb, respectively. Tungsten diboride (o) (*P6₃/mmc*, JCPDS 01-073-1244) appears at 20 at.% Tb.

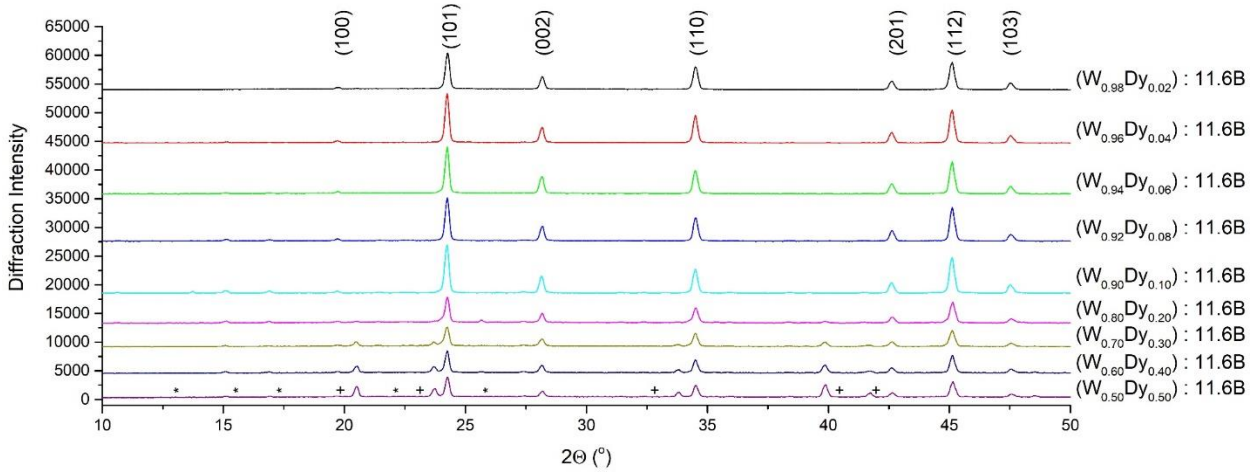
(100)
(101)
(002)
(110)
(201)
(112)
(103)
Diffraction Intensity
2Θ (°)
(W0.98Dy0.02) : 11.6B
(W0.96Dy0.04) : 11.6B
(W0.94Dy0.06) : 11.6B
(W0.92Dy0.08) : 11.6B
(W0.90Dy0.10) : 11.6B
(W0.80Dy0.20) : 11.6B
(W0.70Dy0.30) : 11.6B
(W0.60Dy0.40) : 11.6B
(W0.50Dy0.50) : 11.6B

(a)

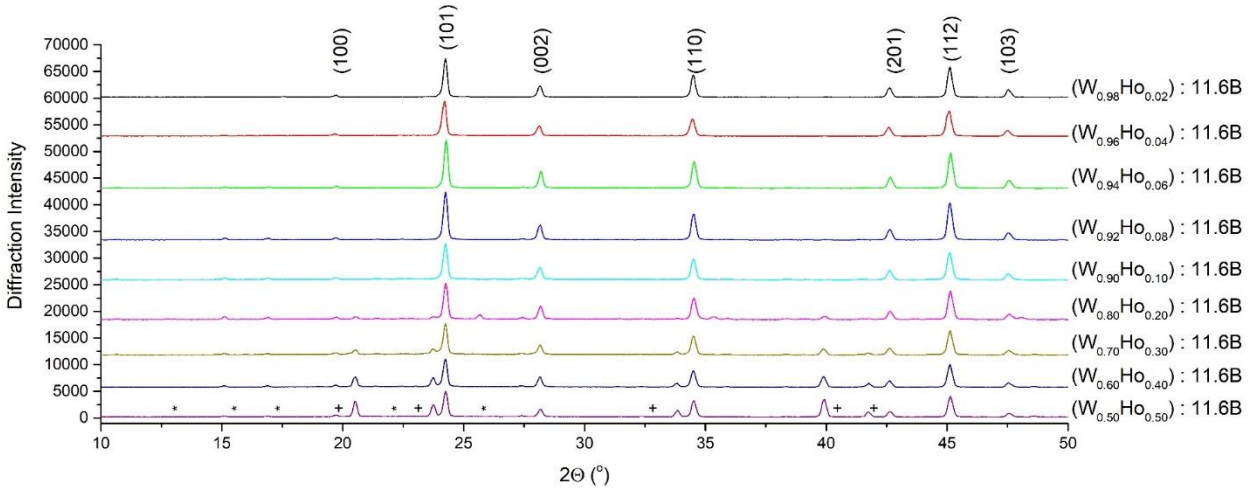
(100)
(101)
(002)
(110)
(201)
(112)
(103)
Diffraction Intensity
2Θ (°)
(W0.98Ho0.02) : 11.6B
(W0.96Ho0.04) : 11.6B
(W0.94Ho0.06) : 11.6B
(W0.92Ho0.08) : 11.6B
(W0.90Ho0.10) : 11.6B
(W0.80Ho0.20) : 11.6B
(W0.70Ho0.30) : 11.6B
(W0.60Ho0.40) : 11.6B
(W0.50Ho0.50) : 11.6B

(b)

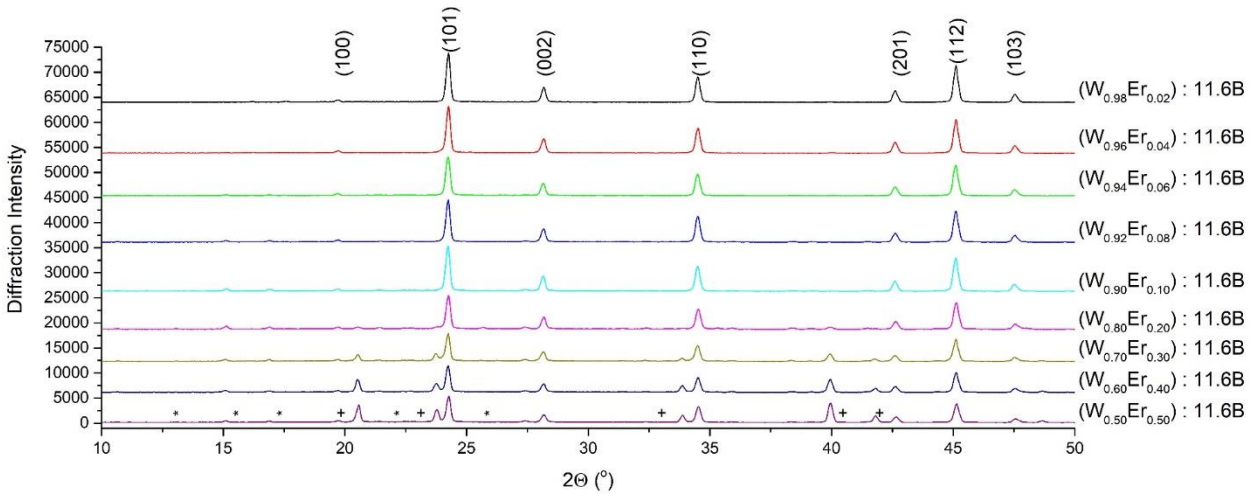

(c)

Figure 8-5. Powder XRD patterns (10 – 50° 2Θ) of alloys with a nominal composition of ($W_{1-x}M_x$) : 11.6B, where M is: (a) Dy, (b) Ho and (c) Er. (b) For ($W_{1-x}Dy_x$) : 11.6B, WB_4 (*P6₃/mmc*, JCPDS 00-019-1373) peaks are present all concentrations of Dy; higher boride phases (*) DyB_{66} ($Fm\bar{3}c$, JCPDS 00-024-1351) and (+) DyB_{12} ($Fm\bar{3}m$, JCPDS 00-024-1338) appear at 4 and 20 at.% Tb, respectively; (b) For ($W_{1-x}Ho_x$) : 11.6B, WB_4 peaks are present at all concentrations of Ho; higher boride phases (*) HoB_{66} ($Fm\bar{3}c$, JCPDS 00-025-0373) and (+) HoB_{12} ($Fm\bar{3}m$, JCPDS 00-012-0103) appear at 6 and 20 at.% Ho, respectively; (c) For ($W_{1-x}Er_x$) : 11.6B, WB_4 peaks are present at all concentrations of Er; higher boride phases (*) ErB_{66} ($Fm\bar{3}c$, JCPDS 00-024-1405) and (+) ErB_{12} ($Fm\bar{3}m$, JCPDS 00-011-0580) appear at 6 and 20 at.% Er, respectively.

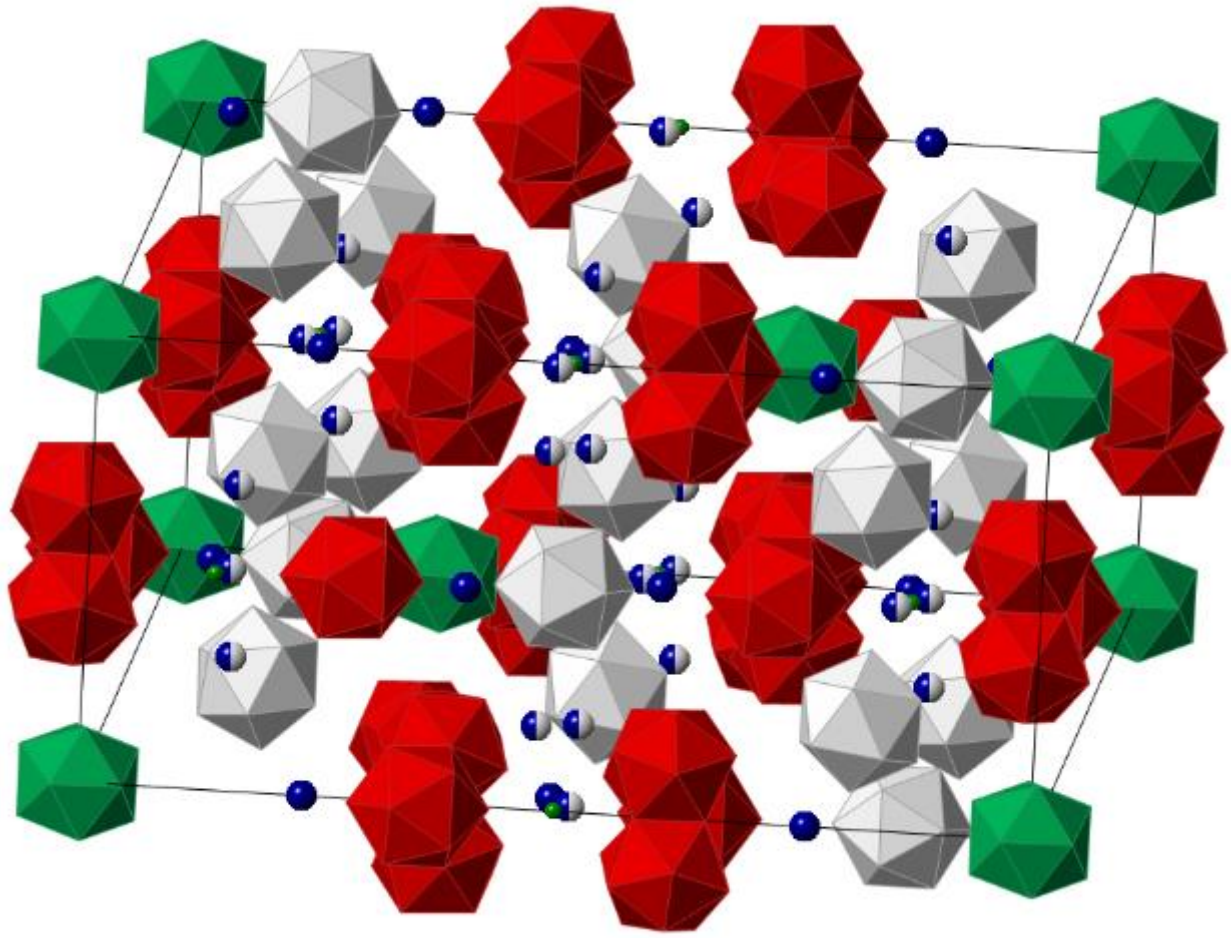

Figure 8-6. Crystal structure of the solid solution of Sc in β-rhombohedral boron ($ScB_{\sim 24}$) solved in the $R\bar{3}m$ space group (reference code in Cambridge Crystallographic Data Center (CCDC) 1565340) details are given in Table 8-2. Scandium atoms are in blue (two-tone coloring indicates partial occupancy), boron atoms are in green; red, gray and green icosahedra represent the three independent 24 boron atoms arrangements. Sc(2) and Sc(4) have a site occupancy of 0.34 and 0.09 respectively, with their positions sometimes being occupied by boron atoms.

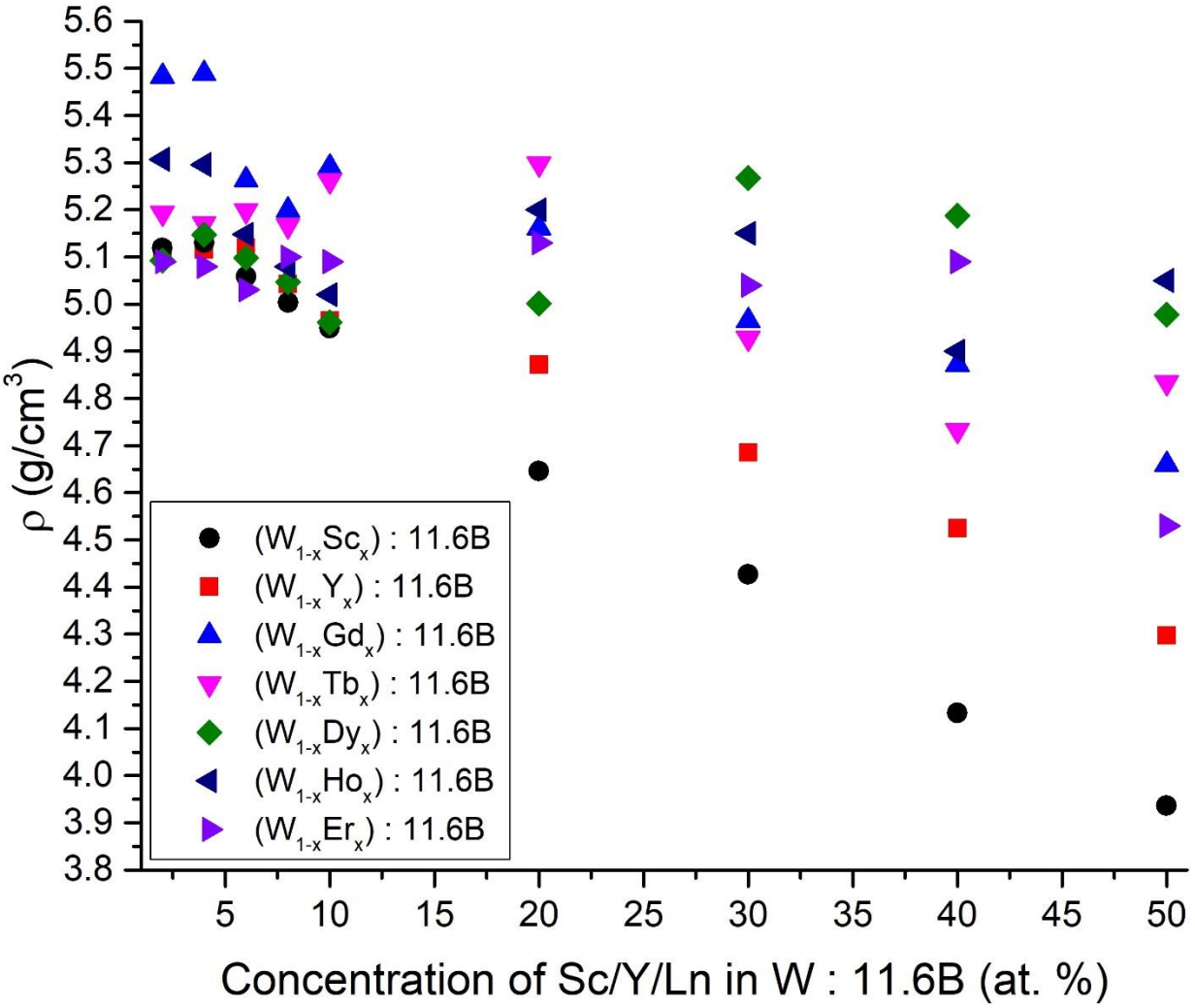

Figure 8-7. Density (g/cm^3) of samples of alloys with the nominal composition of $(W_{1-x}M_x)$: 11.6B with Sc, Y, Gd, Tb, Dy, Ho and Er. The XRD density for WB_4 is 8.4 g/cm^3 and for WB_2 12.76 g/cm^3.[55] The pycnometric density of a sample of WB_4 prepared with a nominal composition of W : B = 1 : 11.6 is 5.15 g/cm^3, this density is lower than the XRD density because of the presence of excess of boron. The greatest change in density is for the alloy with the nominal composition of $(W_{1-x}Sc_x)$: 11.6 B, which changes from 5.15 g/cm^3 to 3.94 g/cm^3 (50 at.% Sc), due to the low density of scandium.

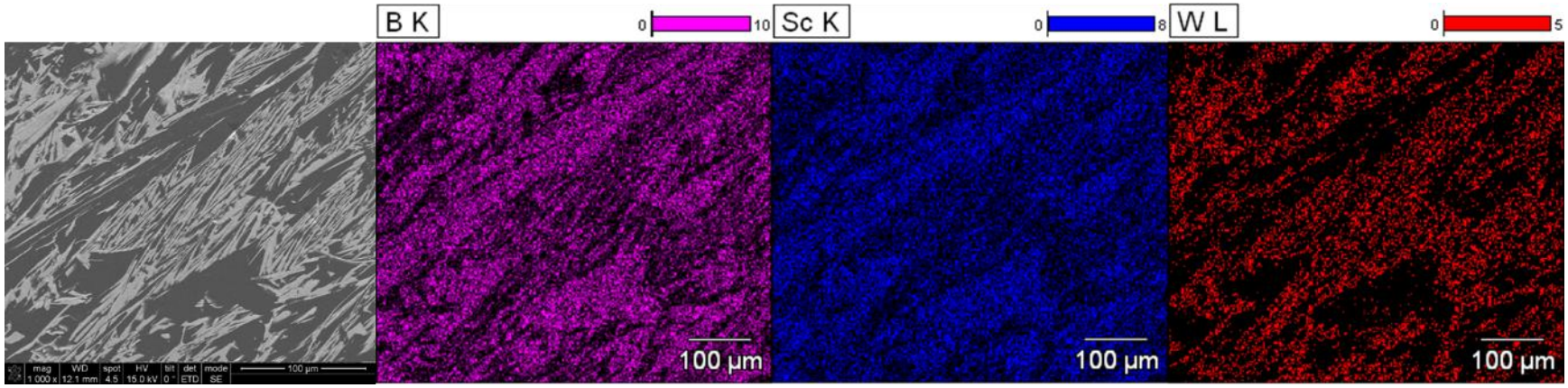

Figure 8-8. Elemental maps for boron (K line), scandium (K line) and tungsten (L line) for an alloy with a nominal composition of ($W_{0.75}Sc_{0.25}$) : 11.6B. The elemental maps show the presence of both scandium and tungsten in the metal-boron phase; the boron rich areas are the solid solution of scandium in β-rhombohedral boron ($ScB_{24\text{-}28}$, $R\bar{3}m$, Figure S1, CCDC 1565340).[36]

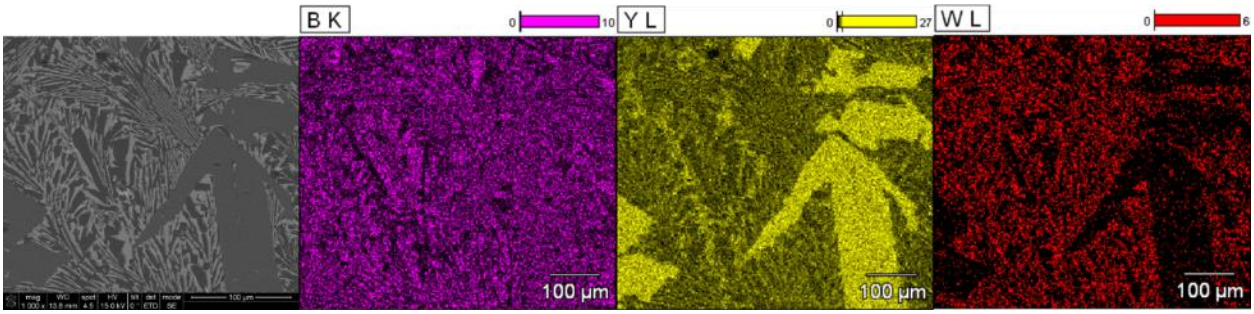

(a)

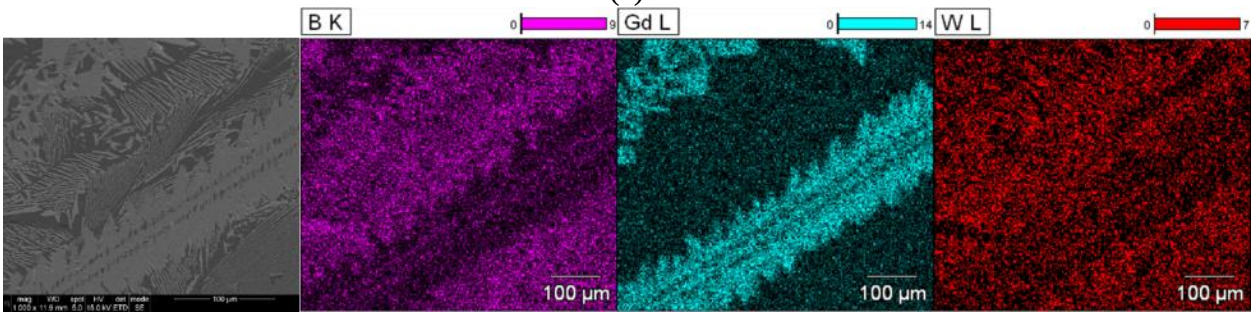

(b)

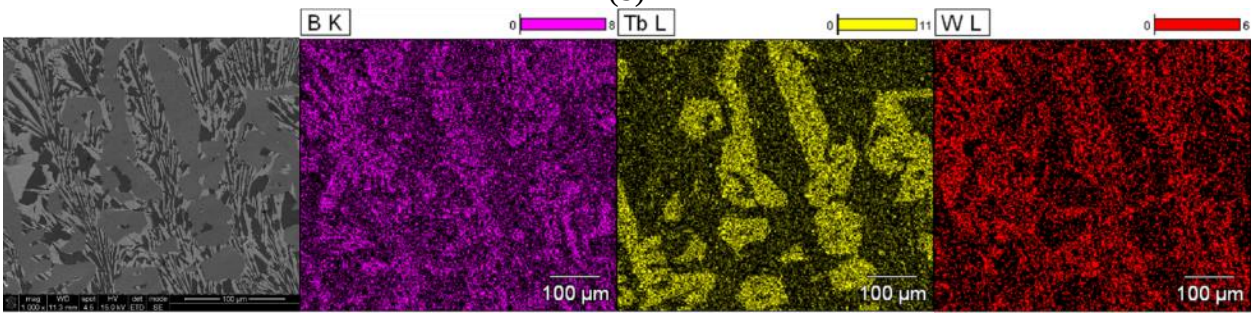

(c)

Figure 8-9. Elemental maps for boron (K line), yttrium (L line), gadolinium (L line), terbium (L line) and tungsten (L line) for alloys with the following nominal compositions: (a) ($W_{0.50}Y_{0.50}$) : 11.6B, (b) ($W_{0.50}Gd_{0.50}$) : 11.6B and (c) ($W_{0.50}Tb_{0.50}$) : 11.6B. For ($W_{0.50}Y_{0.50}$) : 11.6B and ($W_{0.50}Tb_{0.50}$) : 11.6B alloys, the yttrium and terbium-rich areas correspond to YB_{12} and TbB_{12} ($Fm\bar{3}m$), while for ($W_{0.50}Gd_{0.50}$) : 11.6B alloy the gadolinium-rich areas correspond to GdB_6 ($Pm\bar{3}m$) phases, respectively. The boron rich areas correspond to YB_{66}, GdB_{66} and TbB_{66} ($Fm\bar{3}c$), respectively.

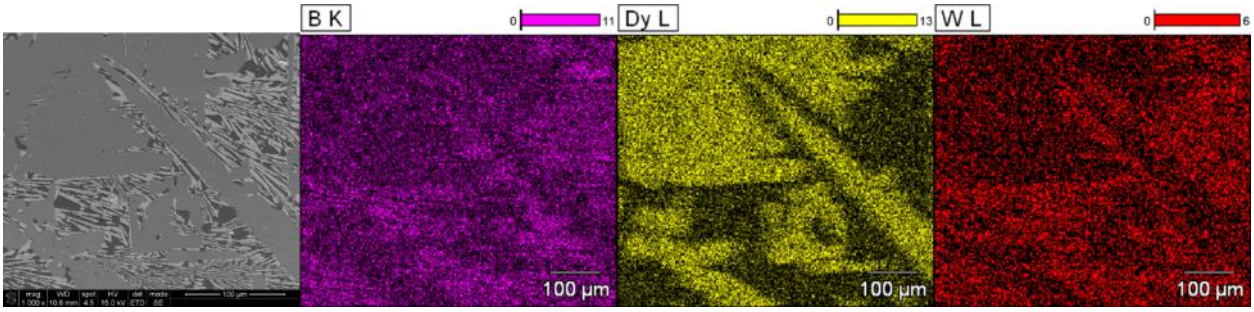

(a)

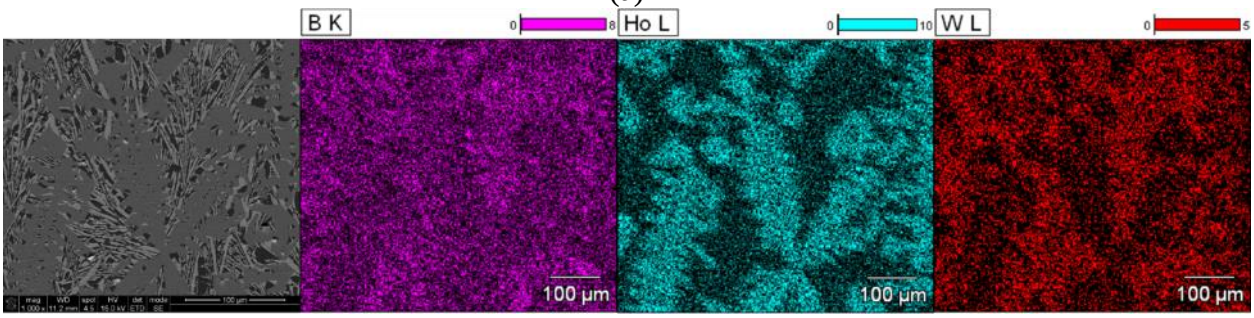

(b)

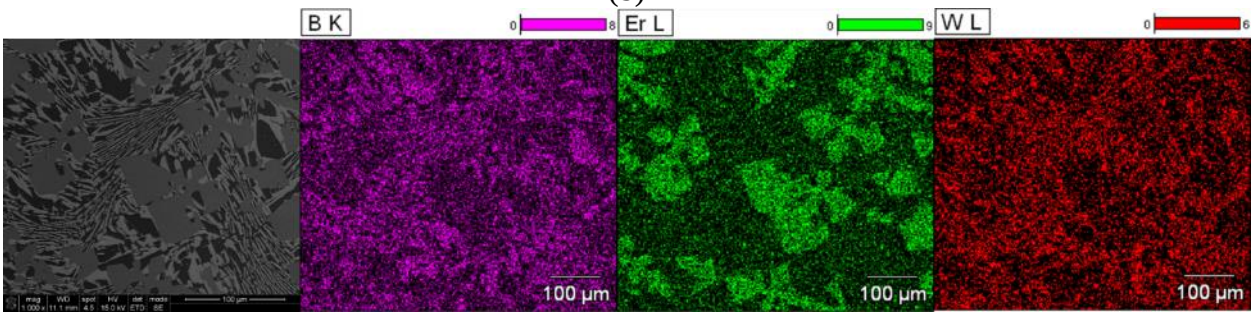

(c)

Figure 8-10. Elemental maps for boron (K line), dysprosium (L line), holmium (L line), erbium (L line) and tungsten (L line) for the alloys with the following nominal compositions: (a) ($W_{0.50}Dy_{0.50}$) : 11.6B, (b) ($W_{0.50}Ho_{0.50}$) : 11.6B and (c) ($W_{0.60}Er_{0.40}$) : 11.6B. For each of the three alloys the lanthanide rich areas correspond to the dodecaboride phases: DyB_{12}, HoB_{12} and ErB_{12} (all $Fm\bar{3}m$), respectively. The boron rich areas correspond to DyB_{66}, HoB_{66} and ErB_{66} (all $Fm\bar{3}c$), respectively.

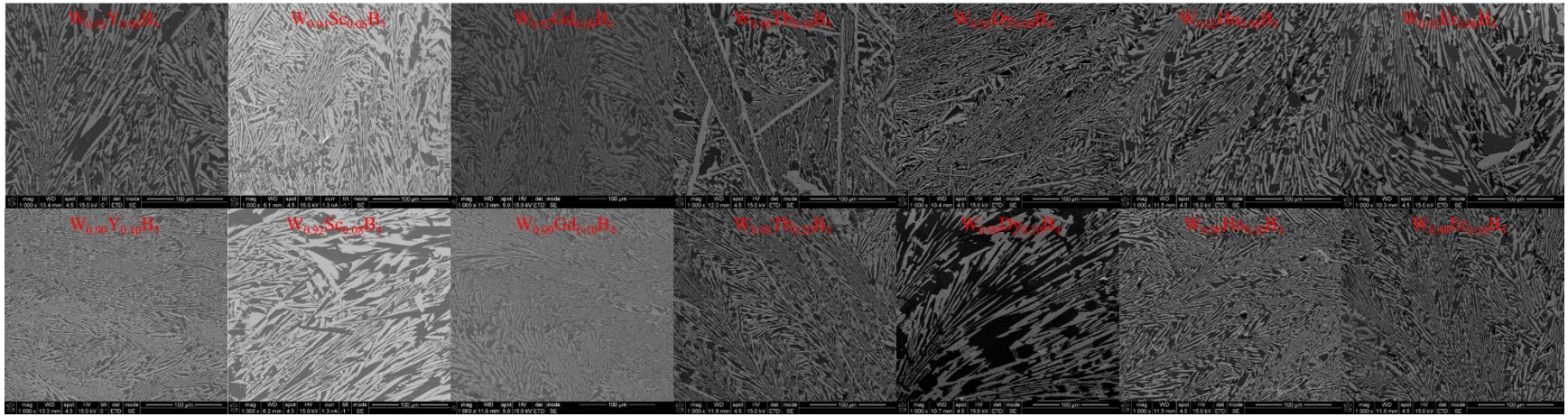

Figure 8-11. SEM images for WB_4 as its alloys with Sc, Y, Gd, Tb, Dy, Ho and Er, showing a change in morphology of the grains. For Sc a change of morphology occurs at 6 - 8 at.% Sc, resulting in a decrease in the size of the metal boride and boron grains. For Y and lanthanides the change of morphology (dendritic pattern) occurs at 8 – 10 at.% lanthanide substitution in WB_4, except for Tb, where it occurs at 10 - 20 at.% Tb. All SEM images were taken at 1000x magnification; the scale bars are 100 μm (a complete set of SEM images can be seen in Figure S5).

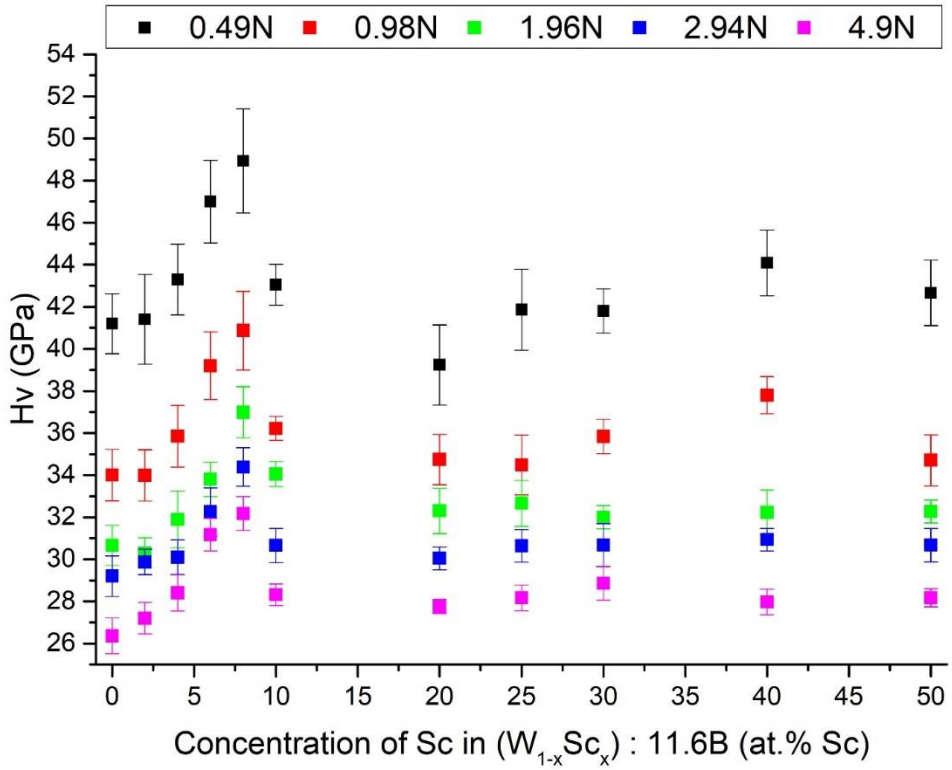

Figure 8-12. Vickers micro-indentation hardness of alloys with a nominal composition of $(W_{1-x}Sc_x)$: 11.6B alloys with Sc at low (0.49 N) to high (4.9 N) loading.

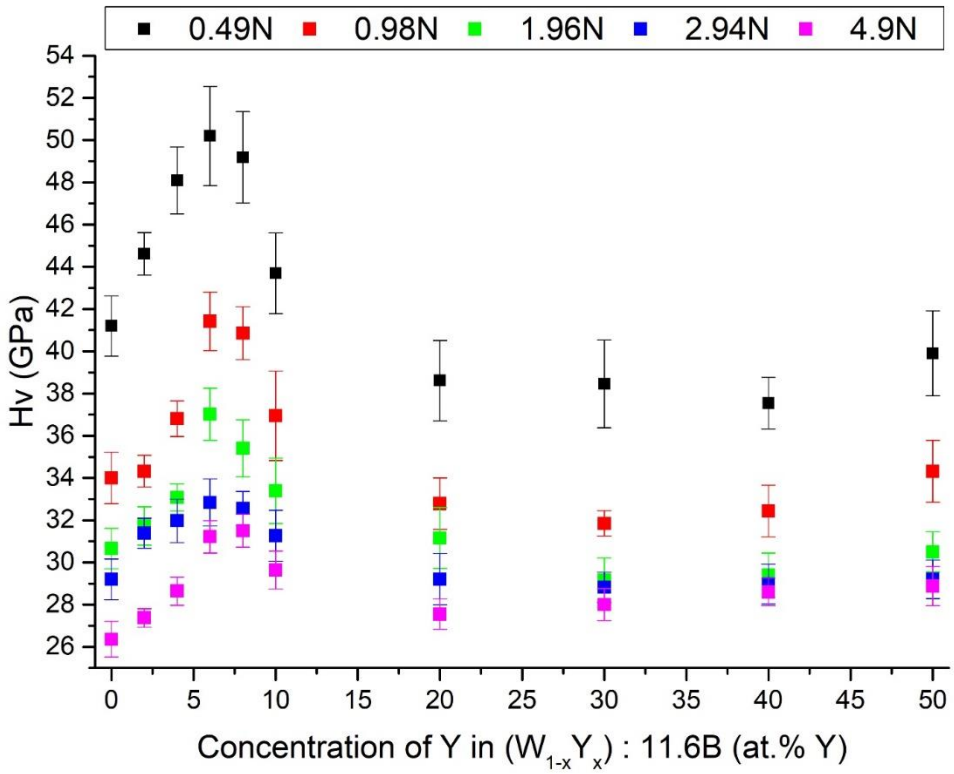
0.49N
0.98N
1.96N
2.94N
4.9N
Hv (GPa)
Concentration of Y in (W1-xYx) : 11.6B (at.% Y)

(a)

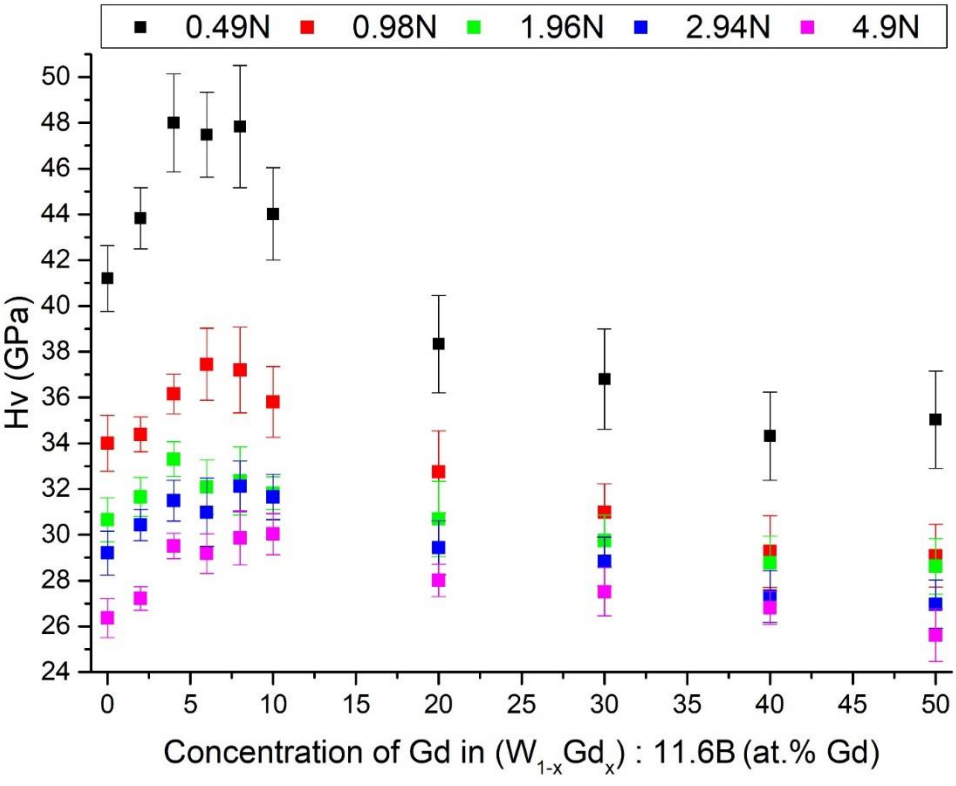
0.49N
0.98N
1.96N
2.94N
4.9N
Hv (GPa)
Concentration of Gd in (W1-xGdx) : 11.6B (at.% Gd)

(b)

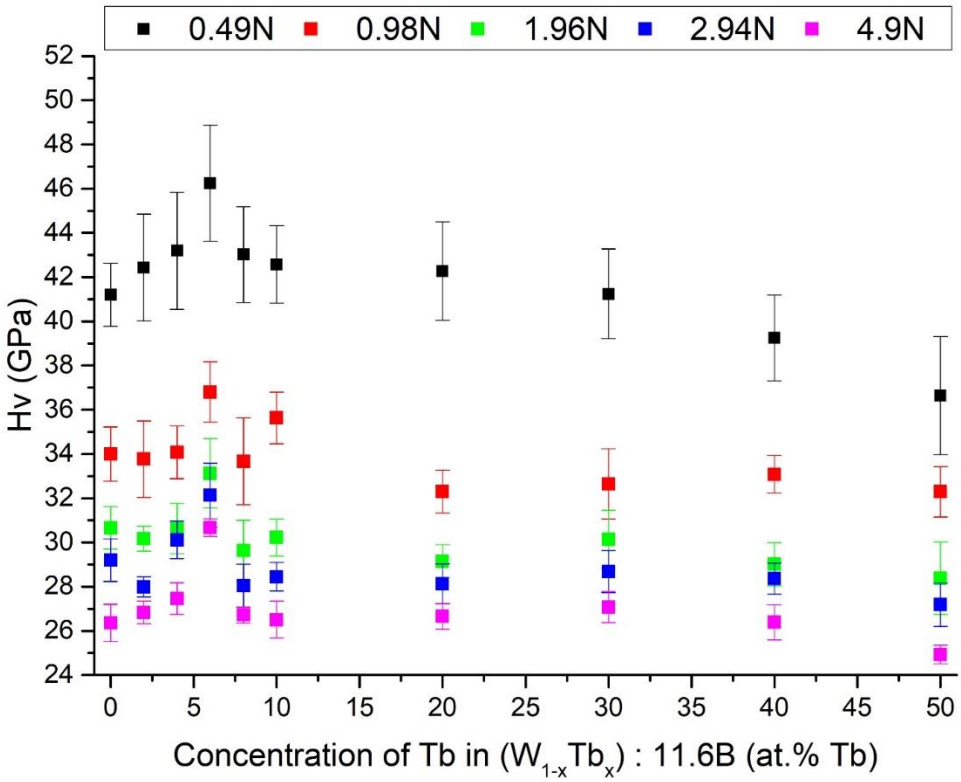

(c)

Figure 8-13. Vickers micro-indentation hardness of alloys with a nominal composition of $(W_{1-x}M_x)$: 11.6B where M is: (a) Y, (b) Gd and (c) Tb at low (0.49 N) to high (4.9 N) loading.

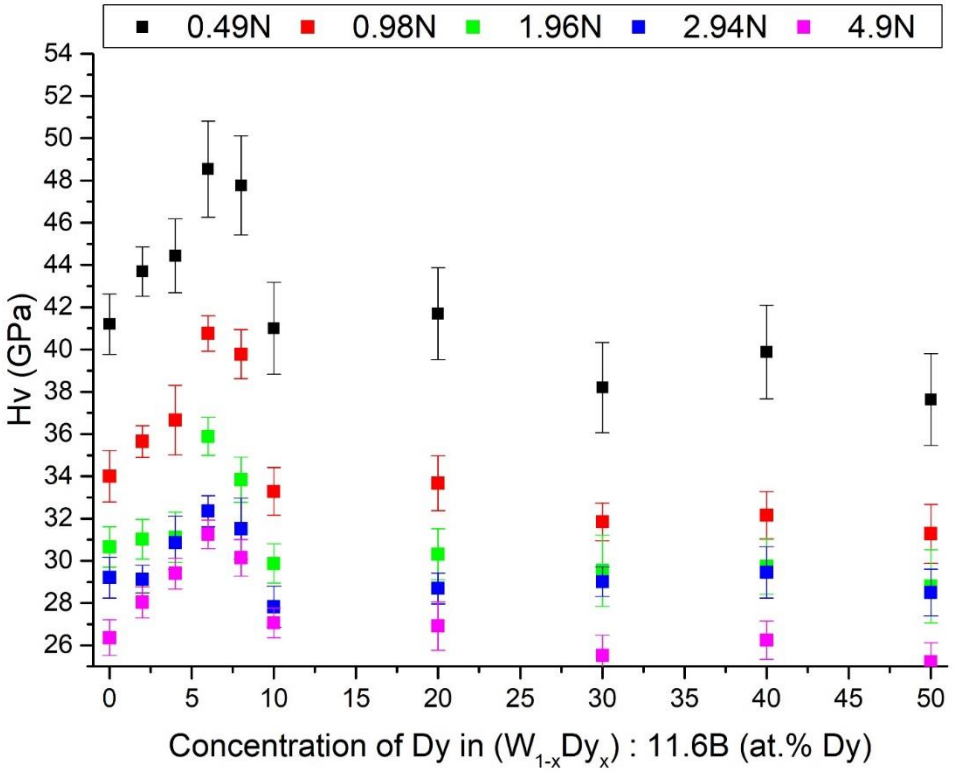
0.49N
0.98N
1.96N
2.94N
4.9N
Hv (GPa)
Concentration of Dy in ($W_{1-x}Dy_x$) : 11.6B (at.% Dy)

(a)

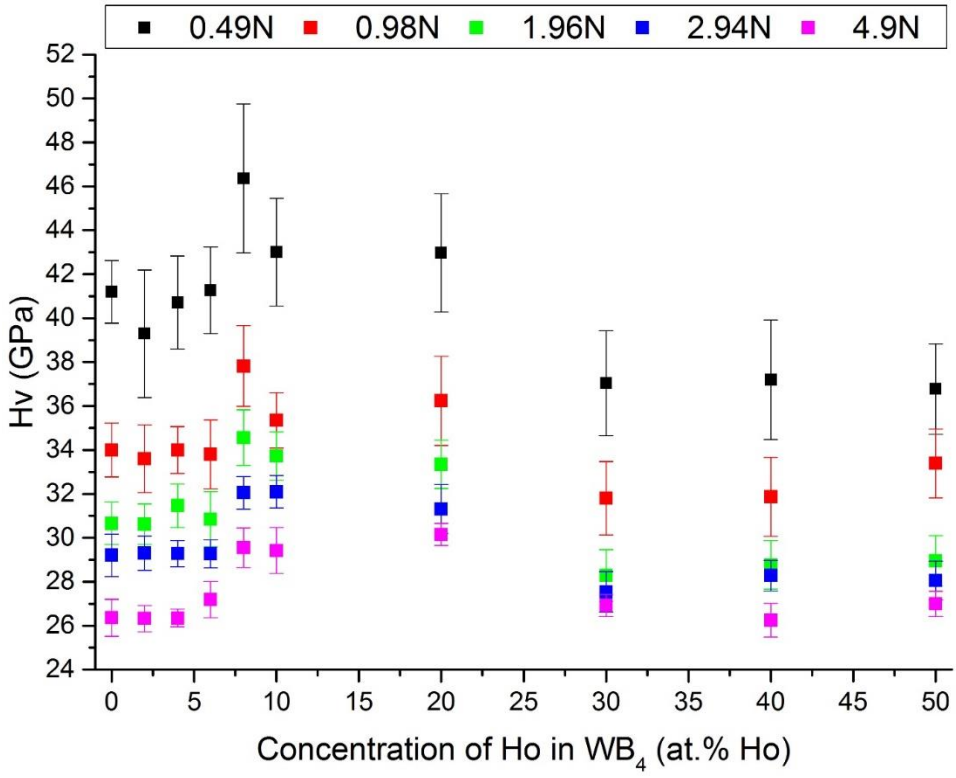
0.49N
0.98N
1.96N
2.94N
4.9N
Hv (GPa)
Concentration of Ho in WB_4 (at.% Ho)

(b)

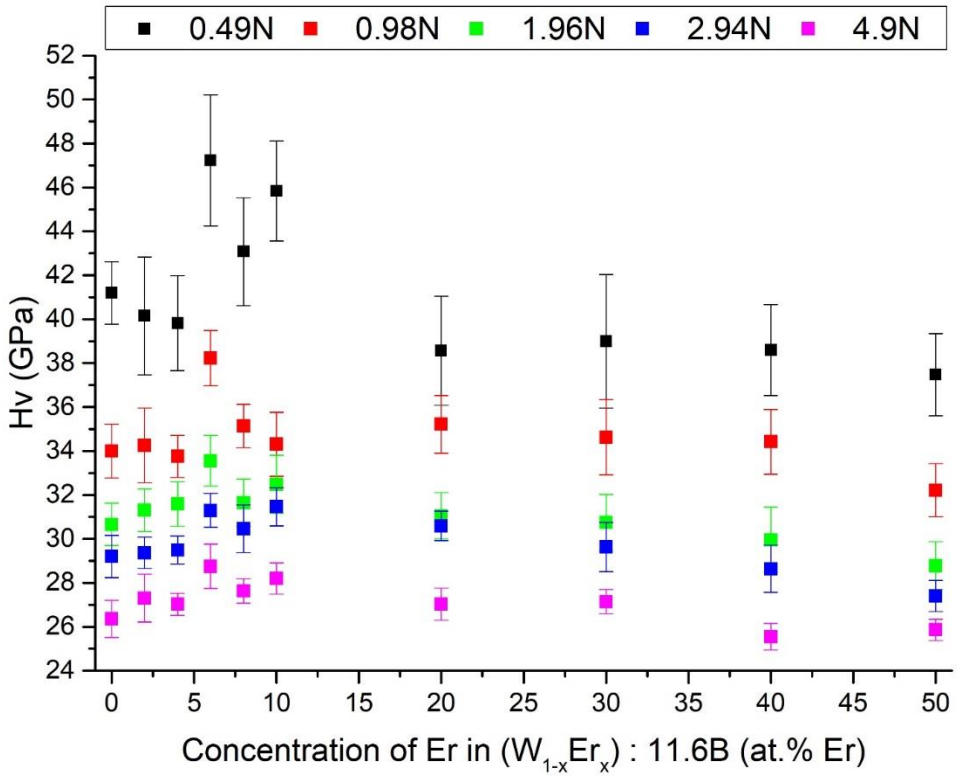

(c)

Figure 8-14. Vickers micro-indentation hardness of alloys with a nominal composition of $(W_{1-x}M_x)$: 11.6B, where M is : (a) Dy, (b) Ho and (c) Er at low (0.49 N) to high (4.9 N) loading.

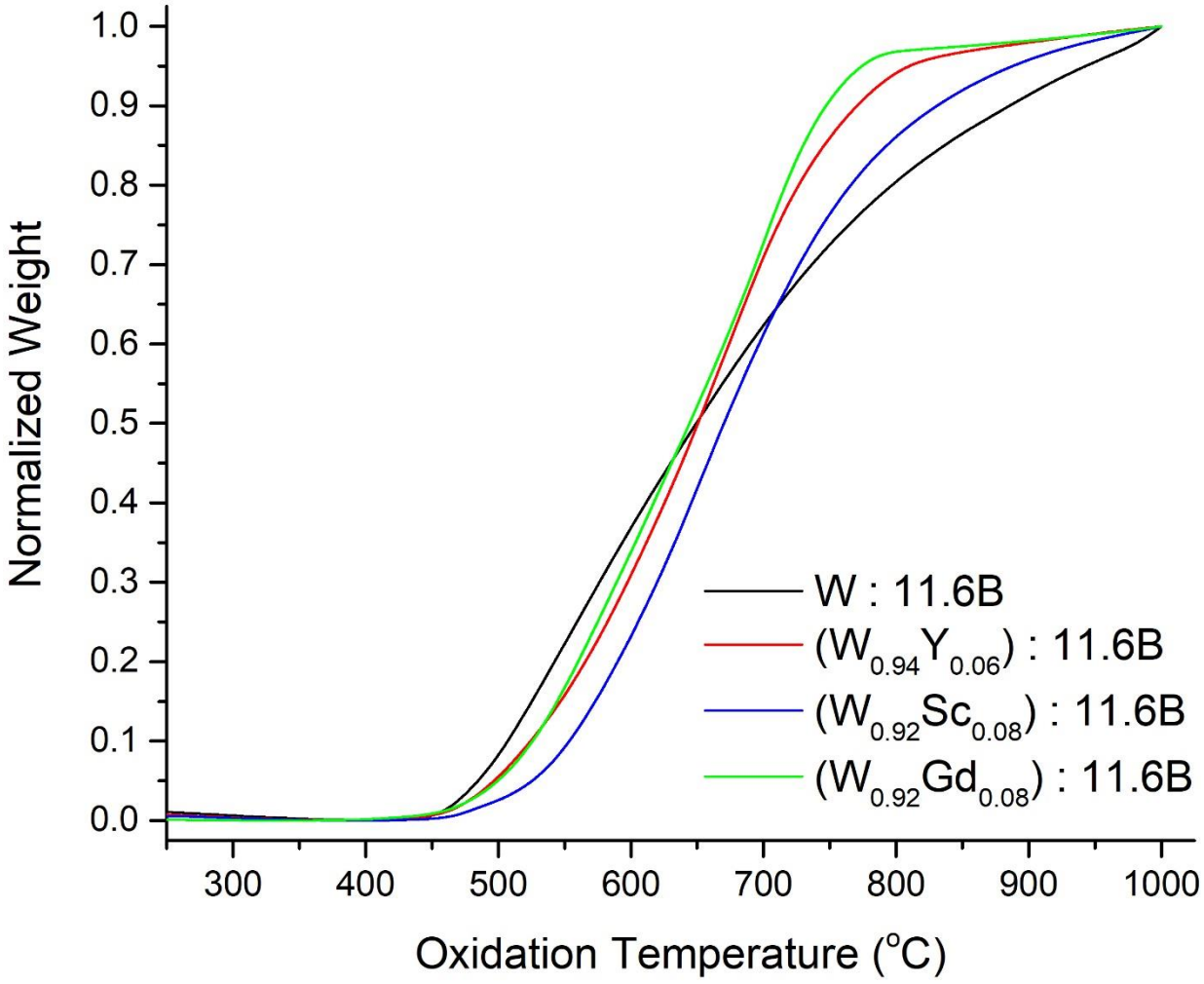

Figure 8-15. Thermal stability of alloys with a nominal composition of $(W_{1-x}M_x)$: 11.6B, where M is: Y, Sc and Gd. These data show that the oxidation resistance for $(W_{0.94}Y_{0.06})$: 11.6B is ~470 °C, $(W_{0.92}Sc_{0.08})$: 11.6B is ~525 °C and $(W_{0.92}Gd_{0.08})$: 11.6B is ~465 °C, compared to ~450 °C for W : 11.6B. Oxidation resistance temperature was determined using extrapolated oxidation onset - temperature that denotes the temperature at which the weight loss begins. The extrapolated temperature onset (tangent to the part of the curve where there is no change in the slope gradient) is used because it is reproducible between TGA analysis on different instruments (ASTM E1131-08(2014); ISO 11358-1:2014).[34,35]

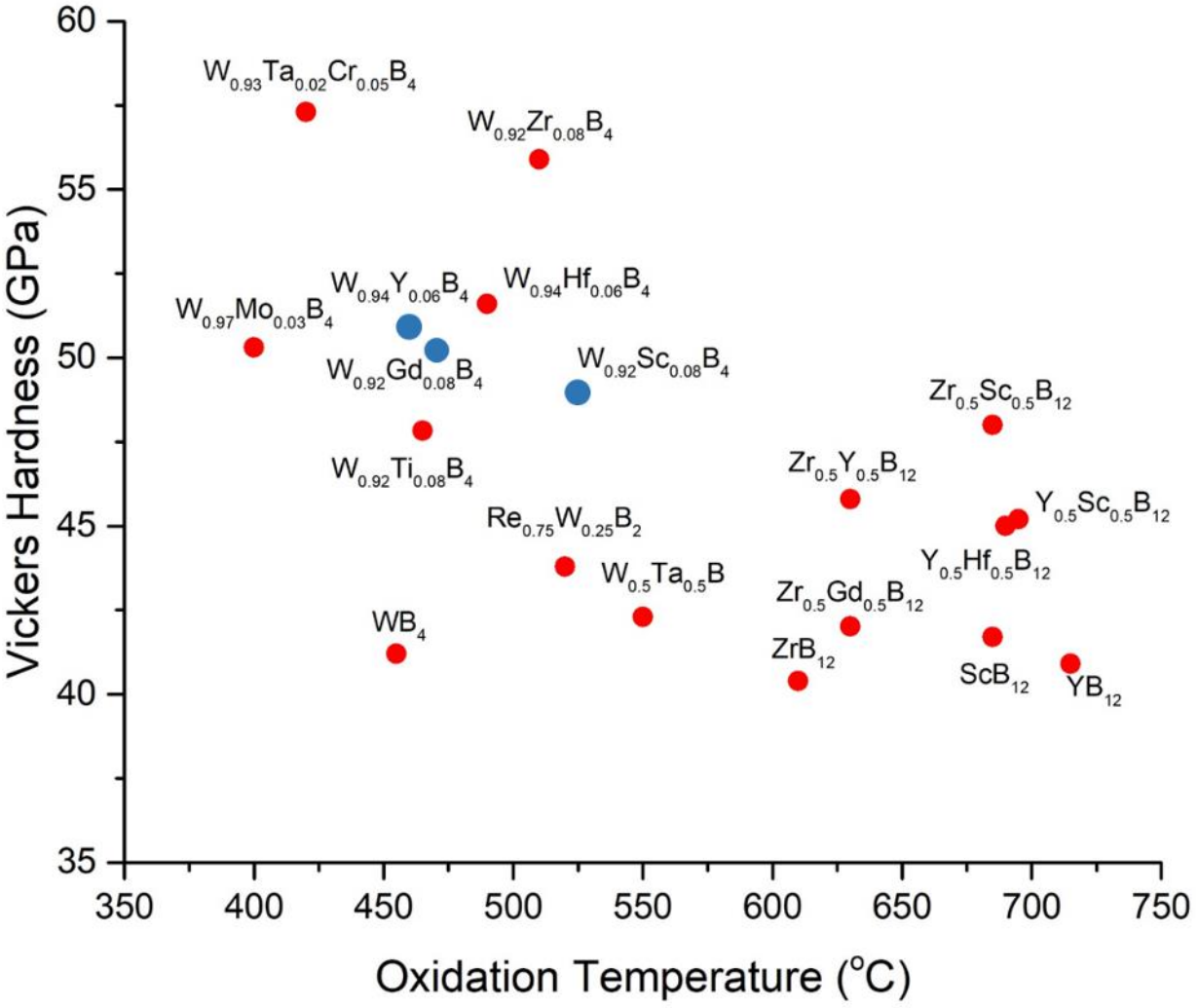

Figure 8-16. Plot of oxidation resistance (°C) *vs*. Vickers hardness (GPa) at 0.49 N (50 gf) loading for select metal borides. All MB_4 phases, have a nominal composition of M : B = 1 : 11.6; all MB_{12} phases, have a nominal composition of M : B = 1 : 20; the MB_2 phase has a nominal composition of M : B = 1 : 2.25; the MB phase was prepared stoichiometrically (M : B = 1 : 1). Data references: WB_4,[23] $W_{0.93}Ta_{0.02}Cr_{0.05}B_4$;[56] $W_{0.97}Mo_{0.03}B_4$;[19] $W_{0.92}Zr_{0.08}B_4$, $W_{0.94}Hf_{0.06}B_4$ and $W_{0.92}Ti_{0.08}B_4$;[20] $Zr_{0.5}Y_{0.5}B_{12}$, $Zr_{0.5}Sc_{0.5}B_{12}$, $Y_{0.5}Sc_{0.5}B_{12}$, ZrB_{12}, YB_{12} and ScB_{12};[5] $W_{0.5}Ta_{0.5}B$;[4] $W_{0.94}Y_{0.06}B_4$, $W_{0.92}Sc_{0.08}B_4$ and $W_{0.92}Gd_{0.08}B_4$ (this work, shown as blue circles).

REFERENCES

1. Chung, H.-Y. *et al.* Synthesis of Ultra-Incompressible Superhard Rhenium Diboride at Ambient Pressure. *Science (80-.).* **316,** 436–439 (2007).

2. Chung, H.-Y. *et al.* Response to Comment on 'Synthesis of Ultra-Incompressible Superhard Rhenium Diboride at Ambient Pressure'. *Science (80-.).* **318,** 1550 (2007).

3. Mohammadi, R. *et al.* Tungsten tetraboride, an inexpensive superhard material. *Proc. Natl. Acad. Sci. U. S. A.* **108,** 10958–10962 (2011).

4. Yeung, M. T. *et al.* Superhard Monoborides: Hardness Enhancement through Alloying in W1−xTaxB. *Adv. Mater.* 6993–6998 (2016). doi:10.1002/adma.201601187

5. Akopov, G. *et al.* Superhard mixed transition metal dodecaborides. *Chem. Mater.* **28,** 6605–6612 (2016).

6. Akopov, G., Yeung, M. T., Turner, C. L., Li, R. L. & Kaner, R. B. Stabilization of HfB12 in Y1-xHfxB12 under Ambient Pressure. *Inorg. Chem.* **55,** 5051–5055 (2016).

7. Akopov, G., Sobell, Z. C., Yeung, M. T. & Kaner, R. B. Stabilization of LnB_{12} (Ln = Gd, Sm, Nd, and Pr) in $Zr_{1-x}Ln_xB_{12}$ under Ambient Pressure. *Inorg. Chem.* **55,** 12419–12426 (2016).

8. Kiessling, R., Samuelson, O., Lindstedt, G. & Kinell, P.-O. The Borides of Manganese. *Acta Chemica Scandinavica* **4,** 146–159 (1950).

9. Akopov, G., Yeung, M. T. & Kaner, R. B. Rediscovering the Crystal Chemistry of Borides. *Adv. Mater.* **29,** (2017).

10. Lundström, T. Borides: Solid-state Chemistry. in *Encyclopedia of Inorganic Chemistry* 481–494 (2006).

11. Fokwa, B. P. T. Borides: Solid-State Chemistry. *Encycl. Inorg. Bioinorg. Chem.* 1–14 (2014). doi:10.1002/9781119951438.eibc0022.pub2

12. Albert, B. & Hillebrecht, H. Boron: Elementary challenge for experimenters and theoreticians. *Angew. Chemie - Int. Ed.* **48,** 8640–8668 (2009).

13. Samsonov, G. V., Markovskii, L. Y., Zhigach, A. F. & Valyashko, M. G. *Boron, Its Compounds and Alloys [in Russian]*. (House of the Academy of the Sciences Ukrainian SSR, 1960).

14. Buschow, K. H. J. Magnetic Properties of Borides. in *Boron and Refractory Borides* (ed. Matkovich, V. I.) 494–515 (Springer Berlin Heidelberg, 1977). doi:10.1007/978-3-642-66620-9_26

15. Samsonov, G. V., Serebriakova, T. I. & Neronov, V. A. *Borides [in Russian]*. (Atomizdat, 1975).

16. Yeung, M. T., Mohammadi, R. & Kaner, R. B. Ultraincompressible, Superhard Materials. *Annu. Rev. Mater. Res.* **46,** 465–485 (2016).

17. Bodrova, L. G., Koval'chenko, M. S. & Serebryakova, T. I. Preparation of tungsten tetraboride. *Sov. Powder Metall. Met. Ceram.* **13,** 1–3 (1974).

18. Lech, A. T., Turner, C. L., Mohammadi, R., Tolbert, S. H. & Kaner, R. B. Structure of superhard tungsten tetraboride: A missing link between MB 2 and MB 12 higher borides. *Proc. Natl. Acad. Sci.* **112,** 3223–3228 (2015).

19. Mohammadi, R. *et al.* Enhancing the Hardness of Superhard Transition-Metal Borides: Molybdenum-Doped Tungsten Tetraboride. *Chem. Mater.* **28,** 632–637 (2016).

20. Akopov, G., Yeung, M. T., Turner, C. L., Mohammadi, R. & Kaner, R. B. Extrinsic hardening of superhard tungsten tetraboride alloys with group 4 transition metals. *J. Am. Chem. Soc.* **138,** 5714–5721 (2016).

21. Yeung, M. T. *et al.* Superhard W0.5Ta0.5B nanowires prepared under ambient pressure. *Appl. Phys. Lett.* **109,** 203107 (2016).

22. Portnoi, K. I., Romashov, V. M., Levinskii, Y. V. & Romanovich, I. V. Phase diagram of the system tungsten-Boron. *Sov. Powder Metall. Met. Ceram.* **6,** 398–402 (1967).

23. Akopov, G. *et al.* Effects of Variable Boron Concentration on the Properties of Superhard Tungsten Tetraboride. *J. Am. Chem. Soc.* **139,** 17120–17127 (2017).

24. Lutterotti, L., Chateigner, D., Ferrari, S. & Ricote, J. Texture, residual stress and structural analysis of thin films using a combined X-ray analysis. *Thin Solid Films* **450,** 34–41 (2004).

25. Lutterotti, L., Bortolotti, M., Ischia, G., Lonardelli, I. & Wenk, H. R. Rietveld texture analysis from diffraction images. *Zeitschrift fur Krist. Suppl.* **1,** 125–130 (2007).

26. Lutterotti, L. Maud Rev. 2.55. *Maud Rev. 2.55, Univ. Trento-Italy, Dep. Ind. Eng. Trento, Italy* (2015).

27. Lutterotti, L. Total pattern fitting for the combined size-strain-stress-texture determination in thin film diffraction. *Nucl. Instruments Methods Phys. Res. Sect. B Beam Interact. with Mater. Atoms* **268,** 334–340 (2010).

28. Lutterotti, L., Matthies, S., Wenk, H. R., Schultz, A. S. & Richardson, J. W. Combined texture and structure analysis of deformed limestone from time-of-flight neutron diffraction spectra. *J. Appl. Phys.* **81,** 594–600 (1997).

29. Lutterotti, L., Bortolotti, M., Ischia, G., Lonardelli, I. & Wenk, H. R. Rietveld texture analysis from diffraction images. *Zeitschrift fur Krist. Suppl.* **1,** 125–130 (2007).

30. Sheldrick, G. M. *SHELXS-97, A Program for Crystal Structure Solution*. (University of Gottingen, 1997).

31. Sheldrick, G. M. *SHELXL-97, A Program for Crystal Structure Solution*. (University of Gottingen, 1997).

32. Sheldrick, G. M. *SHELXS-2014, A Program for Crystal Structure Refinement*. (University of Gottingen, 2014).

33. Sheldrick, G. M. Crystal structure refinement with SHELXL. *Acta Crystallogr. Sect. C Struct. Chem.* **71,** 3–8 (2015).

34. ASTM E1131 − 08. *ASTM E1131-08(2014) - Standard Test Method for Compositional Analysis by Thermogravimetry*. *ASTM International* (ASTM International, 2014). doi:https://doi.org/10.1520/E1131

35. *ISO 11358-1:2014 - Plastics -Thermogravimetry (TG) of polymers -Part 1: General principles*. (2014).

36. Callmer, B. A Single-Crystal Diffractometry Boron Investigation of Scandium in beta-rhombohedral boron. *J. Solid State Chem.* **23,** 391–398 (1978).

37. Werheit, H. *et al.* Raman scattering and isotopic phonon effects in dodecaborides. *J. Phys.*

Condens. Matter **23,** (2011).

38. Bruskov, V. A. & Zavalii, L. V. Crystal Structure of ScB12. *Izv. Akad. Nauk SSSR, Neorg. Mater.* **24,** 506–507 (1988).

39. Matkovich, V. I., Economy, J., Giese, R. F. & Barrett, R. The structure of metallic dodecarborides. *Acta Crystallogr.* **19,** 1056–1058 (1965).

40. Mikhalenko, S. I. I., Zavalii, L. V. V., Kuz'ma, Y. B. & Boiko, L. I. I. Isothermal sintering of the Sc-W-B and Sc-Re-B systems at 1000oC. *Sov. Powder Metall. Met. Ceram.* **30,** 681–683 (1991).

41. Peshev, P., Etourneau, J. & Naslain, R. Boron-Scandium System. *Mat. Res. Bull.* **5,** 319–328 (1970).

42. Liao, P. K. & Spear, K. E. The B-Y (boron-yttrium) system. *J. Phase Equilibria* **16,** 521–524 (1995).

43. Liao, P. K., Spear, K. E. & Schlesinger, M. E. The B-Gd (Boron-Gadolinium) System. **17,** 330–334 (1996).

44. Liao, P. K. & Spear, K. E. B-Tb (Boron-Terbium). in *Binary Alloy Phase Diagrams, Vol .1* (ed. Massalski, T. B.) 542–544 (ASM International, 1990).

45. Liao, P. K. & Spear, K. E. B-Dy (Boron-Dysprosium). in *Binary Alloy Phase Diagrams, Vol. 1* (ed. Massalski, T. B.) 476–478 (ASM International, 1990).

46. Liao, P. K. & Spear, K. E. B-Ho (Boron-Holmium). in *Binary Alloy Phase Diagrams, Vol. 1* (ed. Massalski, T. B.) 491–493 (ASM International, 1990).

47. Liao, P. K., Spear, K. E. & Schlesinger, M. E. The B-Er (Boron-Erbium) System. *J. Phase Equilib.* **17,** 326–329 (1996).

48. Mikhalenko, S. I., Chaban, N. F. & Kuz'ma, Y. B. New Borides with the Structure of the Er3CrB7 Type and Phase Diagrams of the System Y-W-B [in Russian]. *Inorg. Mater.* **28,** 2092–2095 (1992).

49. Chaban, N. F. & Bilonizhko, N. S. Isothermal Sections of Phase-Equilibrium Diagrams for the Systems {Terbium, Dysprosium}-Tungsten-Boron at 1270 K. *Powder Metall. Met. Ceram.* **32,** 928–929 (1994).

50. Chaban, N. F. & Kuz'ma, Y. B. Isothermal Section of the System Erbium-Tungsten-Boron at 1270 K. *Powder Metall. Met. Ceram.* **10,** 845–847 (1990).

51. Slater, J. C. Atomic Radii in Crystals. *J. Chem. Phys.* **41,** 3199–3204 (1964).

52. Cannon, J. F., Cannon, D. M. & Tracy Hall, H. High pressure syntheses of SmB2 and GdB12. *J. Less-Common Met.* **56,** 83–90 (1977).

53. Cannon, J. F. & Farnsworth, P. B. High pressure syntheses of ThB12 and HfB12. *J. Less-Common Met.* **92,** 359–368 (1983).

54. Mar, R. W. & Stout, N. D. High Temperature Enthalpies of Binary Dodecaborides. *J. Chem. Phys.* **57,** 5342–5349 (1972).

55. Kuz'ma, Y. B., Serebryakova, T. I. & Plakhina, A. M. The polymorphic transformation of W2B5. *Russ. J. Inorg. Chem.* **12,** 288–289 (1967).

56. Mohammadi, R. *et al.* Toward inexpensive superhard materials: Tungsten tetraboride-based solid solutions. *J. Am. Chem. Soc.* **134,** 20660–20668 (2012).

CHAPTER 9. SUPERHARD METAL BORIDES: A LOOK FORWARD

ABSTRACT

Previous efforts towards the synthesis of materials with superior mechanical properties (e.g., superhardness, high bulk modulus and high shear modulus) have focused on binary metal boride structures with short covalent bonds. In this paper, we discuss the methods of enhancing the intrinsic and extrinsic hardening factors commonly used to achieve these properties. As the realm of binary metal borides has all but been exhausted, there is a need to move to ternary and higher borides as well as to achieve greater morphological control at the nanoscale. The use of ternary and higher borides as starting materials provides a multitude of diverse compositional and structural combinations. These compounds merit further investigation as they offer the potential for the optimization of mechanical properties.

DISCUSSION

Metal borides possess many remarkable mechanical,[1–4] optical,[5] magnetic[5] and thermal[6] properties. Among the mechanical properties, hardness, and superhardness in particular, is a very important and appealing property as it has a host of potential applications, such as in materials for tools and abrasives. Superhardness is defined as a material exhibiting a Vickers hardness (H_v) above 40 GPa at a particular applied load, ideally at the asymptotic limit, i.e. the highest load, but more realistically at 0.49 N of applied load. The hardness at the lower load is important since most cutting operations are actually under low load. Among the hardest materials known are several elemental compounds (diamond[7,8] and γ-boron[9,10]) as well as nitrides (e.g. cubic-BN[11]), carbides

(e.g. $Ti_{0.8}Sc_{0.2}C$ and TiB_2-B_4C composite)[12–14] and borides (e.g. $W_{0.93}Ta_{0.02}Cr_{0.05}B_4$ and $W_{0.92}Zr_{0.08}B_4$),[15,16] all of which are not only superhard, but have a Vickers hardness greater than 50 GPa at 0.49 N of applied load or at the asymptotic limit as in the case of cubic-BN and diamond. However, cubic-BN and diamond are expensive since their bulk synthesis requires high temperature/high pressure conditions. Therefore, recent efforts to make new superhard materials have focused on compounds with short covalent bonds such as borides that can be made at ambient pressure. Binary metal borides can be further hardened through solid solution formation. To increase hardness even further, it is now important to consider ternary and higher metal borides as well as morphological control of the grain structure. Therefore, an understanding of the underlying principles of mechanical properties is needed to make additional advancements in the field of hard metal borides.

Hardness is a function of many variables, but generally can be considered a weighted sum of intrinsic and extrinsic hardening effects and factors. Intrinsic effects depend on the composition of the metal boride as well as the underlying arrangement of atoms: metal atoms for sub-borides (M:B $< 1:1$) and boron atoms for other metal borides (M:B $\geq 1:1$). The boron arrangement can range from lone metal and boron atoms to chains, networks and backbones of boron atoms in higher borides. Generally, for a material to be intrinsically hard, it must possess both a high bulk modulus (resistance to volume change) and a high shear modulus (resistance to shape change, i.e. deformation). Bulk modulus directly correlates with the incompressibility (elastic stiffness) of a material, while shear modulus correlates to the bending of bonds as well as to the direction and plane of shear.[17–19]

On the other hand, extrinsic effects depend strongly on the surface morphology and grain structure of the material, such as grain hardening, i.e. the Hall-Petch effect,[20–24] patterning and

nanomorphology.[16] Enhancing each of these factors leads to the increased hardness observed in metal borides. Intrinsic effects can be improved through the formation of solid solutions and alloys. Substitutional solid solution formation is predominantly governed by the Hume-Rothery rules requiring similarity of crystal structures, oxidation state (valency), electronegativity and atomic size of the initial metal and the dopant (no greater than 15% difference in atomic radii).[25–28] Forming a solid solution can influence the hardness of a material through solid solution hardening effects, where due to the different atomic size of the doping metal, the crystal lattice is locally distorted and as a result dislocations can be pinned and hardness enhanced.[25–27,29] Intrinsic hardness is the result of the effects of two predominant factors: atomic size (radius) and electronic effects (valence electron density). Generally, the higher the electron density of the metal in a boride, the harder the resulting phase, for example, ReB_2 and WB_4. However, there are exceptions, such as OsB_2, where although Os metal has a higher valence electron density than Re, OsB_2 is about half as hard as ReB_2. The hardness of OsB_2 versus ReB_2 can be explained by the fact that in OsB_2, the boron nets are arranged in a "boat" conformation as opposed to the "chair" structure in ReB_2. The "boat" conformation is influenced by antibonding interactions of the osmium and boron dimers, resulting in longer boron-boron bonds, which as a result are weaker than in ReB_2, where all boron-boron bonding is enhanced.[30] On the other hand, the arrangement of boron can play an important role, as borides with a backbone of boron atoms forming B_{12} icosahedra (e.g. boron itself, known as β-rhombohedral boron, MB_{50} and MB_{66}) as well as true cage compounds (cubic-UB_{12} ($Fm\bar{3}m$) and tetragonal-ScB_{12} (*I4/mmm*) structures) all form hard and superhard materials. For instance, although the bulk modulus of ZrB_{12} is much lower than values for ReB_2 and WB_4, it still exhibits superhardness.[31,32] The high hardness of mechanically isotropic ZrB_{12} originates from the 3-dimensional covalent network of highly symmetric B - B clusters similar to those observed

in B_6O.[33] These examples illustrate that incompressibility does not necessarily lead to high hardness.

The other important factor is atomic size (in an appropriate metal coordination environment), as it usually governs what boride phases a particular metal can form. Here, Hägg's ratio[34] (the ratio of boron to metal atom radii) can be applied for metals, and phase formation can be predicted. According to this ratio, for most transition metals, the critical value is 0.59, above which metals form metastable structures instead of the normal cubic or hexagonal higher metal boride structures (e.g. MB_4, MB_6, MB_{12}). For example, the Hägg's ratio for tungsten is 0.63, which correlates with W forming a defect $WB_{4(hex)}$ structure, which is different from other metal tetraborides that exhibit a $UB_{4(tet)}$ structure.[34,35]

The atomic size is an extremely sensitive value, as the difference in size between Ti, W and Re is enough to cause their diborides to have vastly different arrangements of boron atoms, and thus, affect their hardness on going from flat hexagonal boron sheets for TiB_2 (r_{Ti} = 1.40 Å,[36] AlB_2-structure, *P6/mmm*), to alternating flat and corrugated sheets for WB_2 (r_W = 1.35 Å,[36] WB_2-structure, *P6₃/mmc*), to corrugated sheets for ReB_2 (r_{Re} = 1.35 Å,[36] ReB_2-structure, *P6₃/mmm*).[1,30] Furthermore, in the abovementioned example, OsB_2 has a totally different, orthorhombic, structure (r_{Os} = 1.30 Å,[36] RuB_2-structure, *Pmmn*), yet the radius of Os is very close to that of Re. Furthermore, the relative atomic size of metals is so important that it makes a difference between a phase being stable at ambient pressure or requiring high pressure synthesis to form. For example, both Zr and Hf have similar atomic radii due to the lanthanide contraction (1.55 Å);[36] however, in a 12 coordinate environment Hf has a slightly smaller atomic size than Zr (1.580 vs. 1.603 Å),[37] rendering ZrB_{12} a phase that can be synthesized at ambient pressure, while HfB_{12} requires 6.5 GPa to form,[37,38] although these high pressure dodecaborides can be stabilized in solid solutions.[39–41]

Furthermore, the relative atomic size in solid solutions can lead to limited solubility or the formation of a completely new ternary boride, with a structure different from the parent binary phases, such as in the system $Re_{1-x}Y_xB_2$. In this example the parent phases are hexagonal YB_2 (r_Y = 1.80 Å[36]) and ReB_2, and at 50/50 at.% metal substitution a new orthorhombic (although nominally a diboride) phase forms with the stoichiometry $YReB_4$[42] ($YCrB_4$-structure, *Pbam*) due to the relative size of the metals being outside of the range stipulated by the Hume-Rothery rules (<15% atomic radius difference) as illustrated in **Figure 9-1**. Additionally, there exists a whole array of other pseudo-diboride structures, such as Y_2ReB_6[43–45] (Pbam), Y_3ReB_7[45,46] (Cmcm) and YMo_3B_7[47–49] (Pnma) as shown in **Figures 9-1 and 9-2**. The first two structures ($YReB_4$ and Y_2ReB_6) resemble layered structures, similar to AlB_2 diborides. However, instead of having boron arranged in sheets of hexagons, these structures have boron atoms arranged in 5-, 6- and 7-member rings. For example, Y_3ReB_7 has boron atoms arranged in corrugated cages. In the YMo_3B_7 structure, the boron atoms are arranged in stacked hexagonal bands, 6 hexagons wide and infinite in length, while the metal atoms are arranged in chains. The last two structures in particular show how much of an effect metal atoms can have on the structure of the resulting boride, as the main difference is in the number of metals in the first or second position.

In order to enhance extrinsic effects, morphology, patterning and grain size need to be controlled. This can be achieved through the addition of secondary metals which alter the cooling rate of the resultant boride sample.[50–54] For example, the addition of Zr to WB_4, causes not only a change in patterning, but a nano-grain morphology at an 8 at.% doping level (**Figure 9-3**).[16] These methods can be further expanded to the synthesis of bulk nano-forms of known superhard materials, for example nanowires of $W_{0.5}Ta_{0.5}B$.[55,56] Patterning can be achieved through the use of doping metals which exhibit limited solubility and form phases with a vastly different melting temperature

relative to the main phase: e.g. 3225 °C for TiB_2[57] vs. 2020 °C for WB_4[58]. For example, the addition of Ti to WB_4, causes the formation of TiB_2, which has a melting point over 1000 °C higher than WB_4, and as such forms before WB_4, thus providing a template for the growth of WB_4 grains (**Figure 9-4**).[16]

Further investigation of WB_4 with other dodecaboride forming transition metals and lanthanides has led to additional fine-grained morphologies (**Figure 9-5**).[59] These doping metals are completely soluble in the WB_4 defect cuboctahedral structure with increasing metal concentration until equilibrium is achieved with the doping metal's highest boride or boron-rich boride phase. The observed phase equilibrium can be attributed to the reduction in total energy through the formation of the most thermodynamically favorable phase(s). Coexistence of the WB_4 parent phase with a boron-rich phase results in "dendritic" nanopatterning and consequently, smaller grains. This change in morphology and reduction in grain size, pins dislocations in the bulk material, thus, enhancing the overall hardness.

Another factor affecting mechanical properties comes from the fact that some boride phases, e.g. WB_4 and ZrB_{12}, cannot be prepared in pure form using stoichiometric compositions. This necessitates using either excess boron or allowing lower boride phases to form, which can lead to inferior mechanical properties. WB_4 requires a minimum metal to boron ratio of 1:8.5, but is usually prepared from a melt at a ratio of 1:12, with lower ratios resulting is some WB_2 impurity.[60] Although, it was found that WB_4 can be prepared almost stoichiometrically using ~32 at.% Ta substitution, the resulting phase exhibited lower hardness.[60] Similarly, ZrB_{12} has to be prepared at a metal to boron ratio of 1:20 in order to avoid the ZrB_2 phase.[32] Although in a solid solution with YB_{12} no lower phases exist at almost stoichiometric composition. Therefore, for many phases it is

still relevant to try to find compositions that result from using stoichiometric amounts of reactants, yet possess similar mechanical properties.

CONCLUSIONS

All of the abovementioned factors: formation of solid solutions, changes in surface morphology and patterning are not only relevant to mechanical properties, but to oxidation resistance, magnetic, electronic and optical properties as well as other potential applications not usually attributed to borides such as catalysis.[61] Furthermore, going to the nanoscale[62,63] can potentially improve many of the properties listed above.[64–66] In addition, recent works in the field have highlighted a simple synthesis of nanoscale transition metal borides with a wide range of different morphologies (nanorods, nanosheets, nanoprisms, nanoplates and nanoparticles) using the redox chemistry of $Sn/SnCl_2$.[67] Moreover, metal borides are capable of forming layered structures with the addition of aluminum, which can be further etched to form 2D nanosheets.[68–70]

Although it is difficult if not impossible to devise simple rules (due to hardness being an aggregate of many factors) for what can be expected in terms of effects on hardness from using a particular metal dopant in each and every case, it is possible to describe general trends. In case of intrinsic hardness effects, such as substitutional metal doping (Hume-Rothery rules),[25–27,29] the main effect on hardness is through solid solution hardening, which causes lattice distortions and consequently pins dislocations. In case of extrinsic hardening, the main effect of the metals is through changes in morphology: through templating, due to the difference of phase melting points (e.g. the addition of group 4 or 5 metals), nanomorphology, due to rapid cooling resulting in a large number of

nucleation sites and small grain size (e.g. the addition of scandium or zirconium), or patterning (e.g. the addition of yttrium or lanthanides).

The study of metal borides is a very old field, as such the limits of the binary boride world have all but been exhausted. Therefore, it is necessary to move to ternary and higher borides as starting materials. These compositions are all the more challenging due to factors such as phase stability relative to metal substitutions and simultaneous equilibrium of several phases in the product. The vast array of determined crystal structures to date offers the potential for targeted approaches towards structure and property predictions.[71] Although there is almost no data for mechanical properties of ternary (e.g. $YReB_4$, Y_2ReB_6, Y_3ReB_7 and YMo_3B_7) and higher borides, a comprehensive understanding of the intrinsic and extrinsic factors discussed above can be utilized to approximate hardness on the basis of structure and chemical bonding.

ACKNOWLEDGMENTS

We thank the National Science Foundation Division of Materials Research, Grant DMR-1506860 (R.B.K.) and Virginia Commonwealth University Startup Grant 137422 (R.M.) for financial support.

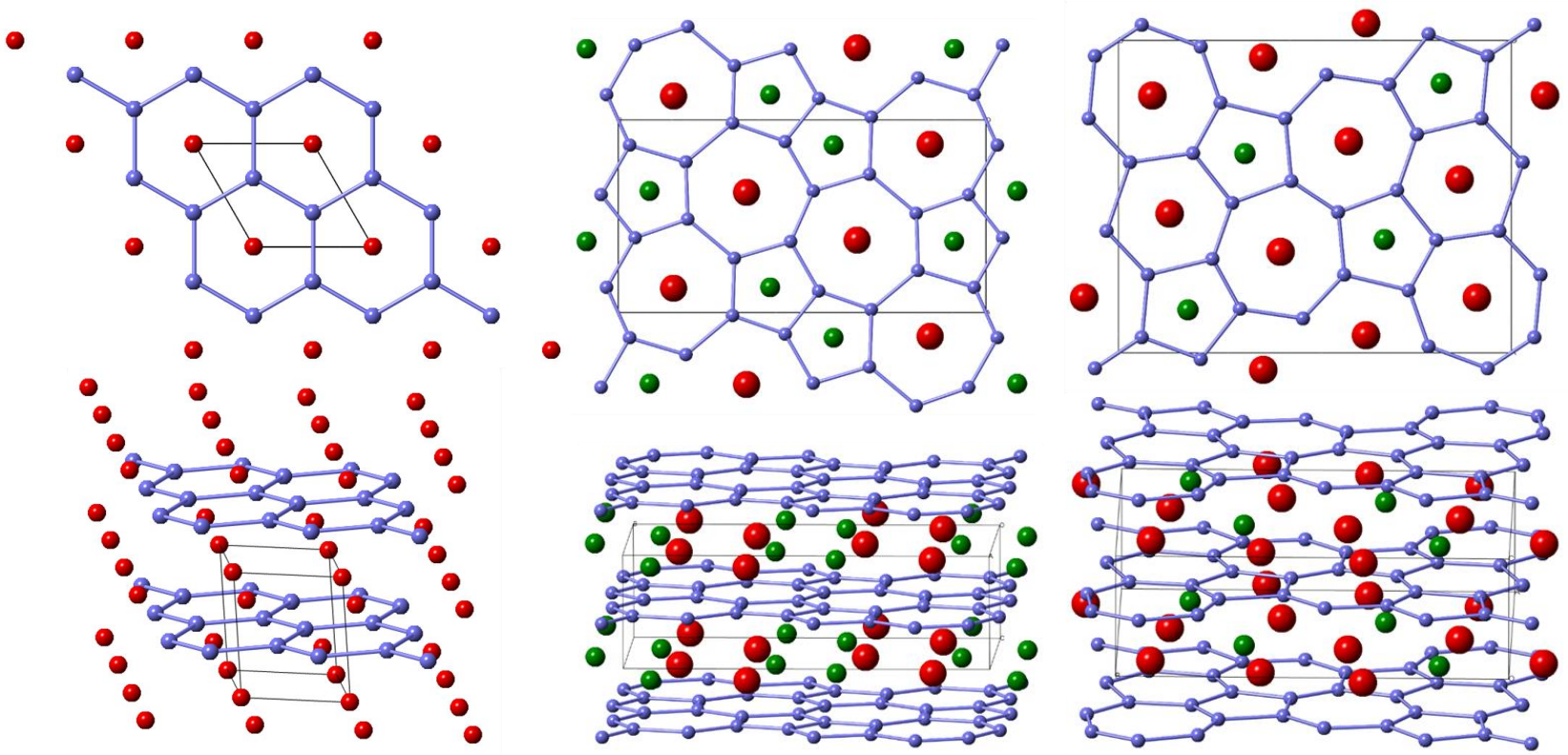

Figure 9-1. Crystal structures of: (**left**) AlB_2 (*P6/mmm*, ICSD (Inorganic Crystal Structure Database) 193381), (**middle**) $YReB_4$ (*Pbam*, ICSD 615278), (**right**) Y_2ReB_6 (*Pbam*, ICSD 16187). For AlB_2, aluminum atoms are shown in red, for the other two structures: yttrium atoms are shown in red, rhenium in green; for all structures boron atoms are shown in blue-gray. Note that each can be considered a layered structure. In AlB_2 the boron atoms are arranged in sheets of hexagons, however, in the other two structures the boron atoms are arranged in 5-, 6- and 7-member rings.

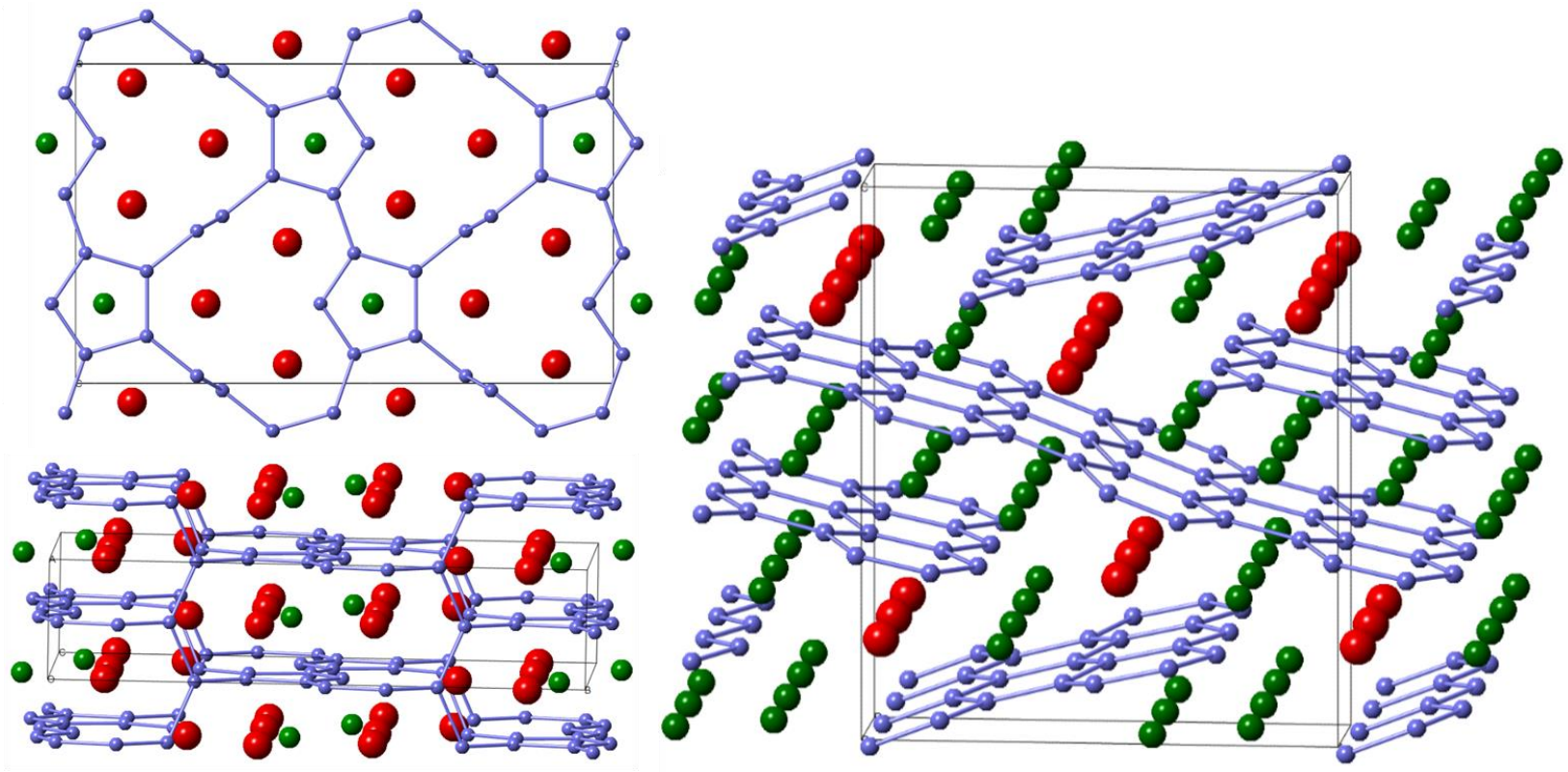

Figure 9-2. Crystal structures of: (**left**) Y_3ReB_7 (*Cmcm*, ICSD 64595) and (**right**) YMo_3B_7 (*Pnma*, ICSD 243846). Yttrium atoms are shown in red, rhenium and molybdenum are green, boron are blue-gray. For the first structure the boron atoms are arranged in corrugated cages, while for the second structure, the boron atoms are arranged in stacked hexagonal bands, 6 hexagons wide and infinite in length, while the metal atoms are arranged in chains.

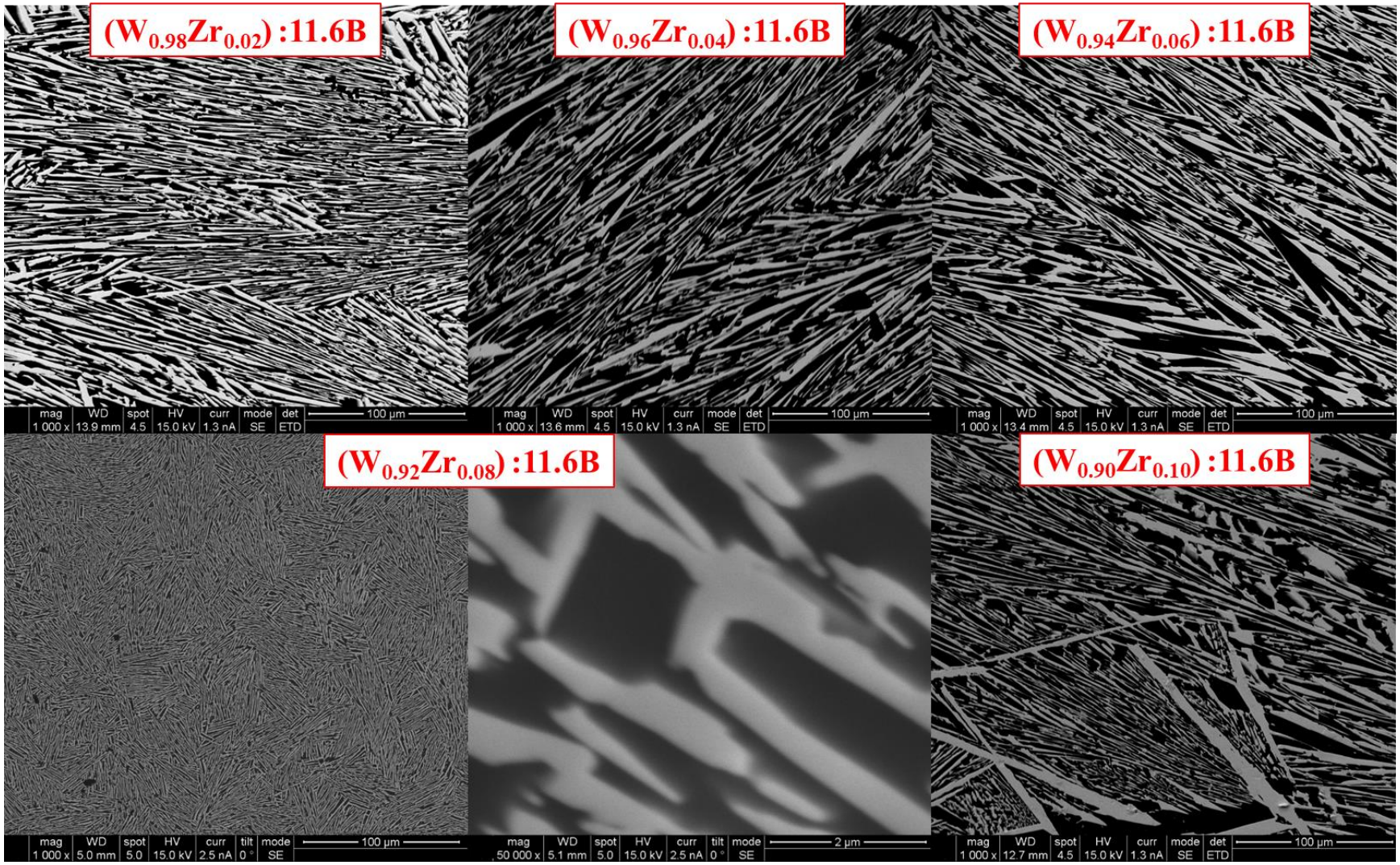

Figure 9-3. SEM images of the alloys of WB_4 with 2-10 at.% Zr taken at 1000x magnification and 50,000x for the hardest composition, $W_{0.92}Zr_{0.08}B_4$, showing changes in morphology. The drastic change of surface morphology at 8 at.% Zr can be attributed to a decomposition from a meta-stable W-Zr dodecaboride phase. "Reprinted (adapted) with permission from (Akopov, G.; Yeung, M. T.; Turner, C. L.; Mohammadi, R.; Kaner, R. B. Extrinsic Hardening of Superhard Tungsten Tetraboride Alloys with Group 4 Transition Metals. *J. Am. Chem. Soc.* **2016**, *138* (17), 5714–5721). Copyright (2016) American Chemical Society."

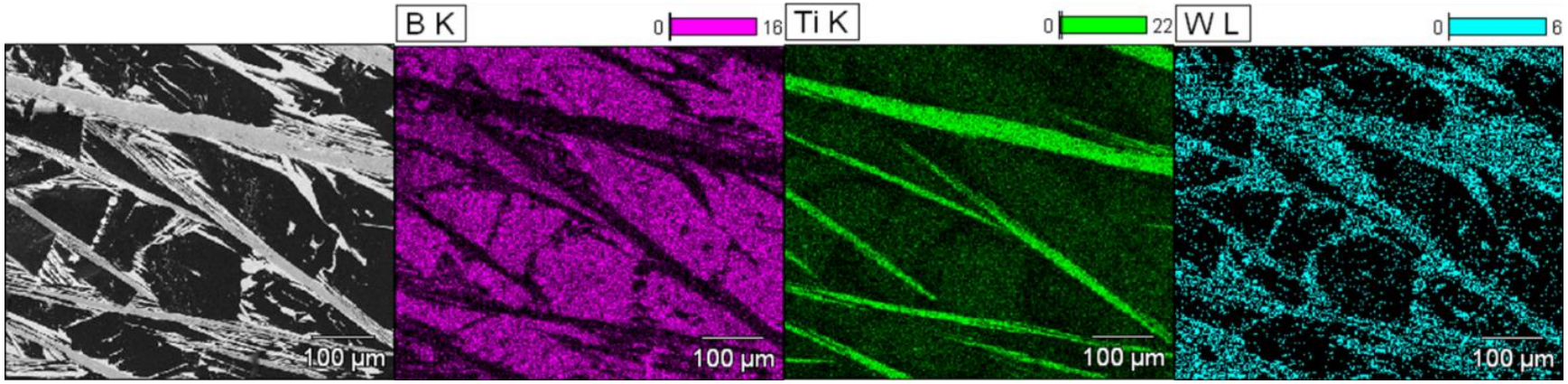

Figure 9-4. Elemental maps for boron (K line), titanium (K line) and tungsten (L line) for the $W_{0.50}Ti_{0.50}B_4$ alloy showing the presence of titanium in TiB_{50} (β-rhombohedral boron doping phase of titanium) corresponding to boron rich areas and TiB_2 in tungsten rich areas. "Reprinted (adapted) with permission from (Akopov, G.; Yeung, M. T.; Turner, C. L.; Mohammadi, R.; Kaner, R. B. Extrinsic Hardening of Superhard Tungsten Tetraboride Alloys with Group 4 Transition Metals. *J. Am. Chem. Soc.* **2016**, *138* (17), 5714–5721). Copyright (2016) American Chemical Society."

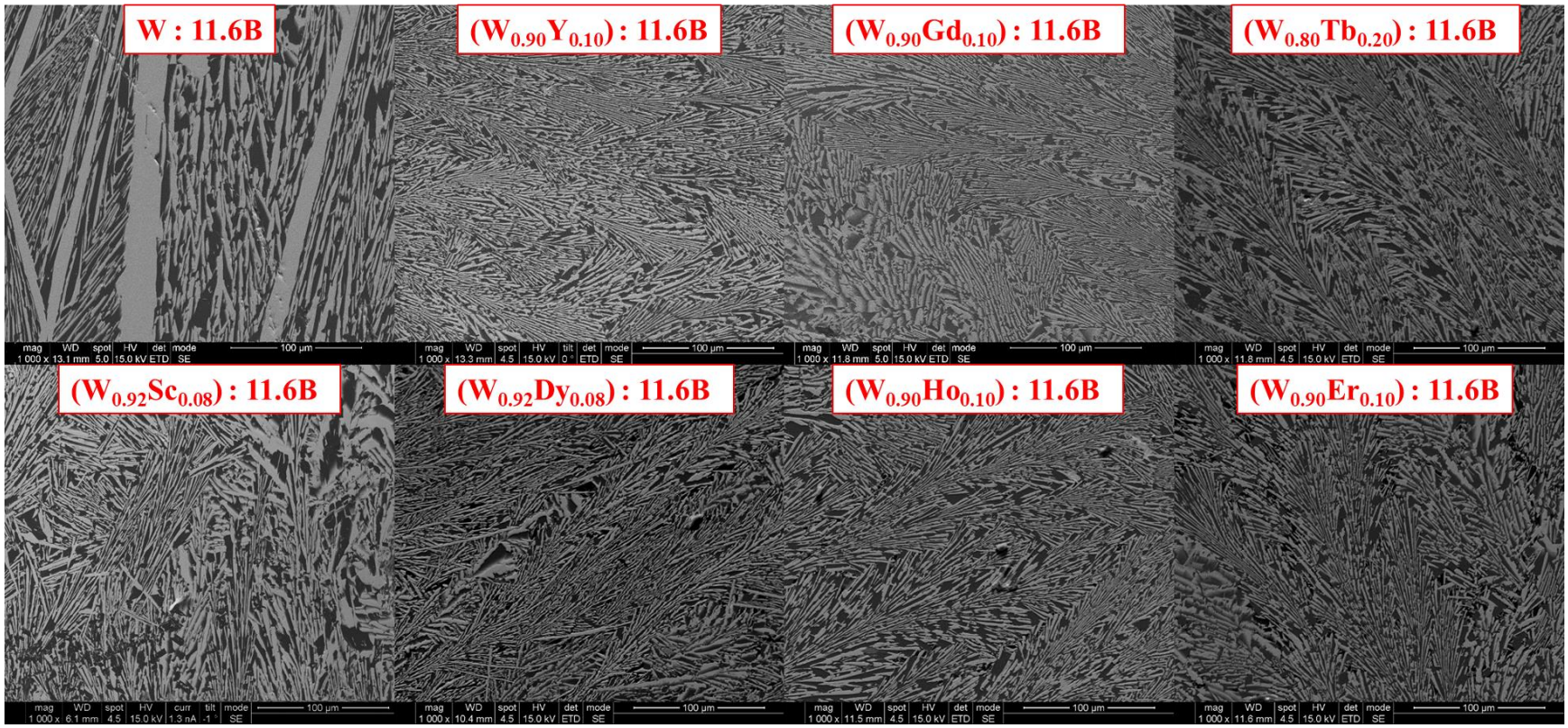

Figure 9-5. SEM images for WB_4 as its alloys with Sc, Y, Gd, Tb, Dy, Ho and Er, showing a change in morphology of the grains. For Sc a change of morphology occurs at 6 - 8 at.% Sc, resulting in a decrease in the size of the metal boride and boron grains. For Y and lanthanides the change of morphology (dendritic pattern) occurs at 8 – 10 at.% lanthanide substitution in WB_4, except for Tb, where it occurs at 10 - 20 at.% Tb. All SEM images were taken at 1000x magnification; the scale bars are 100 µm. "Reprinted (adapted) with permission from (Akopov, G.; Yeung, M. T.; Roh, I.; Sobell, Z. C.; Yin, H.; Mak, W. H.; Khan, S. I.; Kaner, R. B. Effects of Dodecaboride Forming Metals on the Properties of Superhard Tungsten Tetraboride. *Chem. Mater.* **2018**, 10.1021/acs.chemmater.8b01464). Copyright (2018) American Chemical Society."

REFERENCES

(1) Akopov, G.; Yeung, M. T.; Kaner, R. B. Rediscovering the Crystal Chemistry of Borides. *Adv. Mater.* **2017**, *29*, 1604506.

(2) Yeung, M. T.; Mohammadi, R.; Kaner, R. B. Ultraincompressible, Superhard Materials. *Annu. Rev. Mater. Res.* **2016**, *46* (1), 465–485.

(3) Fokwa, B. P. T. Borides: Solid-State Chemistry. *Encycl. Inorg. Bioinorg. Chem.* **2014**, 1–14.

(4) Albert, B.; Hillebrecht, H. Boron: Elementary Challenge for Experimenters and Theoreticians. *Angew. Chemie - Int. Ed.* **2009**, *48* (46), 8640–8668.

(5) Scheifers, J. P.; Zhang, Y.; Fokwa, B. P. T. Boron: Enabling Exciting Metal-Rich Structures and Magnetic Properties. *Acc. Chem. Res.* **2017**, *50* (9), 2317–2325.

(6) Samsonov, G. V.; Serebriakova, T. I.; Neronov, V. A. *Borides [in Russian]*; Atomizdat: Moscow, 1975.

(7) Lonsdale, K. Further Comments on Attempts by H. Moissan, J.B. Hannay and Sir Charles Parsons to Make Diamonds in the Laboratory. *Nature* **1962**, *196*, 104–106.

(8) Dub, S.; Lytvyn, P.; Strelchuk, V.; Nikolenko, A.; Stubrov, Y.; Petrusha, I.; Taniguchi, T.; Ivakhnenko, S. Vickers Hardness of Diamond and CBN Single Crystals: AFM Approach. *Crystals* **2017**, *7* (12), 369.

(9) Solozhenko, V. L.; Kurakevych, O. O.; Oganov, A. R. On the Hardness of a New Boron Phase, Orthorhombic γ-B28. *J. Superhard Mater.* **2008**, *30* (6), 428–429.

(10) Oganov, A. R.; Chen, J.; Gatti, C.; Ma, Y.; Ma, Y.; Glass, C. W.; Liu, Z.; Yu, T.; Kurakevych, O. O.; Solozhenko, V. L. Ionic High-Pressure Form of Elemental Boron. *Nature* **2009**, *457* (7231), 863–867.

(11) Greim, J.; Schwetz, K. A. Boron Carbide, Boron Nitride, and Metal Borides. In *Ullmann's Encyclopedia of Industrial Chemistry*; Wiley-VCH Verlag GmbH & Co. KGaA, 2006; Vol. 6, pp 219–236.

(12) Samsonov, G. V.; Makarenko, G. N.; Kosolapova, T. Y. On Carbides of Scandium and Complex Carbides of Scandium-Titanium [in Russian]. *Proc. Acad. Sci. USSR* **1962**, *144* (5), 1062–1065.

(13) Krushinskii, A. N. Conditions of Preparation of Complex Carbide Alloys Containing Scandium Carbide. *Sov. Powder Metall. Met. Ceram.* **1965**, *4* (11), 906–911.

(14) Portnoi, K. I.; Samsonov, G. V.; Frolova, K. I. Some Properties of Alloys of Titanium Boride and Double Titanium-Chromium Boride Wuth Boron Carbide. *Zhurnal Prikl. Khimii* **1958**, *33* (3), 577–582.

(15) Mohammadi, R.; Xie, M.; Lech, A. T.; Turner, C. L.; Kavner, A.; Tolbert, S. H.; Kaner, R. B. Toward Inexpensive Superhard Materials: Tungsten Tetraboride-Based Solid Solutions. *J. Am. Chem. Soc.* **2012**, *134* (51), 20660–20668.

(16) Akopov, G.; Yeung, M. T.; Turner, C. L.; Mohammadi, R.; Kaner, R. B. Extrinsic Hardening of Superhard Tungsten Tetraboride Alloys with Group 4 Transition Metals. *J. Am. Chem. Soc.* **2016**, *138* (17), 5714–5721.

(17) Kaner, R. B.; Gilman, J. J.; Tolbert, S. H. Designing Superhard Materials. *Science* **2005**, *308* (5726), 1268–1269.

(18) Gilman, J. J.; Cumberland, R. W.; Kaner, R. B. Design of Hard Crystals. *Int. J. Refract. Met. Hard Mater.* **2006**, *24* (1–2), 1–5.

(19) Levine, J. B.; Tolbert, S. H.; Kaner, R. B. Advancements in the Search for Superhard Ultra-Incompressible Metal Borides. *Adv. Funct. Mater.* **2009**, *19* (22), 3519–3533.

(20) Hall, E. O. The Deformation and Ageing of Mild Steel .3. Discussion of Results. *Proc. Phys. Soc. London Sect. B* **1951**, *64*, 747–753.

(21) Petch, N. J. The Cleavage Strength of Polycrystals. *J. Iron Steel Inst.* **1953**, *174*, 25–28.

(22) Li, Y.; Bushby, A. J.; Dunstan, D. J. The Hall–Petch Effect as a Manifestation of the General Size Effect. *Proc. R. Soc. A Math. Phys. Eng. Sci.* **2016**, *472*, 20150890.

(23) Eshelby, J. D.; Frank, F. C.; Nabarro, F. R. N. XLI. The Equilibrium of Linear Arrays of Dislocations. *London, Edinburgh, Dublin Philos. Mag. J. Sci.* **1951**, *42* (327), 351–364.

(24) Smith, W.; Hashemi, J. *Foundations of Materials Science and Engineering*, 4th ed.; McGaw-Hill, 2006.

(25) Hume-Rothery, W. *Atomic Theory for Students of Metallurgy*, 5th ed.; The Institute of Metals: London, 1969.

(26) Hume-Rothery, W.; Smallman, R. W.; Haworth, C. W. *The Structure of Metals and Alloys*; The Institute of Metals: London, 1969.

(27) Hume-Rothery, W.; Powell, H. M. On the Theory of Super-Lattice Structures in Alloys. *Z. Krist.* **1935**, *91*, 23.

(28) Cottrell, A. H. *An Introduction to Metallurgy*; Edward Arnold Publishers Ltd.: London, 1967.

(29) Fleischer, R. L. Substitutional Solution Hardening. *Acta Metall.* **1961**, *11*, 203–209.

(30) Robinson, P. J.; Liu, G.; Ciborowski, S.; Martinez-martinez, C.; Chamorro, J. R.; Zhang, X.; Mcqueen, T. M.; Bowen, K. H.; Alexandrova, A. N. Mystery of Three Borides: Differential Metal − Boron Bonding Governing Superhard Structures. *Chem. Mater.* **2017**, *29*, 9892–9896.

(31) Ma, T.; Li, H.; Zheng, X.; Wang, S.; Wang, X.; Zhao, H.; Han, S.; Liu, J.; Zhang, R.; Zhu, P.; et al. Ultrastrong Boron Frameworks in ZrB12: A Highway for Electron Conducting. *Adv. Mater.* **2017**, *29* (3), 1–7.

(32) Akopov, G.; Yeung, M. T.; Sobell, Z. C.; Turner, C. L.; Lin, C. W.; Kaner, R. B. Superhard Mixed Transition Metal Dodecaborides. *Chem. Mater.* **2016**, *28* (18), 6605–6612.

(33) He, D.; Shieh, S. R.; Duffy, T. S. Strength and Equation of State of Boron Suboxide from Radial X-Ray Diffraction in a Diamond Cell under Nonhydrostatic Compression. *Phys. Rev. B - Condens. Matter Mater. Phys.* **2004**, *70* (18), 1–9.

(34) Hägg, G. Ubergangselementen in' Binaren Sistem Mit Bor, Kohlenstoff Und Stickstoff. *Z. Phys. Chem.* **1931**, *B12*, 33.

(35) Samsonov, G. V.; Markovskii, L. Y. Y.; Zhigach, A. F.; Valyashko, M. G. *Boron, Its Compounds and Alloys [in Russian]*; House of the Academy of the Sciences Ukrainian SSR: Kiev, 1960.

(36) Slater, J. C. Atomic Radii in Crystals. *J. Chem. Phys.* **1964**, *41* (10), 3199–3204.

(37) Cannon, J. F.; Farnsworth, P. B. High Pressure Syntheses of ThB12 and HfB12. *J. Less-Common Met.* **1983**, *92* (2), 359–368.

(38) Cannon, J. F.; Cannon, D. M.; Tracy Hall, H. High Pressure Syntheses of SmB2 and GdB12. *J. Less-Common Met.* **1977**, *56* (1), 83–90.

(39) Akopov, G.; Sobell, Z. C.; Yeung, M. T.; Kaner, R. B. Stabilization of LnB12 (Ln = Gd, Sm, Nd, and Pr) in Zr(1– x)Ln(x)B12 under Ambient Pressure. *Inorg. Chem.* **2016**, *55* (23), 12419–12426.

(40) Akopov, G.; Yeung, M. T.; Turner, C. L.; Li, R. L.; Kaner, R. B. Stabilization of HfB12 in Y1-XHfxB12 under Ambient Pressure. *Inorg. Chem.* **2016**, *55* (10), 5051–5055.

(41) Akopov, G.; Roh, I.; Sobell, Z. C.; Yeung, M. T. M. T.; Kaner, R. B. R. B. Investigation of Ternary Metal Dodecaborides (M1M2M3)B12 (M1, M2 and M3 = Zr, Y, Hf and Gd). *Dalton Trans.* **2018**, *47* (19), 6683–6691.

(42) Chaban, N. F.; Mikhalenko, S. I.; Kuz'ma, Y. B. Component Interactions in {Y,Gd,Tm}-Mo-B Ternary Systems at 1270K. *Powder Metall. Met. Ceram.* **2000**, *39*, 48–53.

(43) Kuz'ma, Y. B.; Svarichevskaya, S. I. Crystal Structure of Y2ReB6 and Its Analogues. *Sov. Phys. Crystallogr.* **1972**, *17* (3), 569–571.

(44) Kuz'ma, Y. B.; Mykhalenko, S. I.; Akselrud, L. G. Redermination of the Structure of the Compound Y3ReB7 and Related Compounds. *J. Less-Common Met.* **1986**, *117* (1–2), 29–35.

(45) Mikhalenko, S. I.; Kuz'ma, Y. B.; Sobolev, A. S. Yttrium-Rhenium-Boron and Lanthanum-Rhenium-Boron Systems. *Sov. Powder Met. Met. Ceram.* **1977**, *1* (169), 48–50.

(46) Chaban, N. F.; Akselrud, L. G.; Bruskov, V. A.; Kuz'ma, Y. B. Crystal Structure of the New Boride Er3CrB7. *Sov. Phys. Crystallogr.* **1985**, *30* (1), 108–109.

(47) Mikhalenko, S. I.; Babizhetskii, V. S.; Hartl, H.; Kuz'ma, Y. B. New YMo3B7 Boride and Its Structure. *Crystallograhy Reports* **1995**, *40* (3), 424–427.

(48) Mikhalenko, S. I.; Chaban, N. F.; Kuz'ma, Y. B. New Borides LnMo3B7 (Ln = Tb, Dy, Ho, Er, Tm) with the YMo3B7 Structure. *Inorg. Mater.* **1995**, *31* (11), 1282–1285.

(49) Salamakha, L.; Sologub, O.; Rizzoli, C.; Michor, H.; Gonçalves, A. P.; Rogl, P.; Bauer, E. Crystal Structure and Physical Properties of UMo3B7. *Intermetallics* **2017**, *85*, 180–186.

(50) Turnbull, D. Metastable Structures in Metallurgy. *Metall. Trans. A, Phys. Metall. Mater. Sci.* **1981**, *12 A* (5), 695–708.

(51) Huston, E. L.; Cahn, J. W.; Hilliard, J. E. Spinodal Decomposition during Continuous Cooling. *Acta Metall.* **1966**, *14* (9), 1053–1062.

(52) Lopez, V. M. H.; Sano, N.; Sakurai, T.; Hirano, K. A Study of Phase Decomposition in Cu-Ni-Fe Alloys. *Acta Met. Mater.* **1993**, *41* (1), 265–271.

(53) Butler, E. P.; Thomas, G. Structure and Properties of Spinodally Decomposed Cu-Ni-Fe Alloys. *Acta Metall.* **1970**, *18*, 347–366.

(54) Cahn, J. W. On Spinodal Decomposition. *Acta Metall.* **1961**, *9* (9), 795–801.

(55) Yeung, M. T.; Akopov, G.; Lin, C.-W. W.; King, D. J.; Li, R. L.; Sobell, Z. C.; Mohammadi, R.; Kaner, R. B. Superhard W0.5Ta0.5B Nanowires Prepared at Ambient Pressure. *Appl. Phys. Lett.* **2016**, *109* (20), 3–6.

(56) Yeung, M. T.; Lei, J.; Mohammadi, R.; Turner, C. L.; Wang, Y.; Tolbert, S. H.; Kaner, R. B. Superhard Monoborides: Hardness Enhancement through Alloying in W1−xTaxB. *Adv. Mater.* **2016**, *28*, 6993–6998.

(57) Murray, J. L.; Liao, P. K.; Spear, K. E.; Murray J.L., Liao P.K., and S. K. E. B-Ti (Boron-Titanium). In *Binary Alloy Phase Diagrams, Vol. 1*; Massalski, T. B., Ed.; ASM International: Materials Park, 1990; pp 544–548.

(58) Duschanek, H., Rogl, P.; Duschanek, H.; Rogl, P.; Duschanek, H., Rogl, P.; Duschanek, H.; Rogl, P. Critical Assessment and Thermodynamic Calculation of the Binary System Boron-Tungsten (B-W). *J. Phase Equilibria* **1995**, *16* (2), 150–161.

(59) Akopov, G.; Yeung, M. T.; Roh, I.; Sobell, Z. C.; Yin, H.; Mak, W. H.; Khan, S. I.; Kaner, R. B. Effects of Dodecaboride Forming Metals on the Properties of Superhard Tungsten Tetraboride. *Chem. Mater.* **2018**, *30*, 3559–3570.

(60) Akopov, G.; Roh, I.; Sobell, Z. C.; Yeung, M. T.; Pangilinan, L.; Turner, C. L.; Kaner, R. B. Effects of Variable Boron Concentration on the Properties of Superhard Tungsten Tetraboride. *J. Am. Chem. Soc.* **2017**, *139* (47), 17120–17127.

(61) Park, H.; Encinas, A.; Scheifers, J. P.; Zhang, Y.; Fokwa, B. P. T. Boron-Dependency of Molybdenum Boride Electrocatalysts for the Hydrogen Evolution Reaction. *Angew. Chemie - Int. Ed.* **2017**, *56* (20), 5575–5578.

(62) Carenco, S.; Portehault, D.; Boissière, C.; Mézailles, N.; Sanchez, C. Nanoscaled Metal Borides and Phosphides: Recent Developments and Perspectives. *Chem. Rev.* **2013**, *113*, 7981–8065.

(63) Portehault, D.; Delacroix, S.; Gouget, G.; Grosjean, R.; Chan-Chang, T.-H.-C. Beyond the Compositional Threshold of Nanoparticle-Based Materials. *Acc. Chem. Res.* **2018**, *51*, 930–939.

(64) Gouget, G.; Debecker, D. P.; Kim, A.; Olivieri, G.; Gallet, J. J.; Bournel, F.; Thomas, C.; Ersen, O.; Moldovan, S.; Sanchez, C.; et al. In Situ Solid-Gas Reactivity of Nanoscaled Metal Borides from Molten Salt Synthesis. *Inorg. Chem.* **2017**, *56* (15), 9225–9234.

(65) Han, W.; Wang, Z.; Li, Q.; Lian, X.; Liu, X.; Fan, Q.; Zhao, Y. Semiconductor-Insulator Transition in a YbB6 Nanowire with Boron Vacancy. *J. Solid State Chem.* **2018**, *262* (April), 244–250.

(66) Han, W.; Qiu, Y.; Zhao, Y.; Zhang, H.; Chen, J.; Sun, S.; Lan, L.; Fan, Q.; Li, Q. Low-Temperature Synthesis and Electronic Transport of Topological Insulator SmB_6 Nanowires. *CrystEngComm* **2016**, *18* (41), 7934–7939.

(67) Jothi, P. R.; Yubuta, K.; Fokwa, B. P. T. A Simple , General Synthetic Route toward Nanoscale Transition Metal Borides. *Adv. Mater.* **2018**, *1704181*, 1–6.

(68) Ade, M.; Hillebrecht, H. Ternary Borides Cr_2AlB_2, Cr_3AlB_4, and Cr_4AlB_6: The First Members of the Series $(CrB_2)_nCrAl$ with n = 1, 2, 3 and a Unifying Concept For . *Inorg. Chem.* **2015**, *54* (13), 6122–6135.

(69) Alameda, L. T.; Holder, C. F.; Fenton, J. L.; Schaak, R. E. Partial Etching of Al from MoAlB Single Crystals to Expose Catalytically Active Basal Planes for the Hydrogen Evolution Reaction. *Chem. Mater.* **2017**, *29* (21), 8953–8957.

(70) Zhang, H.; Xiang, H.; Dai, F. zhi; Zhang, Z.; Zhou, Y. First Demonstration of Possible Two-Dimensional MBene CrB Derived from MAB Phase Cr2AlB2. *J. Mater. Sci. Technol.* **2018**, 1–5.

(71) Oliynyk, A. O.; Mar, A. Discovery of Intermetallic Compounds from Traditional to Machine-Learning Approaches. *Acc. Chem. Res.* **2018**, *51* (1), 59–68.